A High-Efficiency Grid-Tie Battery Energy Storage System

Hao Qian

Dissertation submitted to the faculty of the Virginia Polytechnic Institute and State University in partial fulfillment of the requirements for the degree of

Doctor of Philosophy
In
Electrical Engineering

Jih-Sheng Lai, Chair
Wensong Yu
Kathleen Meehan
Douglas K. Lindner
Douglas J. Nelson

August 31, 2011
Blacksburg, Virginia

Keywords: Microgrid, lithium-ion battery, battery energy storage system, battery management system, bidirectional ac-dc converter, inverter mode, rectifier mode

A High-Efficiency Grid-Tie Battery Energy Storage System

Hao Qian

ABSTRACT

Lithium-ion based battery energy storage system has become one of the most popular forms of energy storage system for its high charge and discharge efficiency and high energy density. This dissertation proposes a high-efficiency grid-tie lithium-ion battery based energy storage system, which consists of a LiFePO4 battery based energy storage and associated battery management system (BMS), a high-efficiency bidirectional ac-dc converter and the central control unit which controls the operation mode and grid interface of the energy storage system. The BMS estimates the state of charge (SOC) and state of health (SOH) of each battery cell in the pack and applies active charge equalization to balance the charge of all the cells in the pack. The bidirectional ac-dc converter works as the interface between the battery pack and the ac grid, which needs to meet the requirements of bidirectional power flow capability and to ensure high power factor and low THD as well as to regulate the dc side power regulation.

A highly efficient dual-buck converter based bidirectional ac-dc converter is proposed. The implemented converter efficiency peaks at 97.8% at 50-kHz switching frequency for both rectifier and inverter modes. To better utilize the dc bus voltage and eliminate the two dc bus bulk capacitors in the conventional dual-buck converter, a novel bidirectional ac-dc converter is proposed by replacing the capacitor leg of the dual-buck converter based single-phase bidirectional ac-dc converter with a half-bridge switch leg. Based on the single-phase bidirectional ac-dc converter topology, three novel three-phase bidirectional ac-dc converter topologies are proposed.

In order to control the bidirectional power flow and at the same time stabilize the system in mode transition, an admittance compensator along with a quasi-proportional-

resonant (QPR) controller is adopted to allow smooth startup and elimination of the steady-state error over the entire load range. The proposed QPR controller is designed and implemented with a digital controller. The entire system has been simulated in both PSIM and Simulink and verified with hardware experiments. Small transient currents are observed with the power transferred from rectifier mode to inverter mode at peak current point and also from inverter mode to rectifier mode at peak current point.

The designed BMS monitors and reports all battery cells parameters in the pack and estimates the SOC of each battery cell by using the Coulomb counting plus an accurate open-circuit voltage model. The SOC information is then used to control the isolated bidirectional dc-dc converter based active cell balancing circuits to mitigate the mismatch among the series connected cells. Using the proposed SOC balancing technique, the entire battery storage system has demonstrated more capacity than the system without SOC balancing.

To my parents

Genrong Qian and Youzhu Xu

To my wife and son

Yanfei Shen and Siyuan Qian

Acknowledgements

With sincere gratitude in my heart, I would like to thank my advisor, Dr. Jason Lai, for his guidance, encouragement and support throughout this work and my study here at Virginia Tech. His extensive knowledge, broad vision, zealous research attitude and creative thinking have been a source of inspiration for me. I was so lucky to have the opportunity to pursue my graduate study as his student at the Future Energy Electronics Center (FEEC).

I would like to express my appreciation to Dr. Wensong Yu. I am incredibly fortunate to have had the opportunity to work with him. The experience working with him is a great time period which I will never forget. His guidance and patience during my research are greatly appreciated.

I am also grateful to the other members of my advisory committee, Dr. Kathleen Meehan, Dr. Douglas K. Lindner and Dr. Douglas J. Nelson for their valuable suggestions and numerous help.

I wish to give my special thank to Dr. Jianhui Zhang for his help in the system design and circuit implementation. I learned a lot from him and from our discussion during the time we were working together.

It has been a great pleasure to work with so many talented colleagues in the FEEC. I would like to thank Mr. Gary Kerr, Dr. Chien-Liang Chen, Mr. Pengwei Sun, Mr. Wei-Han Lai, Mr. Hidekazu Miwa, Mr. Chris Hutchens, Mr. Ahmed Koran, Mr. Daniel Martin, Mr. Bret Whitaker, Mr. Ben York and Mr. Zidong Liu for their helpful discussions, great supports and precious friendship. I would also like to thank the former FEEC members, Dr. Junhong Zhang, Dr. Sung-Yeul Park, Dr. Rae-Young Kim, Mr. William Gatune and Mr. Seungryul Moon for their great help during my research work.

I highly appreciate my wife, Yanfei Shen, for the love and understanding, encouragement, and sacrifice. It was your love that gave me the strength and the courage to go through this special journey. Thanks to my lovely son, Siyuan, who brings me the pride and happiness of being a father.

My deepest gratitude is sent to my parents, Genrong Qian and Youzhu Xu, for their love and support.

This work was supported by National Semiconductor Corporation (Santa Clara, CA).

Table of Contents

ABSTRACT ii
Dedication. iv
Acknowledgements v
List of Figures x
List of Tables xv
Chapter 1 Introduction 1
1.1 Background 1
1.2 State-of-the-art Battery Management System 3
1.2.1 Introduction to Battery Management System 3
1.2.2 SOC Estimation 3
1.2.3 Charge Equalization 4
1.3 State-of-the-art Bidirectional AC-DC Converter 6
1.3.1 Introduction to Bidirectional AC-DC Converter 6
1.3.2 Single-Phase Bidirectional AC-DC Converter 7
1.3.3 Three-Phase Bidirectional AC-DC Converter 9
1.3.4 Soft-Switching Techniques in Bidirectional AC-DC Converter 12
1.4 State-of-the-art Bidirectional AC-DC Converter Control 13
1.5 Research Motivation 14
1.5.1 Battery SOC Estimation Challenge 14
1.5.2 Charge Equalizer Design Challenge 14
1.5.3 Bidirectional AC-DC Converter Topology 14
1.5.4 Bidirectional AC-DC Converter Mode Transition Control 15
1.6 Research Outline 15
Chapter 2 Dual-Buck Converter Based Bidirectional AC-DC Converter 19
2.1 Introduction 19
2.2 Motivation for High-Efficiency Bidirectional AC-DC Converter 21
2.3 Proposed Single-Phase Bidirectional AC-DC Converter 24
2.3.1 Single-Phase Bidirectional AC-DC Converter Topology 24

2.3.2 Operating Principle 25
2.3.3 Inductor Design and Optimization 29
2.3.4 Zero-Crossing Distortion and Solution 32
2.3.5 Simulation Results 40
2.3.6 Experimental Results 42
2.4 Single-Phase Bidirectional AC-DC Converter with Magnetic Integration 45
2.4.1 Coupled Inductor in Series with Small Inductors 46
2.4.2 Two Coupled Inductors in Series 54
2.5 Summary 63
Chapter 3 Novel Bidirectional AC-DC Converter 65
3.1 Introduction 65
3.2 Novel Single-Phase Bidirectional AC-DC Converter 65
3.2.1 Topology 65
3.2.2 Operating Principle 66
3.2.3 Simulation Results 69
3.2.4 Experimental Results 70
3.3 Novel Single-Phase Bidirectional AC-DC Converter with Magnetic Integration 71
3.3.1 Coupled Inductor in Series with Small Inductors 73
3.3.2 Two Coupled Inductors in Series 82
3.4 Novel Three-Phase Bidirectional AC-DC Converter 93
3.4.1 Novel Three-Phase Bidirectional AC-DC Converter Topologies 95
3.4.2 Operating Principle 97
3.4.3 Simulation Results 99
3.5 Summary 102
Chapter 4 Unified Controller for Bidirectional Power Flow Control 103
4.1 Introduction 103
4.2 Unified Controller Concept 103
4.3 Unified Controller Design 107
4.3.1 Modeling of the Power Stage 107
4.3.2 Unified Controller Design 109

4.3.3 Discretization of the QPR current controller 113
4.4 Simulation Results 116
4.4.1 PSIM Simulation 116
4.4.2 Simulink Simulation 118
4.5 Experimental Results 121
4.6 Summary 122
Chapter 5 Grid-Tie Battery Energy Storage System Design 123
5.1 Introduction 123
5.2 Battery Management System Configuration 124
5.3 SOC Estimation 126
5.4 Charge Equalization 128
5.5 System Control and Power Management 129
5.6 Experimental Results 132
5.6.1 Battery Pack Charging and Discharging Waveforms 132
5.6.2 Effectiveness of the SOC Balancing Control 133
5.6.3 System Efficiency 136
5.7 Summary 137
Chapter 6 Conclusions and Future Work 138
6.1 Summary 138
6.2 Future Work 140
References 142

List of Figures

Figure 1.1 Simplified diagram of the lithium-ion battery energy storage system 2
Figure 1.2 Classification of conventional charge equalization methods 5
Figure 1.3 Illustration of bidirectional power flow..... 6
Figure 1.4 Circuit diagram of a single-phase four-switch bidirectional ac-dc converter 7
Figure 1.5 Circuit diagram of the proposed bidirectional ac-dc converter. 8
Figure 1.6 Circuit diagram of the novel bidirectional ac-dc converter. 9
Figure 1.7 Circuit diagram of a three-phase six-switch bidirectional ac-dc converter. 9
Figure 1.8 Circuit diagram of a three-phase bidirectional ac-dc converter with split capacitors for neutral connection. 10
Figure 1.9 Circuit diagram of a three-phase four-leg bidirectional ac-dc converter.11
Figure 1.10 Circuit diagram of a novel three-phase bidirectional ac-dc converter. 11
Figure 1.11 Circuit diagram of a three-phase coupled magnetic type ZVS inverter. 12
Figure 2.1 One day wind energy production of Tehachapi in April 2005. 20
Figure 2.2 Energy storage systems based microgrid configuration. 21
Figure 2.3 Circuit diagram of the traditional single-phase four-switch bidirectional ac-dc converter. 22
Figure 2.4 Operating under inverter mode for one switching cycle. (a) S_1 and S_4 are on. (b) Diode of S_3 and S_4 are on. 23
Figure 2.5 Circuit diagram of the proposed bidirectional ac-dc converter. 24
Figure 2.6 Definition of different modes based on phase angle difference between voltage and current waveforms. (a) Circuit diagram. (b)Inverter mode (In phase). (c) i_{ac} lags v_{ac} by 90°. (d) i_{ac} leads v_{ac} by 90°. (e) Rectifier mode (180° Out of phase). 25
Figure 2.7 Operating under rectifier mode with pure active power transferring. (a) Conceptual voltage and current waveform. (b) a_1 is on. (c) D_1 is on. (d) a_2 is on. (e) D_2 is on. 26
Figure 2.8 Operating under inverter mode with pure active power transferring. (a) Conceptual voltage and current waveform. (b) a_1 is on. (c) D_1 is on. (d) a_2 is on. (e) D_2 is on. 28
Figure 2.9 Operating under active and reactive power transferred between ac grid and dc source. (a) Conceptual voltage and current waveform. (b) Region 1, a_2 and D_2 are on. (c) Region 2, a_1 and D_1 are on. (d) Region 3, a_1 and D_1 are on. (e) Region 4, a_2 and D_2 are on. 29
Figure 2.10 Waveforms of ac voltage, ac current and inductor currents under split SPWM. 32
Figure 2.11 Equivalent circuit of the converter under split SPWM. 33
Figure 2.12 Current waveform of DCM near zero-crossing region under split SPWM. 33
Figure 2.13 Current waveforms under joint SPWM. 34

Figure 2.14 Equivalent circuit of the converter under joint SPWM. 35
Figure 2.15 Current waveform near zero-crossing region under joint SPWM. 35
Figure 2.16 Simulation results of the converter under split SPMW. (a) Waveforms over cycles. (b) Waveforms near zero-crossing region 36
Figure 2.17 Simulation results of the converter under joint SPMW. (a) Waveforms over cycles. (b) Waveforms near zero-crossing region. 37
Figure 2.18 Simulation results of the converter under the proposed new SPMW. (a) Waveforms over cycles. (b) Waveforms near zero-crossing region. 38
Figure 2.19 Experimental results of the converter. (a) Results under split SPWM. (b) Results under the proposed new SPWM. 39
Figure 2.20 Simulation results under (a) rectifier mode and (b) inverter mode, both with v_{ac} = 30 V_{rms} and i_{ac} = 23 A_{rms}. 40
Figure 2.21 Simulation results with reactive power flow. (a) Current leads voltage by 90°. (b) Current lags voltage by 90°. 41
Figure 2.22 Experimental results under (a) rectifier mode and (b) inverter mode, both with v_{ac} = 30 V_{rms} and i_{ac} = 23 A_{rms}. 42
Figure 2.23 Experimental results with reactive power flow. (a) Current leads voltage by 90°. (b) Current lags voltage by 90°. 43
Figure 2.24 Prototype of the proposed bidirectional ac-dc converter. 44
Figure 2.25 Experimental efficiency for both rectifier and inverter modes. 44
Figure 2.26 The proposed converter operating under inverter mode during the period when ac current is positive. 45
Figure 2.27 The proposed converter operating under inverter mode during the period when ac current is negative. 45
Figure 2.28 Bidirectional ac-dc converter with one coupled inductor. 46
Figure 2.29 The proposed converter operating during the period when ac current is positive. The inactive components are shown in dashed lines. 47
Figure 2.30 The proposed converter operating during the period when ac current is negative. The inactive components are shown in dashed lines. 47
Figure 2.31 Symmetrical model of the proposed converter with one coupled inductor under inverter mode. 48
Figure 2.32 The proposed converter with one coupled inductor operating under inverter mode when ac current is positive and a_1 is on. 49
Figure 2.33 The proposed converter with one coupled inductor operating under inverter mode when ac current is positive and D_1 is on. 50
Figure 2.34 Simulation results of the proposed converter with one coupled inductor under (a) rectifier mode and (b) inverter mode. 52
Figure 2.35 Experimental results of the proposed converter with one coupled inductor under (a) rectifier mode and (b) inverter mode. 53
Figure 2.36 Bidirectional ac-dc converter with two coupled inductors. 54
Figure 2.37 The proposed converter operating during the period when ac current is positive. The inactive components are shown in dashed lines. 54
Figure 2.38 The proposed converter operating during the period when ac current is negative. The inactive components are shown in dashed lines. 55
Figure 2.39 Symmetrical model of the proposed converter with two coupled inductors under rectifier mode. 56

Figure 2.40 The proposed converter with two coupled inductors operating under rectifier mode when ac current is positive and a_1 is on. 58
Figure 2.41 The proposed converter with two coupled inductors operating under rectifier mode when ac current is positive and D_1 is on. 58
Figure 2.42 Simulation results of the proposed converter with two coupled inductors under (a) rectifier mode and (b) inverter mode. 61
Figure 2.43 Experimental results of the proposed converter with two coupled inductors under (a) rectifier mode and (b) inverter mode. 62
Figure 3.1 Circuit diagram of the proposed novel single-phase bidirectional ac-dc converter. 65
Figure 3.2 Operating under rectifier mode with pure active power transferring. (a) Conceptual voltage and current waveform. (b) a_1 is on. (c) D_1 is on. (d) a_2 is on. (e) D_2 is on. 66
Figure 3.3 Operating under rectifier mode with pure active power transferring. (a) Conceptual voltage and current waveform. (b) a_1 is on. (c) D_1 is on. (d) a_2 is on. (e) D_2 is on. 68
Figure 3.4 Simulation results under (a) rectifier mode and (b) inverter mode. 69
Figure 3.5 Experimental results under (a) rectifier mode and (b) inverter mode. ... 70
Figure 3.6 The proposed converter operating under rectifier mode during the period when ac current is positive. 71
Figure 3.7 The proposed converter operating under rectifier mode during the period when ac current is negative. 71
Figure 3.8 The proposed converter operating under inverter mode during the period when ac current is positive. 72
Figure 3.9 The proposed converter operating under inverter mode during the period when ac current is negative. 72
Figure 3.10 Novel bidirectional ac-dc converter with one coupled inductor. 73
Figure 3.11 The proposed converter with one coupled inductor operating under rectifier mode during the period when ac current is positive. 73
Figure 3.12 The proposed converter with one coupled inductor operating under rectifier mode during the period when ac current is negative. 74
Figure 3.13 The proposed converter with one coupled inductor operating under inverter mode during the period when ac current is positive. 75
Figure 3.14 The proposed converter with one coupled inductor operating under inverter mode during the period when ac current is negative. 75
Figure 3.15 Symmetrical model of the proposed novel converter with one coupled inductor under inverter mode. 76
Figure 3.16 The proposed novel converter with one coupled inductor operating under inverter mode when ac current is positive and a_1 and a_4 are on. 77
Figure 3.17 The proposed novel converter with one coupled inductor operating under inverter mode when ac current is positive and D_1 and a_4 are on. 78
Figure 3.18 Simulation results of the proposed converter with one coupled inductor under (a) rectifier mode and (b) inverter mode. 80
Figure 3.19 Experimental results of the proposed converter with one coupled inductor under (a) rectifier mode and (b) inverter mode. 81
Figure 3.20 Novel bidirectional ac-dc converter with two coupled inductors. 82

Figure 3.21 The proposed converter with two coupled inductors operating under inverter mode during the period when ac current is positive. 82
Figure 3.22 The proposed converter with two coupled inductors operating under inverter mode during the period when ac current is negative. 83
Figure 3.23 The proposed novel converter with two coupled inductors operating under rectifier mode during the period when ac current is positive..... 84
Figure 3.24 The proposed novel converter with two coupled inductors operating under rectifier mode during the period when ac current is negative..... 84
Figure 3.25 Symmetrical model of the proposed novel converter with two coupled inductors under rectifier mode. 85
Figure 3.26 The proposed novel converter with two coupled inductors operating under rectifier mode when ac current is positive and D_1 and a_3 are on. 87
Figure 3.27 The proposed novel converter with two coupled inductors operating under rectifier mode when ac current is positive and a_1 and a_3 are on. 87
Figure 3.28 Picture of the constructed separate inductors. 90
Figure 3.29 Picture of the constructed two coupled inductors..... 90
Figure 3.30 Simulation results of the proposed converter with two coupled inductors under (a) rectifier mode and (b) inverter mode. 91
Figure 3.31 Experimental results of the proposed converter with two coupled inductors under (a) rectifier mode and (b) inverter mode. 92
Figure 3.32 Circuit diagram of the traditional three-phase six-switch bidirectional ac-dc converter. 93
Figure 3.33 Operating under inverter mode for one switching cycle. (a) S_1, S_6 and S_2 are on. (b) Diode of S_4, S_6 and S_2 are on. 94
Figure 3.34 Circuit diagram of a novel three-phase bidirectional ac-dc converter. 95
Figure 3.35 Circuit diagram of a novel three-phase bidirectional ac-dc converter with split capacitors for neutral connection. 96
Figure 3.36 Circuit diagram of a novel three-phase bidirectional ac-dc converter with extra leg..... 96
Figure 3.37 Ideal three-phase current waveforms..... 97
Figure 3.38 Operating under inverter mode phase angle is between 60° and 120°. (a) Gate signals. (b) Mode 1, D_1, b_2 and b_3 are on. (c) Mode 2, a_1, b_2 and b_3 are on. (d) Mode 3, a_1, D_4 and D_6 are on. 99
Figure 3.39 Simulation results under (a) rectifier mode and (b) inverter mode. ... 100
Figure 3.40 Simulation results with reactive power flow. (a) Current leads voltage by 90°. (b) Current lags voltage by 90°. 101
Figure 4.1 Separate controller controlled system. 104
Figure 4.2 Unified controller controlled system. 104
Figure 4.3 Operating under rectifier mode with pure active power transferring. (a) Conceptual voltage and current waveform. (b) a_1 is on. (c) D_1 is on. 105
Figure 4.4 Operating under inverter mode with pure active power transferring. (a) Conceptual voltage and current waveform. (b) a_1 is on. (c) D_1 is on. 106
Figure 4.5 Circuit diagram of the bidirectional ac-dc converter with current control loop. 108
Figure 4.6 Block diagram of the current control loop. 109

Figure 4.7 Block diagram of the current control loop with the adding admittance compensator. 110
Figure 4.8 Block diagram of the current control loop with the adding admittance compensator for derivation. 110
Figure 4.9 Circuit diagram of the bidirectional ac-dc converter with current control loop and admittance compensation. 111
Figure 4.10 Bode plot of the compensated loop gain $T_i(s)$. 112
Figure 4.11 Block diagram representation of the digital resonant controller. 114
Figure 4.12 Digital implementation of resonant controller in FPGA. 114
Figure 4.13 Bode plots of the analog controller, the digital controller, and the digital controller with truncation. 115
Figure 4.14 Comparison of frequency response magnitudes of the analog controller, the digital controller, and the digital controller with truncation. 116
Figure 4.15 Power stage in PSIM. 116
Figure 4.16 Control circuit in PSIM. 117
Figure 4.17 Simulation results under (a) rectifier mode and (b) inverter mode, both with v_{ac} = 30 V_{rms} and i_{ac} = 28 A_{rms}. 118
Figure 4.18 Power stage in PSIM. 118
Figure 4.19 Control circuit in Simulink. 119
Figure 4.20 Simulation results under (a) rectifier mode and (b) inverter mode, both with v_{ac} = 30 V_{rms} and i_{ac} = 28 A_{rms}. 120
Figure 4.21 Experimental results of seamless energy transfer. (a) Changing from rectifier mode to inverter mode at the peak current point. (b) Changing from inverter mode to rectifier mode at the peak current point. 121
Figure 5.1 Circuit diagram of a lithium-ion battery energy storage system 123
Figure 5.2 Proposed BMS configuration. 125
Figure 5.3 (a) Open circuit voltage versus SOC curve. (b) SOC look-up tables for different temperatures. 127
Figure 5.4 One battery module in the box. 130
Figure 5.5 Control block diagram for the battery energy storage system 130
Figure 5.6 Experimental results of repetitively charging and discharging of the battery pack with a SOC between 30% and 70%. (a) Voltage versus time. (b) SOC versus time 133
Figure 5.7 Experimental results of discharging and charging of one battery module. (a) Discharging without SOC balancing control. (b) Charging without SOC balancing control. (c) Discharging with SOC balancing control. (d) Charging with SOC balancing control. 135
Figure 5.8 Experimental results of repetitively charging and discharging of the battery pack with SOC ranging between 30% and 70%. 136

List of Tables

Table 1.1 Comparison of different SOC estimation schemes 4
Table 2.1 Forecast generation in California by technology-nameplate ratings 19
Table 2.2 Comparison of design results based on different Kool Mμ cores 31
Table 3.1 Different switching combinations 68
Table 5.1 Comparison of different SOC estimation schemes 126

Chapter 1 Introduction

1.1 Background

With the increased concerns on environment and cost of energy, more renewable energy sources are integrated into the power grid in the form of distributed generation (DG). California has mandated that 20% of its power come from renewables by 2010 and 33% by 2020. Many other states and countries have similar regulations. The renewable energy source based DG systems are normally interfaced to the grid through power electronic converters and energy storage systems. A systematic organization of these DG systems, energy storage systems, and a cluster of loads forms a microgrid. The microgrid not only has the inherited advantages of single DG system but also offers more control flexibilities to fulfill system reliability and power quality requirement with proper management and control [1]-[6].

Rather than using fossil fuel, energy storage such as battery or ultra-capacitor systems can be used to provide fast frequency regulation, load following and ramping services when the DGs are integrated into the power grid [7]-[17]. Recent developments in lithium-ion battery technology show many advantages compared to lead-acid batteries and nickel-metal hydride batteries, such as high power and energy density, high working cell voltage, low self-discharge rate and high charge-discharge efficiency [18]-[22].

As shown in Figure 1.1, the energy storage system consists of three subsystems, a $LiFePO_4$ battery pack and associated battery management system (BMS), a bidirectional ac-dc converter, and the central control unit which controls the operation mode and grid interface of the energy storage system. The BMS controller monitors the parameters of each battery cell, such as cell voltage, temperature, charge and discharge current; estimates the state of charge (SOC) and state of health (SOH) of each battery cell in the pack. The SOC information is then used to control the charge equalization circuits to mitigate the mismatch among the series connected battery cells. The SOC and SOH information is also used by the central control unit to determine the operating mode of the

energy storage system. The bidirectional ac-dc converter works as the interface between the battery pack and the ac grid, which needs to meet the requirements of bidirectional power flow capability and to ensure high power factor and low THD as well as regulate the dc side power regulation.

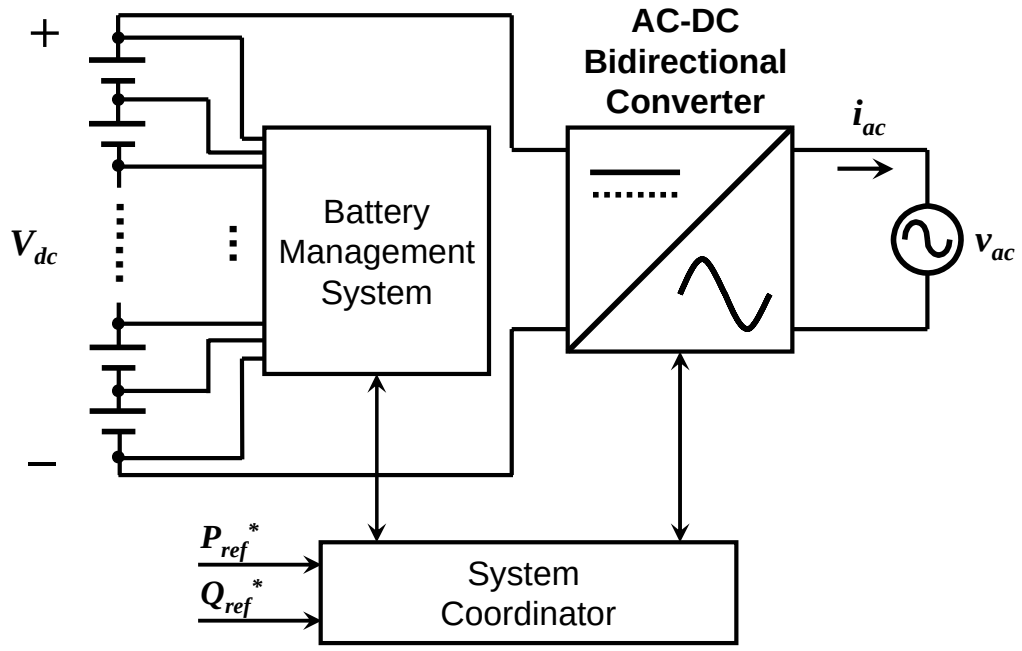

Figure 1.1 Simplified diagram of the lithium-ion battery energy storage system

In this dissertation, a background description and review of the state-of-the-art BMS and bidirectional ac-dc converters [23]-[26] are presented firstly to define this work and its novelty. Then, the challenges will be identified related to the design and control issues in the present battery energy storage systems. The high-efficiency bidirectional ac-dc converter in the dissertation clearly demonstrated the feasibility of bidirectional power flow capability with the proposed control method [27]-[29]. Detailed operating modes and energy transfer mechanism have been described. To better utilize the dc bus voltage and eliminate the two dc bus capacitors, a novel bidirectional ac-dc converter is proposed by replacing the two-capacitor leg of the dual-buck converter based single-phase bidirectional ac-dc converter with a two-switch leg. To further reduce the size of the inductors, several novel topologies with optimized magnetic integration are proposed.

Experimental results have demonstrated that the proposed high-efficiency battery energy storage system effectively mitigates the mismatch among the series connected cells and support reactive power flow and seamless energy transfer.

1.2 State-of-the-art Battery Management System

1.2.1 Introduction to Battery Management System

In a lithium-ion battery system, BMS is the key component to ensure all cell voltages being strictly kept in boundaries for safety operation and cycle life. There are two key functions of the BMS in this work – monitoring and charge equalization.

First, the BMS monitors the status of all the series connected lithium-ion battery cells in the system. The parameters being monitored include cell voltage, cell temperature, charging or discharging current. The voltage, current and temperature information are then processed by the BMS controller to determine the SOC, SOH and capacity of each battery cell.

Second, the BMS applies active balancing to equalize the charge of the cells in the pack and to ensure all the cells operating in the designed SOC range. Due to production deviations, inhomogeneous aging, and temperature difference within the battery pack, there are SOCs or capacities imbalances between battery cells. Minimizing the mismatches across all the cells is important to guarantee the power or energy performance of the pack.

1.2.2 SOC Estimation

SOC is a measure of the amount of electrochemical energy left in a cell or battery. It is expressed as a percentage of the battery capacity and indicates how much charge (energy) stored in an energy storage element. It has been a long-standing challenge for battery industry to precisely estimate the SOC of lithium-ion batteries. The electrochemical reaction inside batteries is very complicated and hard to model electrically in a reasonably accurate way. So far, the state-of-the-art SOC accuracy for electric vehicle/plug-in hybrid EV (EV/PHEV) applications is in the range of 5%-10% [30]-[33].

Table 1.1 shows the comparison of different SOC estimation schemes. Among all the practical techniques, the Coulomb counting plus an accurate open-circuit voltage model is the algorithm being used here to estimate the SOC for its high accuracy with a relatively simple implementation.

Table 1.1 Comparison of different SOC estimation schemes

Technique	Summarized Features	Pros	Cons
Discharge	Discharge with DC current and measure time to a certain threshold	Most accurate	Offline Time and energy consuming
Coulomb counting	Counting charges that have been injected/pumped out of battery	Online Easy	Loss model Need accuracy
Open circuit voltage	VOC-SOC look-up table	Online Accurate	Time consuming
Artificial neural network	Adaptive artificial neural network system	Online	Training data needed
Impedance	Impedance of the battery (RC combination)	Online SOC and SOH	Cost Temp-sensitive
DC resistance	R_{dc}	Online Easy	Cost Temp-sensitive
Kalman filter	Get accurate information out of inaccurate data using Kalman filter	Online Dynamic	Large computing Model needed

1.2.3 Charge Equalization

Due to inevitable differences in chemical and electrical characteristics from manufacturing, aging, and ambient temperatures, there are SOC or capacity imbalances between battery cells. When these unbalanced batteries are left in use without any control, such as cell equalization, the energy storage capacity decreases severely. Thus, charge

equalization for a series connected battery string is necessary to minimize the mismatches across all the cells and extend the battery lifecycle.

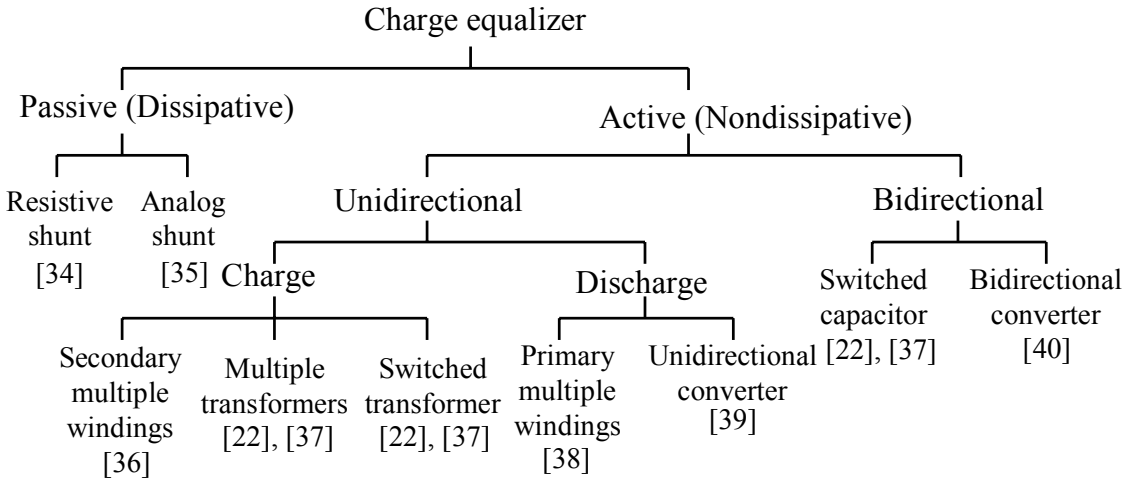

Figure 1.2 Classification of conventional charge equalization methods

Charge balancing methods can be classified into two categories: active and passive [34]-[40]. Active cell balancing helps balance the cells in a battery module to maintain the same voltage or SOC by monitoring and injecting appropriate balancing current into individual battery cell based on the balancing scheme. Compared with the traditional passive cell balancing approach, the active cell balancing offers the advantage of high system efficiency and fast balancing time. As shown in Figure 1.2, the active cell balancing method can be divided into two groups: unidirectional and bidirectional cell balancing. Among these schemes, multiple-winding transformer-based solutions are attractive for their effective low-cost equalization. However, it is difficult to implement multiple windings in a single transformer when the lithium-ion battery string consists of more than 100 cells in electric vehicle (EV) application. The switched capacitor-based solution is also not considered for the long equalization time. A modularized charge equalizer based on switched transformer and bidirectional dc-dc converter schemes is employed in this dissertation. The isolated bidirectional dc-dc converter regulates from the 12-cell battery stack voltage to each individual cell voltage. The average current-mode control is employed such that the average inductor current is regulated to the command current, which is set by the active cell-balancing control algorithm.

1.3 State-of-the-art Bidirectional AC-DC Converter

1.3.1 Introduction to Bidirectional AC-DC Converter

Traditionally, full-wave diode bridge or thyristor converters were employed to synthesize dc voltage from the ac grid. These rectifiers pollute the grid with undesired input ac current harmonics. Ac-dc converters with pulse width modulation (PWM) are employed to increase power factor and reduce current harmonics.

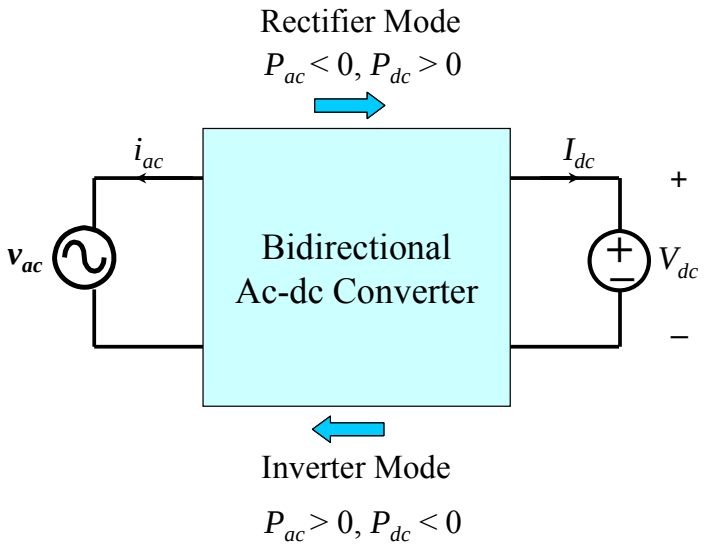

Figure 1.3 Illustration of bidirectional power flow

In a battery energy storage system, a bidirectional ac-dc converter with a proper charging-discharging profile is required to transfer energy between the battery pack and the ac grid. An ac-dc converter with bidirectional power flow capability is shown in Figure 1.3, where P_{ac} is defined as the active power that ac side receives and P_{dc} is defined as the power that dc side receives. The converter works as a rectifier when the power is transferred from ac grid to dc sources ($P_{ac} < 0$ and $P_{dc} > 0$). Alternately, it works as an inverter when the power is transferred from dc sources to ac grid ($P_{ac} > 0$ and $P_{dc} < 0$).

To realize bidirectional power flow in ac-dc converters, the power switch should carry the current in both directions. It is usually implemented with the power Metal-Oxide-

Semiconductor-Field-Effect-Transistor (MOSFET) or the Insulated-Gate Bipolar-Transistor (IGBT) in parallel with a diode.

1.3.2 Single-Phase Bidirectional AC-DC Converter

Various topologies that are capable of running with bidirectional power flow have been proposed [41]-[53]. Basically they are divided into two types: non-isolated and isolated converters, meeting different application requirements. The high-frequency transformer based system is an attractive solution to obtain isolation between ac grid and dc source. However, the non-isolated converters are more attractive because these systems are lower in cost and more efficient.

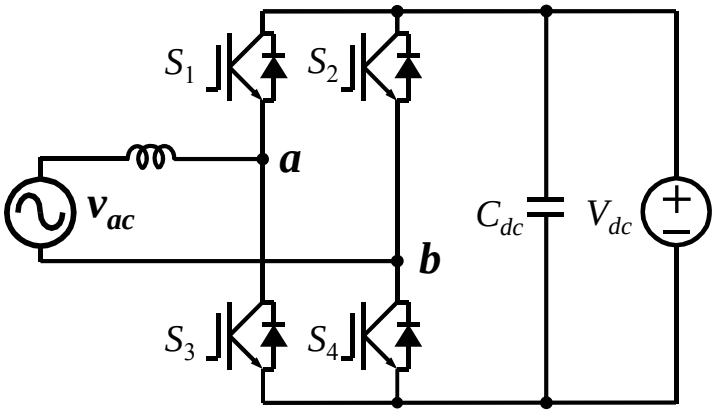

Figure 1.4 Circuit diagram of a single-phase four-switch bidirectional ac-dc converter

For the single-phase converter, the commonly used bidirectional converter topology consists of four power switches as shown in Figure 1.4. For this topology, the power MOSFET cannot be used as the main switch in the high-voltage high-power applications because the intrinsic MOSFET body diode conduction could cause device failure. The IGBT can be used as the main switch for the single-phase converter. However, an IGBT has higher switching and conduction losses compared with a power MOSFET. Also the IGBT only allows operating at a lower switching frequency than the power MOSFET allows, thus resulting in a larger filter size.

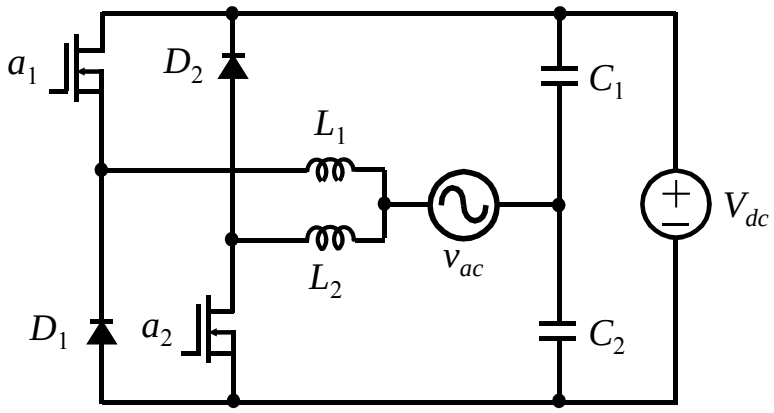

Figure 1.5 Circuit diagram of the proposed bidirectional ac-dc converter.

As shown in Figure 1.5, the high-efficiency bidirectional ac-dc converter in the dissertation adopts opposed current half bridge inverter architecture [23]. Since it consists of two buck converters and also has features of the conventional half bridge inverter, it is named as dual-buck half bridge inverter [24]-[26]. By using MOSFET device, not only can the switching loss be almost eliminated but also the conduction loss can be significantly reduced. The converter exhibits two distinct merits: first, there is no shoot-through issue because no active power switches are connected in series in each phase leg; second, the reverse recovery dissipation of the power switch is greatly reduced because there is no freewheeling current flowing through the body diode of power switches. The converter works as a rectifier when the power is transferred from ac grid to dc source. Alternately, it works as an inverter when the power is transferred from dc source to ac grid. The dissertation will show how this high-efficiency, high-reliability inverter can be used as the interface between the ac grid and the dc energy storage for bidirectional power flow operation [27]-[29]. It can also support reactive power flow and seamless energy transfer.

To better utilize the dc bus voltage and to eliminate the two dc bus capacitors, a novel bidirectional ac-dc converter is derived from Figure 1.5 by replacing the two-capacitor leg with a two-switch leg, as shown in Figure 1.6. The novel bidirectional ac-dc converter keeps the merits of the dual-buck converter based bidirectional ac-dc converter. Meanwhile the two large dc bus capacitors are eliminated.

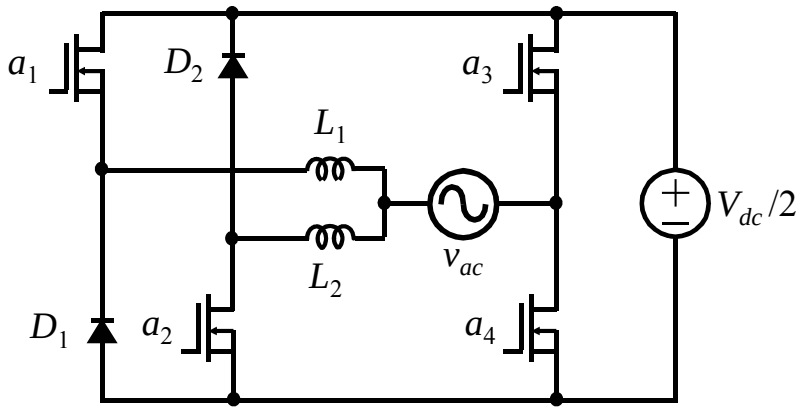

Figure 1.6 Circuit diagram of the novel bidirectional ac-dc converter.

To further reduce the size of the inductors, several novel topologies with optimized magnetic integration are also proposed.

1.3.3 Three-Phase Bidirectional AC-DC Converter

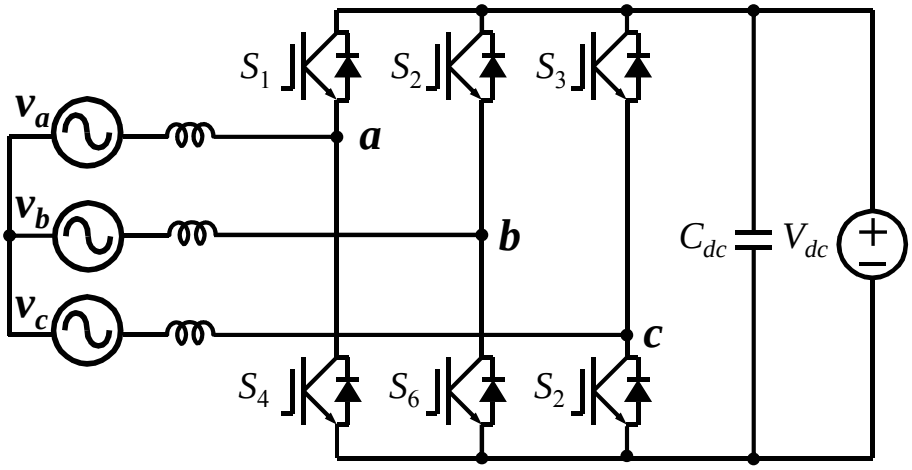

Figure 1.7 Circuit diagram of a three-phase six-switch bidirectional ac-dc converter.

Three-phase ac-dc conversion of electric power is widely employed in motor drive, uninterruptible power supplies, and utility interfaces with renewable sources such as solar photovoltaic systems and battery energy storage systems. Numerous three-phase

topologies that have bidirectional flow capability have been reported [54]-[66]. The commonly used bidirectional converter topology consists of six power switches as shown in Figure 1.7. Without neutral connection, third harmonic will not exist. There is no need to eliminate 3rd, 9th, etc. triplen harmonics. Similar to the single-phase case, the power MOSFET cannot be used as the main switch in the three-phase converter since the intrinsic MOSFET body diode conduction could cause device failure. The IGBT can be used as the main switch for the three-phase converter, but their high switching and conduction losses normally limits to a lower switching frequency and larger filter size.

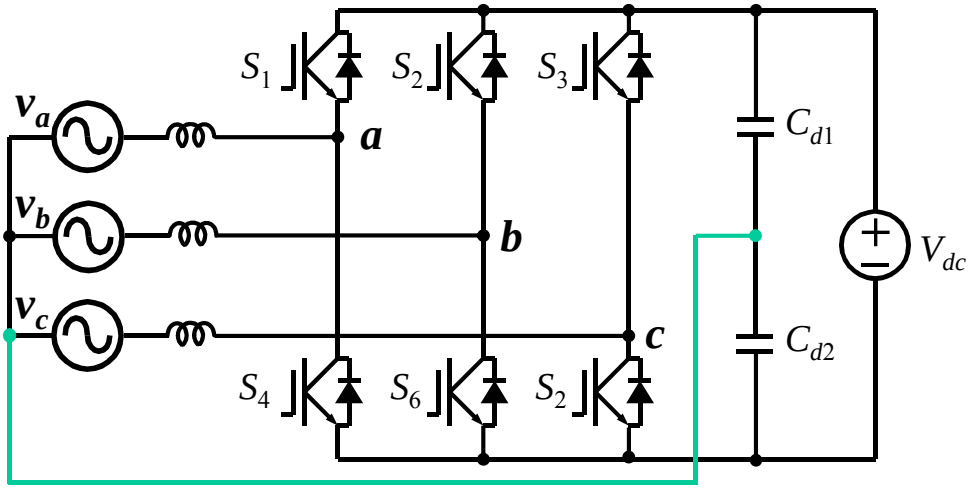

Figure 1.8 Circuit diagram of a three-phase bidirectional ac-dc converter with split capacitors for neutral connection.

Three-phase converter with split capacitors for neutral connection is shown in Figure 1.8. Under unbalanced ac load condition, dc bus capacitors absorb the neutral current to maintain better balanced ac output. The problem with this topology is excessive current stress on split capacitors when ac loads or lines are highly unbalanced.

Three-phase four-leg converter is shown in Figure 1.9. Neutral leg is controlled to equalize the three-phase outputs. The features with this converter are less bulky capacitors and reduced size of passive components. However, control is more complicated.

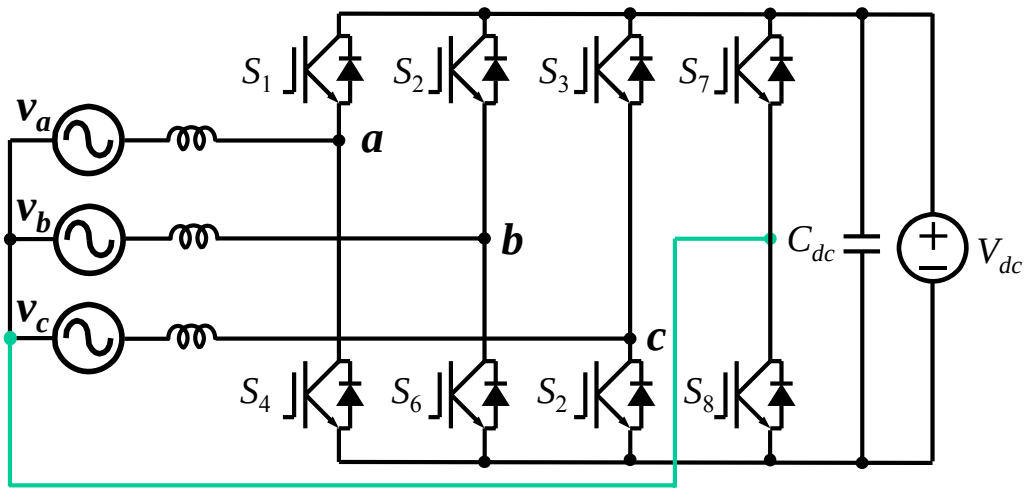

Figure 1.9 Circuit diagram of a three-phase four-leg bidirectional ac-dc converter.

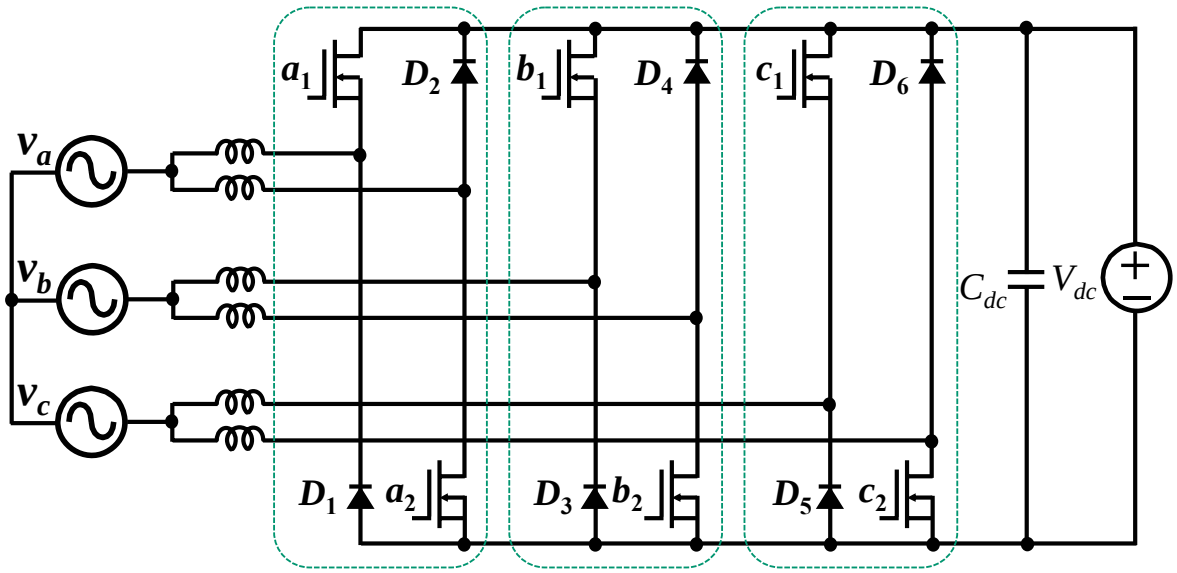

Figure 1.10 Circuit diagram of a novel three-phase bidirectional ac-dc converter.

A novel three-phase converter based on single-phase dual-buck converter is proposed, as shown in Figure 1.10. Besides the features of the single-phase dual-buck converter, the three-phase converter eliminates the two bulky dc bus capacitors.

1.3.4 Soft-Switching Techniques in Bidirectional AC-DC Converter

Soft-switching converters, especially zero-voltage switching (ZVS) inverters, on ac side using either coupled magnetic or split capacitors to reset resonant current have been studied for more than two decades [67]-[80]. Voltage source inverters also can achieve ZVS under rectifier mode. The auxiliary resonant commutated pole (ARCP) inverters achieve zero-voltage turn-on for main devices by using split capacitors to reset the resonant current [67]-[68]. However, the ARCP inverter needs extra control or circuits to balance the two dc link split capacitor voltages. In addition, the control for ZVS is complicated for the ARCP inverters.

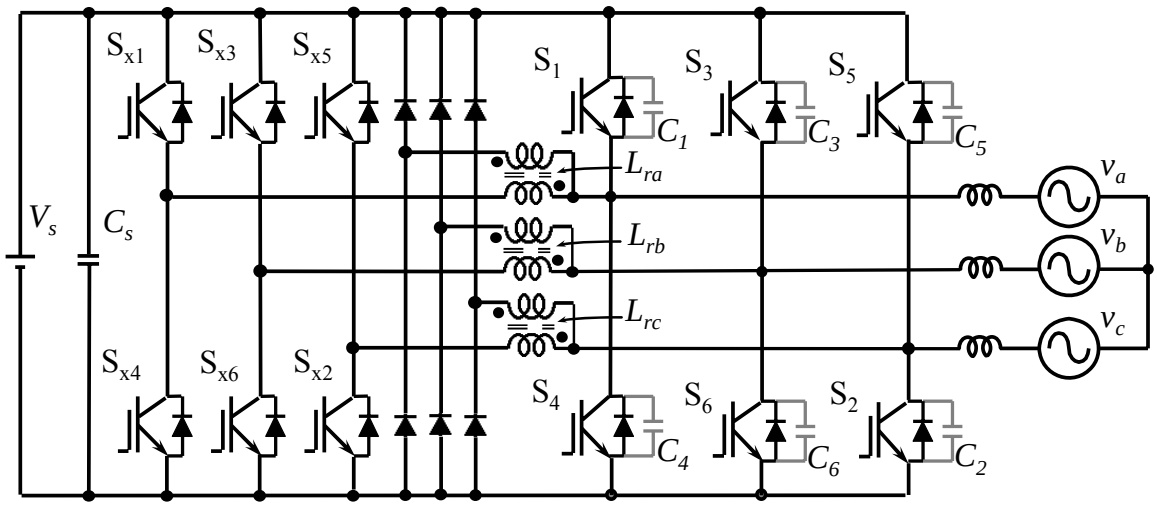

Figure 1.11 Circuit diagram of a three-phase coupled magnetic type ZVS inverter.

As shown in Figure 1.11, the coupled magnetic type ZVS inverters have been proposed to avoid capacitor voltage balance issue [72]-[78]. These inverters all feature zero-voltage turn-on for main devices and zero-current turn-off for auxiliary devices. The control for ZVS is simple because of possible non-unity turns ratio for coupled magnetic [78]. However, the problem with these inverters is that the magnetizing current of the coupled magnetic cannot be reset [73]. A new soft-switching inverter using two small coupled magnetics in one resonant pole was proposed to solve magnetizing current

resetting problem [80]. A variable timing control scheme was also proposed to ensure the main devices operating at ZVS from zero to full load [79].

1.4 State-of-the-art Bidirectional AC-DC Converter Control

Current control is widely used in the grid-tie bidirectional ac-dc converter applications because the grid side voltage is controlled by the ac grid. Current control technologies can by divided into two groups: linear control such as proportional-integral (PI) control and proportional-resonant (PR) control; and non-linear control, such as sliding mode control and hysteresis control.

PI control is the most widely used control method for ac-dc converters. Although the PI control can provide fast dynamic response combined with other control schemes, it still has the steady-state error issue.

PR control can produce high gains at the desired frequencies to eliminate the steady-state error [81]. One problem with this scheme is the numerical accuracy in actual implementation.

Sliding mode control has been proposed in a variable structure control based power conditioning system. It provides fast dynamic response and robustness as a non-linear control scheme, but it is difficult to show numerical data of the stability by applying conventional feedback method.

Hysteresis control provides extremely fast response compared to other control methods. However, it is difficult to filter the high-frequency voltage and current components because the switching frequency is variable.

Various control schemes has been proposed for bidirectional ac-dc converter applications. However, most designs follow the unidirectional ac-dc converter or dc-ac inverter controller design methodology. No mode transition discussion has been addressed since the power management is normally not included in the system design. For the design without smooth mode transition consideration, it will cause large voltage and current stress on devices, which result in device failures.

In the dissertation, an admittance compensator along with a quasi-proportional-resonant controller (QPR) is adopted to allow smooth mode transition and elimination of the steady-state error over the entire load range [82]-[84].

1.5 Research Motivation

1.5.1 Battery SOC Estimation Challenge

SOC is used to determine battery capacity. Among all the practical techniques, Coulomb counting is the most popular method to estimate the battery SOC. However, this method is not very accurate since it does not consider the effects of the temperature and charging and discharging efficiency. On the other hand, there is no way to estimate the initial SOC, and the accuracy depends on sensor precision. Therefore, this dissertation adopts the Coulomb counting along with an accurate open circuit voltage model to estimate the SOC. The open circuit voltage is measured by a 14-bit ADC.

1.5.2 Charge Equalizer Design Challenge

Charge equalizer is used to balance the individual battery cells in a battery module. Among the active cell balancing schemes, bidirectional cell balancing offers the advantage of fast balancing time. However, it is difficult to implement bidirectional cell balancing in a lithium-ion battery string consisting of more than 100 cells in electric vehicle (EV) application. A modularized charge equalizer based on switched transformer and bidirectional converter dc-dc schemes is employed in this dissertation.

1.5.3 Bidirectional AC-DC Converter Topology

The high-efficiency MOSFET dual-buck converter is chosen as the bidirectional ac-dc converter. The major issue with this type of converter is the requirement of two separate inductors. However, without shoot-through concern and dead time requirement, the switching frequency can be pushed higher to reduce the size of the inductor while maintaining low ripple current content. The question is how to design the switching frequency and other parameters. In other words, the tradeoff between efficiency and cost needs to be optimized.

A novel bidirectional ac-dc converter is derived from the dual-buck based bidirectional ac-dc converter.

1.5.4 Bidirectional AC-DC Converter Mode Transition Control

One important design aspect of the system is the smooth power flow transition control of the bidirectional ac-dc converter. For the battery energy storage system, the control needs to manage the wide range current in and out of the batteries and meantime ensure all cell SOCs being strictly kept in boundaries for safety operation. The transition between rectifier mode and inverter mode needs to be fast and smooth enough to guarantee energy effectively transferred without causing system instability and failure.

A unified current controller is proposed to generate only one command instead of two separate commands for rectifier mode and inverter mode. The energy management can switch from one mode to the other mode immediately by changing the phase angle information of the current reference.

1.6 Research Outline

The research outline is list as follows.

- A dual-buck converter based bidirectional ac-dc converter is proposed. The dual-buck converter has not been used in rectifier mode operation. The implemented converter efficiency peaks at 97.8% at 50-kHz switching frequency for both rectifier and inverter modes.
- A novel bidirectional ac-dc MOSFET converter is proposed to eliminate the two dc bus capacitors. The implemented converter efficiency peaks at 98.0% at 50-kHz switching frequency for both rectifier and inverter modes.
- A unified digital controller is proposed to control the bidirectional power flow and stabilize the system in mode transition.
- With SOC balancing, the battery energy storage system has gained much more capacity than the system without SOC balancing.

The dissertation consists of six chapters, which are organized as follows.

Chapter 1 introduces the research background. The main research objective is to design a high-efficiency grid-tie battery energy storage system capable of smoothly transferring energy with grid. Various SOC estimation and charge equalization

approaches are described and discussed for the BMS. Different bidirectional ac-dc converter topologies are investigated. The dual-buck type converter is employed as the bidirectional ac-dc converter. Smooth mode transition in bidirectional power flow control is required in the system design. At last, the research objectives are proposed.

In Chapter 2, a high-efficiency bidirectional ac-dc converter adopts dual-buck converter architecture is proposed. A new SPWM scheme by using split SPWM as the main scheme and joint SPWM as the supplementary scheme for the zero-crossing region is proposed. The proposed bidirectional ac-dc converter consists of two buck converters under inverter mode, each operating during a half line cycle. As a result, the magnetic components are only utilized during the half line cycle. However, the utilization can be improved by integrating magnetic components such as transformers and inductors on the same core. Two different structures of magnetic integration are presented. One is employing one coupled inductor in series with small inductors, and the other is utilizing two coupled inductors in series. The implemented converter efficiency peaks at 97.8% at 50-kHz switching frequency for both rectifier and inverter modes.

In Chapter 3, to better utilize the dc bus voltage and eliminate the two dc bus capacitors, a novel bidirectional ac-dc converter is proposed by replacing the two-capacitor leg of the dual-buck converter based single-phase bidirectional ac-dc converter with a two-switch leg. The novel bidirectional ac-dc converter keeps the merits of the dual-buck converter based bidirectional ac-dc converter. Meanwhile the two large dc bus capacitors and related voltage-balancing control are eliminated. The novel bidirectional ac-dc converter consists of two boost converters under rectifier mode, each operating during a half line cycle. It consists of two buck converters under inverter mode, each operating during a half line cycle. As a result, the magnetic components are only utilized during the half line cycle. The low utilization of the magnetic components may be a serious penalty in terms of weight, power density, and cost. With magnetic integration, the total number of magnetic cores is reduced by half. Based on the single-phase bidirectional ac-dc converter topology, several novel three-phase bidirectional ac-dc converter topologies are proposed. Detailed operating principles are described.

In Chapter 4, in order to control the bidirectional power flow and at the same time stabilize the system in mode transition, a unified digital controller is proposed. The

differences between individual controllers and unified controller are described. The power stage small-signal model is derived for the dual-buck converter based single-phase bidirectional ac-dc converter. Based on the small-signal model, an admittance compensator along with a QPR controller is adopted to allow smooth startup and elimination of the steady-state error over the entire load range. The proposed QPR controller is designed and implemented with a digital controller. Then the coefficients of the digital controller are truncated into certain word length binary representation, so as to be fit to the numbers of bits available to the FPGA for variables and constants. The characteristics of the designed analog resonant controller, digital controller, and truncated digital controller are analyzed. The entire system has been simulated in both PSIM and Simulink and verified with hardware experiments. Both simulation and experimental results match well and validate the design of the proposed unified controller. Small transient currents are observed with the power transferred from rectifier mode to inverter mode at peak current point and also from inverter mode to rectifier mode at peak current point.

In Chapter 5, a high-efficiency grid-tie lithium-ion battery based energy storage system is presented. The system consists of three subsystems, a $LiFePO_4$ battery pack and associated BMS, a bidirectional ac-dc converter, and the central control unit which controls the operation mode and grid interface of the energy storage system. The designed BMS monitors and reports all battery cells parameters in the pack. Based on these parameters, the BMS controller estimates the SOC of each battery cell in the pack. The SOC information is then used to control the active cell balancing circuits to mitigate the mismatch among the series connected cells. The SOC and SOH information is also used by the central control unit to determine the operating mode of the energy storage system. Using the proposed SOC balancing technique, the entire battery storage system has demonstrated more capacity than the system without SOC balancing. Under the charging condition from 30% to 70% SOC and discharging condition from 70% to 30% SOC, the use of SOC balancing technique has 33% more capacity. The round-trip efficiency is 96.5% for the battery pack. The overall round-trip efficiency for the battery energy storage system consisting of battery pack with associated BMS and bidirectional ac-dc converter is 92.6%.

In Chapter 6, the conclusion is drawn, and future works are summarized based upon the implementation experience and experimental results.

Chapter 2 Dual-Buck Converter Based Bidirectional AC-DC Converter

2.1 Introduction

With the increased concerns on environment and cost of energy, renewable energy sources are emerging as attractive power supply sources because they are clean and renewable. In 2008, about 19% of global energy production came from renewables including with 13% traditional biomass and 3.2% hydroelectricity. New renewables such as small hydro, modern biomass, wind, solar, geothermal, and biofuels accounted for another 2.7% and are growing very rapidly [85]. California has mandated that 33% of its power come from renewables by 2020, which is shown in Table 2.1 [86].

Table 2.1 Forecast generation in California by technology-nameplate ratings

	2007 (MW)	20% RPS 2012 (MW)	33% RPS 2020 (MW)
Hydro (over 300 MW)	8,464	8,464	8,464
Nuclear	4,550	4,550	4,550
Fossil	27,205	29,100	33,000
Wind	2,688	7,723	12,826
Solar	481	1,945	6,026
Geothermal	1,556	2,620	3,970
Hydro (up to 30 MW)	822	822	822
Biomass	787	1,008	1,778
Total Renewables	6,344	14,118	25,442
Total	45,653	56,232	71,436

Cumulative global photovoltaic (PV) installation surpassed 21 GW at the end of 2009 [87]. Wind power is growing at the rate of 30% annually, with a worldwide installed capacity of 158 GW in 2009 [87], and is widely used in Europe, Asia, and the United States.

The chart below (Figure 2.1) is from a California study on the irregular output of wind during 24 hours in Tehachapi [88]. It shows that the wind can drop off rapidly in the middle of the morning when the load is increasing as people arrive at work. Storage can save energy when the wind is blowing, and feed that energy back into the grid when the wind stops.

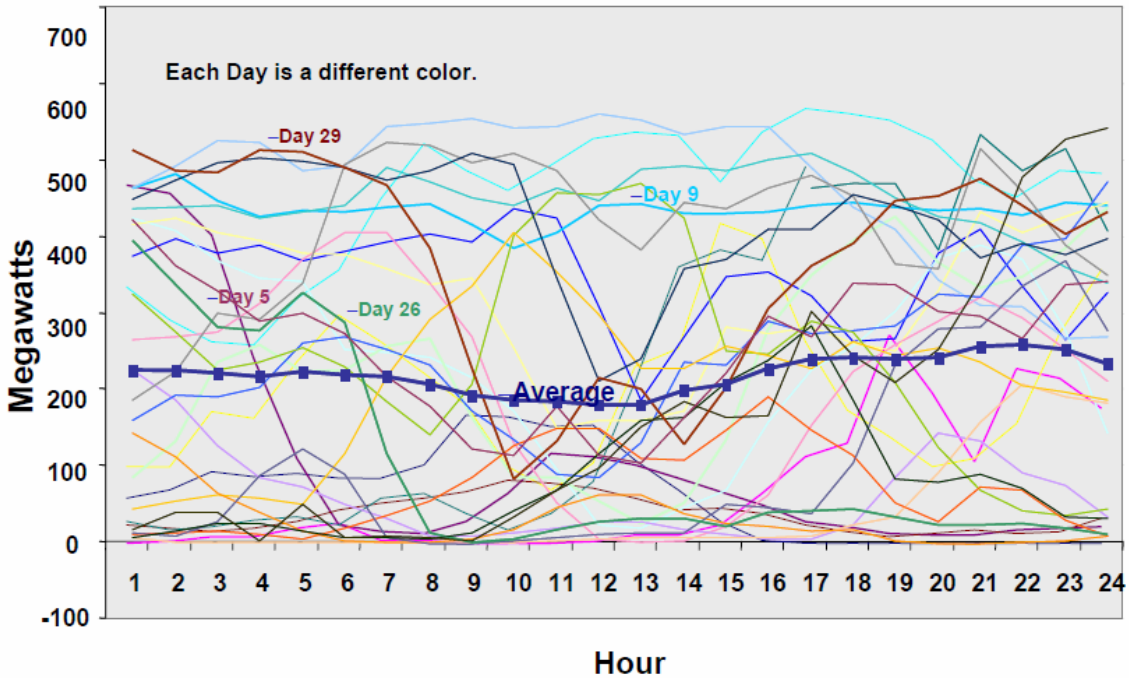

Figure 2.1 One day wind energy production of Tehachapi in April 2005.

The renewable energy source based DG systems are normally interfaced to the grid through power electronic converters and energy storage systems. A systematic organization of these DG systems, energy storage systems, and a cluster of loads forms a microgrid, which is shown in Figure 2.2. Recent developments and advances in energy storage systems and power electronics technologies are making the application of energy storage technologies a viable solution for modern power applications [89]. Storage can be

sized in the kW range up to thousands of MW. Depending upon the utility requirements, energy storage such as battery or flywheel systems can be used to provide fast voltage and frequency regulation (second by second), load shifting (adjusting to shifts in wind and solar over timeframes of minutes to hours), volt-ampere reactive (VAR) support, and black start service. It can be designed for the needs of distribution or transmission. It can be designed for single purpose operation, or for multiple purposes. In order to meet the challenges of practical utility applications, an energy storage system should have ac-dc/dc-ac bidirectional power conversion capability, islanding function, and high round-loop efficiency.

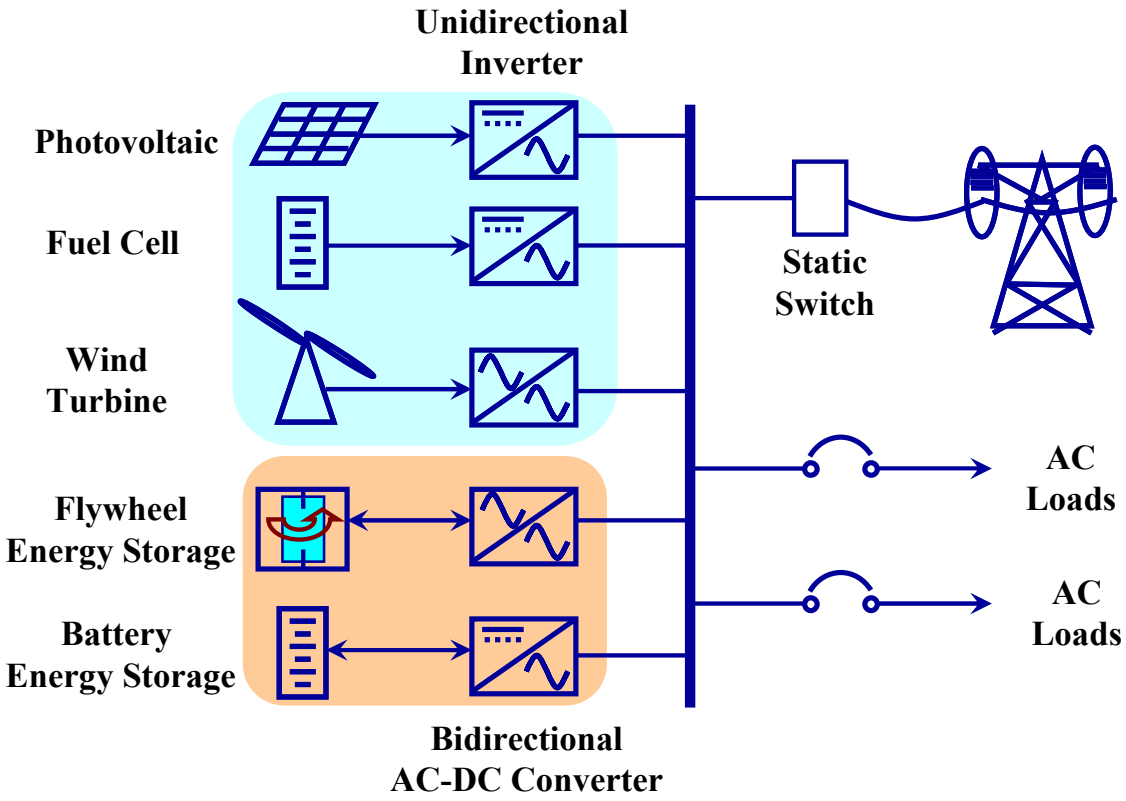

Figure 2.2 Energy storage systems based microgrid configuration.

2.2 Motivation for High-Efficiency Bidirectional AC-DC Converter

The conventional power conversion between ac power and dc power can be classified into two categories: ac-dc conversion, which is known as rectifier mode or power factor

correction (PFC), and dc-ac conversion, which is known as inverter mode. Both conversions are widely used in unidirectional power flow applications.

In a battery energy storage system, a bidirectional ac-dc converter with a proper charging-discharging profile is required to transfer energy between the battery pack and the ac grid. The converter works as a rectifier when the power is transferred from ac grid to battery pack. Alternately, it works as an inverter when the power is transferred from battery pack to ac grid. To realize bidirectional power flow in ac-dc converters, the power switch should carry the current on both directions. It is usually implemented with the power MOSFET or the IGBT in parallel with a diode.

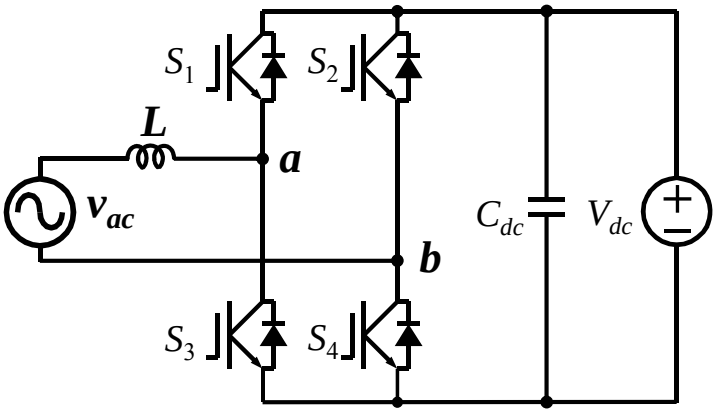

Figure 2.3 Circuit diagram of the traditional single-phase four-switch bidirectional ac-dc converter.

A traditional single-phase four-switch bidirectional ac-dc converter is shown in Figure 2.3. For this topology, the power MOSFET cannot be used as the main switch in the high-voltage high-power applications because the intrinsic MOSFET body diode reverse recovery could cause device failure.

Figure 2.4 shows the sub-operating modes under inverter mode for one switching cycle. When S_1 and S_4 are on, current i_L is increased because the voltage across inductor L is positive. When S_1 is off, Current i_L goes through S_4 and anti-paralleled diode of S_3. Current i_L is decreased because the voltage across inductor L is negative. In this case, if S_3 is replaced by a power MOSFET, the body diode of S_3 will conduct the current. Even if S_3 works under synchronous rectification when S_1 is off, the body diode of S_3 will

conduct the current during the dead time. Excessive reverse recovery current of the body diode will produce a tremendous amount of turn-on loss. Moreover, the loss could cause device failure.

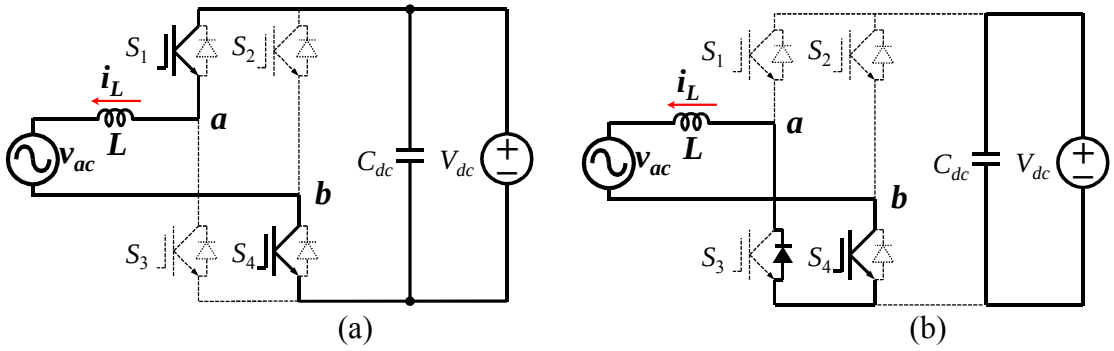

Figure 2.4 Operating under inverter mode for one switching cycle. (a) S_1 and S_4 are on. (b) Diode of S_3 and S_4 are on.

Although the power MOSFET cannot be used as the main switch for the traditional single-phase four-switch bidirectional ac-dc converter, new semiconductor structure and process have made high-voltage power MOSFET much more efficient with exceptionally low on-state drain-to-source resistance (R_{DSon}). Extremely low switching and conduction losses make switching applications even more efficient, more compact, lighter and cooler.

The proposed high-efficiency bidirectional ac-dc converter in this chapter adopts opposed current half bridge inverter architecture [23]. Since it consists of two buck converters and also has features of the conventional half bridge inverter, it is named as dual-buck half bridge inverter [24]-[26]. The converter exhibits two distinct merits: first, there is no shoot-through issue because no active power switches are connected in series in each phase leg; second, the reverse recovery dissipation of the power switch is greatly reduced because there is no freewheeling current flowing through the body diode of power switches. It can also support reactive power flow and seamless energy transfer. For the control scheme, the admittance compensator along with a QPR controller is adopted to allow smooth startup and elimination of the steady-state error over the entire load range. The major issue with this type of converter is the requirement of two separate inductors. However, without shoot-through concern and dead time requirement, the

switching frequency can be pushed higher to reduce the size of the inductor while maintaining low ripple current content. Both simulation and experimental results match very well and validate the design features of the high-efficiency, high-reliability converter. The implemented converter efficiency peaks at 97.8% at 50-kHz switching frequency for both rectifier and inverter modes.

2.3 Proposed Single-Phase Bidirectional AC-DC Converter

2.3.1 Single-Phase Bidirectional AC-DC Converter Topology

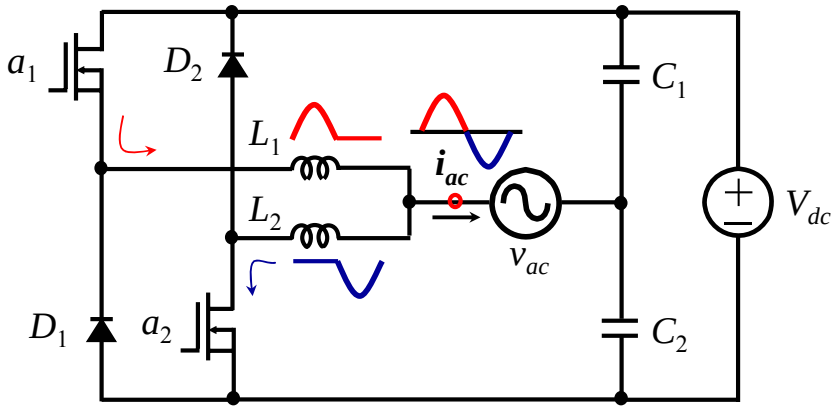

Figure 2.5 Circuit diagram of the proposed bidirectional ac-dc converter.

Figure 2.5 shows the circuit diagram of the proposed dual-buck based bidirectional ac-dc converter [27]-[29]. The circuit consists of two power switches a_1 and a_2, two diodes D_1 and D_2, two inductors L_1 and L_2, and two split dc bus capacitors C_1 and C_2. The converter works as a rectifier when the power is transferred from ac grid to dc source. Alternately, it works as an inverter when the power is transferred from dc source to ac grid. The voltage across each capacitor C_1 and C_2 should be always larger than the peak ac voltage to ensure the circuit works properly throughout the whole line cycle.

In this converter, the leg consisting of a_1 and D_1 conducts positive current, and the leg consisting of a_2 and D_2 conducts negative current. Since a_1 and a_2 only conducts positive current, the power MOSFETs are used as main switches without body diode reverse recovery issue. The features with this converter are: (1) low conduction and turn-off loss

by using power MOSFETs, (2) less electromagnetic interference (EMI) without MOSFET body diode reverse recovery issue, (3) low turn-on loss by using ultrafast reverse recovery diodes, (4) no dead time and short-through concern, (5) bidirectional power flow and reactive power control capability.

2.3.2 Operating Principle

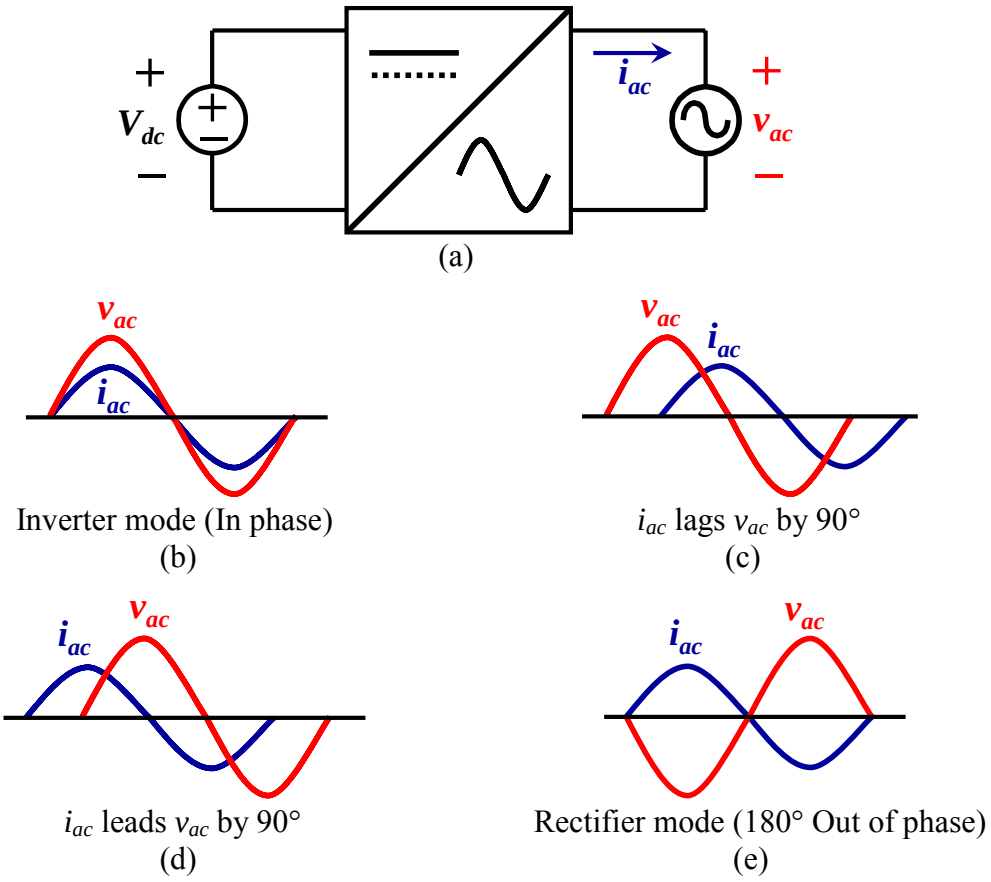

Figure 2.6 Definition of different modes based on phase angle difference between voltage and current waveforms. (a) Circuit diagram. (b)Inverter mode (In phase). (c) i_{ac} lags v_{ac} by 90°. (d) i_{ac} leads v_{ac} by 90°. (e) Rectifier mode (180° Out of phase).

The definition of different power transferring modes based on phase angle difference between voltage and current waveforms are shown in Figure 2.6. For pure active power transferring, there are two modes: inverter mode in which voltage and current are in phase and rectifier mode in which voltage and current are 180° out of phase. For reactive

power transferring, the phase angle differences between voltage and current are neither 0° nor 180°. Two examples with pure reactive power transferring are shown in Figure 2.6(c) in which i_{ac} lags v_{ac} by 90° and Figure 2.6(d) in which i_{ac} leads v_{ac} by 90°.

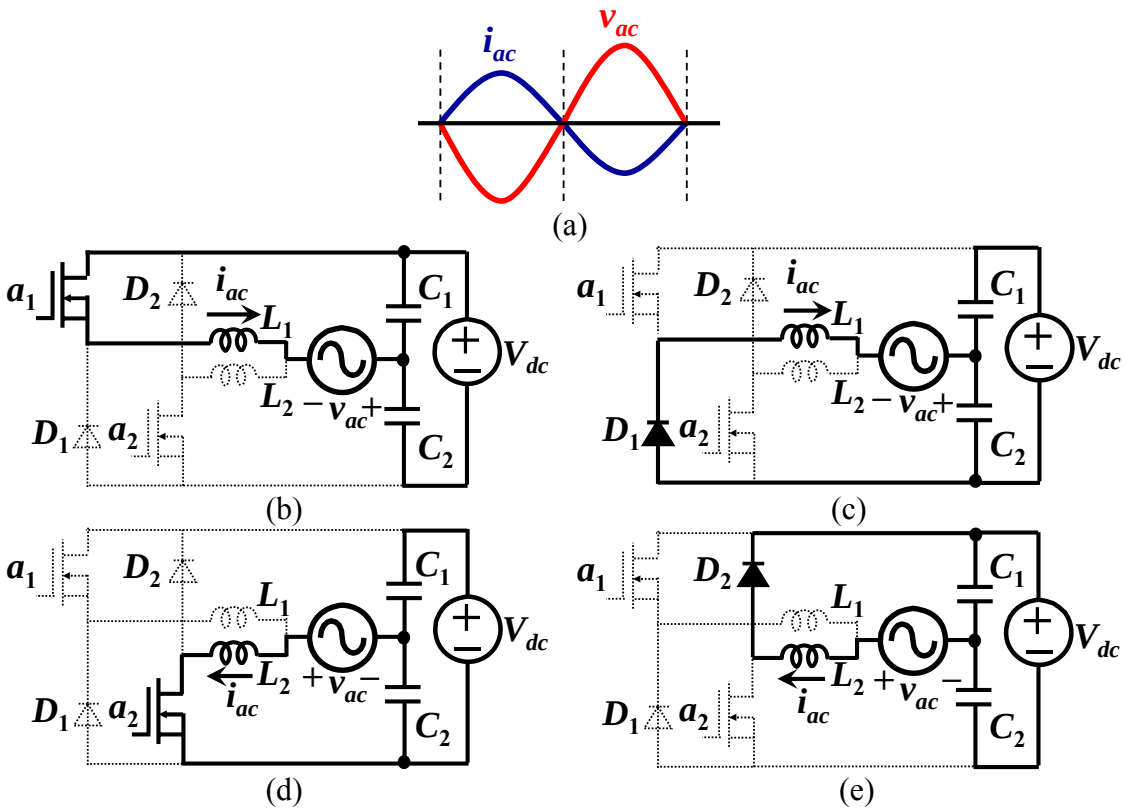

Figure 2.7 Operating under rectifier mode with pure active power transferring. (a) Conceptual voltage and current waveform. (b) a_1 is on. (c) D_1 is on. (d) a_2 is on. (e) D_2 is on.

Figure 2.7 and Figure 2.8 show the four sub-operating modes under rectifier and inverter modes, respectively. For the rectifier mode with pure active power transferring, there are four sub-operating modes depending on the conducting status of a_1, a_2, D_1 and D_2.

In the positive half cycle, leg a_1 and D_1 operates. When a_1 is on, current i_{ac} is increased because the voltage across inductor L_1 is positive,

$$V_{L1} = L_1 \frac{di_{ac}}{dt} = V_{c1} + v_{ac} > 0 . \tag{2.1}$$

Capacitor C_1 is discharged, and the energy of both C_1 and C_2 is transferred to the dc sources. When a_1 is off and D_1 is on, current i_{ac} is decreased because the voltage across inductor L_1 is negative,

$$V_{L1} = L_1 \frac{di_{ac}}{dt} = -V_{c2} + v_{ac} < 0 . \tag{2.2}$$

Capacitor C_2 is charged, and the energy of both C_1 and C_2 is transferred to the dc sources.

In the negative half cycle, leg a_2 and D_2 operates. When a_2 is on, current i_{ac} is increased because the voltage across inductor L_2 is positive,

$$V_{L2} = L_2 \frac{di_{ac}}{dt} = V_{c2} + v_{ac} > 0 . \tag{2.3}$$

Capacitor C_2 is discharged, and the energy of both C_1 and C_2 is transferred to the dc sources. When a_2 is off and D_2 is on, current i_{ac} is decreased because the voltage across the inductor L_2 is negative,

$$V_{L2} = L_2 \frac{di_{ac}}{dt} = -V_{c1} + v_{ac} < 0 . \tag{2.4}$$

Capacitor C_1 is charged, and the energy of both C_1 and C_2 is transferred to the dc sources. Overall, in the positive half cycle C_1 is always discharged, but C_2 is always charged. However, in the negative half cycle C_1 is always charged, but C_2 is always discharged. The charge balance is maintained through the entire line cycle.

For the inverter mode pure active power transferring, all the analysis is similar to that of rectifier mode except that the current and voltage are in phase; therefore, the energy is transferred from dc sources to ac grid. Based on the above analysis, it can be concluded

that C_2 is always charged in the positive half cycle and C_1 is always charged in the negative half cycle, and the charge balance maintains through the entire line cycle.

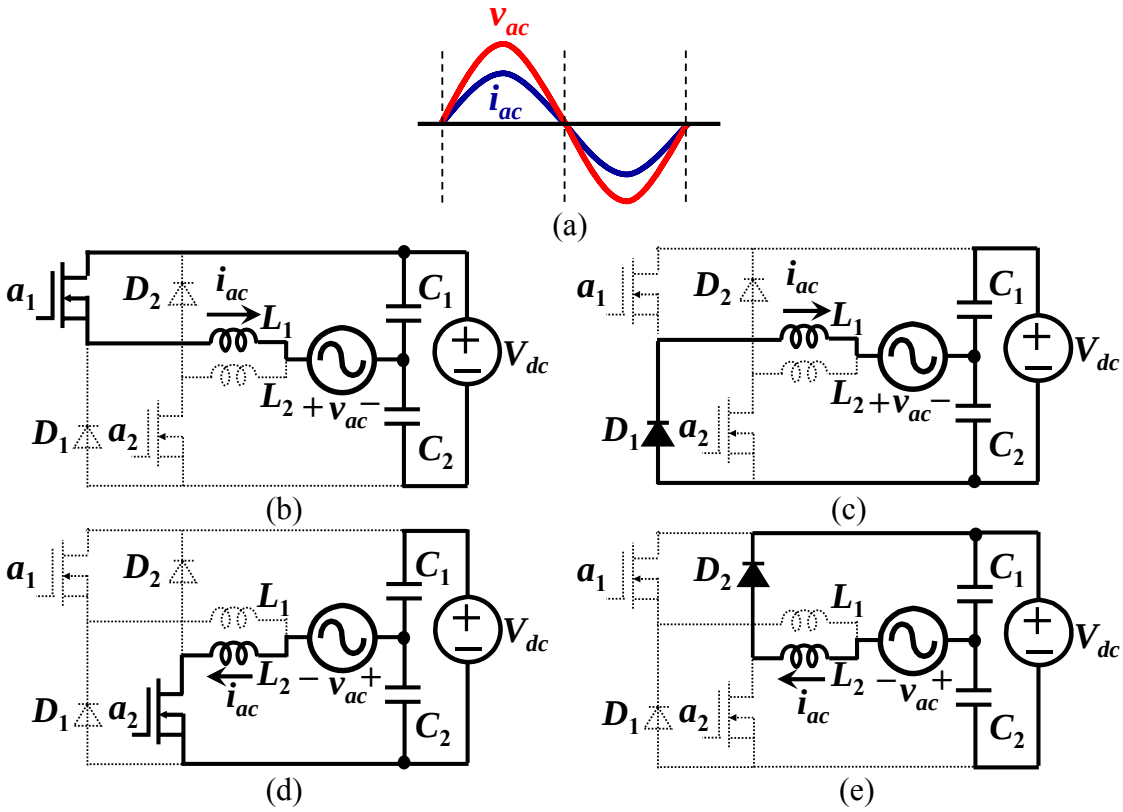

Figure 2.8 Operating under inverter mode with pure active power transferring. (a) Conceptual voltage and current waveform. (b) a_1 is on. (c) D_1 is on. (d) a_2 is on. (e) D_2 is on.

To transfer reactive power between ac grid and dc sources, the operation of the circuit becomes much more complicated. Based on the direction of the ac current and voltage, one ac line cycle can be divided into 4 regions, which is shown in Figure 2.9. Only the leg that conducts current is shown here for simplicity. In region 1, current is negative and voltage is positive. Leg a_2 and D_2 conducts the current. In region 2, both current and voltage are positive. Leg a_1 and D_1 conducts the current. Region 3 is similar to region 2 except that voltage is negative. Region 4 is similar to region 1 except that voltage is negative. Based on above analysis, it can be concluded that the leg consisting of a_1 and

D_1 conducts positive current, and the leg consisting of a_2 and D_2 conducts negative current whenever voltage is positive or negative.

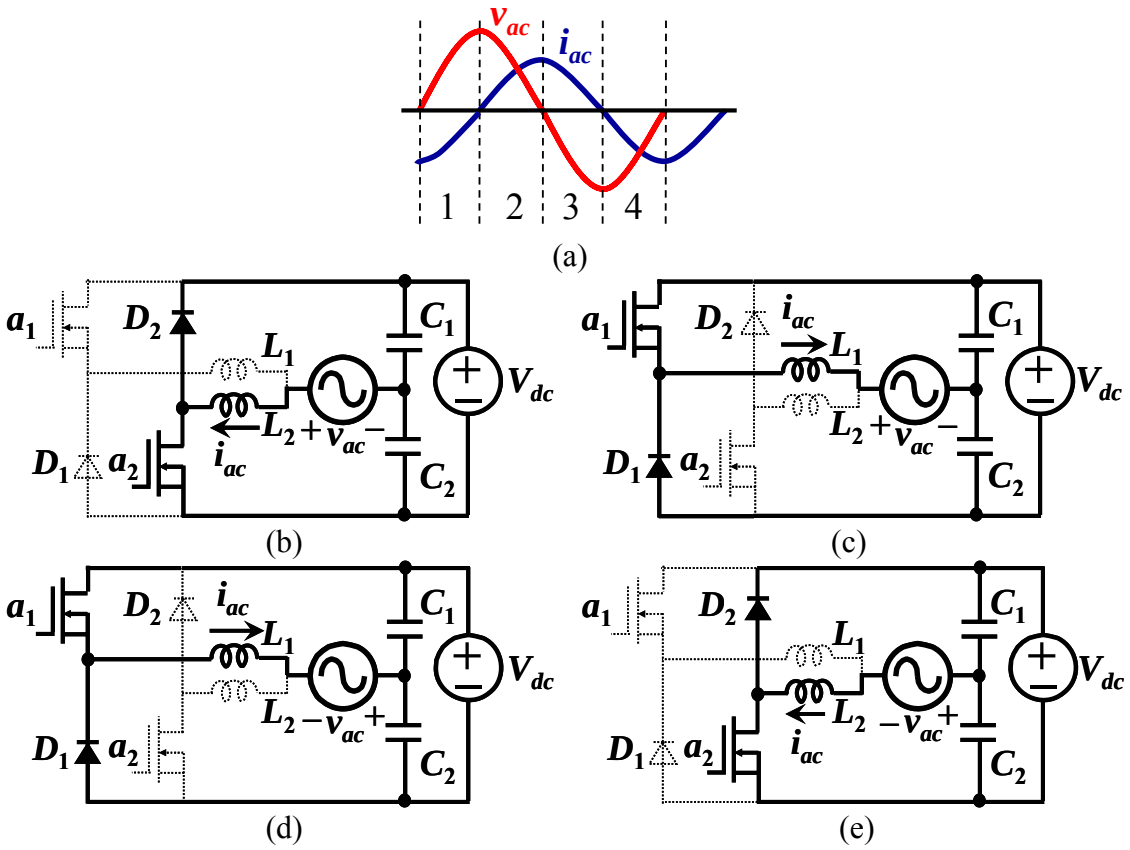

Figure 2.9 Operating under active and reactive power transferred between ac grid and dc source. (a) Conceptual voltage and current waveform. (b) Region 1, a_2 and D_2 are on. (c) Region 2, a_1 and D_1 are on. (d) Region 3, a_1 and D_1 are on. (e) Region 4, a_2 and D_2 are on.

2.3.3 Inductor Design and Optimization

Inductor design has significant impact on system performance, such as the device switching loss, inductor loss, and system volume etc. It is necessary to design and optimize the inductance with all design considerations.

Take Figure 2.8 (b) and (c) as one switching cycle to calculate the inductance. Assume the input power is 1 kW and the ac rms voltage is 30 V, the ac rms current can be calculated as

$$I_{ac\_rms} = \frac{P_{ac}}{v_{ac\_rms}} = \frac{1000}{30} = 33 \text{ A}. \tag{2.5}$$

Ripple current needs to be minimized. 5% peak-to-peak inductor ripple current is used as the design target. The switching frequency of the ac-dc converter is designed as 50 kHz. The inductance can be calculated as

$$L = \frac{\Delta V}{\Delta i}\Delta t = \frac{V_{dc}/2 - v_{ac}}{5\% \cdot I_{pk}} \cdot d_{a1\_inv} T_s . \tag{2.6}$$

From Figure 2.8(b) and (c), when current is positive in the inverter mode, the total volt-seconds applied to the inductor L_1 over one switching period are as follows:

$$(\frac{V_{dc}}{2} - v_{ac}) \cdot d_{a1\_inv} + (-\frac{V_{dc}}{2} - v_{ac}) \cdot (1 - d_{a1\_inv}) = 0 . \tag{2.7}$$

The duty cycle for switch a_1 can be derived as

$$d_{a1\_inv} = \frac{1}{2}(1 + \frac{v_{ac}}{V_{dc}/2}) = \frac{1}{2}(1 + \frac{v_{pk}\sin\omega t}{V_{dc}/2}) = 0.5 \cdot (1 + M\sin\omega t) \tag{2.8}$$

where $M = v_{pk}/(V_{dc}/2)$ is modulation index and sin $\omega t > 0$.

Then the inductance can be calculated as

$$\begin{aligned} L = \frac{\Delta V}{\Delta i}\Delta t = \frac{V_{dc}/2 - v_{ac}}{5\% \cdot I_{pk}} \cdot d_{a1\_inv} T_s = \frac{0.25 \cdot V_{dc}(1 - M\sin\omega t) \cdot (1 + M\sin\omega t) \cdot T_s}{5\% \cdot I_{pk}} \\ \le \frac{0.25 \cdot V_{dc} \cdot T_s}{5\% \cdot I_{pk}} = \frac{0.25 \cdot 120}{5\% \cdot \sqrt{2} \cdot 33} \cdot \frac{1}{50000} = 257 \text{ μH} \end{aligned} . \tag{2.9}$$

Inductor core materials influence the core power loss a lot for the same ripple current. Typical magnetic materials are silicon iron, amorphous, Finemet, ferrite and powder. Silicon iron is not considered because it is very lossy with high frequency components. Amorphous and Finemet are acceptable with loss, but they need air gap to avoid saturation. Audible noise will be a major problem with such materials. Ferrite is good for high frequency, but with high μ, it also needs air gap. Audible noise again is a problem. Powder cores are good choice for PFC circuits as well as inverter filter applications because their higher saturation flux density provides a higher energy storage capability than can be obtained with gapped ferrites of the same size and effective permeability. High saturation flux density can also avoid core saturation during transient or startup when a large transient current spike is likely to occur. Another advantage is it helps reduce the air gap and the related gap loss.

Among the three powder materials, molypermalloy powder, high flux and Kool Mμ, Kool Mμ is preferred for its low core loss and low relative cost. The high flux density and low core losses make Kool Mμ cores excellent for use in PFC circuits as well as inverter applications.

Table 2.2 Comparison of design results based on different Kool Mμ cores

	77191	77192
μ	26	60
A_L (nH/turn^2)	60	138
N (turn)	27 (6 cores)	25 (3 cores) 22 (4 cores)
H_{pk} (Oer)	128.57	119
B_{pk} (G)	3.14	5.59
Core Loss (W)	3.1	1.57
Copper Loss (W)	18.38	10.16
Total Loss (W)	21.48	11.73

Table 2.2 is the comparison of design results based on different Kool Mμ cores. The results show that the copper losses dominate the total losses in this case. The 77192 core is preferred since it generates lower losses than the 77191 core.

Overall, lower-μ type Kool Mμ is preferred for high-power filter applications. However, a tradeoff between core and copper losses should be determined to help overall loss reduction.

2.3.4 Zero-Crossing Distortion and Solution

Sinusoidal pulse width modulation (SPWM) method is a popular linear modulation scheme for rectifiers and inverters. A split SPWM scheme is proposed in this paper.

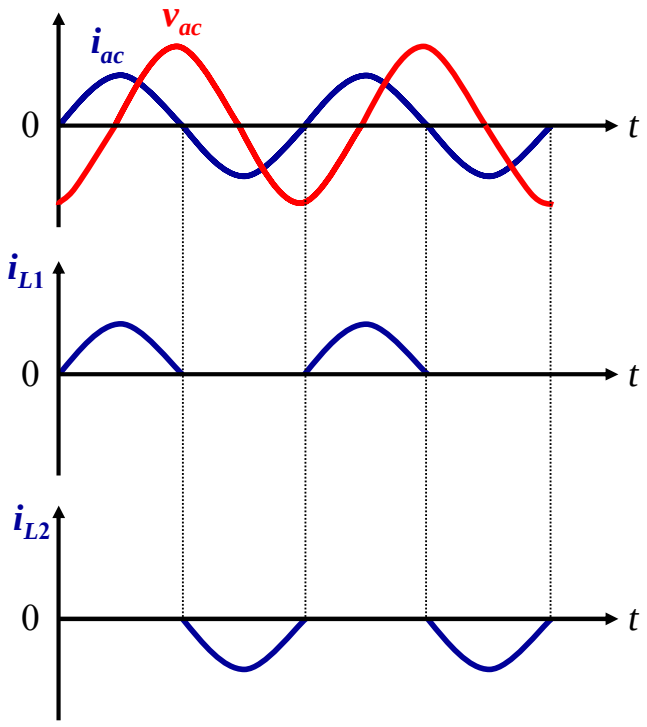

Figure 2.10 Waveforms of ac voltage, ac current and inductor currents under split SPWM.

The basic principle of split SPWM is that leg a_1 & D_1 and leg a_2 & D_2 operate alternatively in one line cycle according to the direction of the ac current i_{ac}. Leg a_1 & D_1 conducts positive half-cycle current while leg a_2 & D_2 conducts negative half-cycle

current. The key waveform of ac voltage, ac current and inductor currents are offered in Figure 2.10. The definition of ac current i_{ac} is defined as

$$i_{ac} = \begin{cases} i_{L1} & i_{ac} > 0 \\ -i_{L2} & i_{ac} \le 0 \end{cases} \tag{2.10}$$

Figure 2.11 shows the equivalent circuit of the converter under split SPWM. In this circuit, v_{L1} and v_{L2} are equivalent square waveform voltage sources.

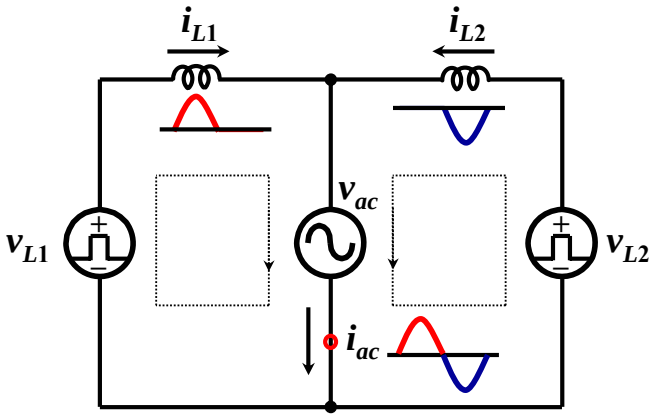

Figure 2.11 Equivalent circuit of the converter under split SPWM.

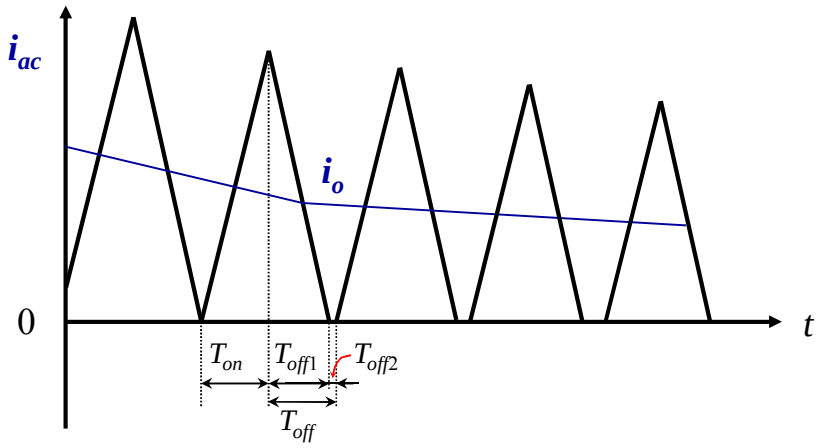

Figure 2.12 Current waveform of DCM near zero-crossing region under split SPWM.

Since only one device is conducting at any given time, conduction and switching losses are relatively low. However, when the inductor currents are small enough, the converter enters discontinuous conduction mode (DCM) as shown in Figure 2.12. The characteristic of the converter changes significantly in DCM and the regulation of ac current requires quick system response.

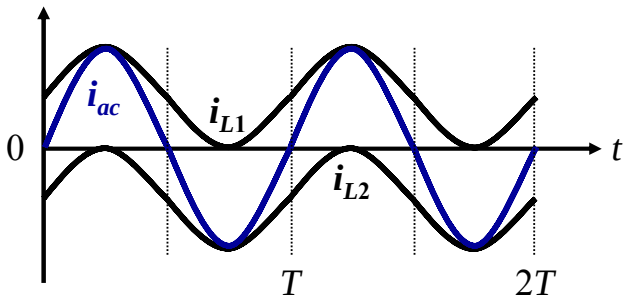

Figure 2.13 Current waveforms under joint SPWM.

To solve the current zero-crossing distortion problem, another SPWM named joint SPWM is proposed.

The basic principle of joint SPWM is that both leg a_1 & D_1 and leg a_2 & D_2 operate at the same time. The positive current goes through leg a_1 & D_1 while the negative current goes through leg a_2 & D_2. The sum of the two currents forms the ac sinusoidal current. The current waveforms are shown in Figure 2.13. The definition of ac current i_{ac} is expressed as

$$i_{ac} = i_{L1} + i_{L2} \tag{2.11}$$

Figure 2.14 shows the equivalent circuit of the converter under joint SPWM. In this circuit, v_{L1} and v_{L2} are equivalent square waveform voltage sources, which swing between $-V_{dc}/2$ and $+V_{dc}/2$.

When the inductor currents are small, the converter is still operating in continuous conduction mode (CCM) as shown in Figure 2.15. Compared with the converter

operating under split SPWM, the switching and conduction losses are doubled under joint SPWM since two devices are conducting at the same time.

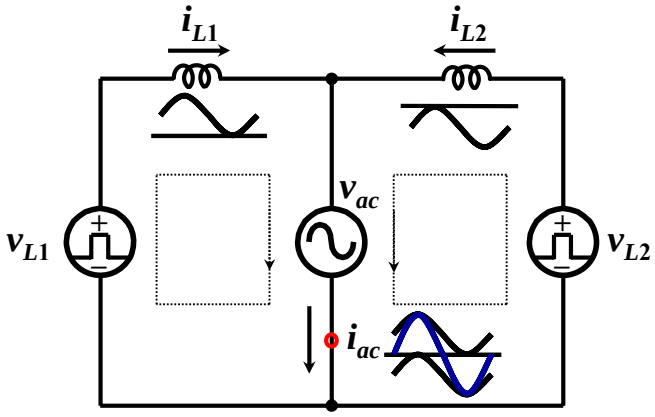

Figure 2.14 Equivalent circuit of the converter under joint SPWM.

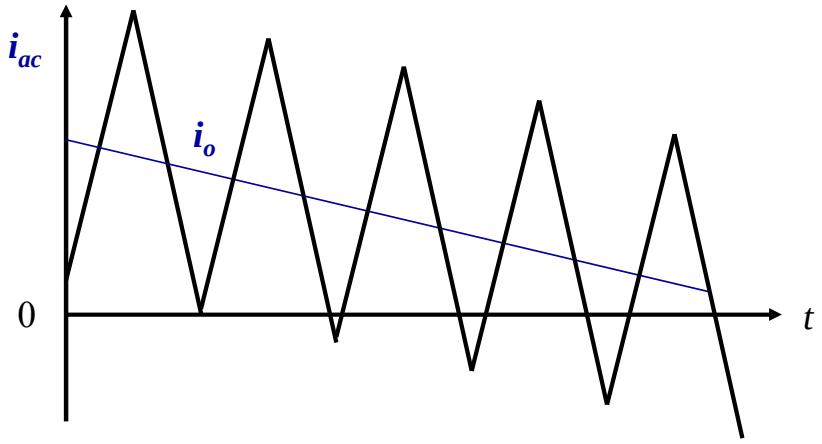

Figure 2.15 Current waveform near zero-crossing region under joint SPWM.

To obtain the advantages of both SPWM schemes, a new SPWM scheme by using split SPWM as the main scheme and joint SPWM as the supplementary scheme for the zero-crossing region is proposed. On one hand, since split SPWM is utilized as the main scheme, conduction and switching losses are relatively low. On the other hand, because joint SPWM is employed for the zero-crossing region, the ac current zero-crossing distortion problem is solved.

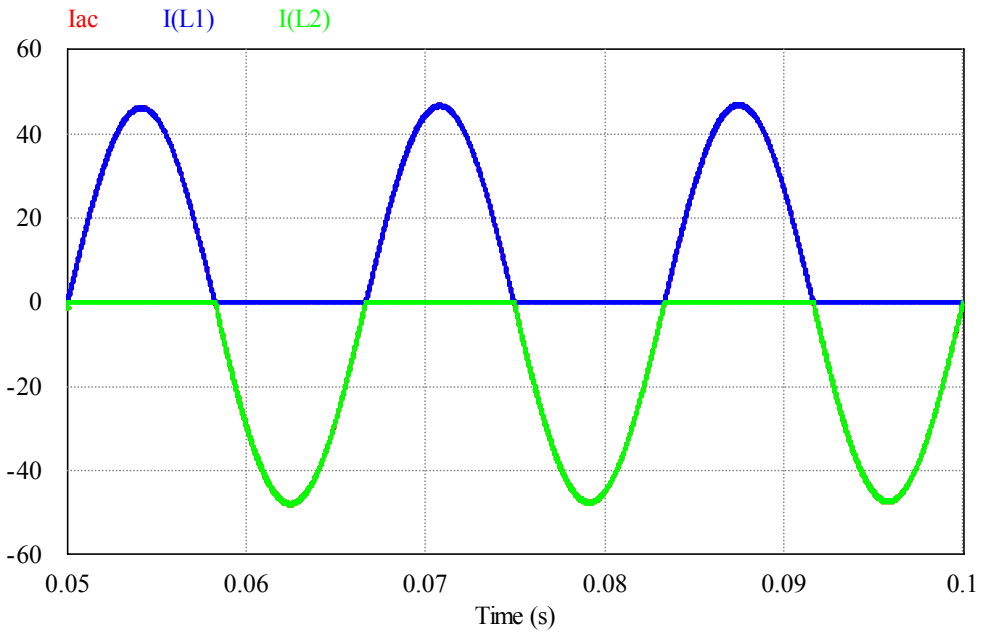

(a)

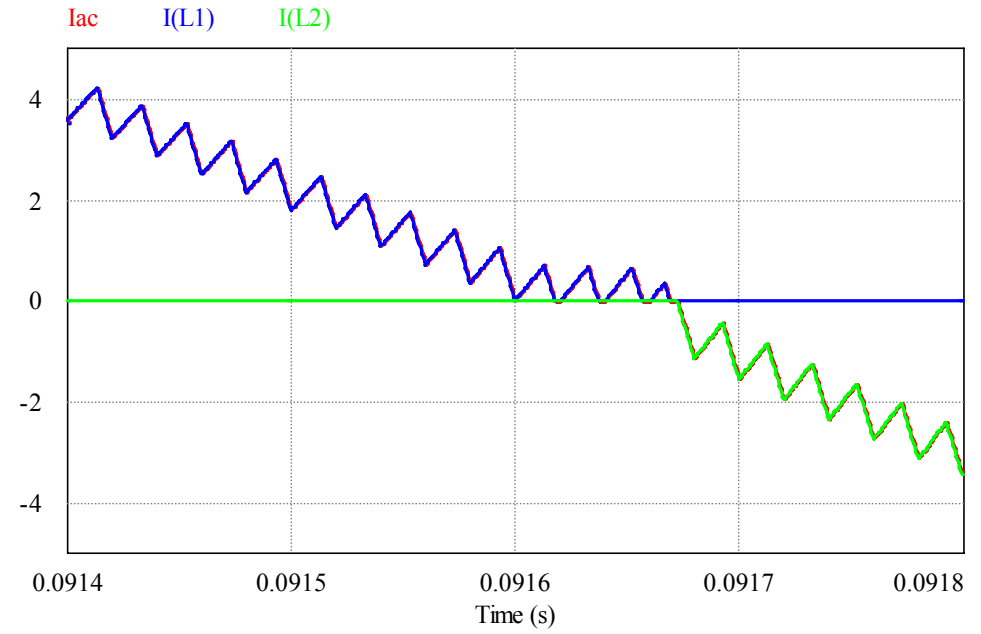

(b)

Figure 2.16 Simulation results of the converter under split SPMW. (a) Waveforms over cycles. (b) Waveforms near zero-crossing region

Figure 2.16 shows the simulation results of the converter under split SPWM. Figure 2.16(a) shows the waveforms over cycles. Figure 2.16(b) shows the waveforms near zero-crossing region.

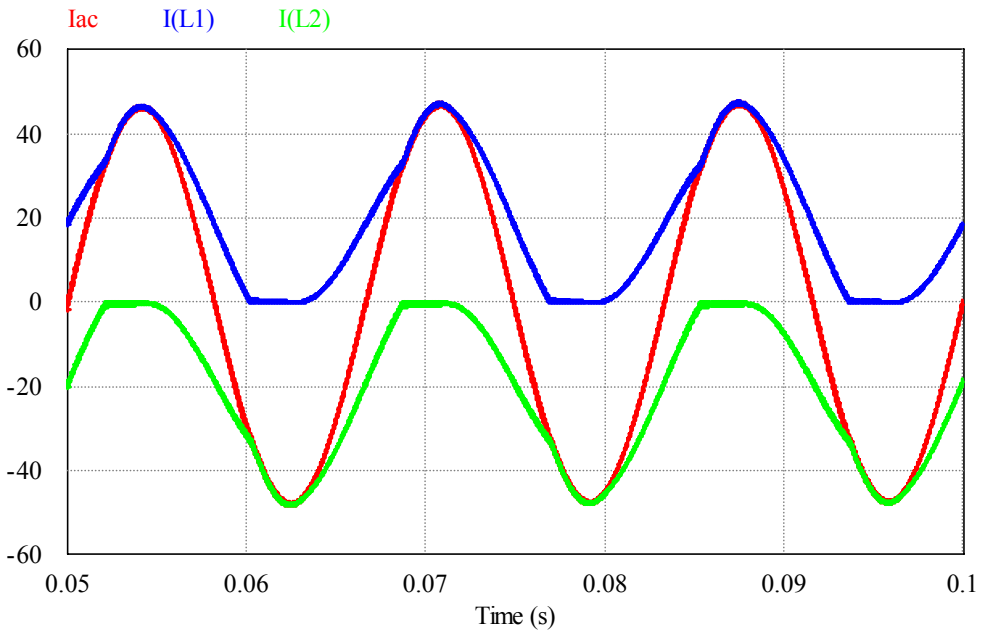

(a)

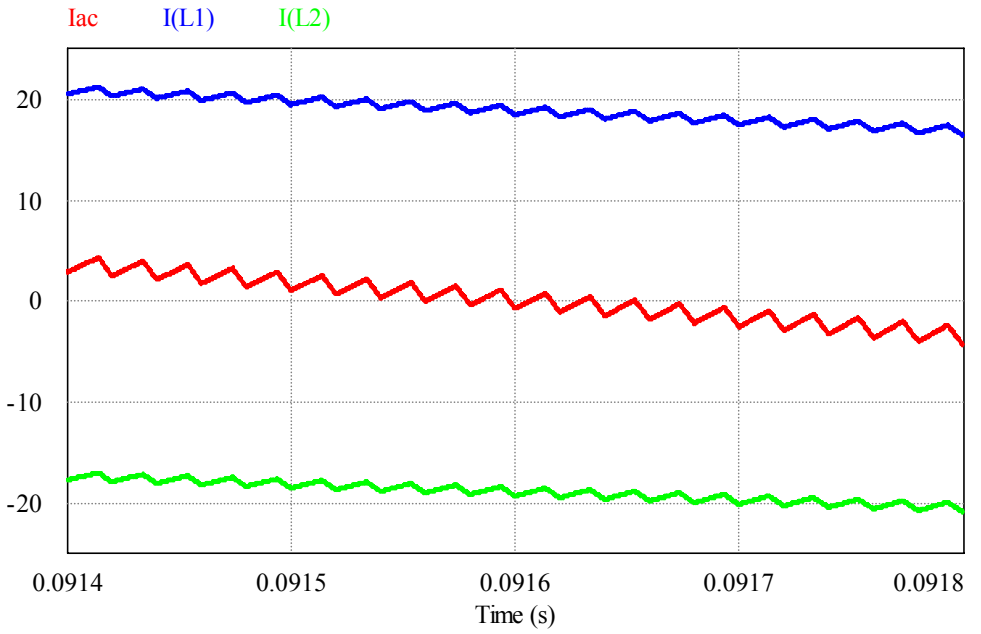

(b)

Figure 2.17 Simulation results of the converter under joint SPMW. (a) Waveforms over cycles. (b) Waveforms near zero-crossing region.

Figure 2.17 shows the simulation results of the converter under joint SPWM. Figure 2.17(a) shows the waveforms over cycles. Figure 2.17(b) shows the waveforms near zero-crossing region.

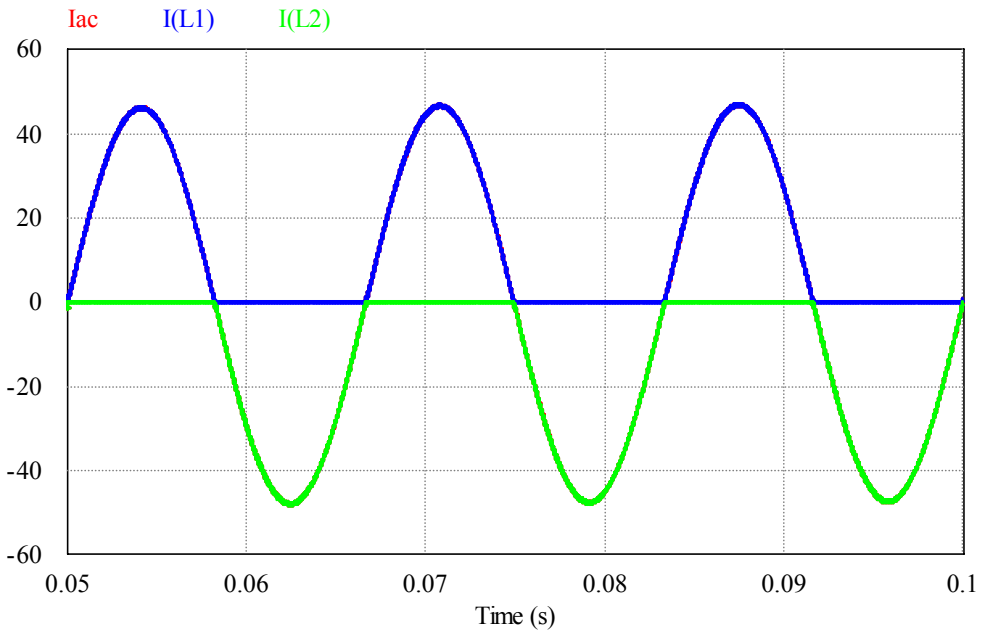

(a)

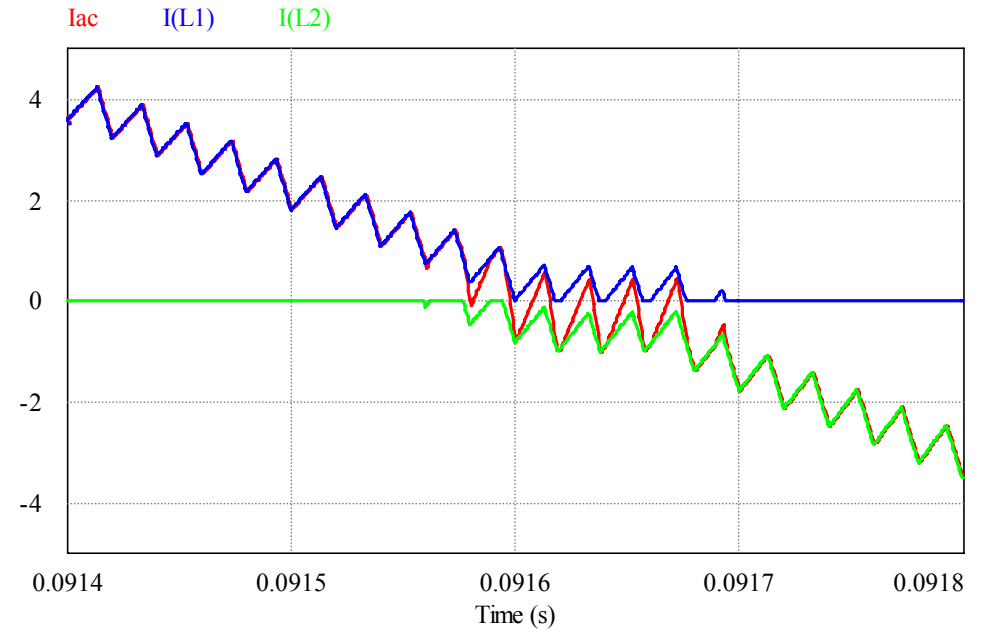

(b)

Figure 2.18 Simulation results of the converter under the proposed new SPMW. (a) Waveforms over cycles. (b) Waveforms near zero-crossing region.

Figure 2.18 shows the simulation results of the converter under the proposed new SPWM. Figure 2.18(a) shows the waveforms over cycles. Figure 2.18(b) shows the waveforms near zero-crossing region.

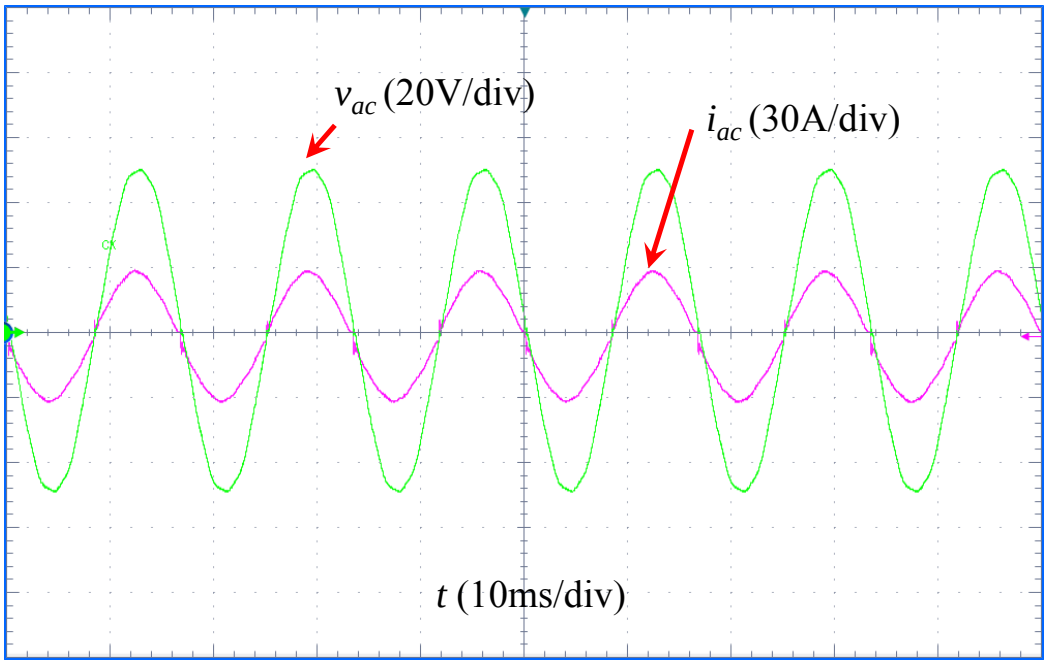

(a)

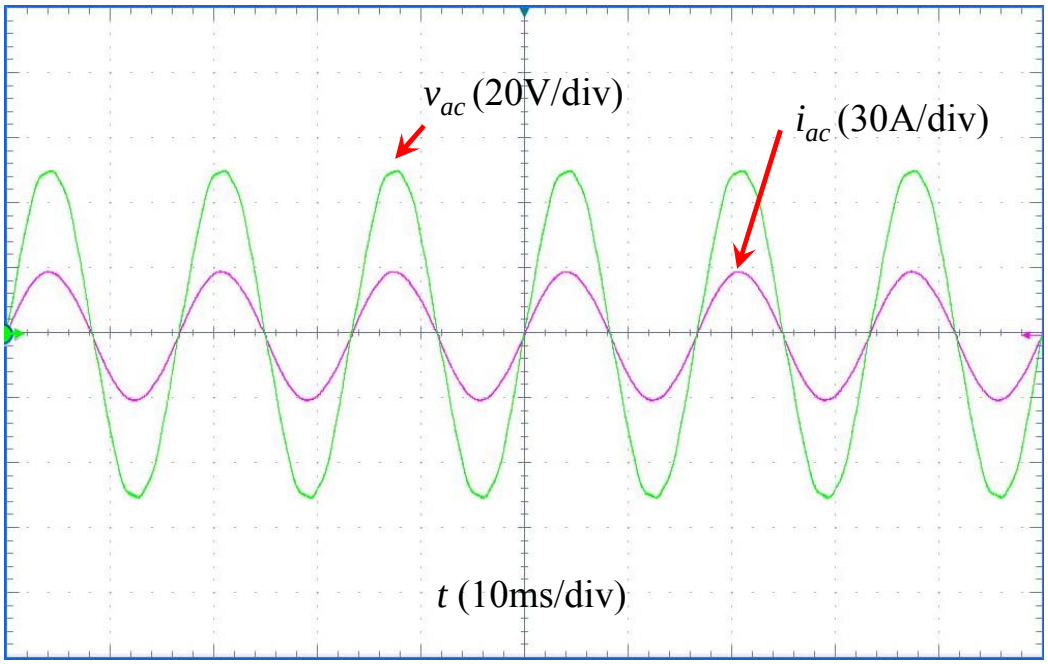

(b)

Figure 2.19 Experimental results of the converter. (a) Results under split SPWM. (b) Results under the proposed new SPWM.

Figure 2.19(a) and (b) show the experimental results of the converter under split SPWM and the proposed new SPWM, respectively. As can be seen in Figure 2.19(b), the proposed new SPWM effectively solves the ac current zero-crossing distortion problem.

2.3.5 Simulation Results

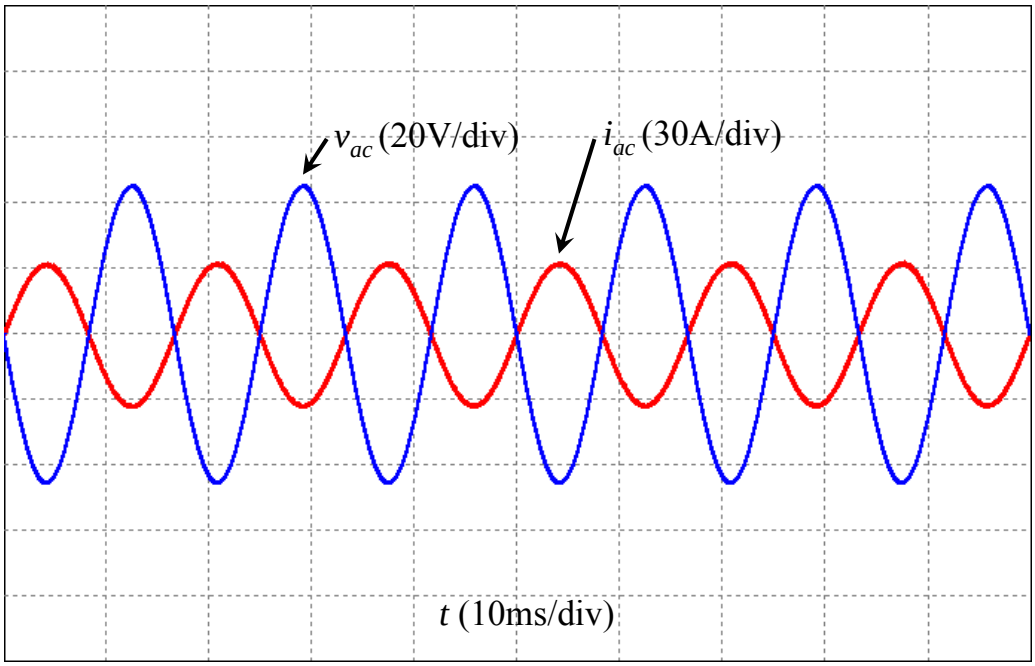

(a)

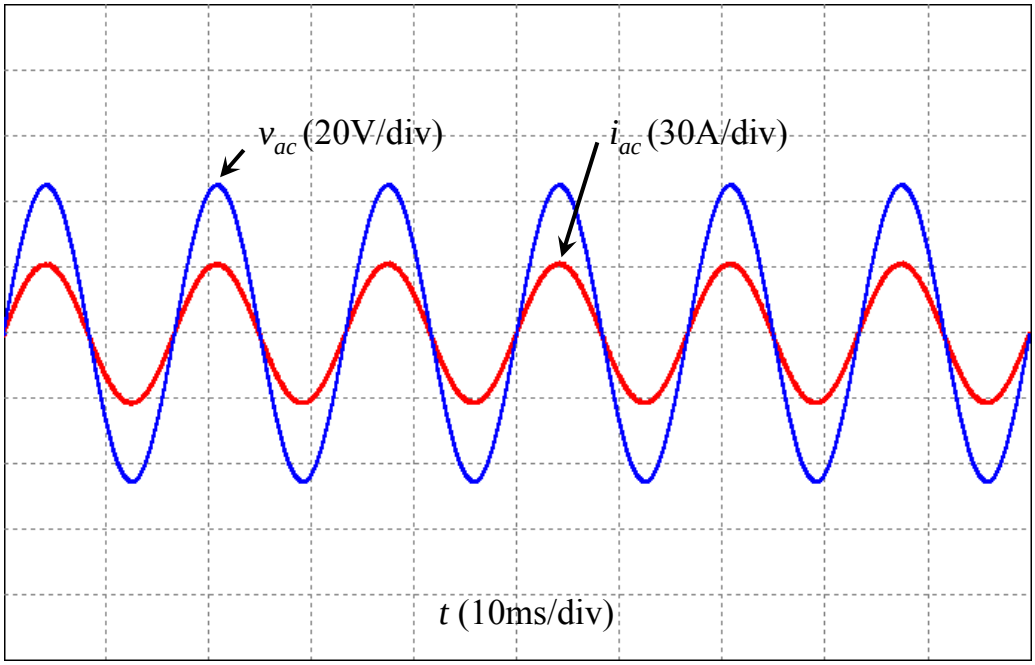

(b)

Figure 2.20 Simulation results under (a) rectifier mode and (b) inverter mode, both with v_{ac} = 30 V_{rms} and i_{ac} = 23 A_{rms}.

Figure 2.20(a) and (b) shows the simulation results under both rectifier and inverter modes for the converter, respectively.

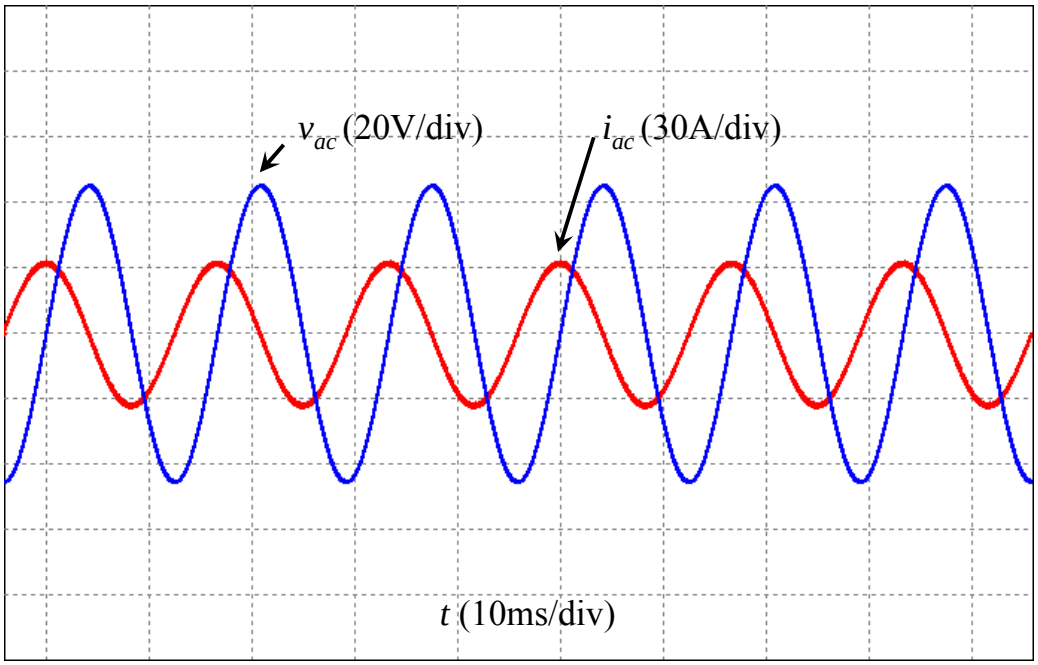

(a)

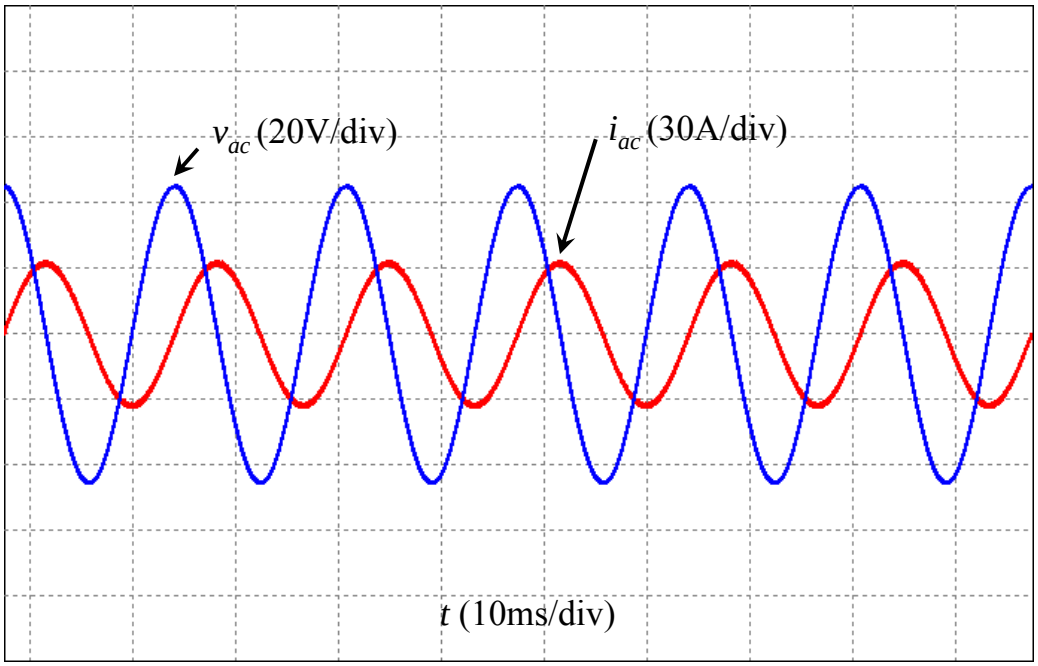

(b)

Figure 2.21 Simulation results with reactive power flow. (a) Current leads voltage by 90°. (b) Current lags voltage by 90°.

Figure 2.21(a) and (b) show simulated waveforms of reactive power flow. Figure 2.21(a) shows current leads voltage by 90°. Figure 2.21(b) shows current lags voltage by 90°.

2.3.6 Experimental Results

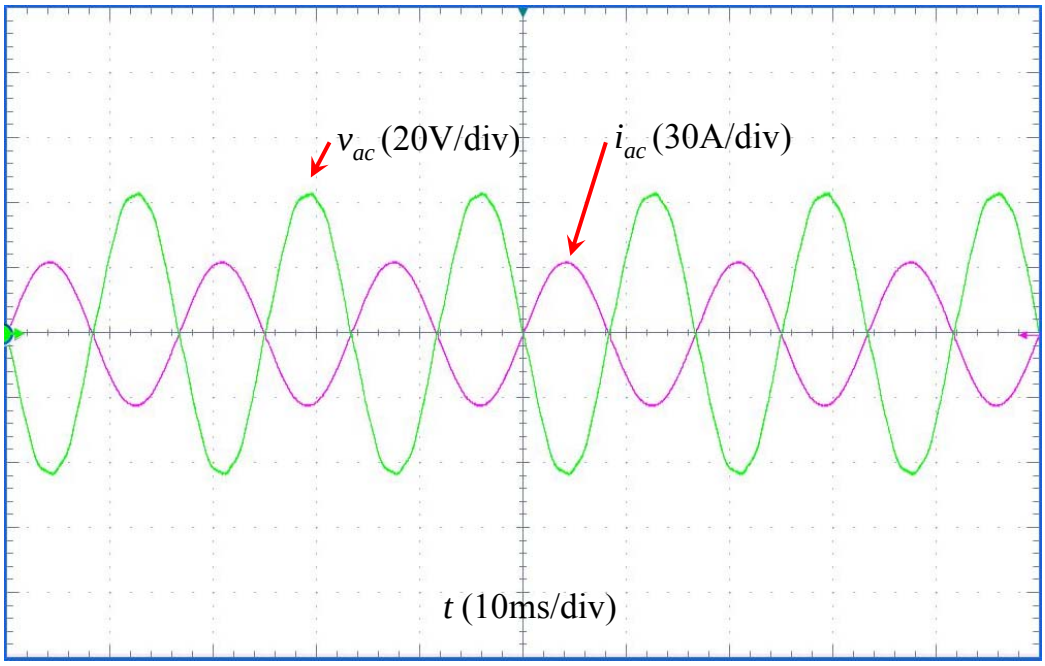

(a)

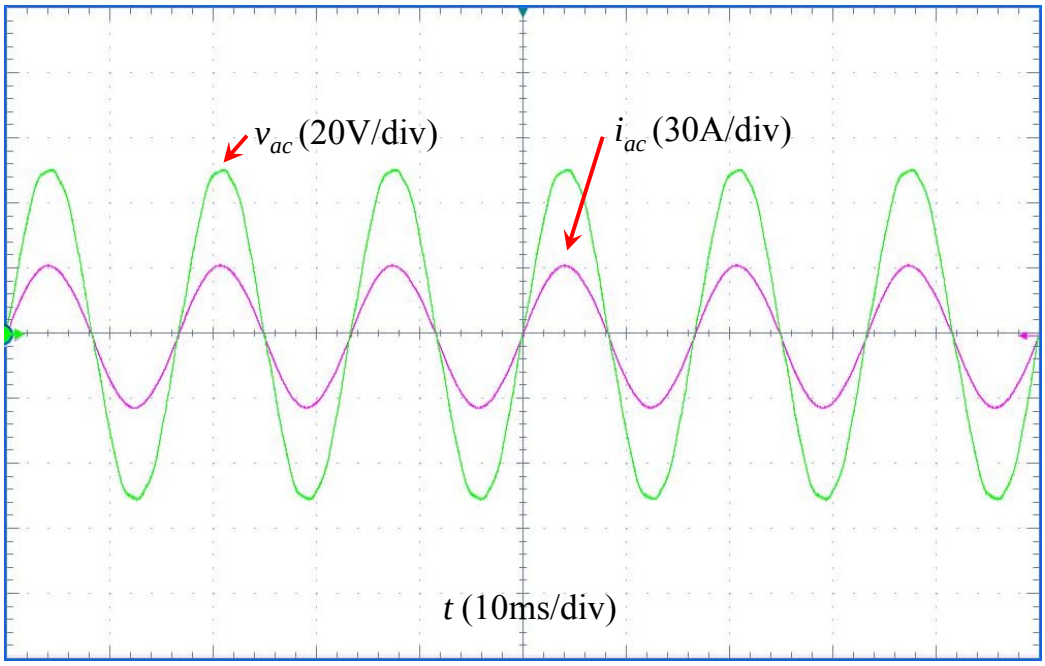

(b)

Figure 2.22 Experimental results under (a) rectifier mode and (b) inverter mode, both with v_{ac} = 30 V_{rms} and i_{ac} = 23 A_{rms}.

Figure 2.22(a) and (b) shows the experimental results under both rectifier and inverter modes for the converter, respectively.

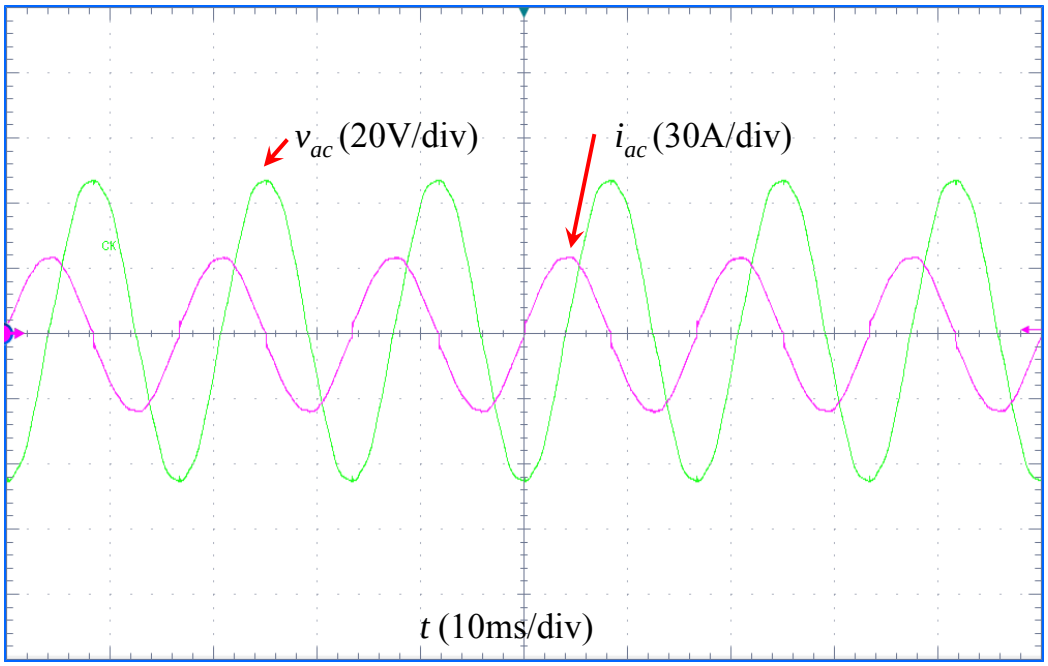

(a)

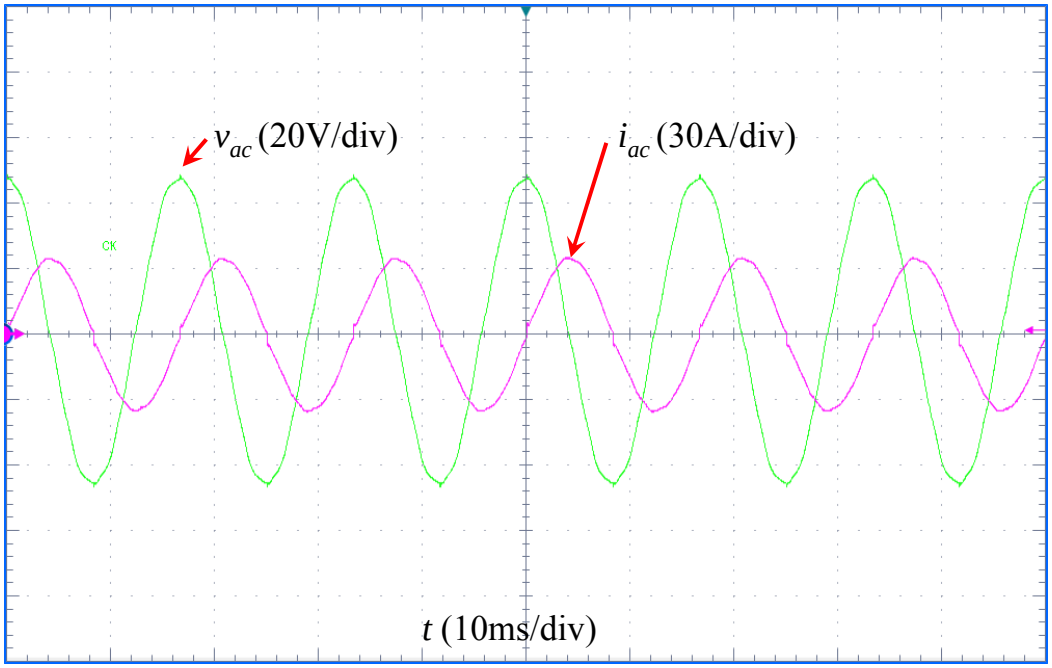

(b)

Figure 2.23 Experimental results with reactive power flow. (a) Current leads voltage by 90°. (b) Current lags voltage by 90°.

Figure 2.23(a) and (b) show experimental waveforms of reactive power flow. Figure 2.23(a) shows current leads voltage by 90°. Figure 2.23(b) shows current lags voltage by 90°.

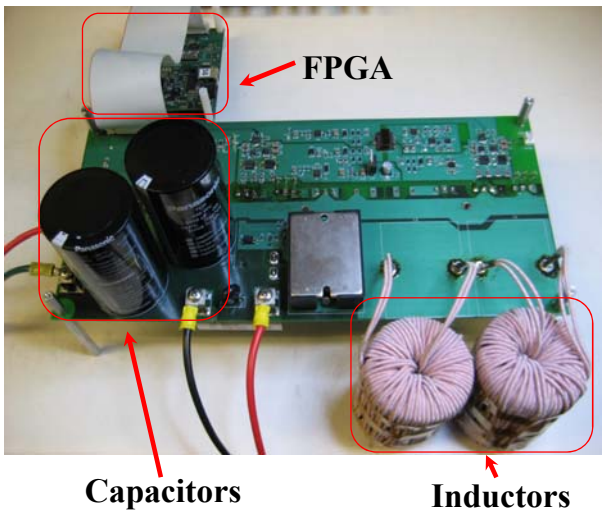

Figure 2.24 Prototype of the proposed bidirectional ac-dc converter.

The bidirectional power flow capability of the proposed circuit is well verified. Figure 2.24 shows the photograph of the bidirectional ac-dc converter prototype. The field-programmable gate array (FPGA) board that implements the controller function is separated from the main power board. Figure 2.25 shows the experimental efficiency of the proposed converter under both rectifier and inverter modes. The efficiency peaks at 97.8% at 50-kHz switching frequency for both rectifier and inverter modes.

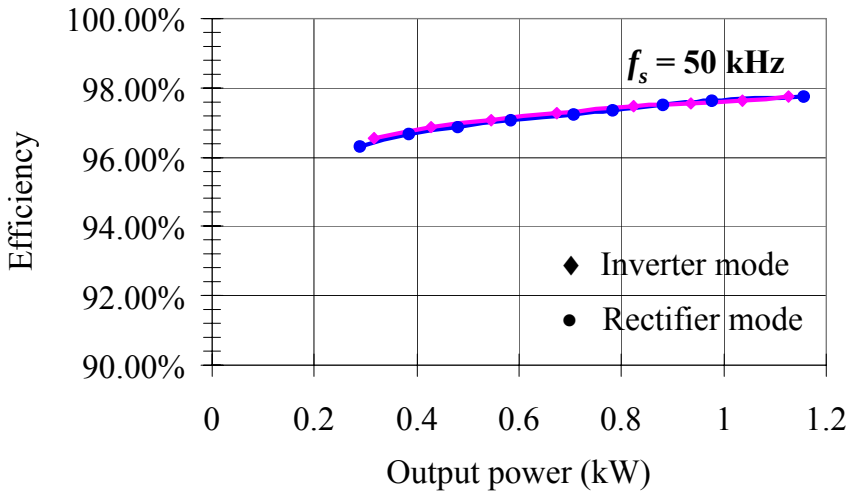

Figure 2.25 Experimental efficiency for both rectifier and inverter modes.

2.4 Single-Phase Bidirectional AC-DC Converter with Magnetic Integration

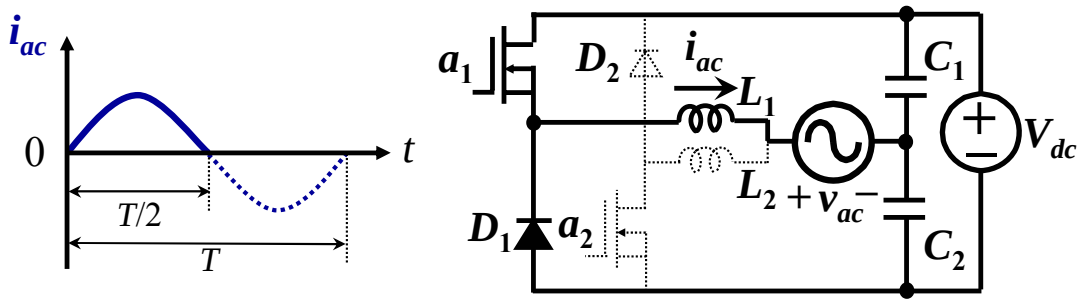

Figure 2.26 The proposed converter operating under inverter mode during the period when ac current is positive.

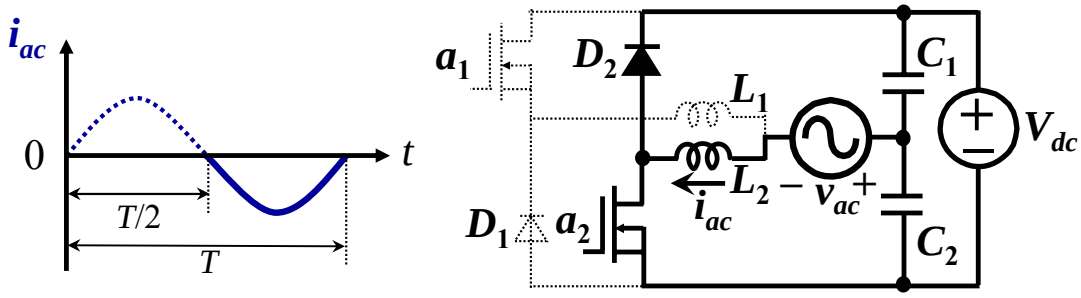

Figure 2.27 The proposed converter operating under inverter mode during the period when ac current is negative.

The proposed single-phase bidirectional ac-dc converter in Figure 2.5 consists of two buck converters under inverter mode. One buck converter operates while the other buck converter is inoperative, as indicated in Figure 2.26 and Figure 2.27. Each converter operates in a half line cycle. Accordingly, the magnetic components, L_1 and L_2, are only utilized in a half line cycle. The low utilization of the magnetic components may impose a serious penalty on system cost and power density.

However, the utilization can be improved by integrating the magnetic components. The utilization of the magnetic components in Figure 2.5 can be significantly improved by employing different coupled inductor structures. Two different structures of magnetic

integration are presented. One is to employ one coupled inductor in series with small inductors and the other one is to utilize two coupled inductors in series.

2.4.1 Coupled Inductor in Series with Small Inductors

The circuit diagram of the implementation with one coupled inductor is shown in Figure 2.28. In the circuit, two small inductors L_a and L_b are employed to block the undesired circulating current due to the imbalance of the inductance of the coupled inductor.

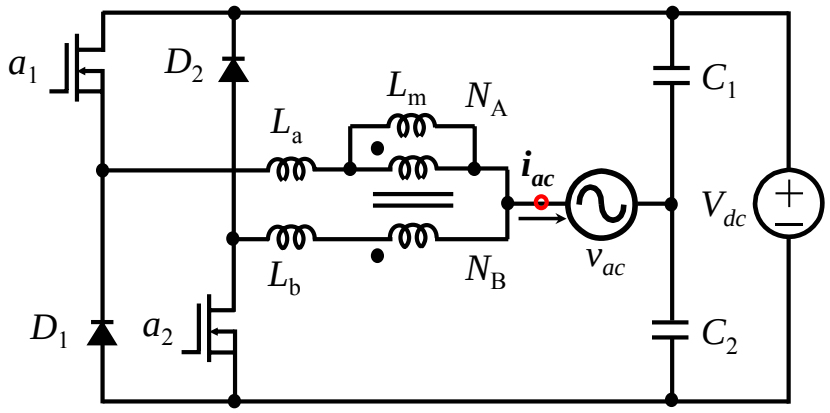

Figure 2.28 Bidirectional ac-dc converter with one coupled inductor.

As shown in Figure 2.29, during the period when ac current is positive (no matter ac voltage is positive or negative), the circuit consists of switch a_1, diode D_1, inductor L_a and winding N_A operates to conduct the current, while the circuit consists of switch a_2, diode D_2, inductor L_b and winding N_B is idle. Similarly, as shown in Figure 2.30, during the period when ac current is negative (no matter ac voltage is positive or negative), the circuit consists of switch a_2, diode D_2, inductor L_b and winding N_B operates to conduct the current, while the circuit consists of switch a_1, diode D_1, inductor L_a and winding N_A is idle.

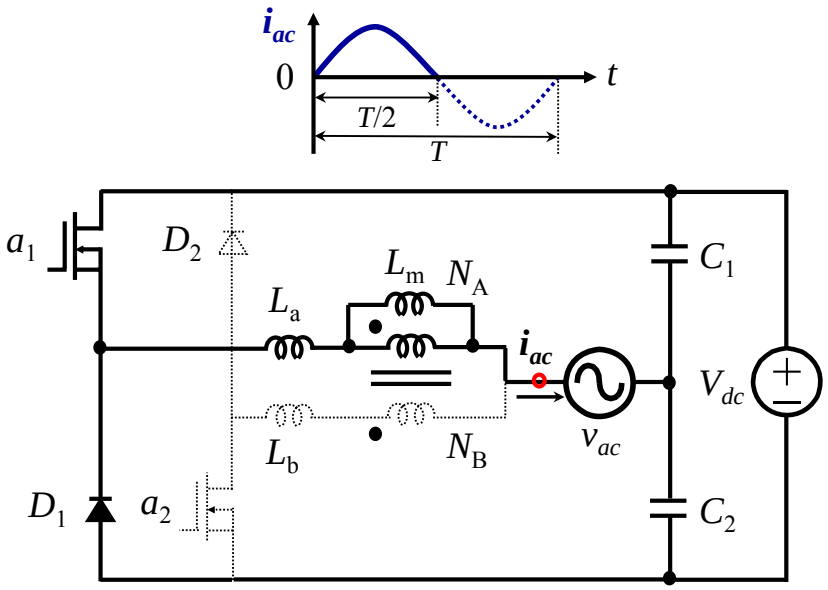

Figure 2.29 The proposed converter operating during the period when ac current is positive. The inactive components are shown in dashed lines.

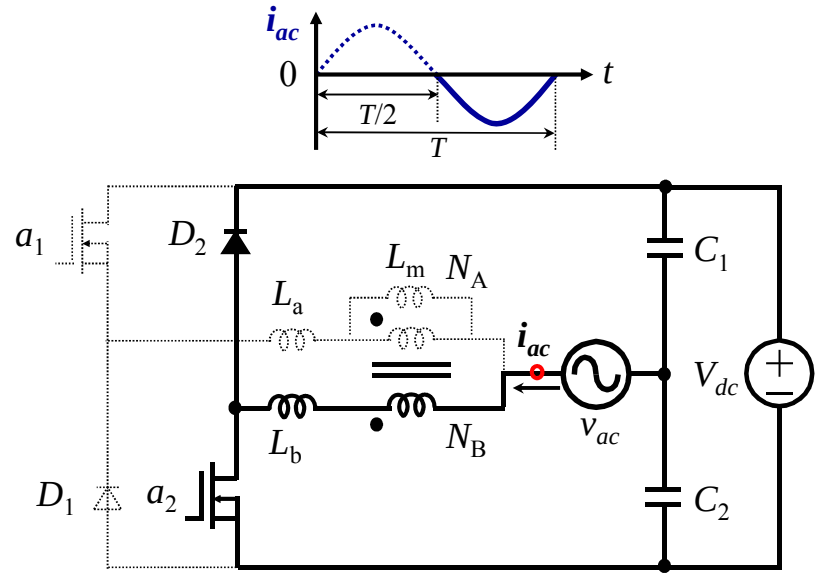

Figure 2.30 The proposed converter operating during the period when ac current is negative. The inactive components are shown in dashed lines.

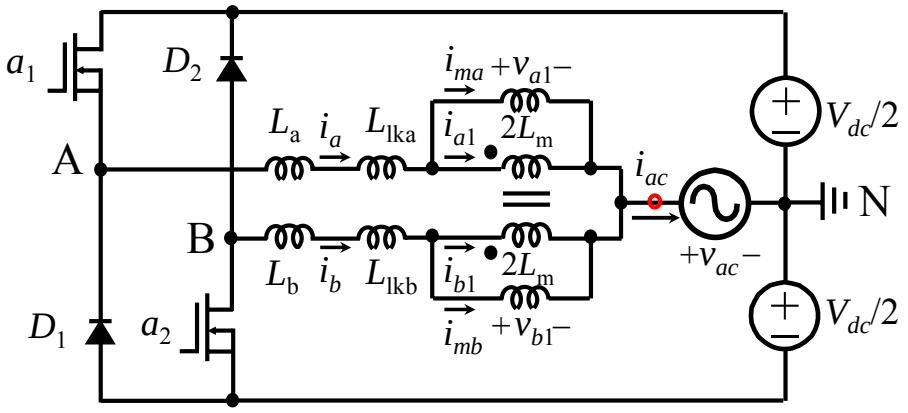

Figure 2.31 Symmetrical model of the proposed converter with one coupled inductor under inverter mode.

In order to analyze the effects of magnetizing and leakage inductance of the coupled inductor on the operation of the bidirectional ac-dc converter under inverter mode in Figure 2.28, the coupled inductor with a unity turns ratio is represented with a symmetrical model, as shown in Figure 2.31 [90]. In the symmetrical model, each side of the coupled inductor is represented with a magnetizing inductance connected in parallel with the corresponding winding and with a leakage inductance connected in series with the corresponding winding. The value of the magnetizing inductance connected in parallel with each winding of the ideal transformer is twice the total magnetizing inductance of the inductor, $L_{ma} = L_{mb} = 2L_m$.

With voltage and current reference directions under inverter mode as in Figure 2.31, the following voltage relationships can be easily established:

$$v_{a1} = v_{b1} \tag{2.12}$$

$$v_{a1} = 2L_m \frac{di_{ma}}{dt} \tag{2.13}$$

$$v_{b1} = 2L_m \frac{di_{mb}}{dt}. \tag{2.14}$$

From (2.12), (2.13) and (2.14), one can obtain

$$i_{ma} = i_{mb} = i_m . \tag{2.15}$$

Similarly, from Figure 2.31, the following current relationship can be written:

$$i_{a1} = -i_{b1} = i_T \tag{2.16}$$

$$i_a = i_{ma} + i_{a1} \tag{2.17}$$

$$i_b = i_{mb} + i_{b1} . \tag{2.18}$$

By using (2.15) and (2.16), current i_a and i_b can be expressed as:

$$i_a = i_m + i_T \tag{2.19}$$

$$i_b = i_m - i_T . \tag{2.20}$$

When leg a_1 and D_1 is operating and leg a_2 and D_2 is idle, one can get $i_b = 0$ and $i_m = i_T$. Apply Kirchhoff's Voltage Law (KVL) when a_1 is on and D_1 is off as shown in Figure 2.32, the following voltage relationship can be obtained

$$\frac{V_{dc}}{2} = (L_a + L_{lka})\frac{di_a}{dt} + 2L_m \frac{di_{ma}}{dt} + v_{ac} . \tag{2.21}$$

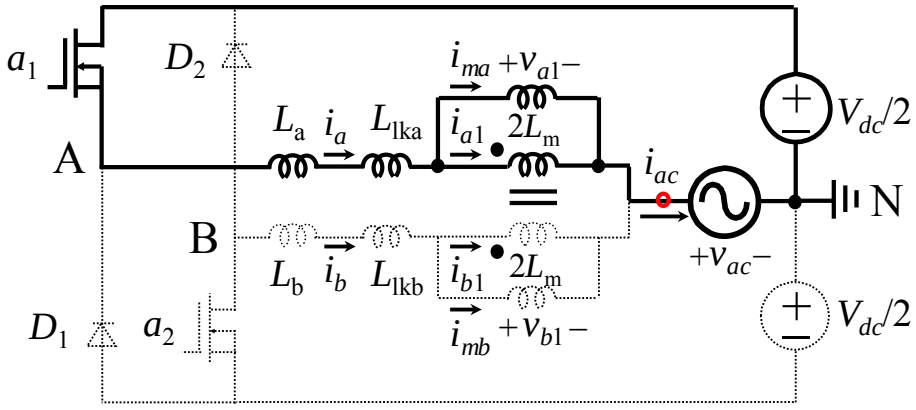

Figure 2.32 The proposed converter with one coupled inductor operating under inverter mode when ac current is positive and a_1 is on.

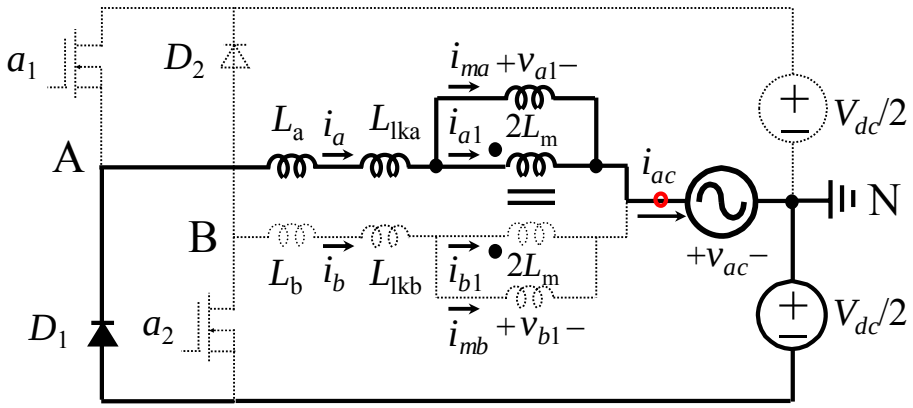

Figure 2.33 The proposed converter with one coupled inductor operating under inverter mode when ac current is positive and D_1 is on.

By using (2.15), (2.19) and (2.21), voltage v_{a1} can be expressed as

$$v_{a1} = L_m \frac{di_a}{dt} = (\frac{V_{dc}}{2} - v_{ac}) \frac{L_m}{(L_a + L_{lka}) + L_m}. \tag{2.22}$$

By using (2.12), the voltage of point B relative to neutral point N can be expressed as

$$-\frac{V_{dc}}{2} < V_{BN} = (\frac{V_{dc}}{2} - v_{ac}) \frac{L_m}{(L_a + L_{lka}) + L_m} + v_{ac} < \frac{V_{dc}}{2}. \tag{2.23}$$

Obviously, a_2 and D_2 will never be forced on.

Apply KVL when a_1 is off and D_1 is on as shown in Figure 2.33, the following voltage relationship can be obtained

$$-\frac{V_{dc}}{2} = (L_a + L_{lka}) \frac{di_a}{dt} + 2L_m \frac{di_{ma}}{dt} + v_{ac}. \tag{2.24}$$

By using (2.15), (2.19) and (2.24), voltage v_{a1} can be expressed as

$$v_{a1} = L_m \frac{di_a}{dt} = (-\frac{V_{dc}}{2} - v_{ac}) \frac{L_m}{(L_a + L_{lka}) + L_m}. \tag{2.25}$$

By using (2.12), the voltage of point B relative to neutral point N can be expressed as

$$-\frac{V_{dc}}{2} < V_{BN} = (-\frac{V_{dc}}{2} - v_{ac}) \frac{L_m}{(L_a + L_{lka}) + L_m} + v_{ac} < \frac{V_{dc}}{2}. \tag{2.26}$$

Again, a_2 and D_2 will never be forced on.

When leg a_2 and D_2 is operating and leg a_1 and D_1 is idle, one can get $i_a = 0$. When a_2 is on and D_2 is off, the voltage of point A relative to neutral N can be expressed as

$$-\frac{V_{dc}}{2} < V_{AN} = -(\frac{V_{dc}}{2} - v_{ac}) \frac{L_m}{(L_b + L_{lkb}) + L_m} - v_{ac} < 0. \tag{2.27}$$

Apparently, a_1 and D_1 will never be forced on.

When a_2 is off and D_2 is on, the voltage of point A relative to neutral N can be expressed as

$$0 < V_{AN} = (\frac{V_{dc}}{2} + v_{ac}) \frac{L_m}{(L_b + L_{lkb}) + L_m} - v_{ac} < \frac{V_{dc}}{2}. \tag{2.28}$$

Similarly, a_1 and D_1 will never be forced on.

Same conclusions can be drawn for the converter operating under rectifier mode.

Figure 2.34(a) and (b) shows the simulation results under both rectifier and inverter modes for the converter, respectively. It can be concluded that one leg operates while the other leg is idle.

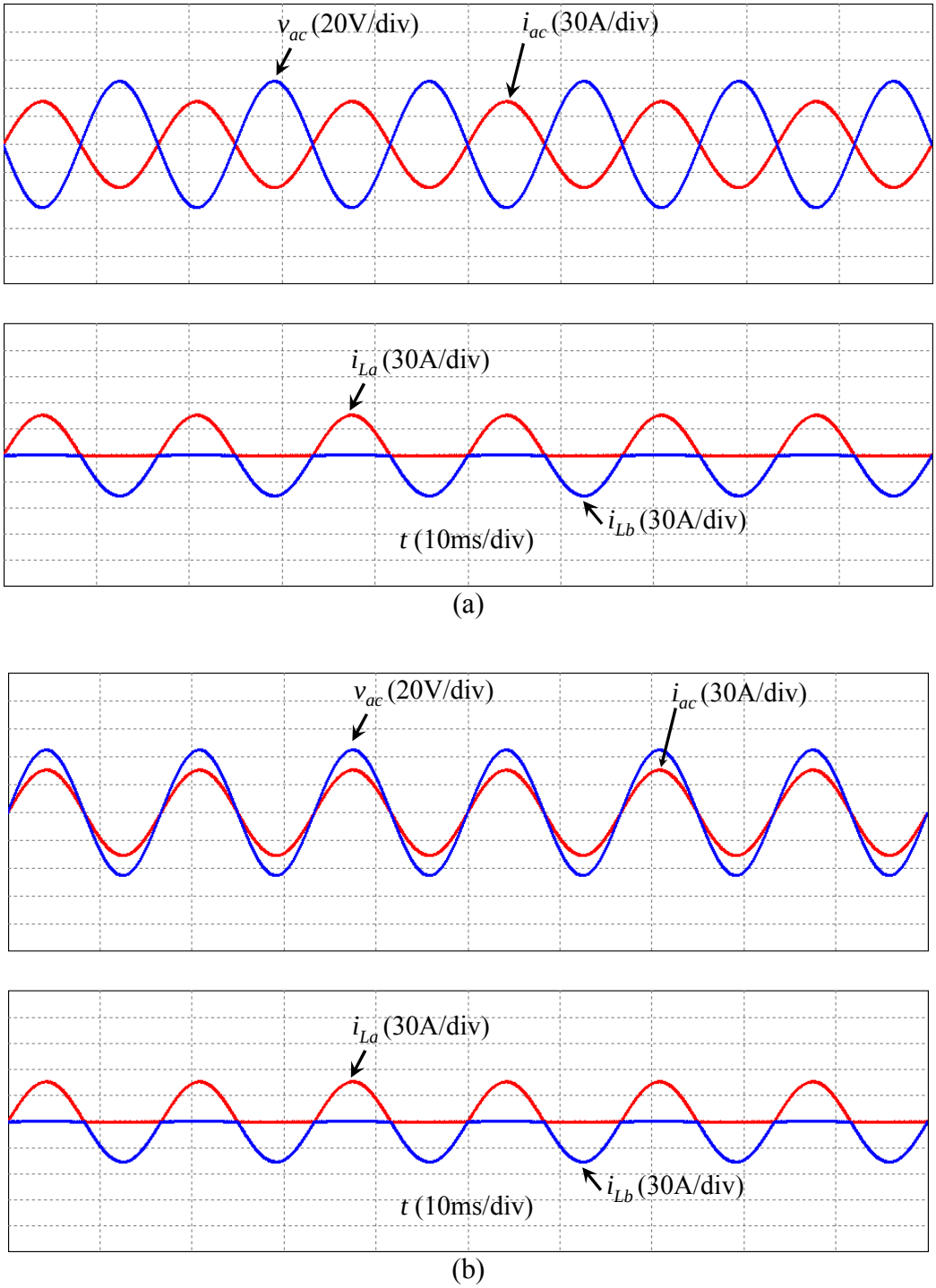

Figure 2.34 Simulation results of the proposed converter with one coupled inductor under (a) rectifier mode and (b) inverter mode.

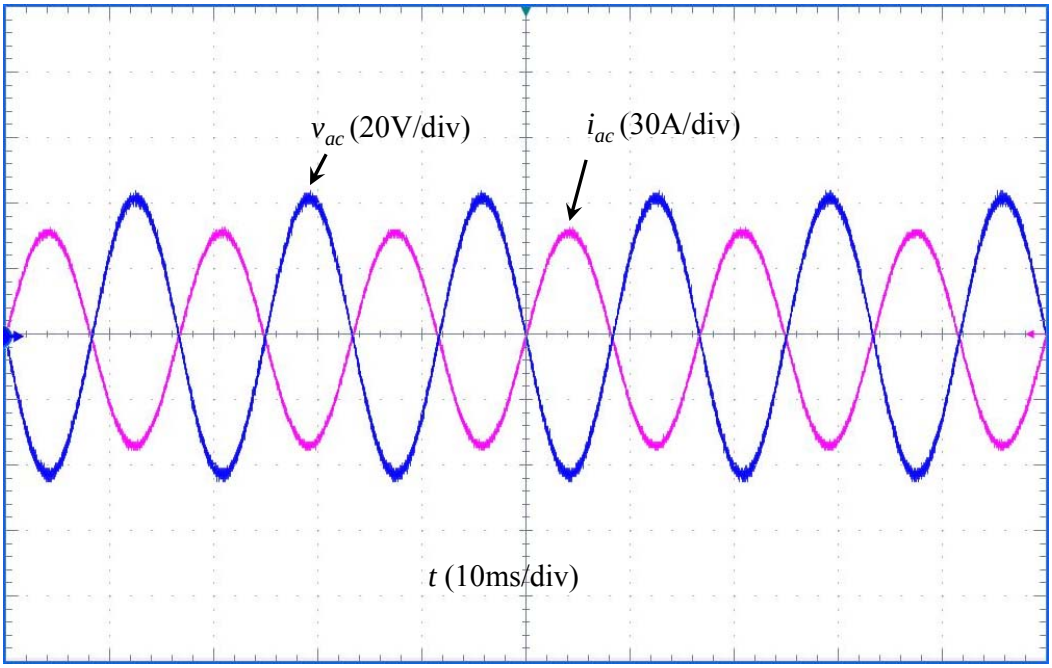

(a)

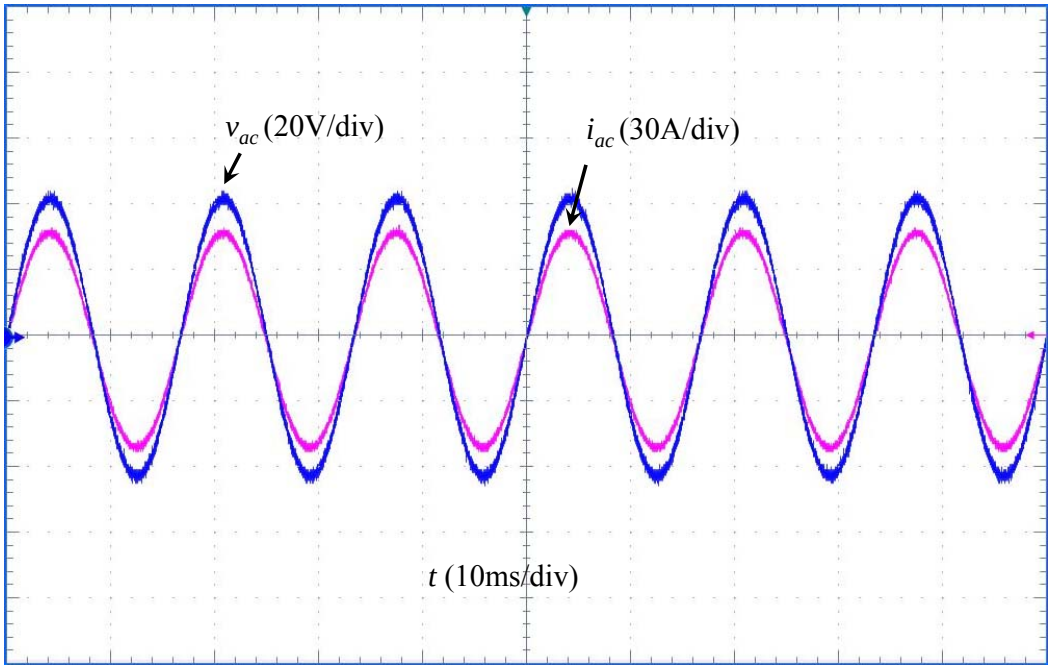

(b)

Figure 2.35 Experimental results of the proposed converter with one coupled inductor under (a) rectifier mode and (b) inverter mode.

Figure 2.35(a) and (b) shows the experimental results under both rectifier and inverter modes for the converter, respectively.

2.4.2 Two Coupled Inductors in Series

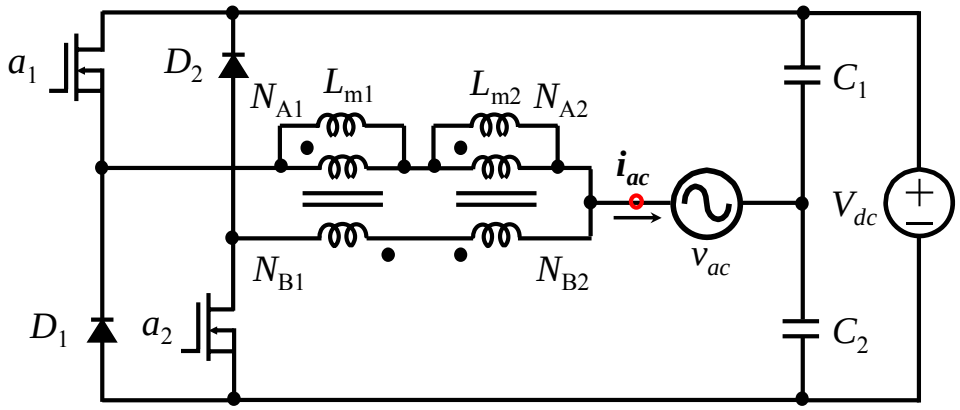

Figure 2.36 Bidirectional ac-dc converter with two coupled inductors.

The other method of magnetic integration is shown in Figure 2.36. Although there are still two coupled inductors in the circuit, the size and weight of the inductors are greatly reduced.

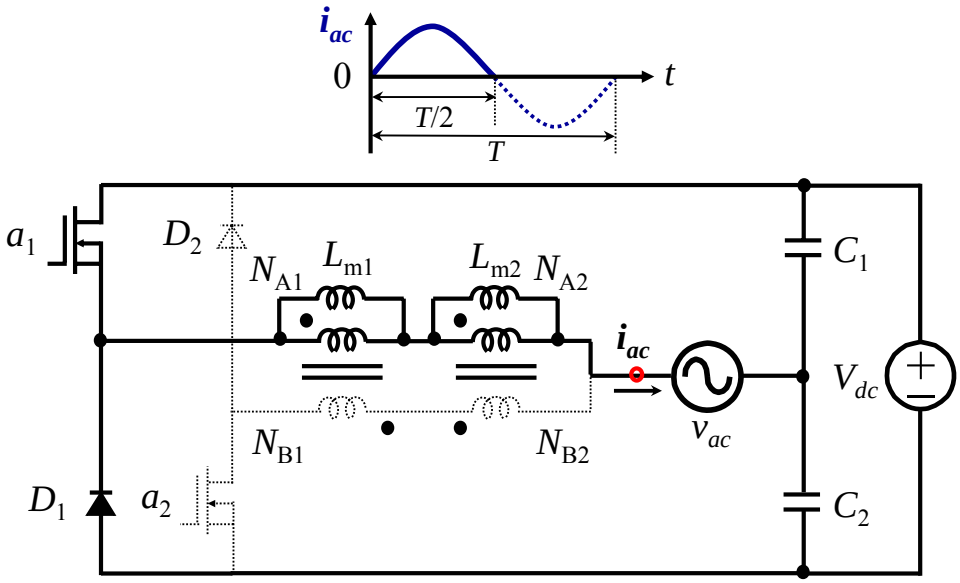

Figure 2.37 The proposed converter operating during the period when ac current is positive. The inactive components are shown in dashed lines.

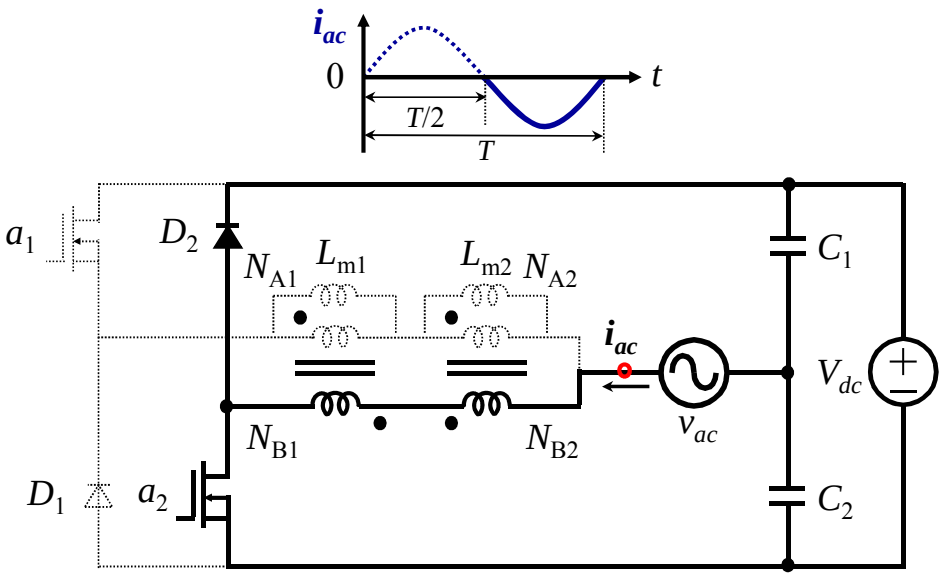

Figure 2.38 The proposed converter operating during the period when ac current is negative. The inactive components are shown in dashed lines.

As shown in Figure 2.37, during the period when ac current is positive (no matter ac voltage is positive or negative), the circuit consists of switch a_1, diode D_1, and windings N_{A1} and N_{A2} operate to conduct the current, while the circuit consists of switch a_2, diode D_2, and windings N_{B1} and N_{B2} is idle. Similarly, as shown in Figure 2.38, during the period when ac current is negative (no matter ac voltage is positive or negative), the circuit consists of switch a_2, diode D_2, and windings N_{B1} and N_{B2} operates to conduct the current, while the circuit consists of switch a_1, diode D_1, and windings N_{A1} and N_{A2} is idle. With magnetic integration, the power density is significantly improved and the weight of the converter is reduced.

In order to analyze the effects of magnetizing and leakage inductance of the coupled inductor on the operation of the bidirectional ac-dc converter under rectifier mode in Figure 2.36, the coupled inductor with a unity turns ratio is represented with a symmetrical model, as shown in Figure 2.39 [90]. In the symmetrical model, each side of the coupled inductor is represented with a magnetizing inductance connected in parallel with the corresponding winding and with a leakage inductance connected in series with the corresponding winding. The value of the magnetizing inductance connected in

parallel with each winding of the ideal transformer is twice the total magnetizing inductance of the inductor.

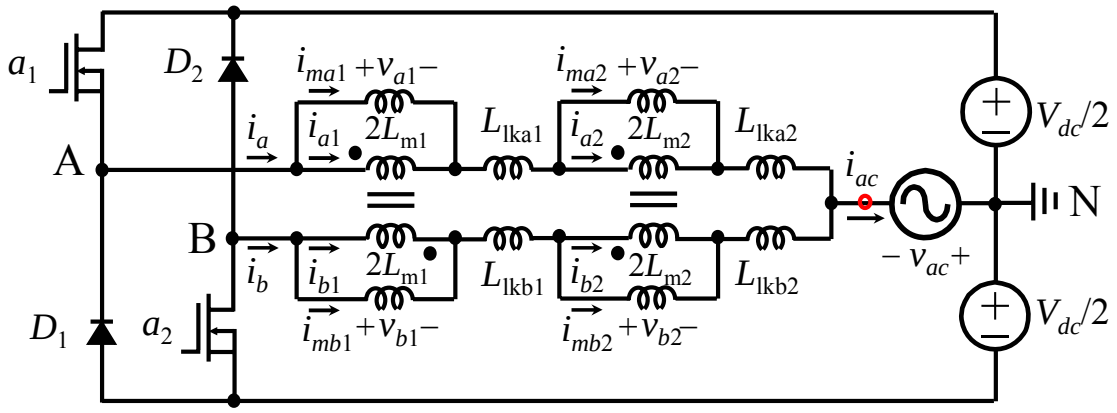

Figure 2.39 Symmetrical model of the proposed converter with two coupled inductors under rectifier mode.

With voltage and current reference directions under rectifier mode as in Figure 2.39, the following voltage relationships can be easily established:

$$v_{a1} = -v_{b1} \tag{2.29}$$

$$v_{a2} = v_{b2} \tag{2.30}$$

$$v_{a1} = 2L_{m1}\frac{di_{ma1}}{dt} \tag{2.31}$$

$$v_{b1} = 2L_{m1}\frac{di_{mb1}}{dt}. \tag{2.32}$$

$$v_{a2} = 2L_{m2}\frac{di_{ma2}}{dt} \tag{2.33}$$

$$v_{b2} = 2L_{m2}\frac{di_{mb2}}{dt}. \tag{2.34}$$

From (2.29), (2.31) and (2.32), one can obtain

$$i_{ma1} = -i_{mb1} = i_{m1} \tag{2.35}$$

whereas from (2.30), (2.33) and (2.34)

$$i_{ma2} = i_{mb2} = i_{m2}\,. \tag{2.36}$$

Similarly, from Figure 2.39, the following current relationship can be written:

$$i_{a1} = i_{b1} \tag{2.37}$$

$$i_{a2} = -i_{b2} \tag{2.38}$$

$$i_a = i_{ma1} + i_{a1} = i_{ma2} + i_{a2} \tag{2.39}$$

$$i_b = i_{mb1} + i_{b1} = i_{mb2} + i_{b2}\,. \tag{2.40}$$

Using (2.35) – (2.38) and adding (2.39) and (2.40), it follows that

$$i_{a1} = i_{b1} = i_{m2} \tag{2.41}$$

$$i_{a2} = -i_{b2} = i_{m1}\,. \tag{2.42}$$

Also, by using (2.35) and (2.41), current i_a can be obtained as

$$i_a = i_{m1} + i_{m2} \tag{2.43}$$

whereas by using (2.35) and (2.41), current i_b can be obtained as

$$i_b = -i_{m1} + i_{m2} \tag{2.44}$$

During the positive ac current half cycle, leg a_1 and D_1 is operating and leg a_2 and D_2 is idle. When a_1 is on and D_1 is off as shown in Figure 2.40, on can get

$$v_{b1} + v_{b2} + (L_{lkb1} + L_{lkb2})\frac{di_b}{dt} = 0. \tag{2.45}$$

The same result (2.45) also can be obtained when a_1 is off and D_1 is on as shown in Figure 2.41.

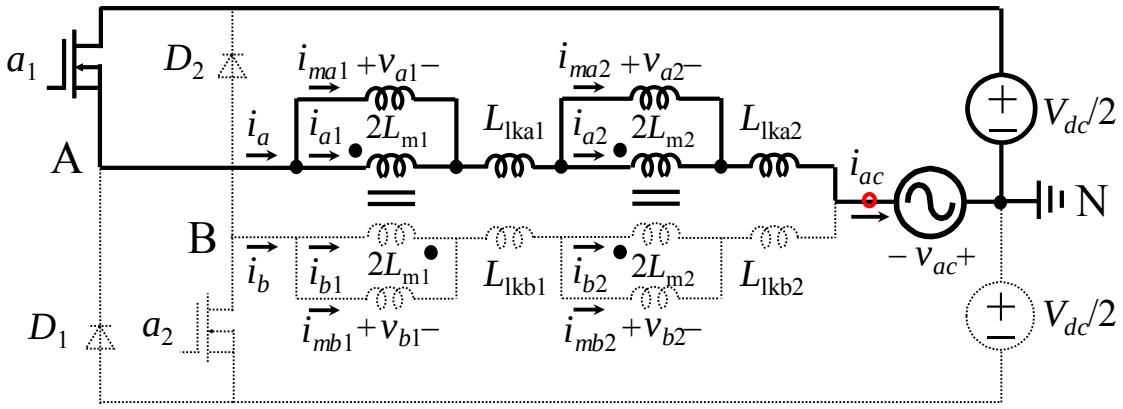

Figure 2.40 The proposed converter with two coupled inductors operating under rectifier mode when ac current is positive and a_1 is on.

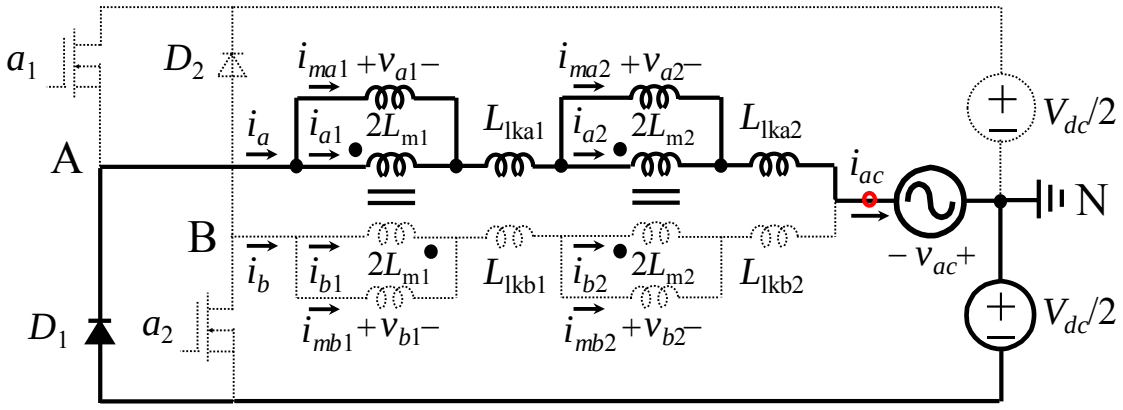

Figure 2.41 The proposed converter with two coupled inductors operating under rectifier mode when ac current is positive and D_1 is on.

Similarly, during the negative ac current half cycle, when leg a_2 and D_2 is operating and leg a_1 and D_1 is idle, one can get

$$v_{a1} + v_{a2} + (L_{lka1} + L_{lka2})\frac{di_a}{dt} = 0. \tag{2.46}$$

Using (2.32), (2.34), (2.35), (2.36), (2.44) and (2.45), the relationship between i_{m1} and i_{m2} during the positive ac current half cycle can be expressed as

$$i_{m1} = \frac{L_{m2} + (L_{lkb1} + L_{lkb2})/2}{L_{m1} + (L_{lkb1} + L_{lkb2})/2} i_{m2}. \tag{2.47}$$

Substituting (2.47) into (2.43) yields

$$i_a = i_{m1} + i_{m2} = \frac{L_{m1} + L_{m2} + (L_{lkb1} + L_{lkb2})}{L_{m1} + (L_{lkb1} + L_{lkb2})/2} i_{m2}. \tag{2.48}$$

whereas substituting (2.47) into (2.44) yields

$$i_b = -i_{m1} + i_{m2} = \frac{L_{m1} - L_{m2}}{L_{m1} + (L_{lkb1} + L_{lkb2})/2} i_{m2}. \tag{2.49}$$

Eliminating i_{m2} from (2.48) and (2.49), the relationship between i_a and i_b can be derives as

$$\frac{i_b}{i_a} = \frac{L_{m1} - L_{m2}}{L_{m1} + L_{m2} + (L_{lkb1} + L_{lkb2})}. \tag{2.50}$$

As can be seen from (2.50), for $L_{m1} = L_{m2}$, no ripple current is returned through windings N_{B1} and N_{B2} regardless of their leakage inductance. If $L_{m1} \neq L_{m2}$, the amount of the ripple current returned through windings N_{B1} and N_{B2} is determined by the difference between the two magnetizing inductances.

Similarly, during the negative ac current half cycle, when leg a_2 and D_2 is operating and leg a_1 and D_1 is idle, the relationship between i_a and i_b can be derives as

$$\frac{i_a}{i_b} = \frac{L_{m1} - L_{m2}}{L_{m1} + L_{m2} + (L_{lka1} + L_{lka2})}. \tag{2.51}$$

Due to symmetrical operation, the behavior of the circuit during the negative ac current half cycle is identical to that during the positive ac current half cycle. If $L_{m1} \neq L_{m2}$, the amount of the ripple current returned through windings N_{A1} and N_{A2} is determined by the difference between the two magnetizing inductances.

Under inverter mode during the positive ac current half cycle, when leg a_1 and D_1 is operating and leg a_2 and D_2 is idle, the relationship between i_a and i_b can be derives as

$$\frac{i_b}{i_a} = \frac{L_{m1} - L_{m2}}{L_{m1} + L_{m2} + (L_{lkb1} + L_{lkb2})}. \tag{2.52}$$

If $L_{m1} \neq L_{m2}$, the amount of the ripple current returned through windings N_{B1} and N_{B2} is determined by the difference between the two magnetizing inductances.

Under inverter mode during the negative ac current half cycle, when leg a_2 and D_2 is operating and leg a_1 and D_1 is idle, the relationship between i_a and i_b can be derives as

$$\frac{i_a}{i_b} = \frac{L_{m1} - L_{m2}}{L_{m1} + L_{m2} + (L_{lka1} + L_{lka2})}. \tag{2.53}$$

Due to symmetrical operation, the behavior of the circuit during the negative ac current half cycle is identical to that during the positive ac current half cycle.

Figure 2.42(a) and (b) shows the simulation results under both rectifier and inverter modes for the converter, respectively. It can be concluded that one leg operates while the other leg is idle.

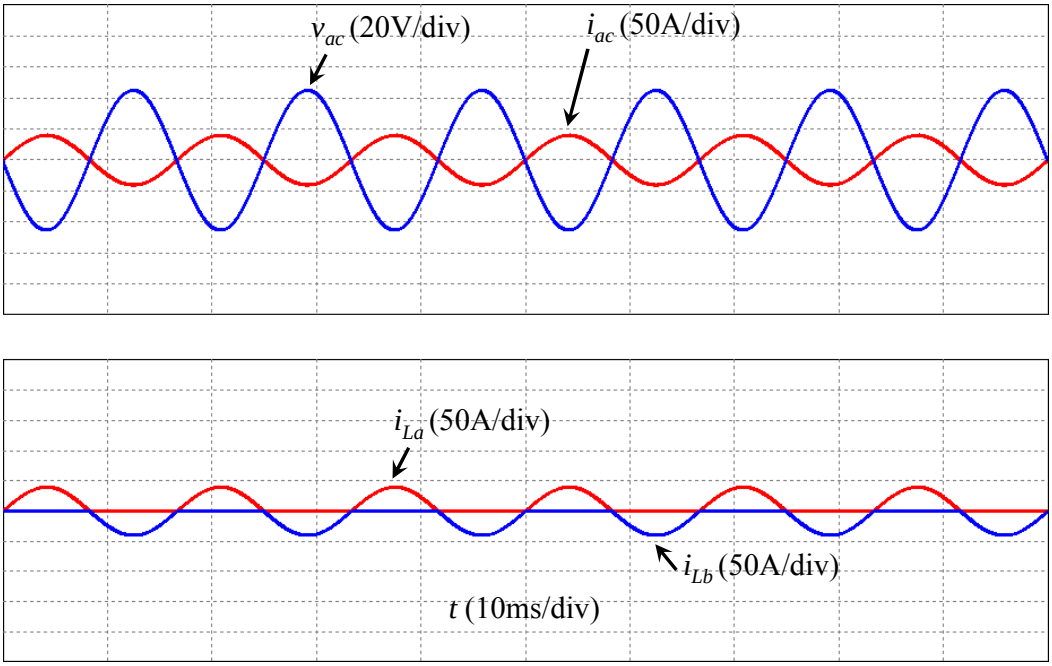

(a)

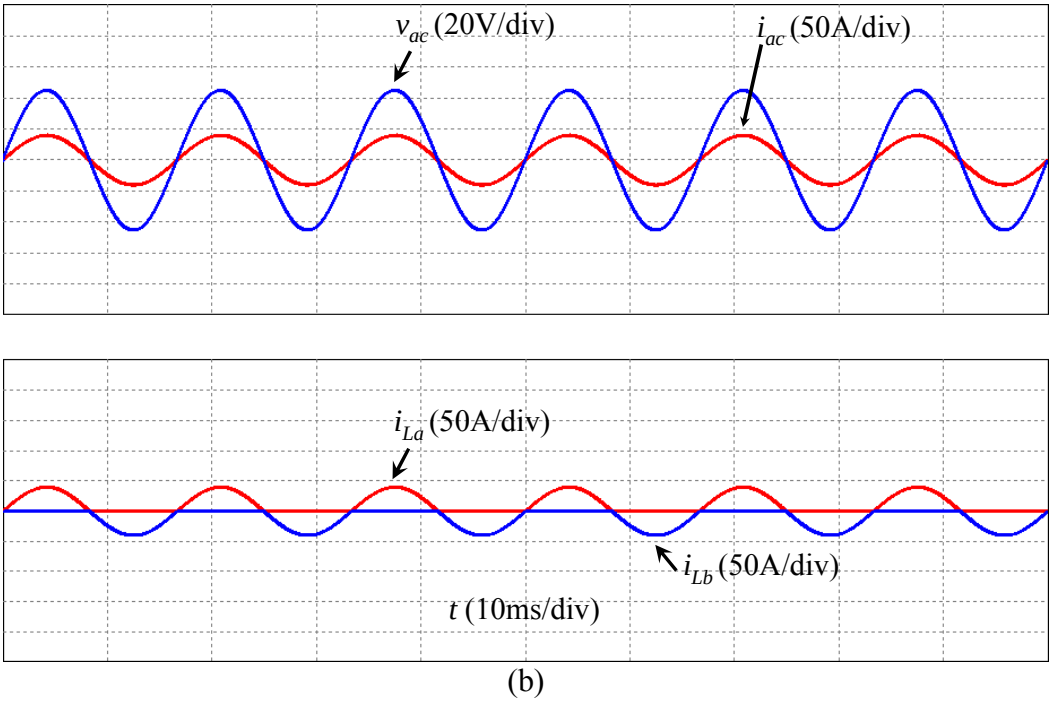

(b)

Figure 2.42 Simulation results of the proposed converter with two coupled inductors under (a) rectifier mode and (b) inverter mode.

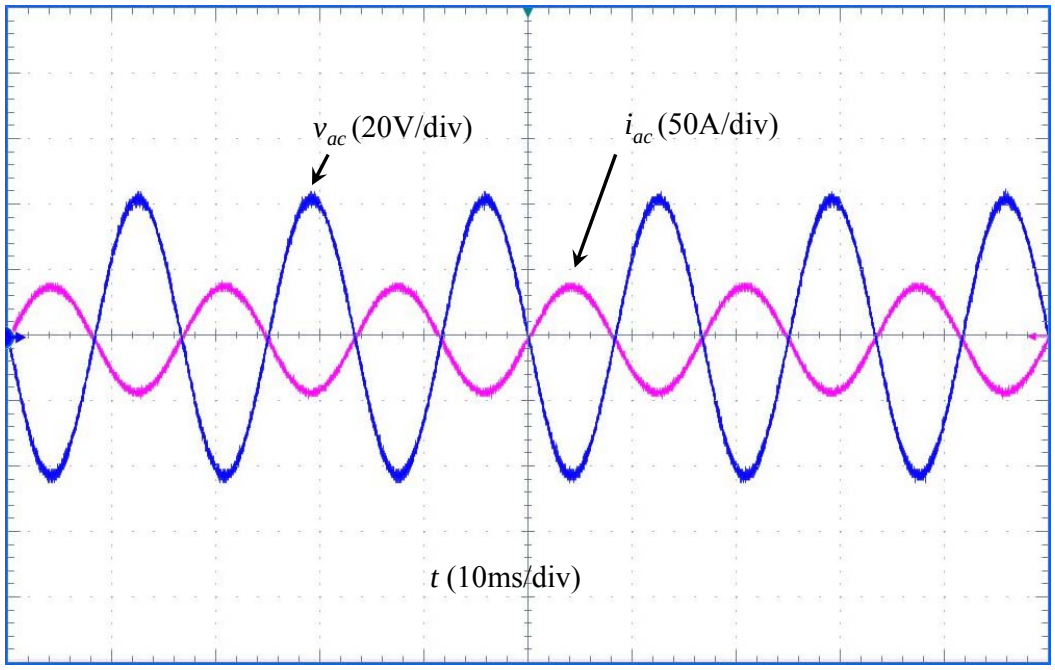

(a)

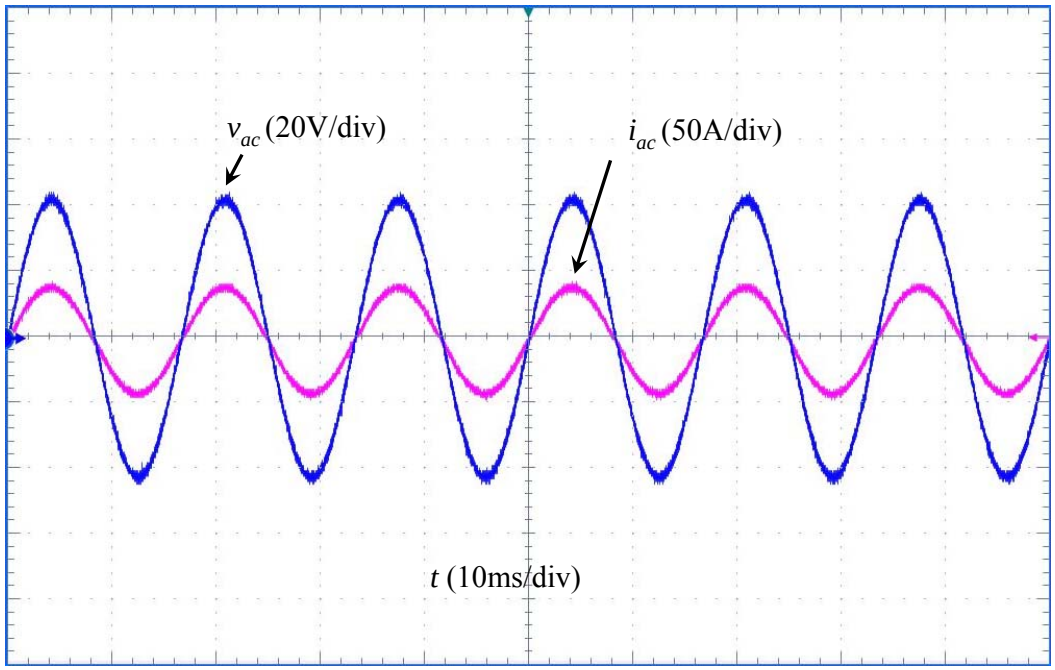

(b)

Figure 2.43 Experimental results of the proposed converter with two coupled inductors under (a) rectifier mode and (b) inverter mode.

Figure 2.43(a) and (b) shows the experimental results under both rectifier and inverter modes for the converter, respectively. The efficiency of the converter with two coupled inductors is the same as the converter without magnetic integration.

2.5 Summary

The renewable energy source based DG systems are normally interfaced to the grid through power electronic converters and energy storage systems. Recent developments and advantages in energy storage and power electronics technologies are making the application of energy storage technologies a viable solution for modern power applications. In order to meet the challenges of practical utility applications, an energy storage system should have ac-dc/dc-ac bidirectional power conversion capability, islanding function, and high round-loop efficiency.

The proposed high-efficiency bidirectional ac-dc converter in this chapter adopts opposed current half bridge inverter architecture. Since it consists of two buck converters and also has features of the conventional half bridge inverter, it is named as dual-buck half bridge inverter. The converter exhibits two distinct merits: first, there is no shoot-through issue because no active power switches are connected in series in each phase leg; second, the reverse recovery dissipation of the power switch is greatly reduced because there is no freewheeling current flowing through the body diode of power switches. The implemented converter efficiency peaks at 97.8% at 50-kHz switching frequency for both rectifier and inverter modes.

A new SPWM scheme by using split SPWM as the main scheme and joint SPWM as the supplementary scheme for the zero-crossing region is proposed. On one hand, since split SPWM is utilized as the main scheme, conduction and switching losses are relatively low. On the other hand, because joint SPWM is employed for the zero-crossing region, the ac current zero-crossing distortion problem is solved.

The proposed bidirectional ac-dc converter consists of two buck converters under inverter mode, each operating during a half line cycle. As a result, the magnetic components are only utilized during the half line cycle. The low utilization of the magnetic components may impose a serious penalty on system cost and power density. However, the utilization can be improved by integrating the magnetic components. Two

different structures of magnetic integration are presented. One is employing one coupled inductor in series with small inductors and the other one is utilizing two coupled inductors in series.

Chapter 3 Novel Bidirectional AC-DC Converter

3.1 Introduction

A dual-buck converter based bidirectional ac-dc converter was proposed in chapter 2, as shown in Figure 2.5. The circuit consists of two power MOSFETs a_1 and a_2, two diodes D_1 and D_2, two inductors L_1 and L_2, and two split dc bus capacitors C_1 and C_2. The voltage across each capacitor C_1 and C_2 should be always larger than the peak ac voltage to ensure the circuit works properly throughout the whole line cycle. The major issues with this type of converter are two large dc bus capacitors, low dc bus voltage utilization, and large-size inductors due to bipolar SPWM control scheme. Also a voltage balance compensator needs to be designed to balance the voltage across the two dc split capacitors.

3.2 Novel Single-Phase Bidirectional AC-DC Converter

3.2.1 Topology

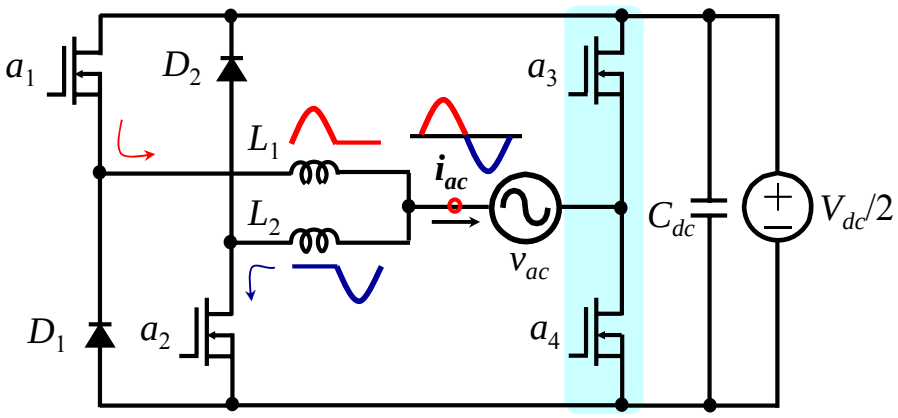

Figure 3.1 Circuit diagram of the proposed novel single-phase bidirectional ac-dc converter.

To better utilize the dc bus voltage, eliminate the two dc bus capacitors, and reduce the size of the inductors, a novel bidirectional ac-dc converter is derived from Figure 2.5 by replacing the two-capacitor leg with a two-switch leg, as shown in Figure 3.1. The novel bidirectional ac-dc converter keeps the merits of the dual-buck converter based bidirectional ac-dc converter. The converter works as a rectifier when the power is transferred from ac grid to dc source. Alternately, it works as an inverter when the power is transferred from dc source to ac grid.

3.2.2 Operating Principle

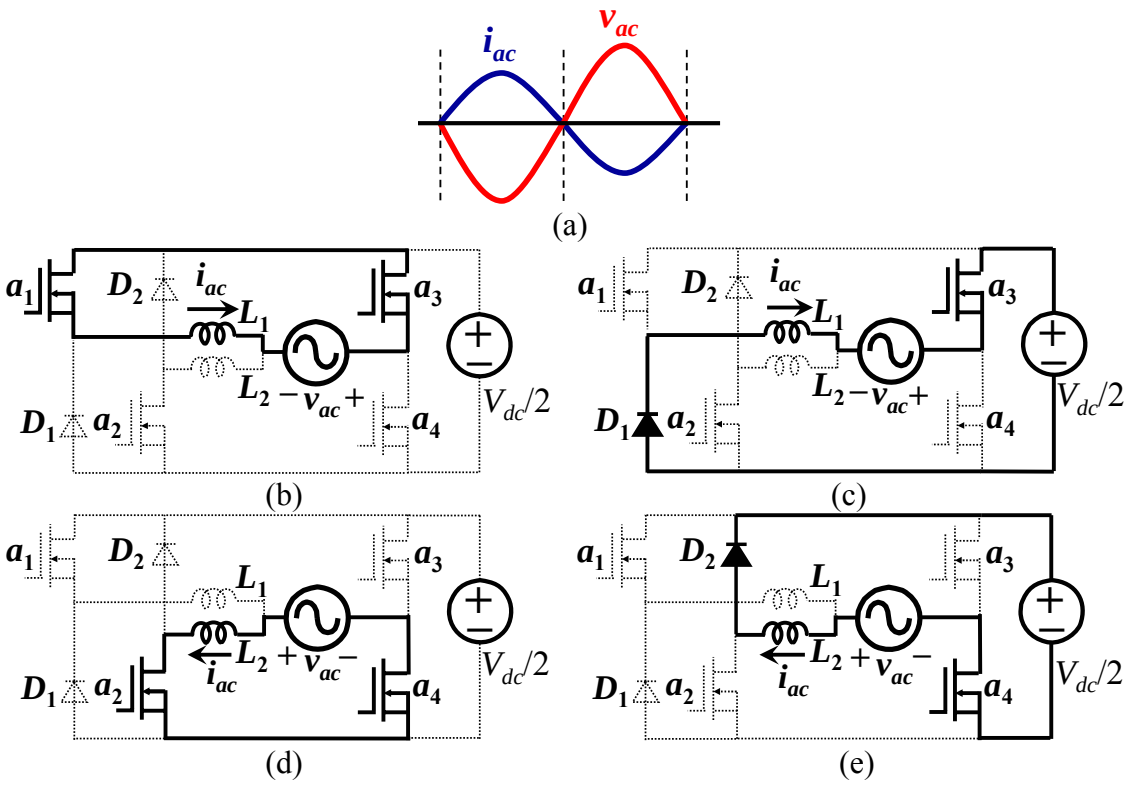

Figure 3.2 Operating under rectifier mode with pure active power transferring. (a) Conceptual voltage and current waveform. (b) a_1 is on. (c) D_1 is on. (d) a_2 is on. (e) D_2 is on.

Figure 3.2 and Figure 3.3 show the four sub-operating modes under rectifier and inverter modes, respectively. For the rectifier mode with pure active power transferring, there are four sub-operating modes depending on the conducting status of a_1, a_2, D_1, D_2,

a_3, and a_4. In the positive current half cycle when $i_{ac} > 0$ ($i_{L2} = 0$) and $v_{ac} < 0$, leg a_1 and D_1 operates and a_3 is always on. When a_1 is on and D_1 is off, current i_{ac} is increased because the voltage across inductor L_1 is positive,

$$V_{L1} = L_1 \frac{di_{ac}}{dt} = v_{ac} > 0 . \tag{3.1}$$

When a_1 is off and D_1 is on, current i_{ac} is decreased because the voltage across inductor L_1 is negative,

$$V_{L1} = L_1 \frac{di_{ac}}{dt} = -\frac{V_{dc}}{2} + v_{ac} < 0 . \tag{3.2}$$

In the negative current half cycle when $i_{ac} < 0$ ($i_{L1} = 0$) and $v_{ac} > 0$, leg a_2 and D_2 operates and a_4 is always on. When a_2 is on and D_2 is off, current i_{ac} is increased because the voltage across inductor L_2 is positive,

$$V_{L2} = L_2 \frac{di_{ac}}{dt} = v_{ac} > 0 . \tag{3.3}$$

When a_2 is off and D_2 is on, current i_{ac} is decreased because the voltage across the inductor L_2 is negative,

$$V_{L2} = L_2 \frac{di_{ac}}{dt} = -\frac{V_{dc}}{2} + v_{ac} < 0 . \tag{3.4}$$

Based on the aforementioned analysis, it can be concluded that leg a_1 and D_1 and leg a_2 and D_2 are controlled by high-frequency SPWM and leg a_3 and a_4 is controlled by low-frequency line-cycle signal.

For the inverter mode with pure active power transferring, all the analysis is similar to that of rectifier mode except that the current and voltage are in phase; therefore, the energy is transferred from dc sources to ac grid. In the positive current half cycle when $i_{ac} > 0$ ($i_{L2} = 0$) and $v_{ac} > 0$, leg a_1 and D_1 operates and a_4 is always on. In the negative current half cycle when $i_{ac} < 0$ ($i_{L1} = 0$) and $v_{ac} < 0$, leg a_2 and D_2 operates and a_3 is

always on. Based on the aforementioned analysis, it can be concluded that the leg a_1 and D_1 conducts positive current, and the leg a_2 and D_2 conducts negative current whenever voltage is positive or negative; a_3 is on in the negative voltage half cycle and a_4 is on in the positive voltage half cycle whenever current is positive or negative.

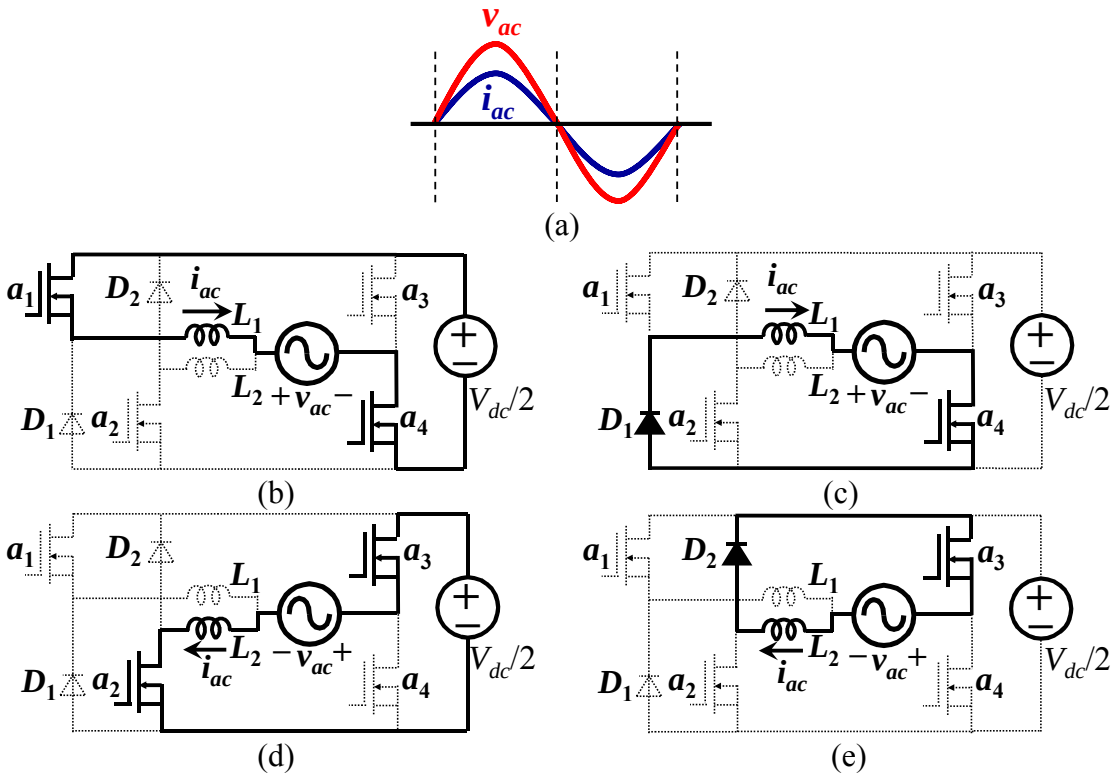

Figure 3.3 Operating under rectifier mode with pure active power transferring. (a) Conceptual voltage and current waveform. (b) a_1 is on. (c) D_1 is on. (d) a_2 is on. (e) D_2 is on.

To transfer reactive power between ac grid and dc sources, the operation of the circuit becomes much more complicated. Based on the phase angle difference between the ac current and voltage, one line cycle can be represented by four different switch combinations, as shown in Table 3.1, in different order.

Table 3.1 Different switching combinations

Conditions	a_1 & D_1	a_2 & D_2	a_3	a_4
$i_{ac} > 0$ ($i_{L2} = 0$) and $v_{ac} > 0$	PWM	OFF	OFF	ON
$i_{ac} > 0$ ($i_{L2} = 0$) and $v_{ac} < 0$	PWM	OFF	ON	OFF
$i_{ac} < 0$ ($i_{L1} = 0$) and $v_{ac} > 0$	OFF	PWM	OFF	ON
$i_{ac} < 0$ ($i_{L1} = 0$) and $v_{ac} < 0$	OFF	PWM	ON	OFF

3.2.3 Simulation Results

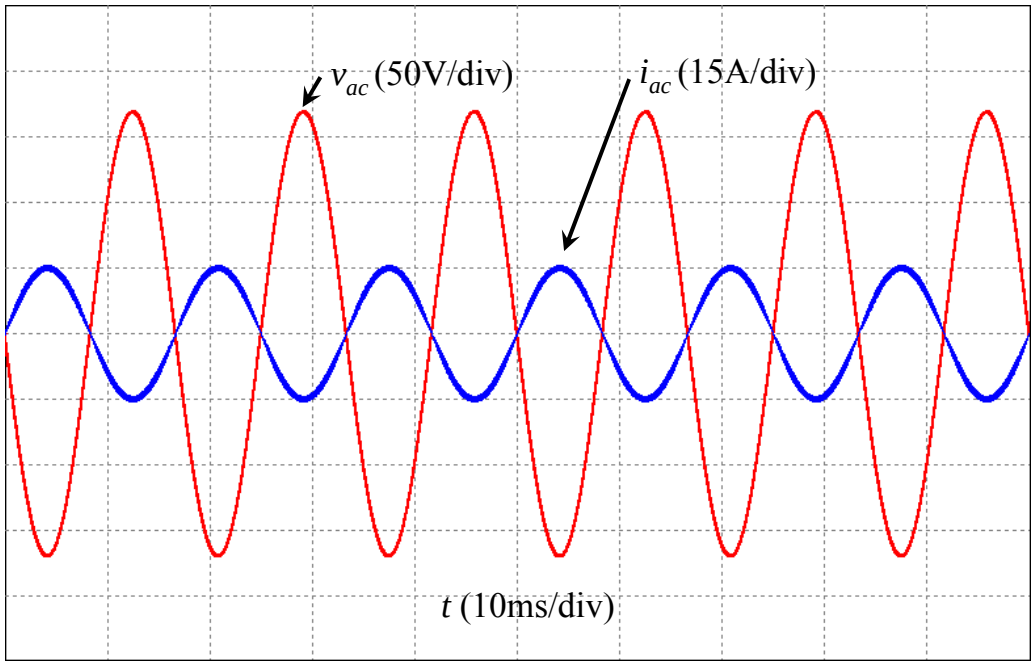

(a)

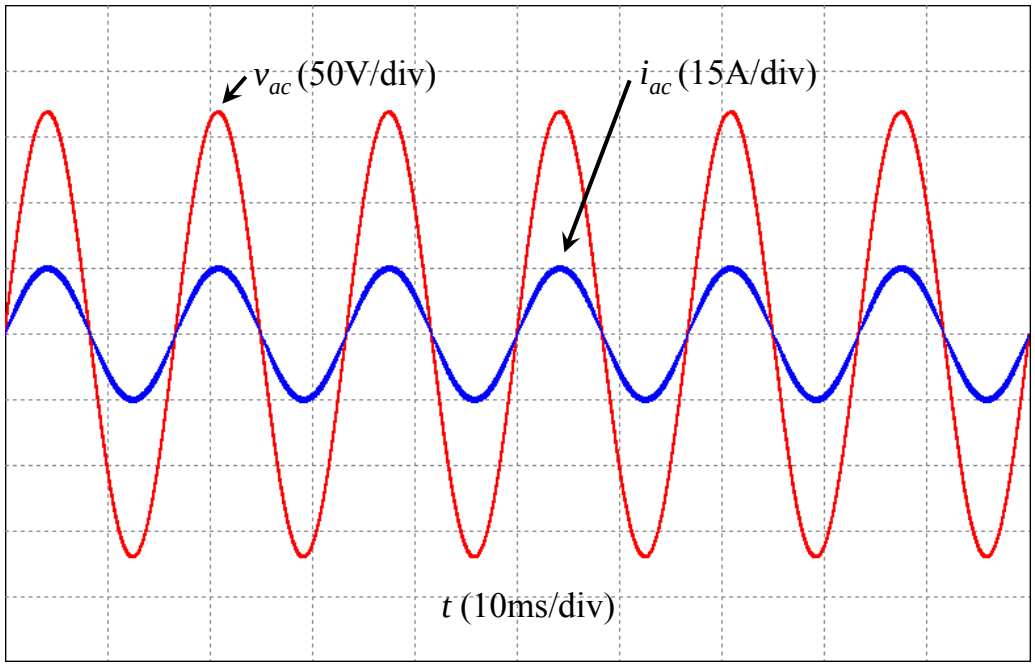

(b)

Figure 3.4 Simulation results under (a) rectifier mode and (b) inverter mode.

Figure 3.4(a) and (b) shows the simulation results under both rectifier and inverter modes for the converter, respectively. Figure 3.4(a) shows current and voltage are out of phase. Figure 3.4(b) shows current and voltage are in phase.

3.2.4 Experimental Results

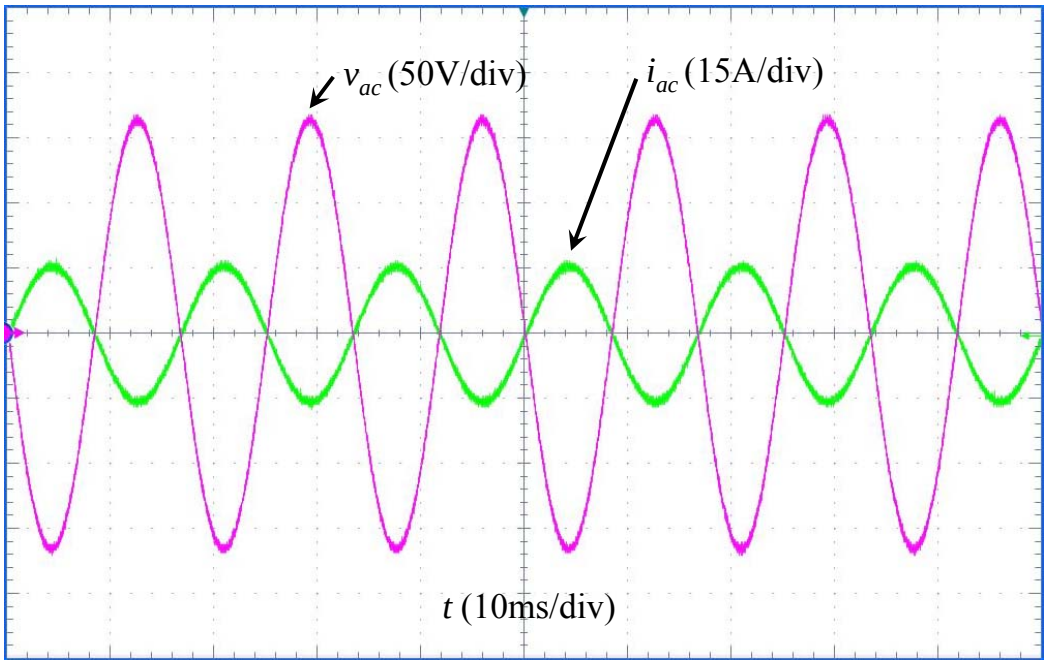

(a)

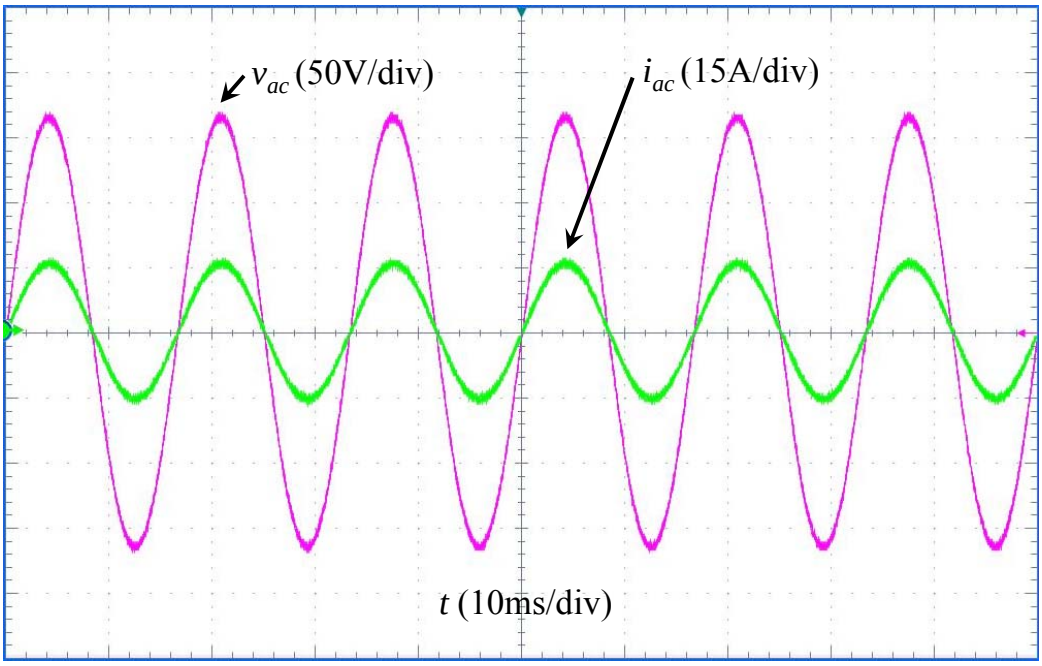

(b)

Figure 3.5 Experimental results under (a) rectifier mode and (b) inverter mode.

Figure 3.5(a) and (b) shows the experimental results under both rectifier and inverter modes for the converter, respectively. Figure 3.5(a) shows current and voltage are out of phase. Figure 3.5(b) shows current and voltage are in phase.

3.3 Novel Single-Phase Bidirectional AC-DC Converter with Magnetic Integration

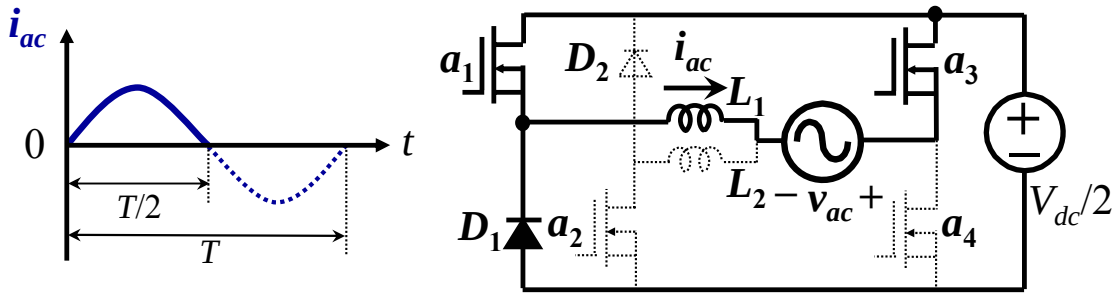

Figure 3.6 The proposed converter operating under rectifier mode during the period when ac current is positive.

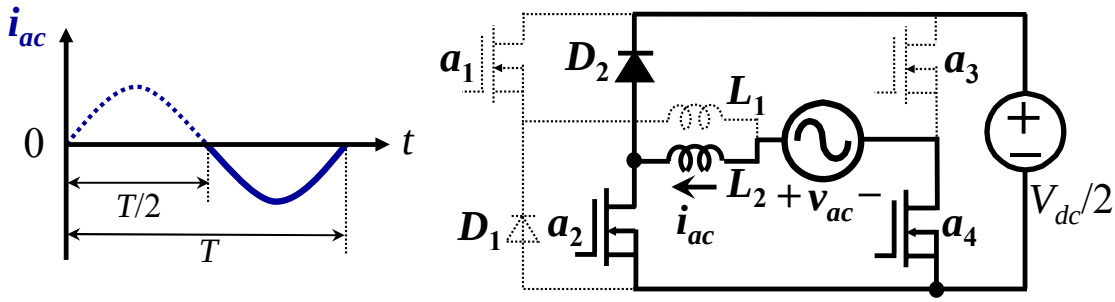

Figure 3.7 The proposed converter operating under rectifier mode during the period when ac current is negative.

The proposed novel single-phase bidirectional ac-dc converter in Figure 3.1 consists of two boost converters under rectifier mode. One boost converter operates while the other boost converter is inoperative, as shown in Figure 3.6 and Figure 3.7. Each boost converter operates in a half line cycle. Consequently, the magnetic components, L_1 and L_2, are only utilized in a half line cycle.

Similarly, the novel single-phase bidirectional ac-dc converter in Figure 3.1 consists of two buck converters under inverter mode. One buck converter operates while the other buck converter is inoperative, as indicated in Figure 3.8 and Figure 3.9. Each buck

converter operates in a half line cycle. As a result, the magnetic components, L_1 and L_2, are only utilized in a half line cycle.

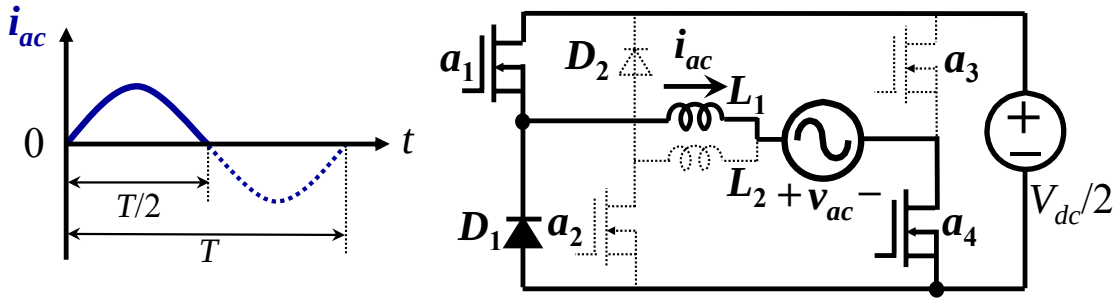

Figure 3.8 The proposed converter operating under inverter mode during the period when ac current is positive.

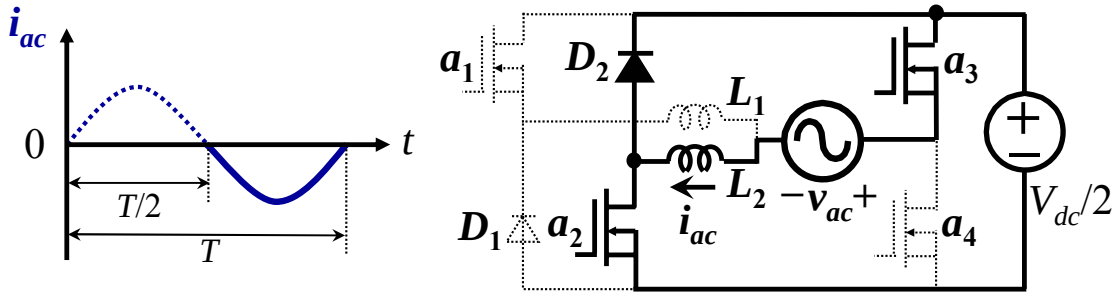

Figure 3.9 The proposed converter operating under inverter mode during the period when ac current is negative.

The low utilization of the magnetic components may impose a serious penalty on system cost and power density. However, the utilization can be improved by integrating the magnetic components. The utilization of the magnetic components in Figure 3.1 can be significantly improved by employing different coupled inductor structures. Two different methods of magnetic integration are proposed. One method is to utilize one coupled inductor in series with small inductors and the other one is to employ two coupled inductors in series.

3.3.1 Coupled Inductor in Series with Small Inductors

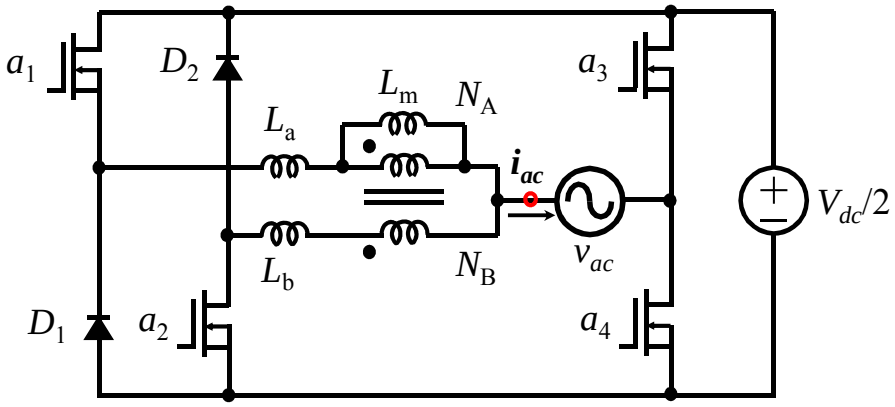

Figure 3.10 Novel bidirectional ac-dc converter with one coupled inductor.

The circuit diagram of the implementation with one coupled inductor is shown in Figure 3.10. In this circuit, two small inductors L_a and L_b are employed to block the undesired circulating current due to the imbalance of the inductance of the coupled inductor.

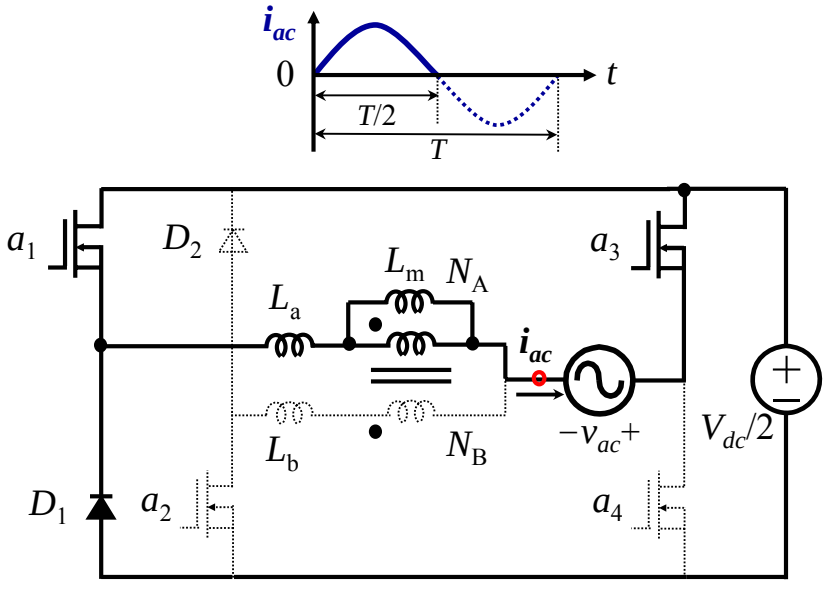

Figure 3.11 The proposed converter with one coupled inductor operating under rectifier mode during the period when ac current is positive.

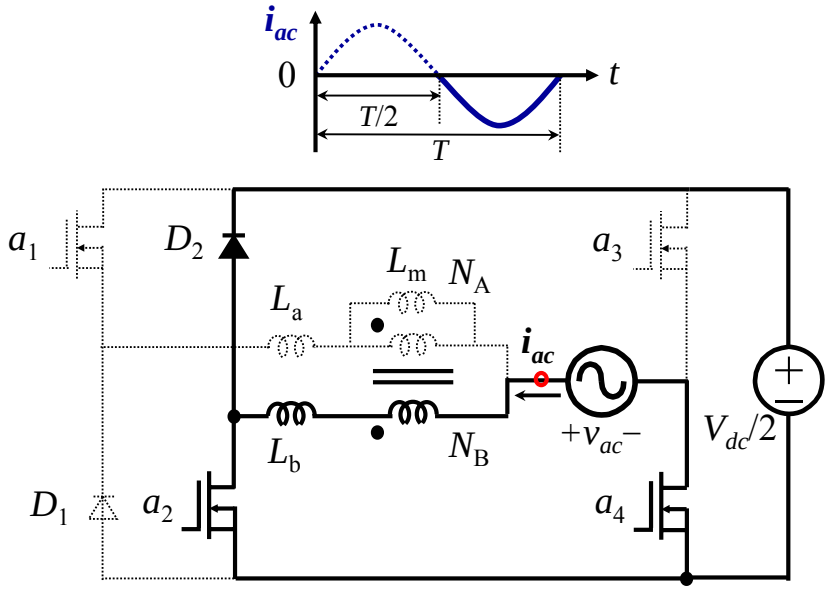

Figure 3.12 The proposed converter with one coupled inductor operating under rectifier mode during the period when ac current is negative.

The proposed magnetic integration method for the bidirectional ac-dc converter in Figure 3.10 consists of two boost converters under rectifier mode. One boost converter operates while the other boost converter is idle, as shown in Figure 3.11 and Figure 3.12. Each boost converter operates in a half line cycle. During the period when ac current is positive, as shown in Figure 3.11, the circuit consists of switch a_1, diode D_1, inductor L_a and winding N_A, and switch a_3 operates to conduct the current, while the circuit consists of switch a_2, diode D_2, inductor L_b and winding N_B, and switch a_4 is idle. Similarly, as shown in Figure 3.12, during the period when ac current is negative, the circuit consists of switch a_2, diode D_2, inductor L_b and winding N_B, and switch a_4 operates to conduct the current, while the circuit consists of switch a_1, diode D_1, inductor L_a and winding N_A, and switch a_3 is idle.

The proposed magnetic integration method for the bidirectional ac-dc converter in Figure 3.10 consists of two buck converters under inverter mode. One buck converter operates while the other buck converter is idle, as shown in Figure 3.13 and Figure 3.14. Each buck converter operates in a half line cycle

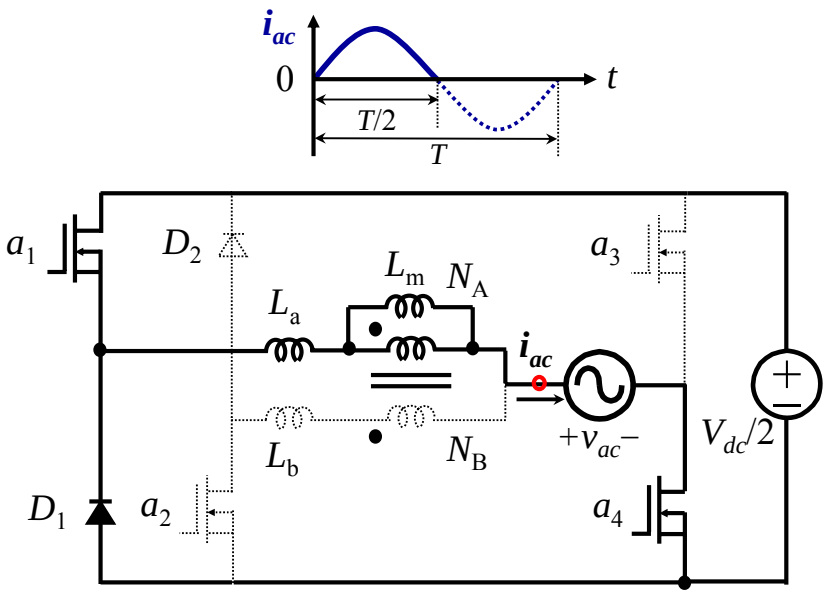

Figure 3.13 The proposed converter with one coupled inductor operating under inverter mode during the period when ac current is positive.

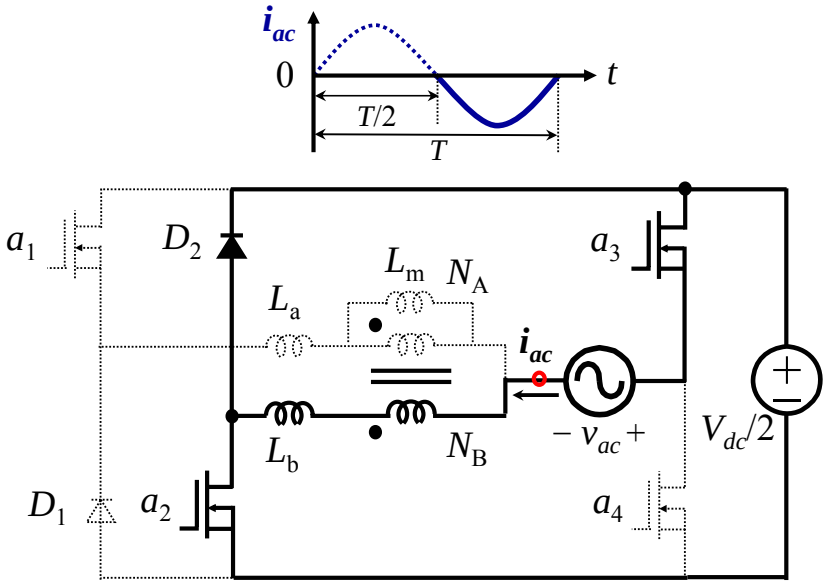

Figure 3.14 The proposed converter with one coupled inductor operating under inverter mode during the period when ac current is negative.

In order to analyze the effects of magnetizing and leakage inductance of the coupled inductor on the operation of the bidirectional ac-dc converter under inverter mode in

Figure 3.13 and Figure 3.14, the coupled inductor with a unity turns ratio is represented with a symmetrical model, as shown in Figure 3.15. In the symmetrical model, each side of the coupled inductor is represented with a magnetizing inductance connected in parallel with the corresponding winding and with a leakage inductance connected in series with the corresponding winding. The value of the magnetizing inductance connected in parallel with each winding of the ideal transformer is twice the total magnetizing inductance of the inductor, $L_{ma} = L_{mb} = 2L_m$.

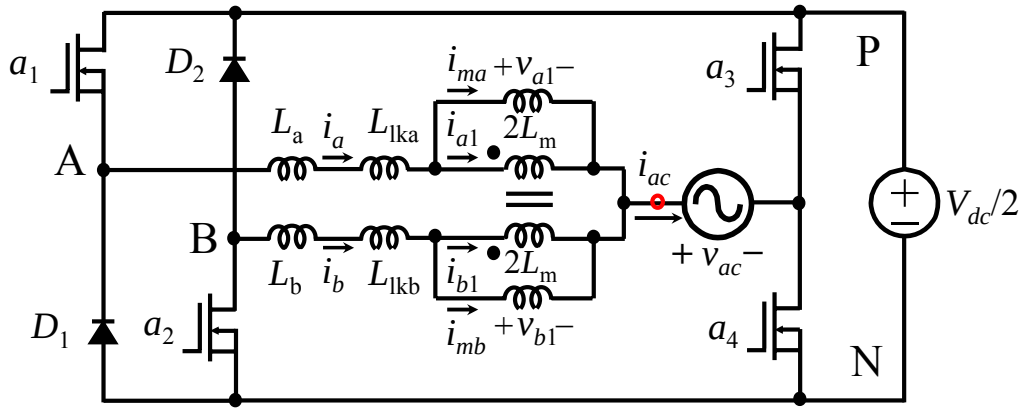

Figure 3.15 Symmetrical model of the proposed novel converter with one coupled inductor under inverter mode.

With voltage and current reference directions under inverter mode as in Figure 3.15, the following voltage relationships can be easily obtained:

$$v_{a1} = v_{b1} \tag{3.5}$$

$$v_{a1} = 2L_m \frac{di_{ma}}{dt} \tag{3.6}$$

$$v_{b1} = 2L_m \frac{di_{mb}}{dt}. \tag{3.7}$$

From(3.5), (3.6) and (3.7), one can obtain

$$i_{ma} = i_{mb} = i_m. \tag{3.8}$$

Similarly, with reference to Figure 3.15, the following current relationship can be written:

$$i_{a1} = -i_{b1} = i_T \tag{3.9}$$

$$i_a = i_{ma} + i_{a1} \tag{3.10}$$

$$i_b = i_{mb} + i_{b1}. \tag{3.11}$$

By using (3.8) and (3.9), current i_a and i_b can be expressed as:

$$i_a = i_m + i_T \tag{3.12}$$

$$i_b = i_m - i_T. \tag{3.13}$$

When leg a_1 and D_1 is operating and leg a_2 and D_2 is idle, one can get $i_b = 0$ and $i_m = i_T$. Apply KVL when a_1 and a_4 are on and D_1 is off as shown in Figure 3.16, the following voltage relationship can be established

$$\frac{V_{dc}}{2} = (L_a + L_{lka})\frac{di_a}{dt} + 2L_m\frac{di_{ma}}{dt} + v_{ac}. \tag{3.14}$$

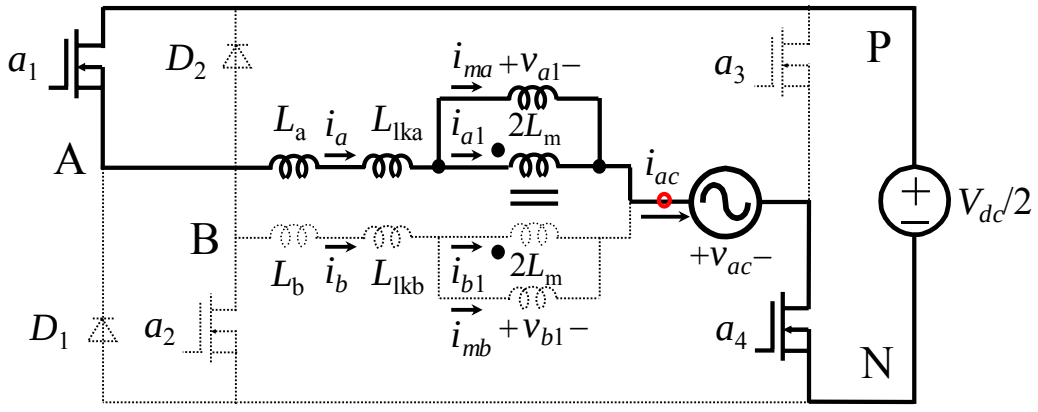

Figure 3.16 The proposed novel converter with one coupled inductor operating under inverter mode when ac current is positive and a_1 and a_4 are on.

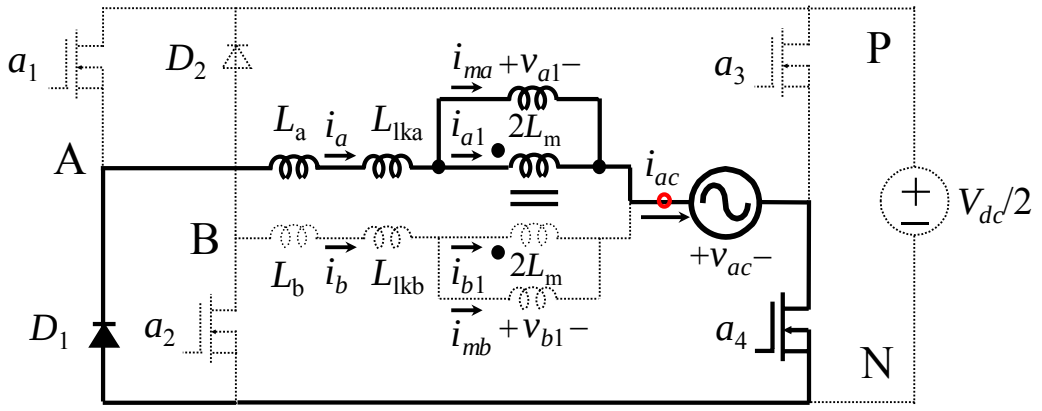

Figure 3.17 The proposed novel converter with one coupled inductor operating under inverter mode when ac current is positive and D_1 and a_4 are on.

By using (3.8), (3.12) and (3.14), voltage v_{a1} can be expressed as

$$v_{a1} = L_m \frac{di_a}{dt} = (\frac{V_{dc}}{2} - v_{ac}) \frac{L_m}{(L_a + L_{lka}) + L_m} . \tag{3.15}$$

Because a_4 is on, by using (3.5), the voltage of point B relative to dc negative terminal N can be expressed as

$$0 < V_{BN} = (\frac{V_{dc}}{2} - v_{ac}) \frac{L_m}{(L_a + L_{lka}) + L_m} + v_{ac} < \frac{V_{dc}}{2} . \tag{3.16}$$

Obviously, a_2 and D_2 will never be forced on.

Apply KVL when a_1 is off and D_1 and a_4 are on as shown in Figure 3.17, the following voltage relationship can be obtained

$$0 = (L_a + L_{lka}) \frac{di_a}{dt} + 2L_m \frac{di_{ma}}{dt} + v_{ac} . \tag{3.17}$$

By using (3.8), (3.12) and (3.17), voltage v_{a1} can be expressed as

$$v_{a1} = L_m \frac{di_a}{dt} = (-v_{ac}) \frac{L_m}{(L_a + L_{lka}) + L_m}. \tag{3.18}$$

Similarly, because a_4 is on, the voltage of point B relative to dc negative terminal N can be expressed as

$$0 < V_{BN} = (-v_{ac}) \frac{L_m}{(L_a + L_{lka}) + L_m} + v_{ac} < v_{ac}. \tag{3.19}$$

Since $v_{ac} < V_{dc}/2$, a_2 and D_2 will never be forced on.

During the period ac current is negative, leg a_2 and D_2 is operating and leg a_1 and D_1 is idle. One can get $i_a = 0$. When a_2 and a_3 are on and D_2 is off, the voltage of dc positive terminal P relative to point A can be expressed as

$$0 < V_{PA} = (\frac{V_{dc}}{2} - v_{ac}) \frac{L_m}{(L_b + L_{lkb}) + L_m} + v_{ac} < \frac{V_{dc}}{2}. \tag{3.20}$$

Apparently, a_1 and D_1 will never be forced on.

When a_2 is off and D_2 and a_3 are on, the voltage of dc positive terminal P relative to point A can be expressed as

$$0 < V_{PA} = (0 - v_{ac}) \frac{L_m}{(L_a + L_{lka}) + L_m} + v_{ac} < v_{ac}. \tag{3.21}$$

Since $v_{ac} < V_{dc}/2$, a_1 and D_1 will never be forced on.

Same conclusion can be drawn for the converter operating under rectifier mode.

Figure 3.18 (a) and (b) shows the simulation results under both rectifier and inverter modes for the converter, respectively. It can be found that one leg operates while the other is idle.

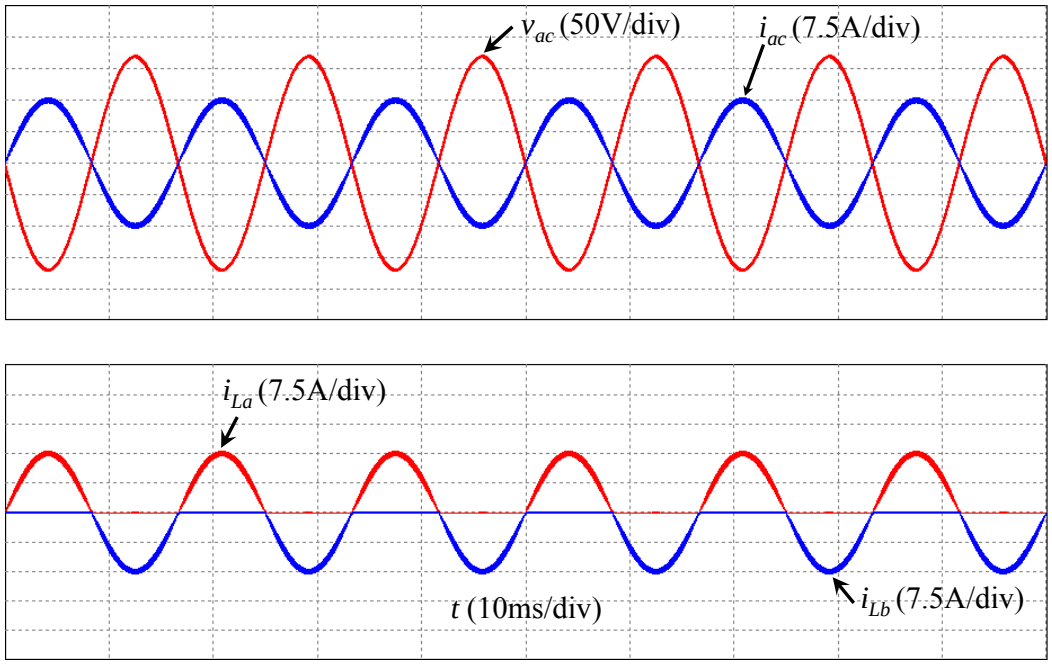

(a)

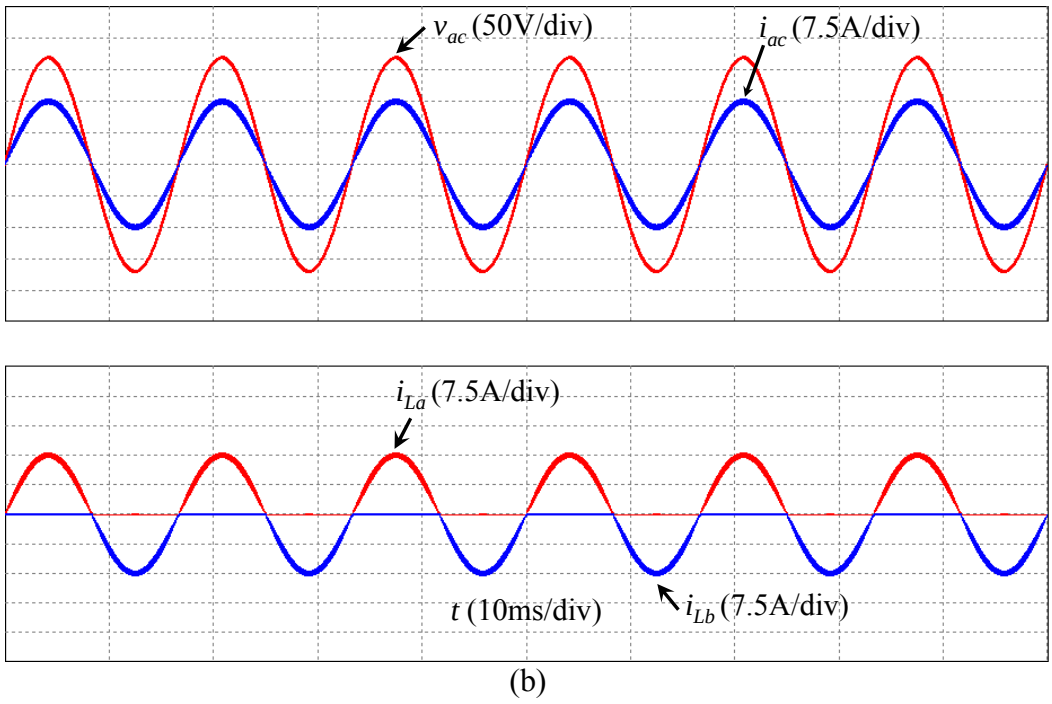

(b)

Figure 3.18 Simulation results of the proposed converter with one coupled inductor under (a) rectifier mode and (b) inverter mode.

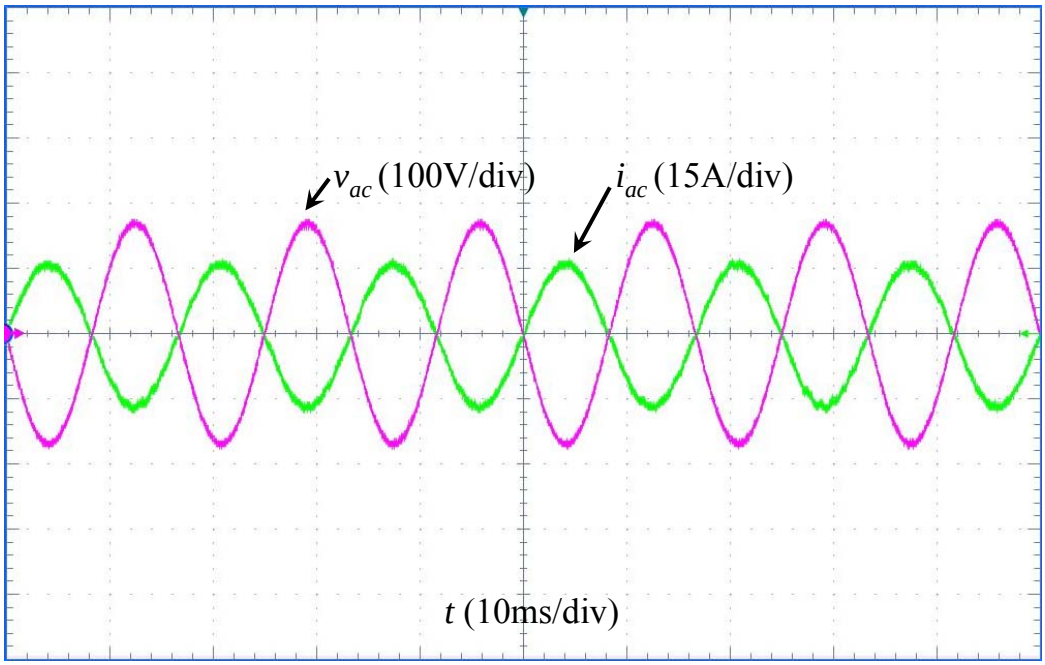

(a)

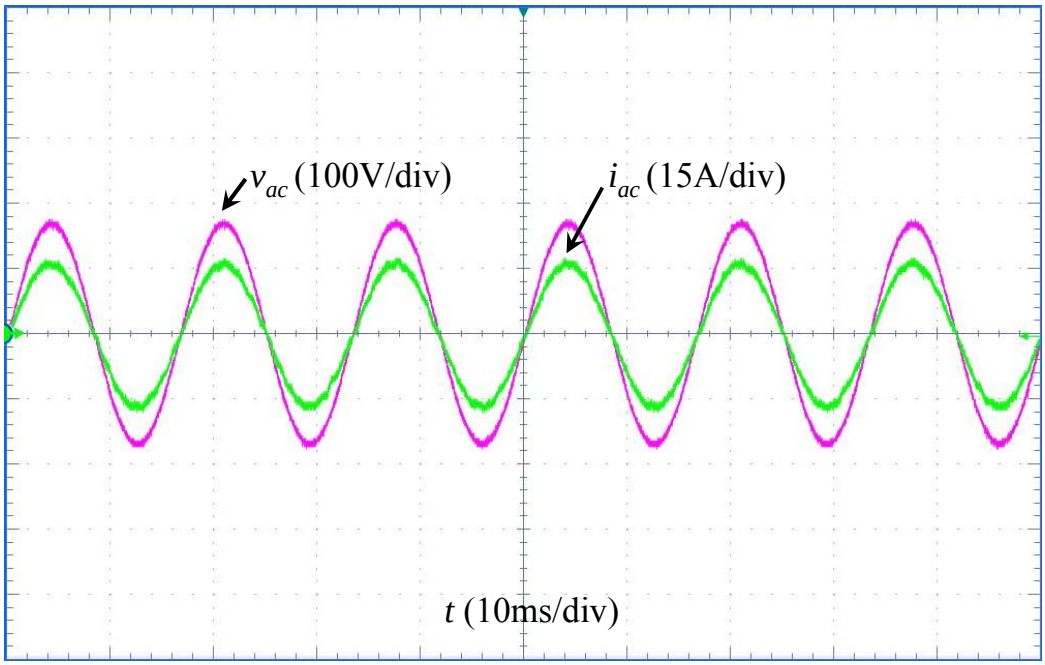

(b)

Figure 3.19 Experimental results of the proposed converter with one coupled inductor under (a) rectifier mode and (b) inverter mode.

Figure 3.19(a) and (b) shows the experimental results under both rectifier and inverter modes for the converter, respectively.

3.3.2 Two Coupled Inductors in Series

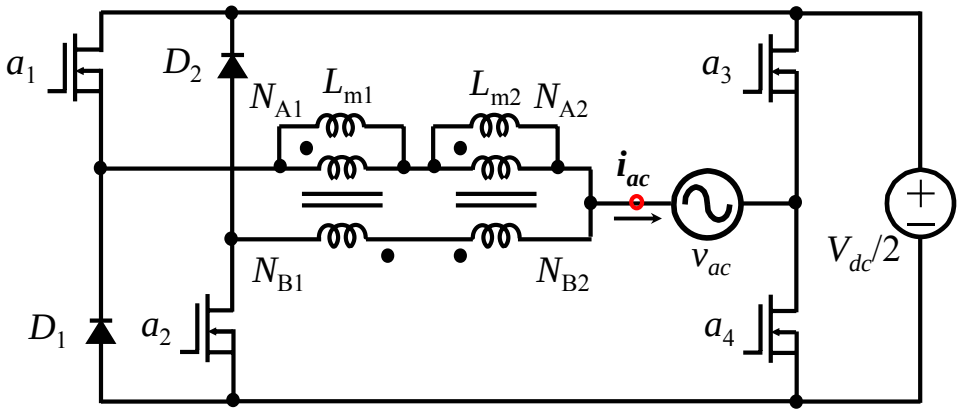

Figure 3.20 Novel bidirectional ac-dc converter with two coupled inductors.

The other approach of magnetic integration is shown in Figure 3.20. The two inductors L_1 and L_2 in Figure 3.1 are replaced by two coupled inductors. Although there are still two coupled inductors in the circuit, the size and weight of the inductors are greatly reduced.

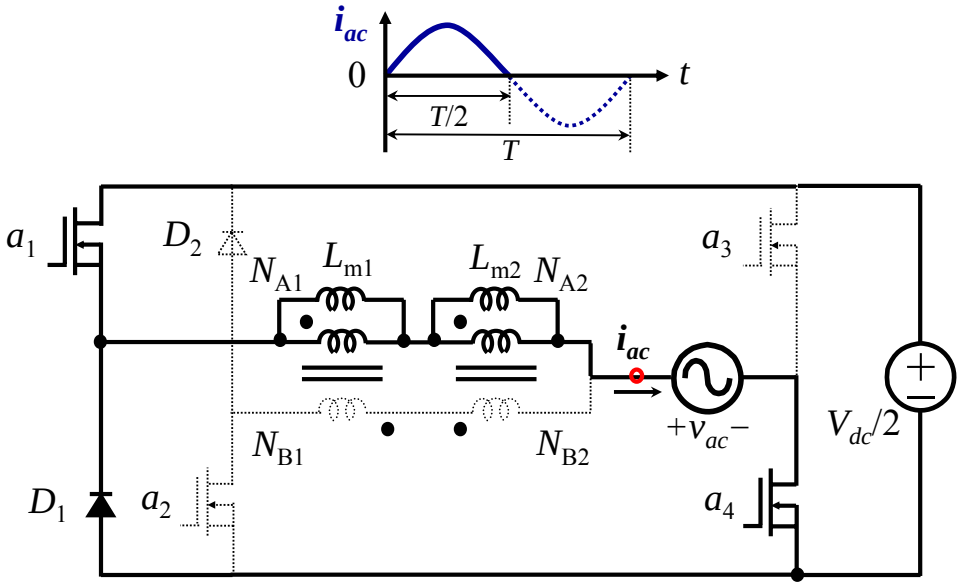

Figure 3.21 The proposed converter with two coupled inductors operating under inverter mode during the period when ac current is positive.

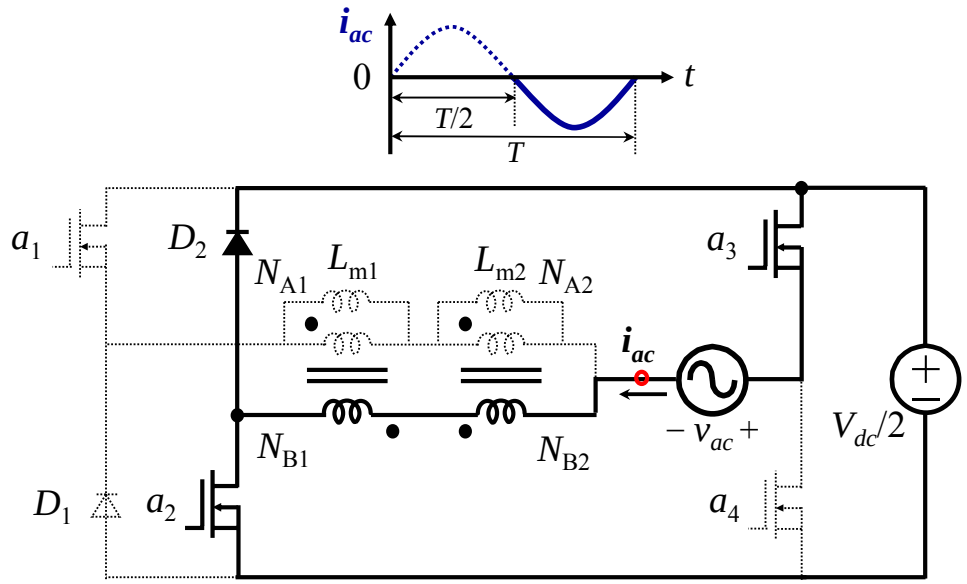

Figure 3.22 The proposed converter with two coupled inductors operating under inverter mode during the period when ac current is negative.

The proposed magnetic integration method for the bidirectional ac-dc converter in Figure 3.20 consists of two buck converters under inverter mode One buck converter operates while the other buck converter is idle, as shown in Figure 3.21 and Figure 3.22. Each buck converter operates in a half line cycle. During the period when ac current is positive, as shown in Figure 3.21, the circuit consists of switch a_1, diode D_1, winding N_{A1} and winding N_{A2}, and switch a_4 operates to conduct the current, while the circuit consists of switch a_2, diode D_2, winding N_{B1} and winding N_{B2}, and switch a_3 is idle. Similarly, as shown in Figure 3.22, during the period when ac current is negative, the circuit consists of switch a_2, diode D_2, winding N_{B1} and winding N_{B2}, and switch a_3 operates to conduct the current, while the circuit consists of switch a_1, diode D_1, winding N_{A1} and winding N_{A2}, and switch a_4 is idle.

The proposed magnetic integration method for the bidirectional ac-dc converter in Figure 3.20 consists of two boost converters under rectifier mode One boost converter operates while the other boost converter is idle, as shown in Figure 3.23 and Figure 3.24. Each boost converter operates in a half line cycle.

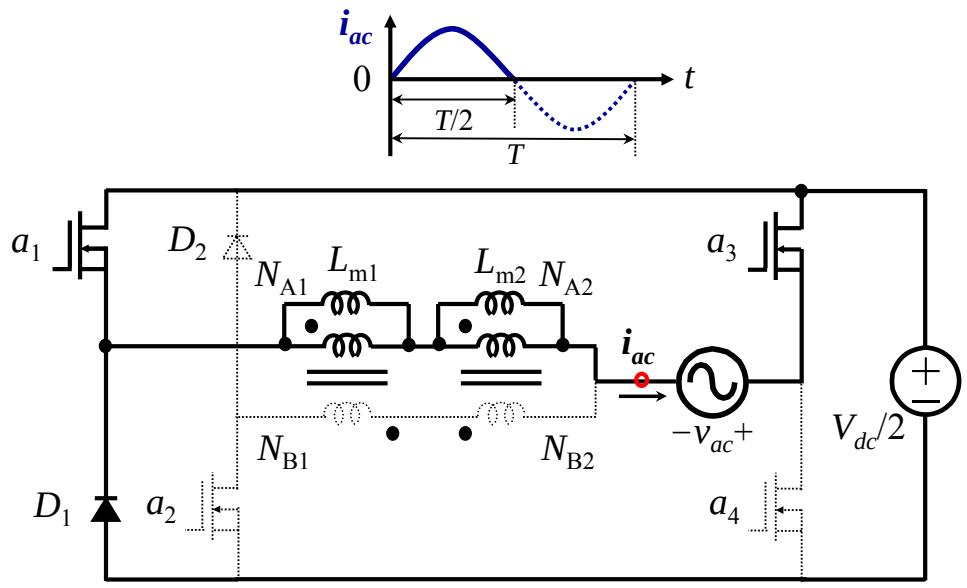

Figure 3.23 The proposed novel converter with two coupled inductors operating under rectifier mode during the period when ac current is positive.

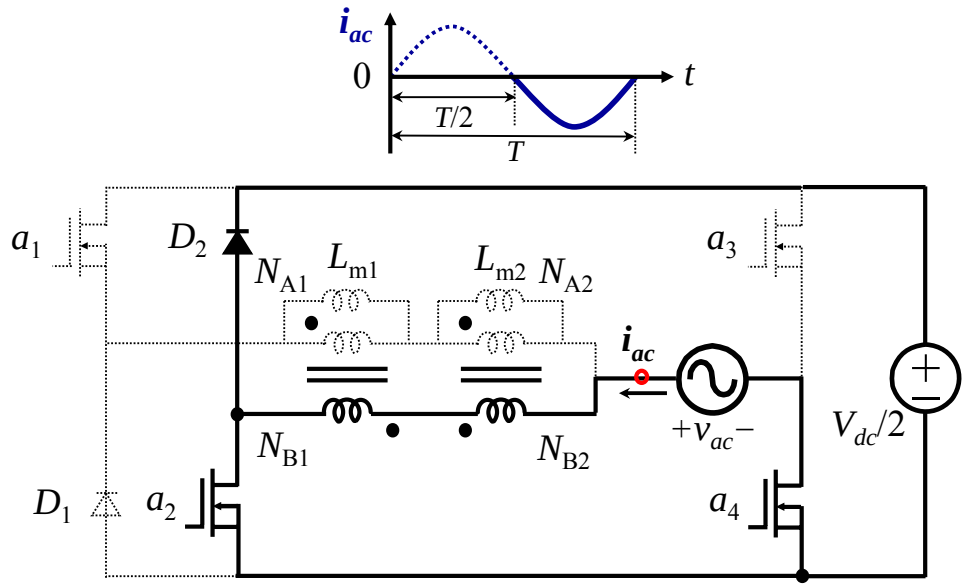

Figure 3.24 The proposed novel converter with two coupled inductors operating under rectifier mode during the period when ac current is negative.

In order to analyze the effects of magnetizing and leakage inductance of the coupled inductor on the operation of the bidirectional ac-dc converter under rectifier mode in

Figure 3.23 and Figure 3.24, the coupled inductor with a unity turns ratio is represented with a symmetrical model, as shown in Figure 3.25. In the symmetrical model, each side of the coupled inductor is represented with a magnetizing inductance connected in parallel with the corresponding winding and with a leakage inductance connected in series with the corresponding winding. The value of the magnetizing inductance connected in parallel with each winding of the ideal transformer is twice the total magnetizing inductance of the inductor.

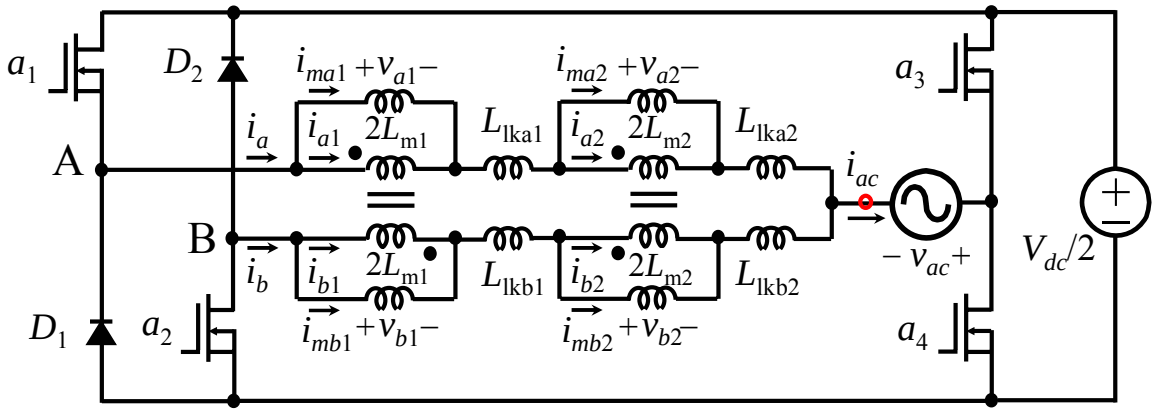

Figure 3.25 Symmetrical model of the proposed novel converter with two coupled inductors under rectifier mode.

With voltage and current reference directions under rectifier mode as in Figure 3.25, the following voltage relationships can be easily obtained:

$$v_{a1} = -v_{b1} \tag{3.22}$$

$$v_{a2} = v_{b2} \tag{3.23}$$

$$v_{a1} = 2L_{m1}\frac{di_{ma1}}{dt} \tag{3.24}$$

$$v_{b1} = 2L_{m1}\frac{di_{mb1}}{dt}. \tag{3.25}$$

$$v_{a2} = 2L_{m2}\frac{di_{ma2}}{dt} \tag{3.26}$$

$$v_{b2} = 2L_{m2}\frac{di_{mb2}}{dt}. \tag{3.27}$$

From (3.22), (3.24) and (3.25), one can obtain

$$i_{ma1} = -i_{mb1} = i_{m1} \tag{3.28}$$

whereas from (3.23), (3.26) and (3.27)

$$i_{ma2} = i_{mb2} = i_{m2}\,. \tag{3.29}$$

Similarly, from Figure 3.25, the following current relationship can be written:

$$i_{a1} = i_{b1} \tag{3.30}$$

$$i_{a2} = -i_{b2} \tag{3.31}$$

$$i_a = i_{ma1} + i_{a1} = i_{ma2} + i_{a2} \tag{3.32}$$

$$i_b = i_{mb1} + i_{b1} = i_{mb2} + i_{b2}\,. \tag{3.33}$$

Using (3.28) – (3.31) and adding (3.32) and (3.33), it follows that

$$i_{a1} = i_{b1} = i_{m2} \tag{3.34}$$

$$i_{a2} = -i_{b2} = i_{m1}\,. \tag{3.35}$$

Also, by using (3.28) and (3.34), current i_a can be obtained as

$$i_a = i_{m1} + i_{m2} \tag{3.36}$$

whereas by using (3.28) and (3.34), current i_b can be obtained as

$$i_b = -i_{m1} + i_{m2} \tag{3.37}$$

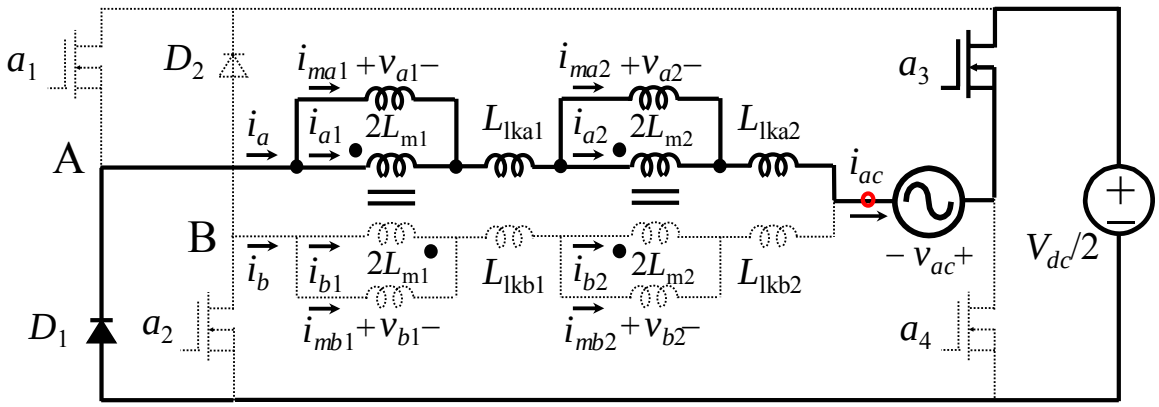

Figure 3.26 The proposed novel converter with two coupled inductors operating under rectifier mode when ac current is positive and D_1 and a_3 are on.

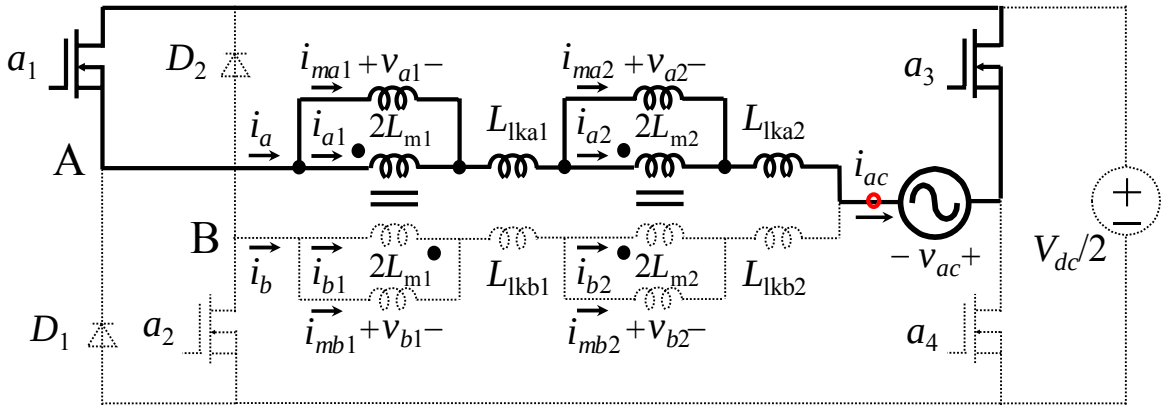

Figure 3.27 The proposed novel converter with two coupled inductors operating under rectifier mode when ac current is positive and a_1 and a_3 are on.

During the positive ac current half cycle, leg a_1 and D_1 is operating and leg a_2 and D_2 is idle. When D_1 and a_3 are on and a_1 is off as shown in Figure 3.26, on can get

$$v_{b1} + v_{b2} + (L_{lkb1} + L_{lkb2}) \frac{di_b}{dt} = 0 . \tag{3.38}$$

The same result (3.38) also can be obtained when a_1 and a_3 are on and D_1 is off as shown in Figure 3.27.

Similarly, during the negative ac current half cycle, when leg a_2 and D_2 is operating and leg a_1 and D_1 is idle, one can get

$$v_{a1} + v_{a2} + (L_{lka1} + L_{lka2}) \frac{di_a}{dt} = 0 . \tag{3.39}$$

Using (3.25), (3.27), (3.28), (3.29), (3.37) and (3.38), the relationship between i_{m1} and i_{m2} during the positive half line cycle can be expressed as

$$i_{m1} = \frac{L_{m2} + (L_{lkb1} + L_{lkb2})/2}{L_{m1} + (L_{lkb1} + L_{lkb2})/2} i_{m2} . \tag{3.40}$$

Substituting (3.40) into (3.36) yields

$$i_a = i_{m1} + i_{m2} = \frac{L_{m1} + L_{m2} + (L_{lkb1} + L_{lkb2})}{L_{m1} + (L_{lkb1} + L_{lkb2})/2} i_{m2} . \tag{3.41}$$

whereas substituting (3.40) into (3.37) yields

$$i_b = -i_{m1} + i_{m2} = \frac{L_{m1} - L_{m2}}{L_{m1} + (L_{lkb1} + L_{lkb2})/2} i_{m2} . \tag{3.42}$$

Eliminating i_{m2} from (3.41) and (3.42), the relationship between i_a and i_b can be derives as

$$\frac{i_b}{i_a} = \frac{L_{m1} - L_{m2}}{L_{m1} + L_{m2} + (L_{lkb1} + L_{lkb2})} . \tag{3.43}$$

As can be seen from (3.43), for $L_{m1} = L_{m2}$, no ripple current is returned through windings N_{B1} and N_{B2} regardless of their leakage inductance. If $L_{m1} \neq L_{m2}$, the amount of

the ripple current returned through windings N_{B1} and N_{B2} is determined by the difference between the two magnetizing inductances.

Similarly, during the negative ac current half cycle, when leg a_2 and D_2 is operating and leg a_1 and D_1 is idle, the relationship between i_a and i_b can be derives as

$$\frac{i_a}{i_b} = \frac{L_{m1} - L_{m2}}{L_{m1} + L_{m2} + (L_{lka1} + L_{lka2})}. \tag{3.44}$$

Due to symmetrical operation, the behavior of the circuit during the negative ac current half cycle is identical to that during the positive ac current half cycle.

Under inverter mode during the positive ac current half cycle, when leg a_1 and D_1 is operating and leg a_2 and D_2 is idle, the relationship between i_a and i_b can be derives as

$$\frac{i_b}{i_a} = \frac{L_{m1} - L_{m2}}{L_{m1} + L_{m2} + (L_{lkb1} + L_{lkb2})}. \tag{3.45}$$

Under inverter mode during the negative ac current half cycle, when leg a_2 and D_2 is operating and leg a_1 and D_1 is idle, the relationship between i_a and i_b can be derives as

$$\frac{i_a}{i_b} = \frac{L_{m1} - L_{m2}}{L_{m1} + L_{m2} + (L_{lka1} + L_{lka2})}. \tag{3.46}$$

Due to symmetrical operation, the behavior of the circuit under inverter mode is identical to that under rectifier mode.

The two separate inductors, L_1 and L_2, are shown in Figure 3.28. Each inductor consists of four 77192 Kool Mμ cores and two paralleled litz wires (22 turns, AWG #14). Figure 3.29 shows the structure of the two coupled inductors. Each coupled inductor consists of two 77192 Kool Mμ cores. Two paralleled litz wires (22 turns, AWG #14) are used for each winding of N_{A1}, N_{B1}, N_{A2}, and N_{B2}.

Figure 3.28 Picture of the constructed separate inductors.

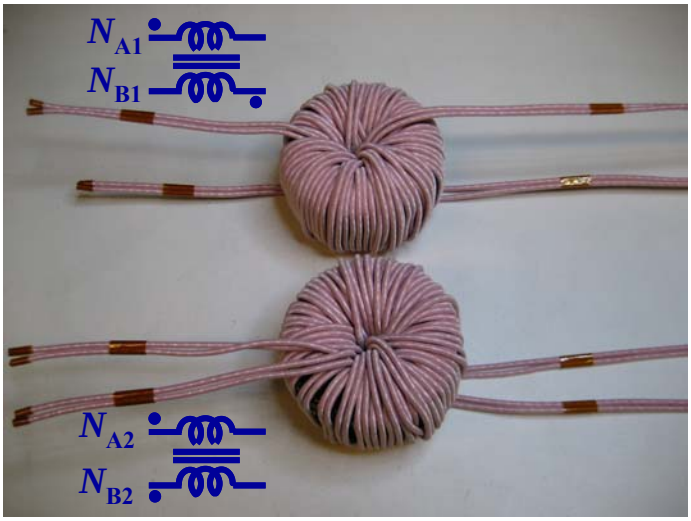

Figure 3.29 Picture of the constructed two coupled inductors.

Figure 3.30(a) and (b) shows the simulation results under both rectifier and inverter modes for the converter, respectively. It can be concluded that one leg operates while the other leg is idle.

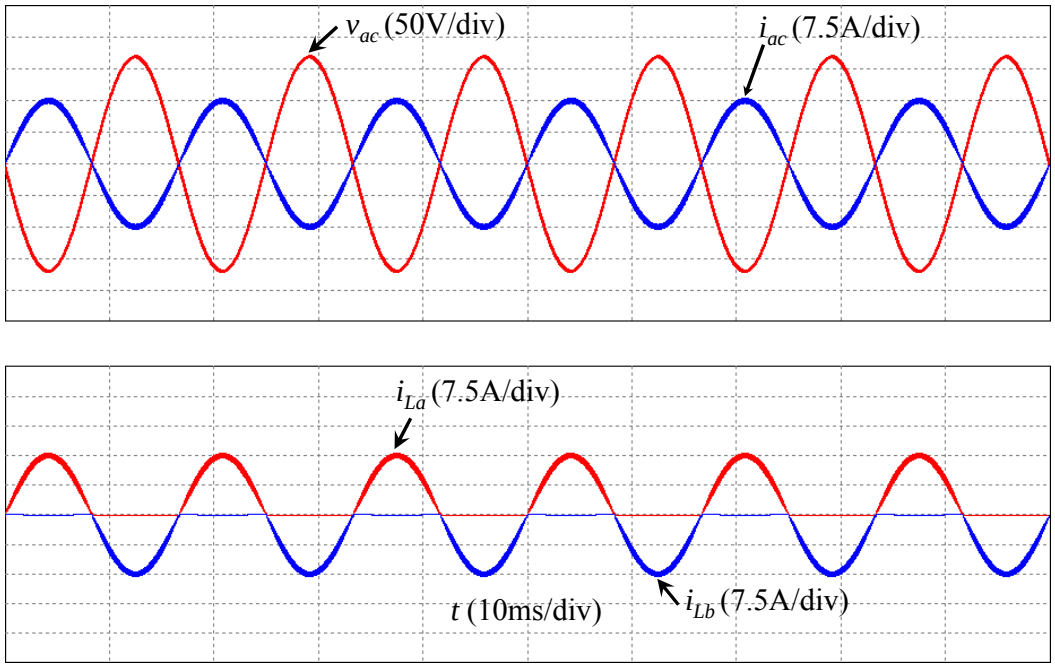

(a)

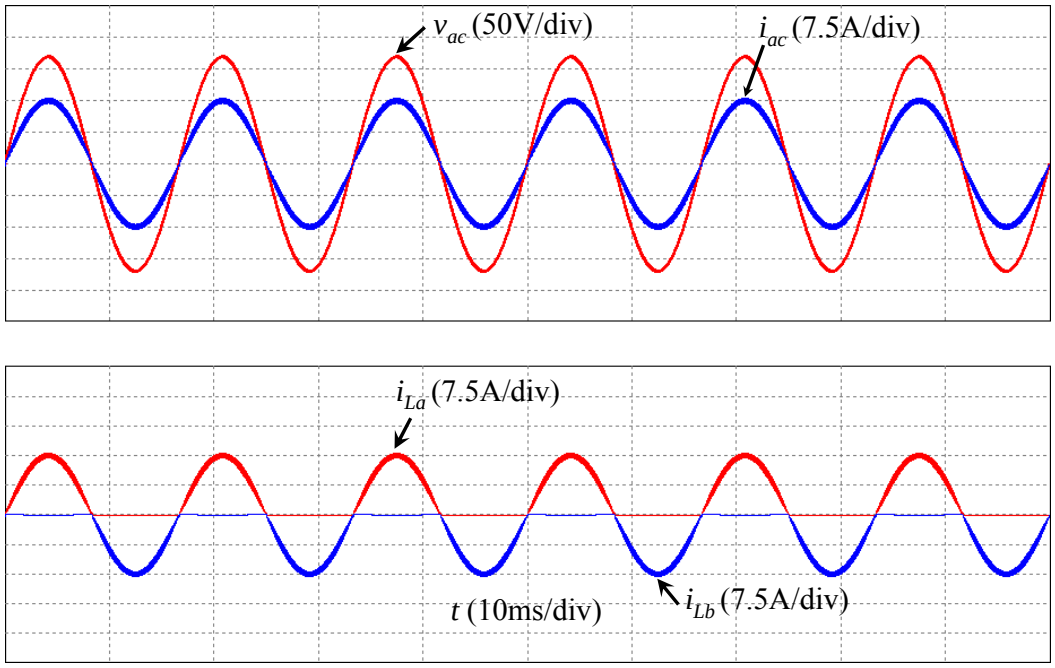

(b)

Figure 3.30 Simulation results of the proposed converter with two coupled inductors under (a) rectifier mode and (b) inverter mode.

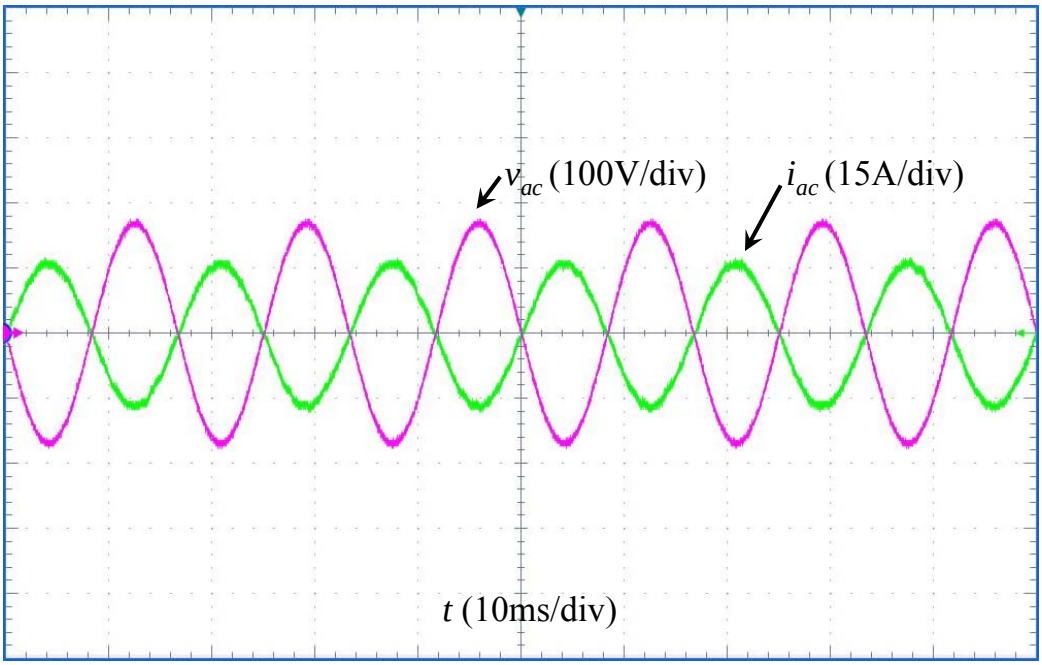

(a)

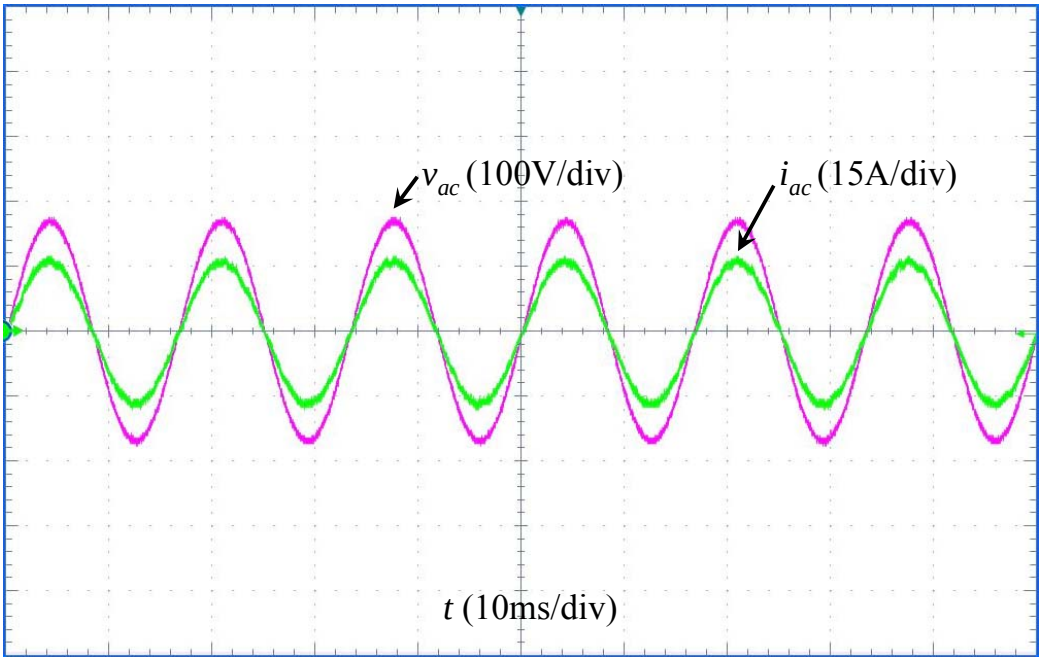

(b)

Figure 3.31 Experimental results of the proposed converter with two coupled inductors under (a) rectifier mode and (b) inverter mode.

Figure 3.31(a) and (b) shows the experimental results under both rectifier and inverter modes for the converter, respectively.

3.4 Novel Three-Phase Bidirectional AC-DC Converter

Three-phase ac-dc conversion of electric power is widely employed in motor drive, uninterruptible power supplies, and utility interfaces with renewable sources such as solar photovoltaic, wind and battery energy storage systems. Numerous three-phase topologies that have bidirectional flow capability have been reported [65]-[84]. The commonly used bidirectional converter topology consists of six power switches as shown in Figure 3.32. Without neutral connection, third harmonic will not exist. There is no need to need to eliminate 3rd, 9th, etc. triplen harmonics. For this topology, the power MOSFET cannot be used as the main switch in the high-voltage high-power applications because the intrinsic MOSFET body diode conduction could cause device failure.

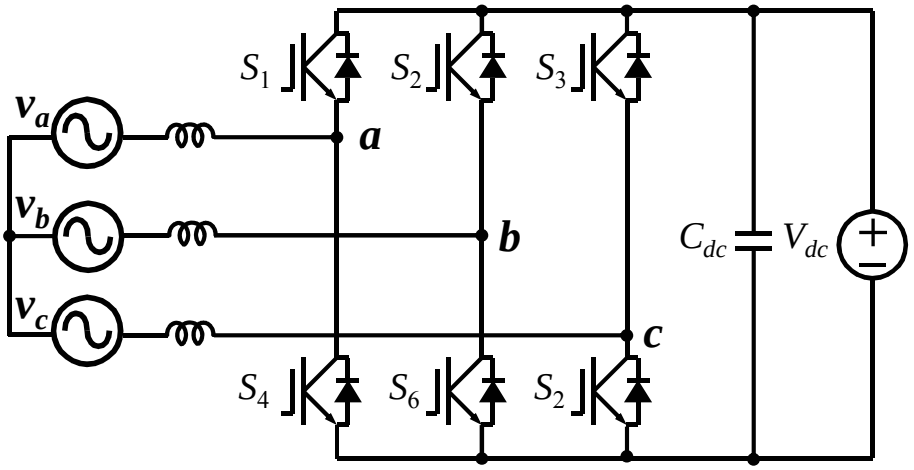

Figure 3.32 Circuit diagram of the traditional three-phase six-switch bidirectional ac-dc converter.

Figure 3.33(a) and (b) show the sub-operating modes under inverter mode for one switching cycle. When S_1, S_6 and S_2 are on as shown in Figure 3.33(a), all diodes are off. When S_1 is off, Current i_a goes through anti-paralleled diode of S_4 as shown in Figure 3.33(b). In this case, if S_4 is replaced by a power MOSFET, the body diode of S_4 will conduct the current. Even if S_4 works under synchronous rectification when S_1 is off, the body diode of S_4 will conduct the current during the dead time. Excessive reverse recovery loss of the body diode could cause device failure.

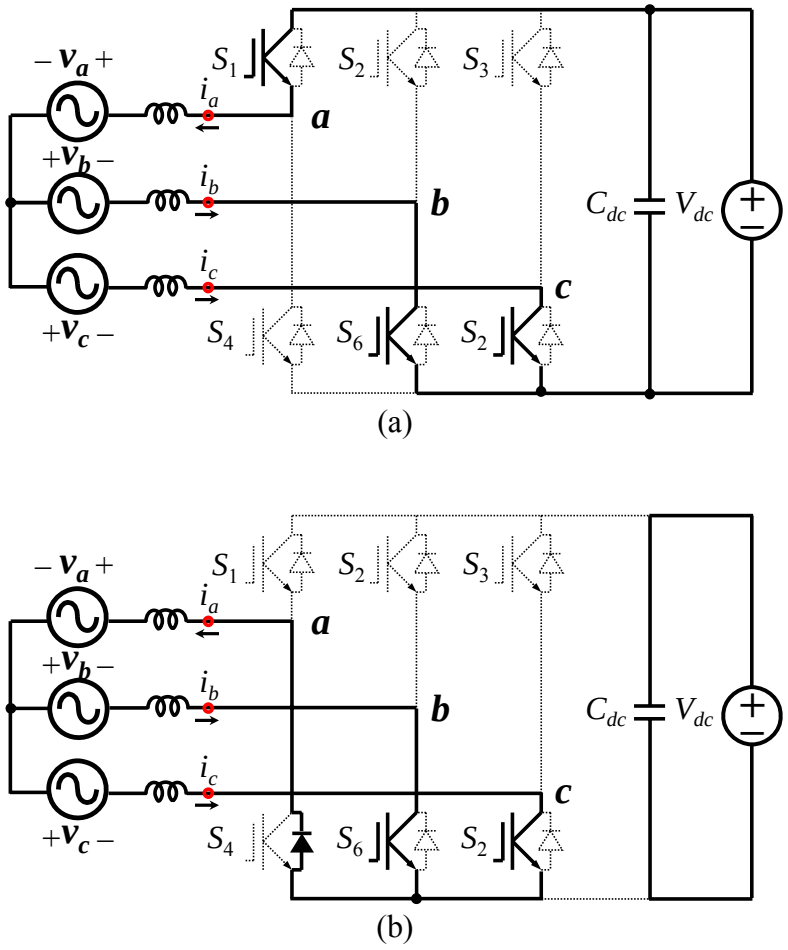

Figure 3.33 Operating under inverter mode for one switching cycle. (a) S_1, S_6 and S_2 are on. (b) Diode of S_4, S_6 and S_2 are on.

The power MOSFET cannot be used as the main switch in the three-phase converter since the intrinsic MOSFET body diode conduction could cause device failure. However, an IGBT has higher switching and conduction losses compared with a power MOSFET. In addition, the IGBT only allows operation at a lower switch frequency than the power MOSFET which results in larger filter size. On the contrary, lots of revolutionary technology has been employed for the high-voltage power MOSFET, which make the MOSFET's R_{DSon} exceptionally low. Extremely low switching and conduction losses make switching applications even more efficient, more compact, lighter and cooler.

In this section, three MOSFET based novel three-phase bidirectional ac-dc converters are proposed.

3.4.1 Novel Three-Phase Bidirectional AC-DC Converter Topologies

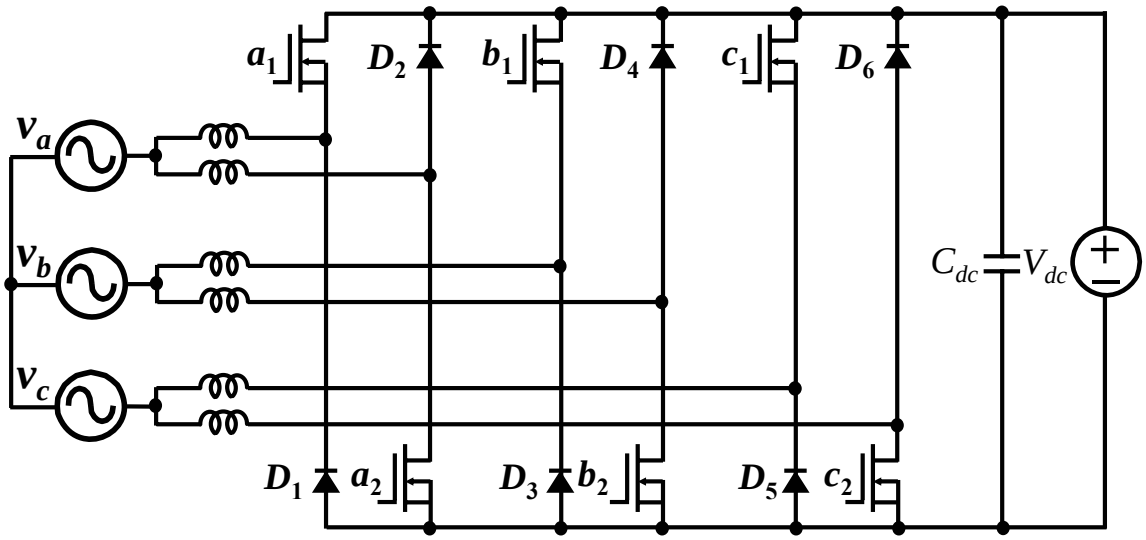

Figure 3.34 Circuit diagram of a novel three-phase bidirectional ac-dc converter.

A novel three-phase bidirectional ac-dc converter is proposed in Figure 3.34. The converter is based on the dual-buck based single-phase bidirectional ac-dc converter, which is shown in Figure 2.5.

The converter exhibits two distinct merits: first, there is no shoot-through issue because no active power switches are connected in series in each phase leg; second, the reverse recovery dissipation of the power switch is greatly reduced because there is no freewheeling current flowing through the body diode of power switches. Using MOSFET as the main device, not only can the switching loss be almost eliminated but also the conduction loss can be significantly reduced. Besides the features of the single-phase dual-buck converter, the three-phase converter eliminates the two bulky dc bus capacitors and related voltage-balancing control algorithm.

The converter works as a rectifier when the power is transferred from ac grid to dc source. Alternately, it works as an inverter when the power is transferred from dc source to ac grid.

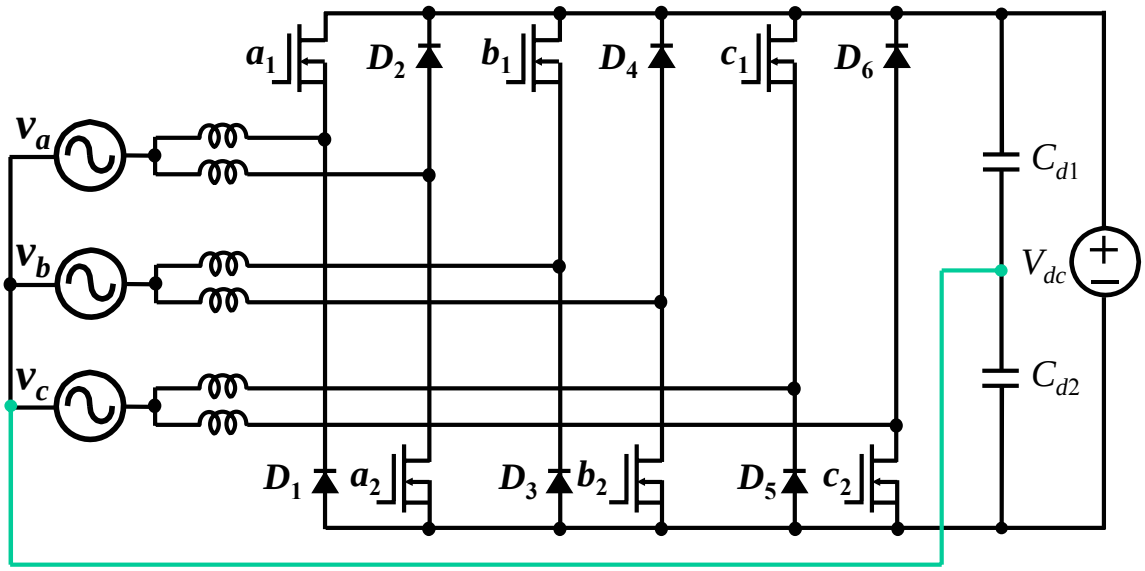

Figure 3.35 Circuit diagram of a novel three-phase bidirectional ac-dc converter with split capacitors for neutral connection.

A novel three-phase converter with split capacitors for neutral connection is shown in Figure 3.35. Under unbalanced ac load condition, dc bus capacitors absorb the neutral current to maintain better balanced ac output. The problem with this topology is excessive current stress on split capacitors when ac load are highly unbalanced.

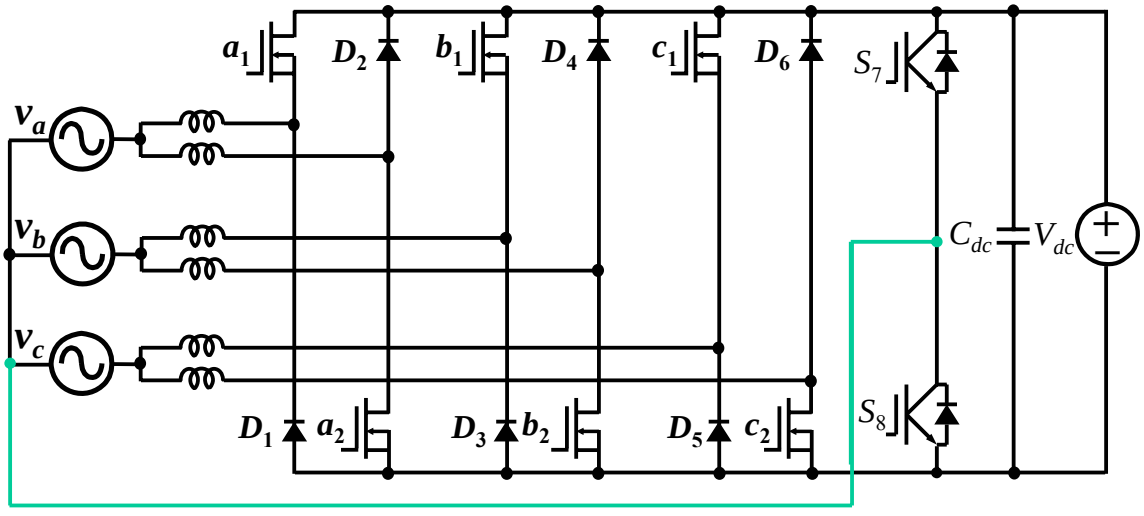

Figure 3.36 Circuit diagram of a novel three-phase bidirectional ac-dc converter with extra leg.

A novel three-phase four-leg converter is shown in Figure 3.36. Neutral leg is controlled to equalize the three-phase outputs. The features with this converter are less bulky capacitors and reduced size of passive components. However, control is more complicated.

3.4.2 Operating Principle

The definition of the different power transferring modes based on phase angle difference between voltage and current waveforms for single-phase bidirectional ac-dc converter are shown in Figure 2.6. The same definition is also applied for the three-phase bidirectional ac-dc converters.

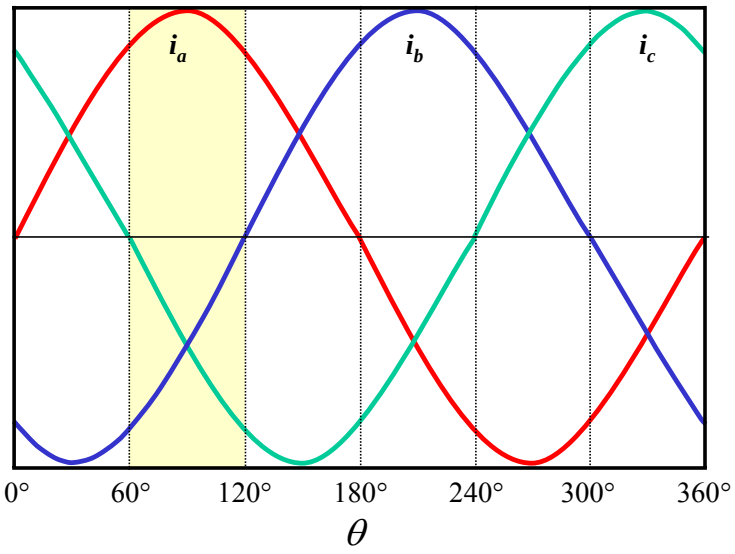

Figure 3.37 Ideal three-phase current waveforms.

The ideal three-phase current waveforms are shown in Figure 3.37. One ac line cycle is divided into six regions. In region 0°–60°, 120°–180°, and 240°–300°, the current waveform in Figure 3.37 have the same pattern, i.e., two phases have current amplitudes higher than that of the other one. In region 60°–120°, 180°–240°, and 300°–360°, the current waveform in Figure 3.37 have the same pattern, i.e., two phases have current amplitudes lower than that of the other one.

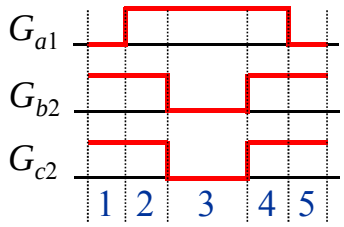
G_{a1}
G_{b2}
G_{c2}
1
2
3
4
5

(a)

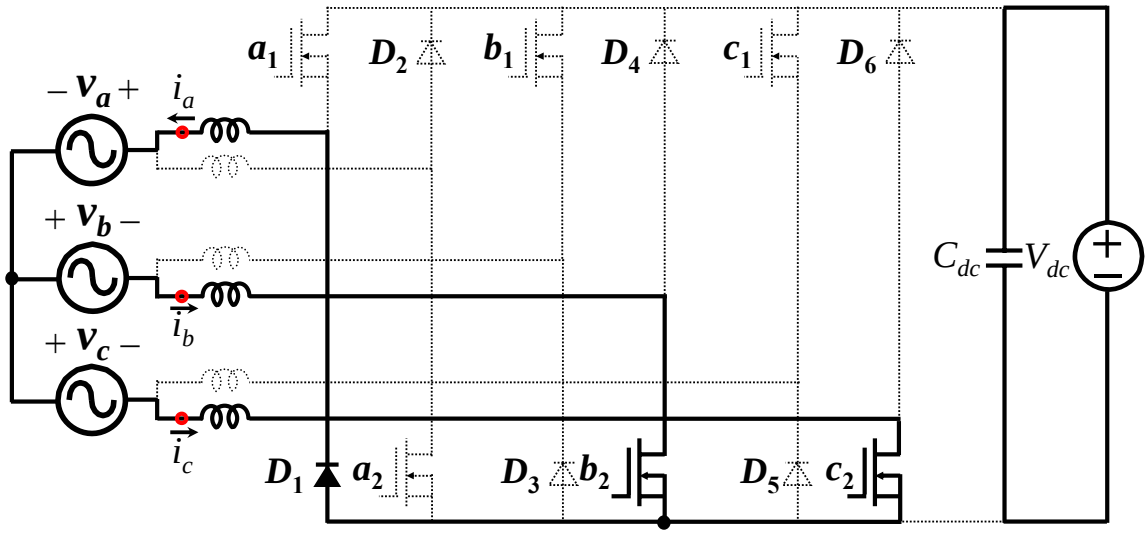
a_1
D_2
b_1
D_4
c_1
D_6
$-v_a+$
i_a
$+v_b-$
i_b
$+v_c-$
i_c
C_{dc}
V_{dc}
D_1
a_2
D_3
b_2
D_5
c_2

(b)

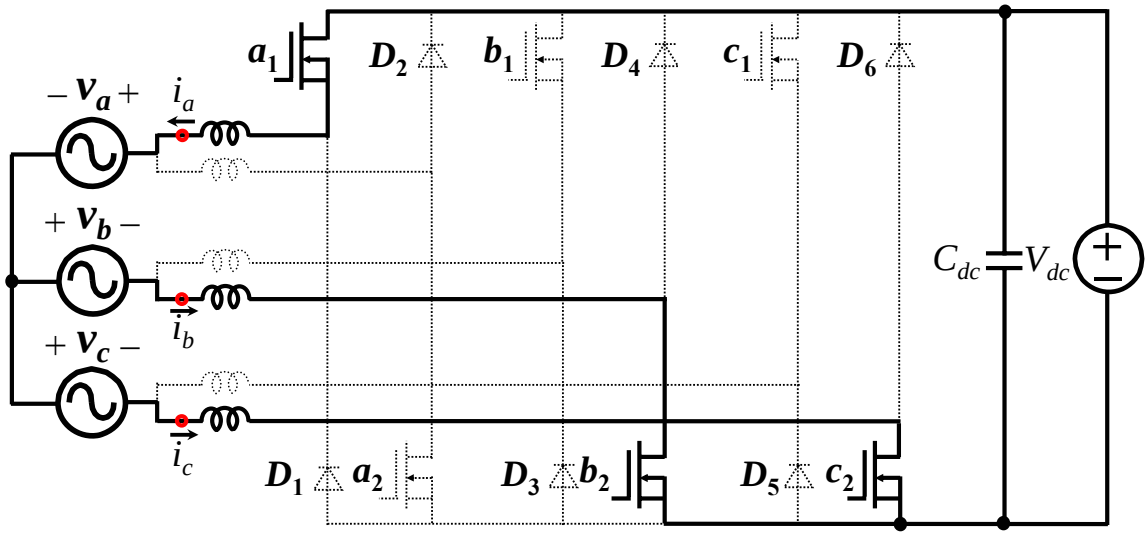
a_1
D_2
b_1
D_4
c_1
D_6
$-v_a+$
i_a
$+v_b-$
i_b
$+v_c-$
i_c
C_{dc}
V_{dc}
D_1
a_2
D_3
b_2
D_5
c_2

(c)

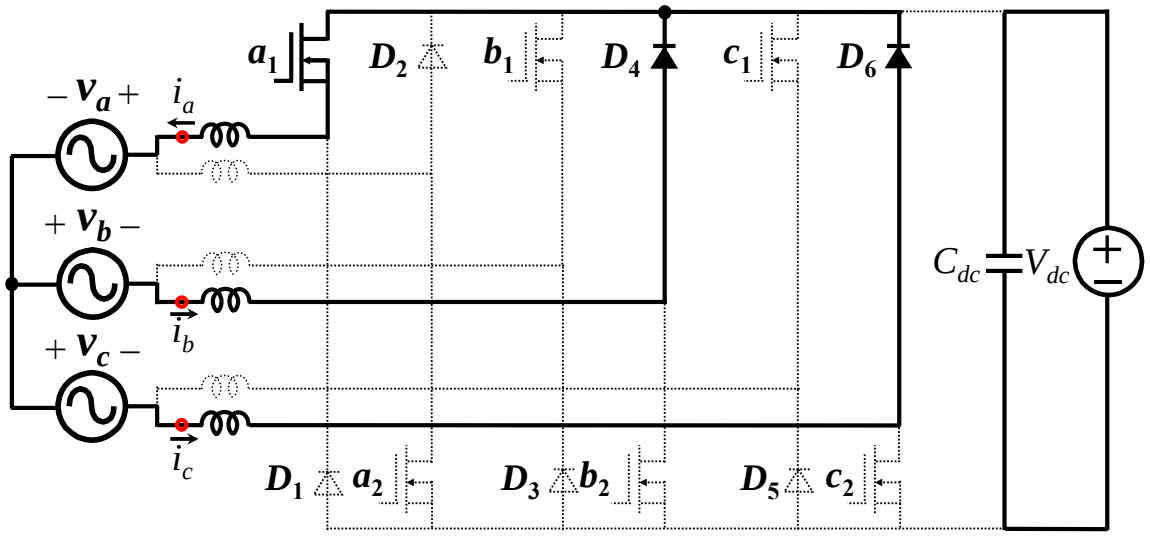

(d)

Figure 3.38 Operating under inverter mode phase angle is between 60° and 120°. (a) Gate signals. (b) Mode 1, D_1, b_2 and b_3 are on. (c) Mode 2, a_1, b_2 and b_3 are on. (d) Mode 3, a_1, D_4 and D_6 are on.

One switching cycle for the converter shown in Figure 3.34 under inverter mode when the phase angle is between 60° and 120° is analyzed as an example. Figure 3.38 shows the gate signals and related sub-operating modes.

In mode 1, D_1, b_2 and b_3 are on. There is no power transferred between dc side and ac side. The currents are freewheeling within the three phases. In mode 2, a_1, b_2 and b_3 are on. The power is transferred from dc side to ac side. In mode 3, a_1, D_4 and D_6 are on. There is no power transferred between dc side and ac side. The currents are freewheeling within the three phases. Mode 4 is the same as mode 2 and Mode 5 is the same as mode 1.

3.4.3 Simulation Results

Figure 3.39(a) and (b) shows the simulation results under both rectifier and inverter modes for the converter shown in Figure 3.34, respectively.

Figure 3.40(a) and (b) show simulated waveforms with reactive power flow for the converter shown in Figure 3.34. Figure 3.40(a) shows current leads voltage by 90°. Figure 3.40(b) shows current lags voltage by 90°.

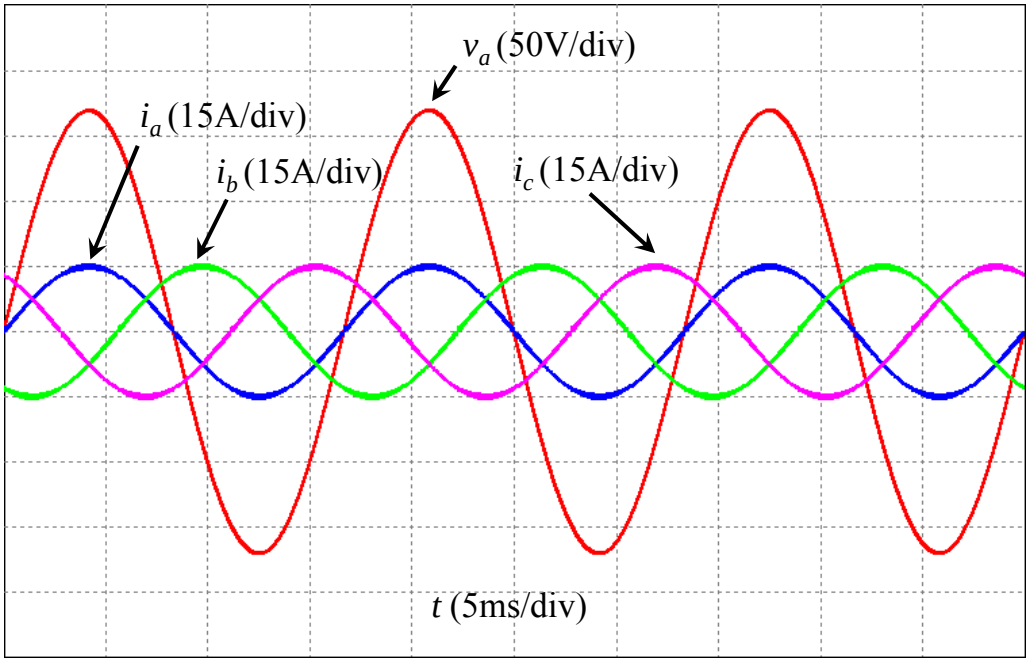

(a)

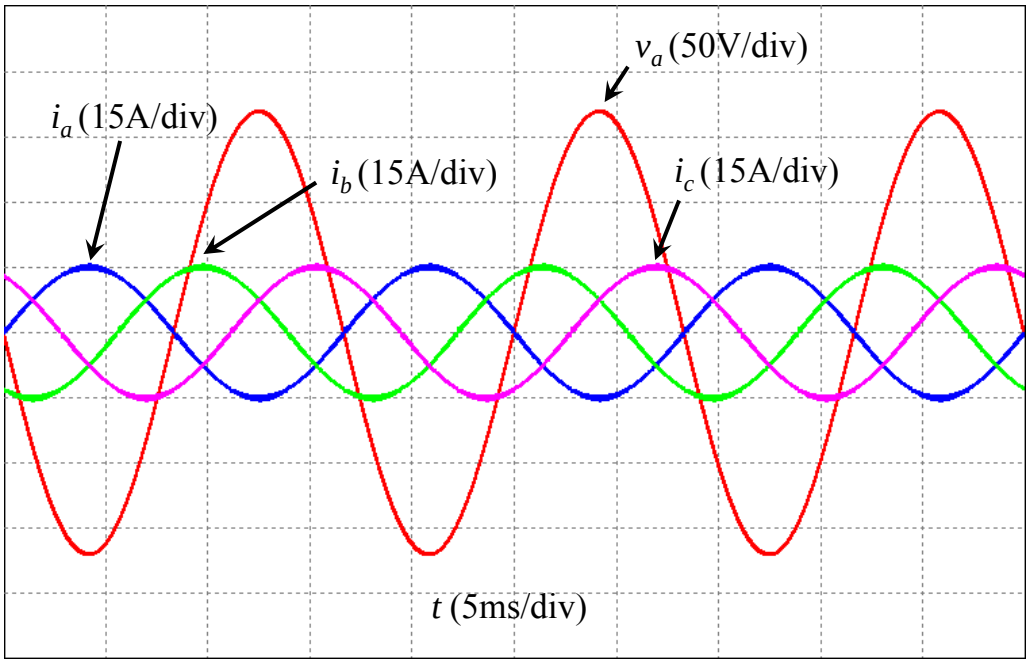

(b)

Figure 3.39 Simulation results under (a) rectifier mode and (b) inverter mode.

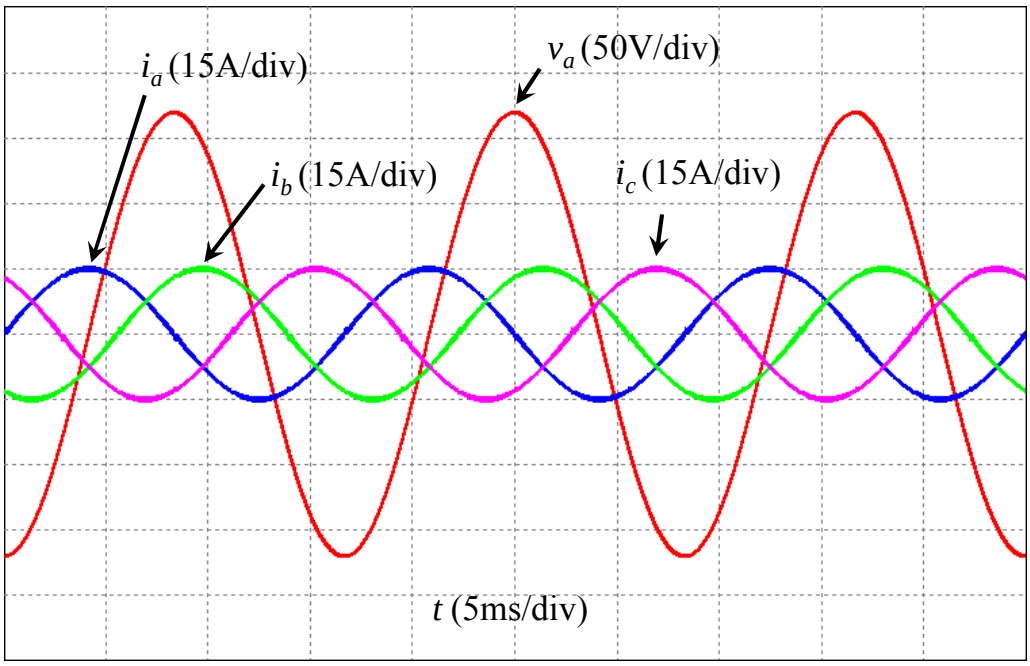

(a)

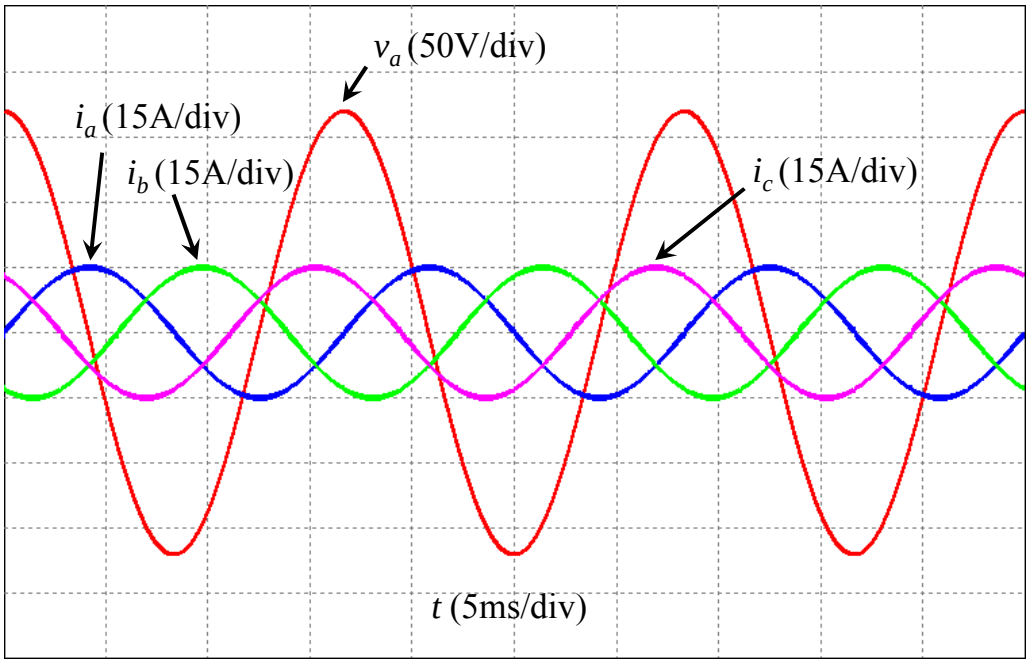

(b)

Figure 3.40 Simulation results with reactive power flow. (a) Current leads voltage by 90°. (b) Current lags voltage by 90°.

3.5 Summary

To better utilize the dc bus voltage and eliminate the two dc bus capacitors, a novel bidirectional ac-dc converter is proposed by replacing the two-capacitor leg of the dual-buck converter based single-phase bidirectional ac-dc converter with a two-switch leg. The novel bidirectional ac-dc converter keeps the merits of the dual-buck converter based bidirectional ac-dc converter. Meanwhile the two large dc bus capacitors and related voltage-balancing control are eliminated. The converter works as a rectifier when the power is transferred from ac grid to dc source. Alternately, it works as an inverter when the power is transferred from dc source to ac grid.

The novel bidirectional ac-dc converter consists of two boost converters under rectifier mode, each operating during a half line cycle. It consists of two buck converters under inverter mode, each operating during a half line cycle. As a result, the magnetic components are only utilized during the half line cycle. The low utilization of the magnetic components may impose a serious penalty on system cost and power density. However, the utilization can be improved by integrating magnetic components. Two different structures of magnetic integration are presented. One is employing one coupled inductor in series with small inductors and the other one is utilizing two coupled inductors in series.

Three novel three-phase bidirectional ac-dc converter topologies are proposed. They keep the merits of the novel single-phase bidirectional ac-dc converter. Detailed operating principles are described.

Overall, a novel single-phase bidirectional ac-dc converter is proposed. With magnetic integration, the total number of the magnetic cores is reduced by half with the same converter efficiency. Based on the single-phase bidirectional ac-dc converter topology, three novel three-phase bidirectional ac-dc converter topologies are proposed.

Chapter 4 Unified Controller for Bidirectional Power Flow Control

4.1 Introduction

The dual-buck converter based single-phase bidirectional ac-dc converter was proposed in chapter 2. With magnetic integration, the power density is significantly improved and the weight of the converter is reduced. In this chapter, the modeling of the power stage is described.

The analog control implementation intends to have difficulties during the mode transition, because the error amplifier of the preferred mode can be saturated during the transition. Digital controller can be easily set to reduce or avoid the delay out of the saturation in the transition.

In order to control the bidirectional power flow and at the same time stabilize the system in mode transition, a unified digital controller is described in this chapter. The basic concept of a unified controller is explained. An admittance compensator along with a QPR controller is adopted to allow smooth startup and elimination of the steady-state error over the entire load range. Both simulation and experimental results match very well and validate the design of the proposed unified controller.

4.2 Unified Controller Concept

Figure 4.1 shows the traditional method of two separate controllers: one for rectifier mode and the other one for inverter mode. The current references i_{ac_rec}* and $i_{ac\text{-}inv}$* are provided by the power management command separately. The mode switch between two different modes is controlled by the mode selection command. To achieve the mode transition, the converter has to gradually decrease the current to zero under one controller and then gradually increase the current to the desired value under the other controller.

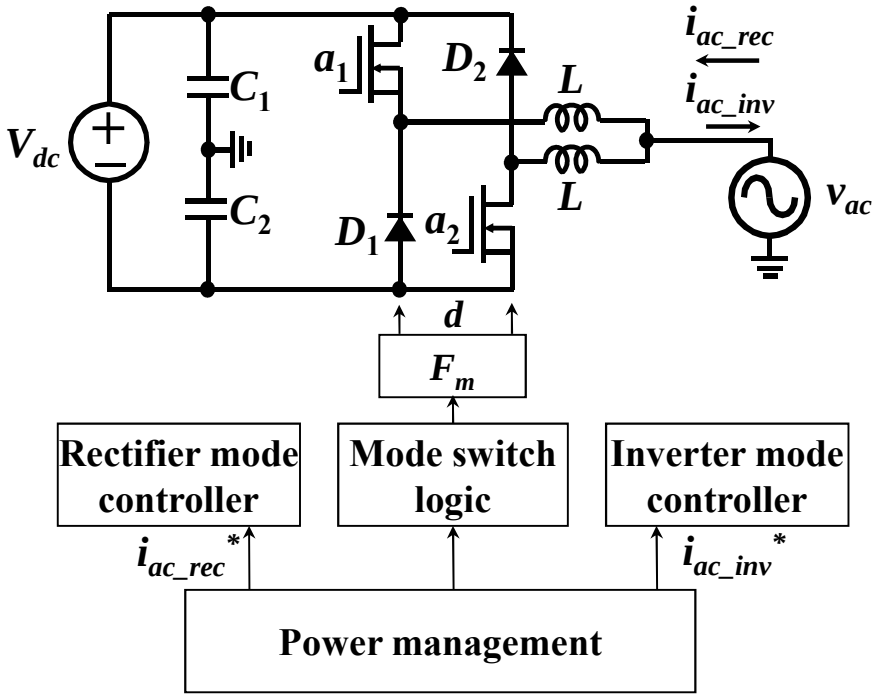

Figure 4.1 Separate controller controlled system.

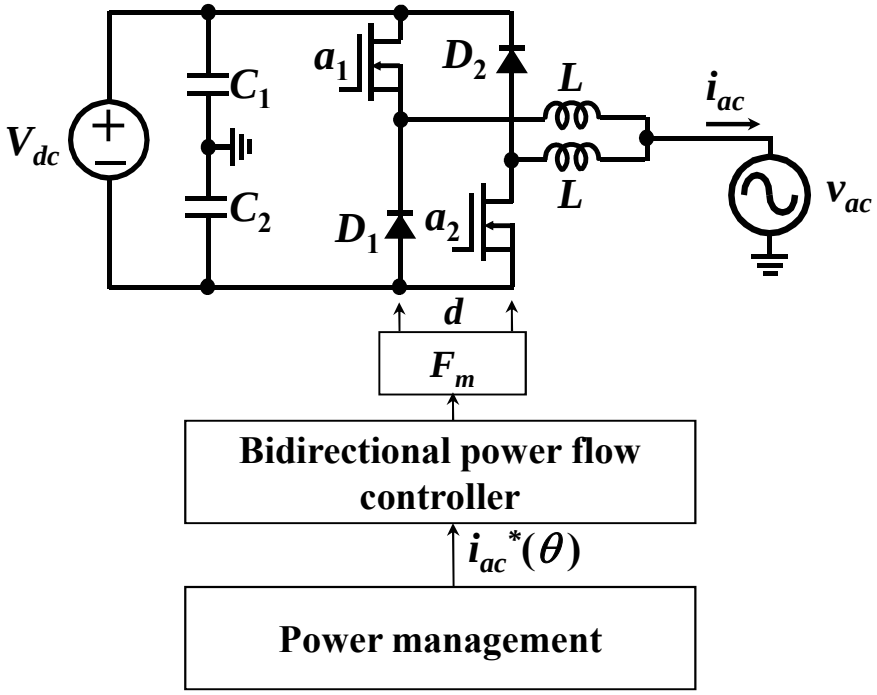

Figure 4.2 Unified controller controlled system.

Instead of individual controllers for each mode shown in Figure 4.1, a unified controller is proposed in Figure 4.2. For the unified controller, the reference is controlled by the parameter θ, which is defined as the phase angle difference between ac current and voltage shown in Figure 2.6. When $\theta = 0$, the ac current is controlled to have the same phase angle relative to the voltage. The converter operates under inverter mode. When $\theta = 180$, the ac current is controlled to have the 180° phase shift relative to the voltage. The converter operates under rectifier mode.

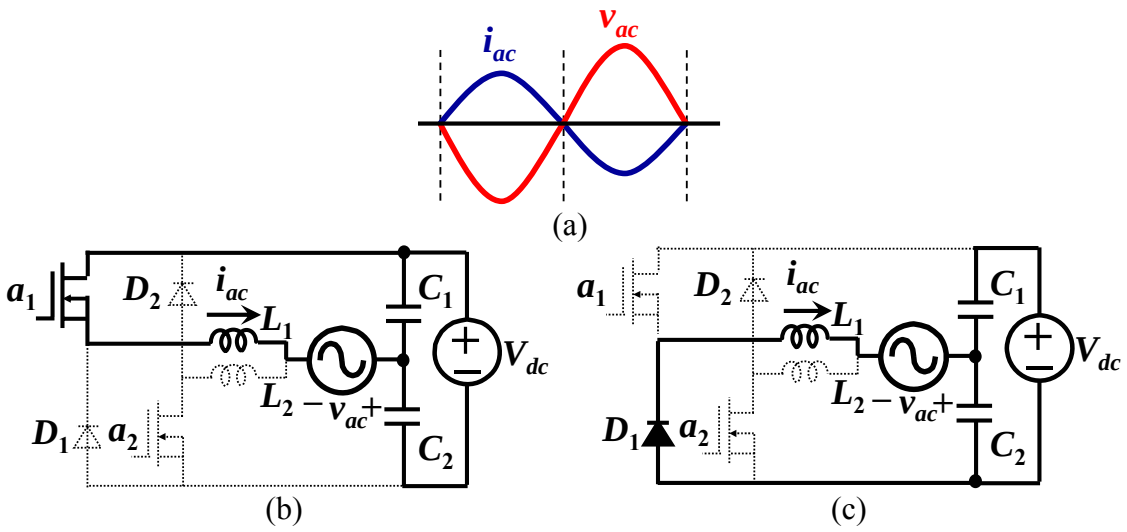

Figure 4.3 Operating under rectifier mode with pure active power transferring. (a) Conceptual voltage and current waveform. (b) a_1 is on. (c) D_1 is on.

From Figure 4.3(b) and (c), when current is positive in the rectifier mode, the total volt-seconds applied to the inductor L_1 over one switching period are

$$(\frac{V_{dc}}{2}+v_{ac})\cdot d_{a1\_rec}+(-\frac{V_{dc}}{2}+v_{ac})\cdot(1-d_{a1\_rec})=0\,. \tag{4.1}$$

The duty cycle for switch a_1 can be derived as

$$d_{a1\_rec} = \frac{1}{2}(1 - \frac{v_{ac}}{V_{dc}/2}) = \frac{1}{2}(1 - \frac{v_{pk}\sin\omega t}{V_{dc}/2}) = 0.5 \cdot (1 - M\sin\omega t)\,. \tag{4.2}$$

where $M = v_{pk}/(V_{dc}/2)$ is modulation index and $\sin\omega t > 0$. Similarly, the duty cycle for switch a_2 in the rectifier mode can be derived as

$$d_{a2\_rec} = 0.5 \cdot (1 + M\sin\omega t)\,. \tag{4.3}$$

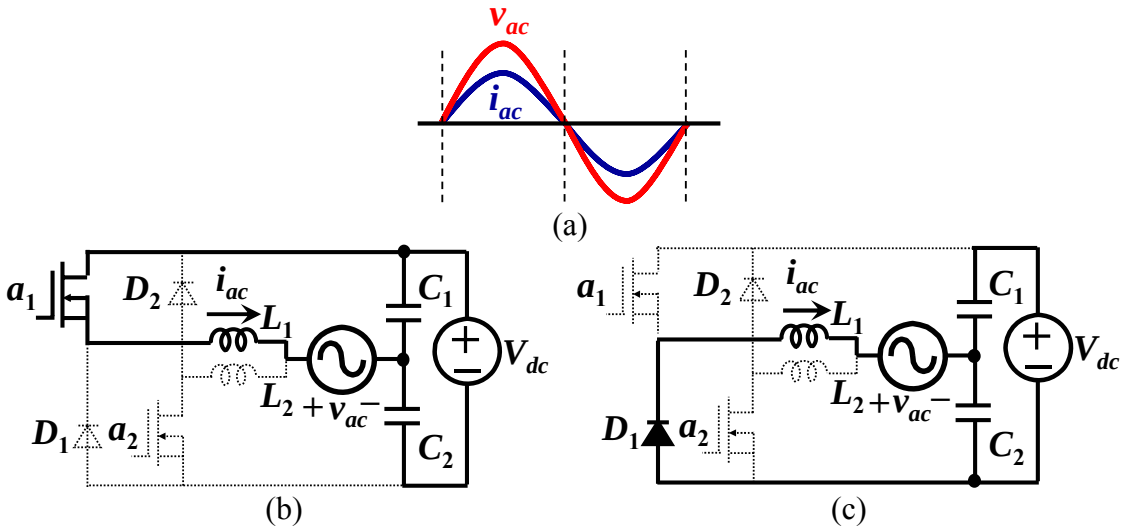

Figure 4.4 Operating under inverter mode with pure active power transferring. (a) Conceptual voltage and current waveform. (b) a_1 is on. (c) D_1 is on.

From Figure 4.4(b) and (c), when current is positive in the inverter mode, the total volt-seconds applied to the inductor L_1 over one switching period are

$$(\frac{V_{dc}}{2} - v_{ac}) \cdot d_{a1\_rec} + (-\frac{V_{dc}}{2} - v_{ac}) \cdot (1 - d_{a1\_rec}) = 0\,. \tag{4.4}$$

The duty cycle for switch a_1 can be derived as

$$d_{a1\_inv} = 0.5 \cdot (1 + M\sin\omega t)\,. \tag{4.5}$$

where $M = v_{pk}/(V_{dc}/2)$ is modulation index and $\sin\omega t > 0$. Similarly, the duty cycle for switch a_2 in the inverter mode can be derived as

$$d_{a2\_inv} = 0.5 \cdot (1 - M \sin \omega t). \tag{4.6}$$

It can be concluded that $d_{a1\_rec} = - d_{a1\_inv}$ and $d_{a2\_rec} = - d_{a2\_inv}$. By changing the phase angle θ from 180° to 0°, current reference is changed from i_{ac}^* to $-i_{ac}^*$. The control output applied to d_{a1} to conduct positive current under rectifier mode will also be used for d_{a1} to conduct positive current under inverter mode. The control output applied to d_{a2} to conduct negative current under rectifier mode will also be used for d_{a2} to conduct negative current under inverter mode. One controller can be used to regulate current under both rectifier and inverter modes by adjusting the phase angle θ.

4.3 Unified Controller Design

4.3.1 Modeling of the Power Stage

The approach of modeling the dual-buck converter based single-phase bidirectional ac-dc converter is the same as the traditional full-bridge dc-ac inverter with bipolar PWM control. Assume the two inductors have the same inductance and the equivalent series resistance (ESR) is r in Figure 4.5, the following voltage relationships can be easily obtained:

$$r i_{ac}(t) + L \frac{d i_{ac}(t)}{dt} = \frac{V_{dc}}{2} \cdot d - v_{ac}. \tag{4.7}$$

The output current i_{ac} can be derived as

$$i_{ac}(s) = \frac{V_{dc}/2}{r + sL} \cdot d - \frac{1}{r + sL} \cdot v_{ac} = G_{id}(s) \cdot d - G_{iv}(s) \cdot v_{ac}. \tag{4.8}$$

where

$$G_{id}(s) = \frac{i_{ac}(s)}{d(s)} = \frac{V_{dc}/2}{r + sL} \tag{4.9}$$

is the control-to-output transfer function, and

$$G_{iv}(s) = \frac{i_{ac}(s)}{v_{ac}(s)} = \frac{1}{r + sL} \tag{4.10}$$

is the current-to-voltage transfer function, which is uncontrolled feed-forward term.

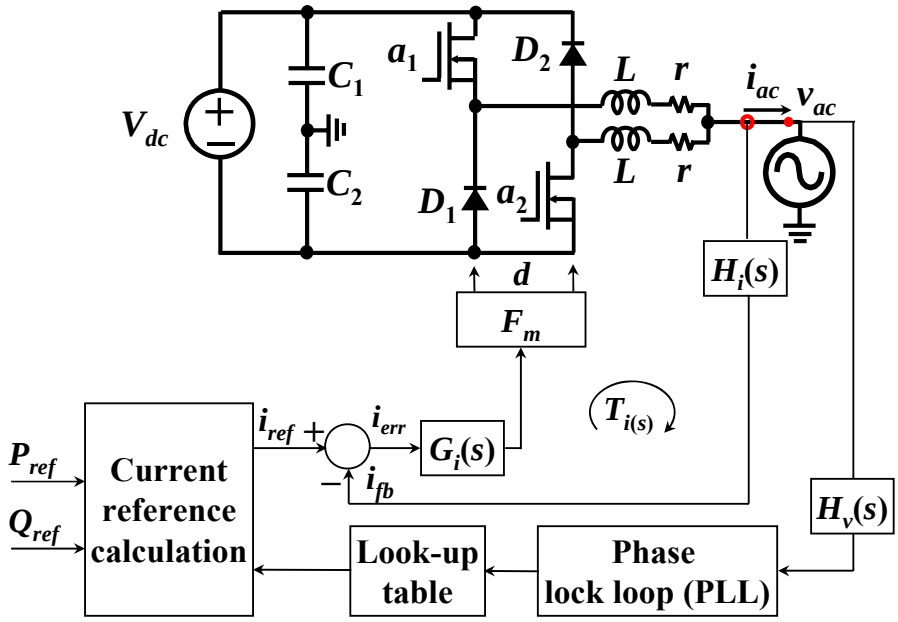

Figure 4.5 Circuit diagram of the bidirectional ac-dc converter with current control loop.

Figure 4.5 shows the complete circuit diagram that includes a current-loop controller. Current command i_{ref} is obtained from the active power reference P_{ref} and the reactive power reference Q_{ref}, which are commanded by the power management, and the ac voltage phase information, which is produced by a digital phase-locked loop (PLL).

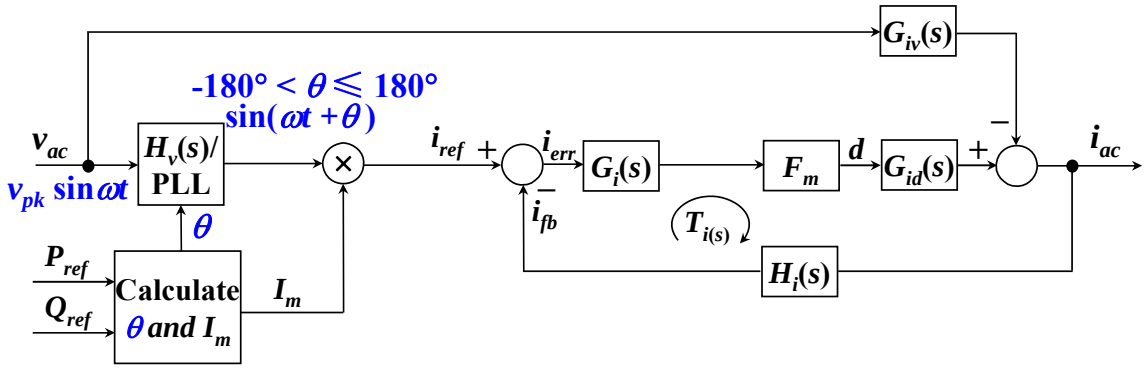

Figure 4.6 Block diagram of the current control loop.

Figure 4.6 shows the block diagram of the compensated system that adds G_i(s). H_v(s) and H_i(s) are voltage and current sensor gains. The current loop controller G_i(s) is designed to compensate the error i_{err} between i_{ref} and the feedback sensed current i_{fb}. By feeding the output of the current loop controller to the PWM block, which is represented by F_m, the output signal is gating signal d.

4.3.2 Unified Controller Design

From Figure 4.6, the overall equivalent admittance can be represented as

$$Y(s) = \frac{i_{ac}(s)}{v_{ac}(s)} = \frac{I_m H_v G_i(s) F_m G_{id}(s)}{1 + T_i} - \frac{G_{iv}(s)}{1 + T_i} = Y_1(s) + Y_2(s) \tag{4.11}$$

where $T_i(s) = G_i(s)F_mG_{id}(s)H_i$ is the loop gain, $Y_1(s) = [I_mH_vG_i(s)F_mG_{id}(s)]/(1+T_i(s))$, and $Y_2(s) = -G_{iv}(s)/(1+T_i(s))$.

The active and reactive power reference command can be used to calculate I_m and θ shown as

$$I_m = \frac{\sqrt{P_{ref}^{\ 2} + Q_{ref}^{\ 2}}}{v_{pk}/2} \tag{4.12}$$

$$\theta = \tan^{-1}\left(\frac{Q_{ref}}{P_{ref}}\right). \tag{4.13}$$

The term $Y_1(s)$ is generated by active and reactive power reference command P_{ref} and Q_{ref}, which provides desired output. The term $Y_2(s)$ is related to the closed-loop voltage-to-current transfer function, which reduces current induced in Y_1. Thus, Y_2 is undesired and needs to be eliminated by the use of the adding admittance compensator $G_c(s)$ shown in Figure 4.7 [82]-[84].

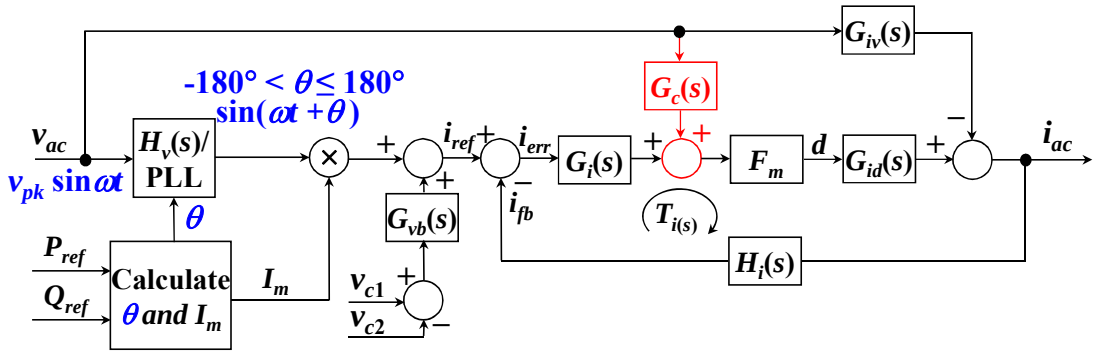

Figure 4.7 Block diagram of the current control loop with the adding admittance compensator.

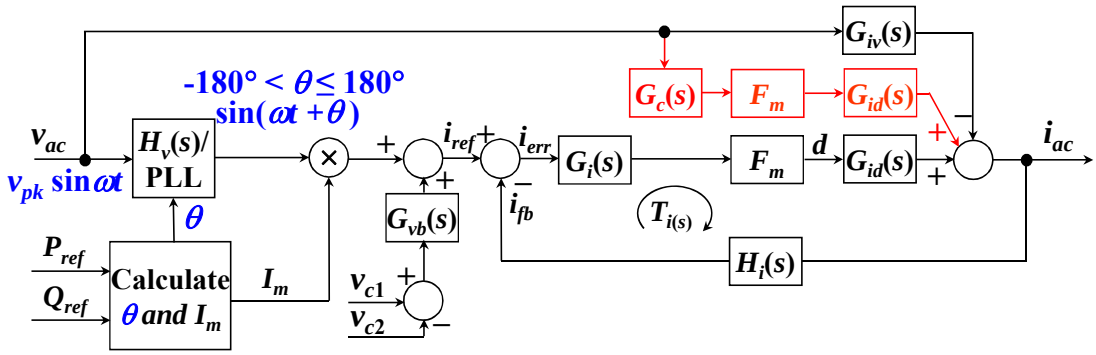

Figure 4.8 Block diagram of the current control loop with the adding admittance compensator for derivation.

Since $G_c(s)$ is used to cancel the term $Y_2(s)$, it can be easily derived from Figure 4.8 as

$$G_c(s) = \frac{G_{iv}(s)}{F_m G_{id}(s)} = \frac{1}{F_m (V_{dc}/2)}. \tag{4.14}$$

Equation (4.14) indicates that G_c(s) is independent of converter transfer functions and proportional with the multiplicative inverse of the half dc bus voltage V_{dc}/2 and the PWM gain F_m.

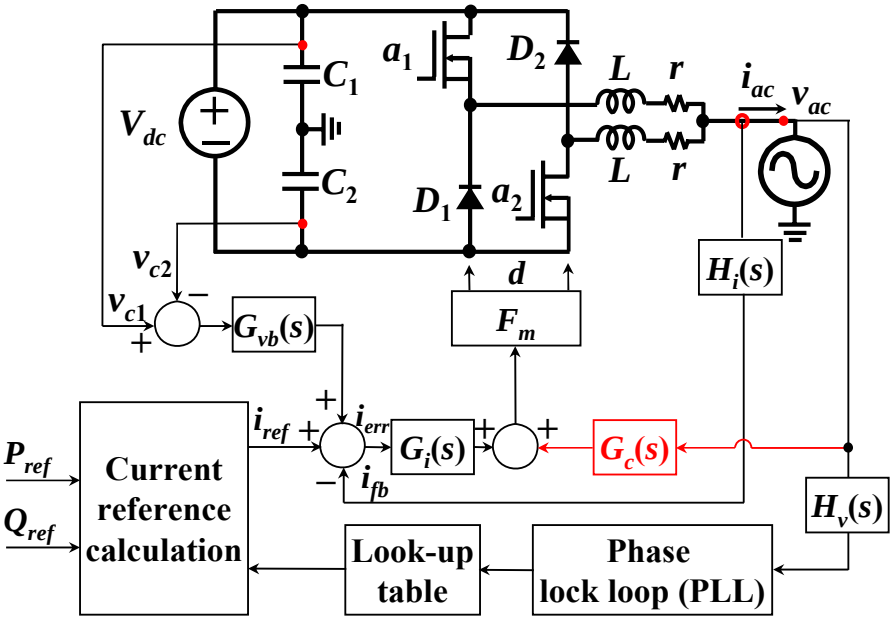

Figure 4.9 Circuit diagram of the bidirectional ac-dc converter with current control loop and admittance compensation.

Figure 4.9 shows the complete circuit diagram that includes G_i(s), G_{vb}(s) and G_c(s). The voltage balance compensator G_{vb}(s) is designed to balance the voltage across the two dc split capacitors, v_{c1} and v_{c2}. The admittance compensator G_c(s) is designed to reject the disturbance from G_{iv}(s).

In order to reduce the steady-state error at the fundamental frequency, or 60 Hz in the designed case, the QPR controller, which is shown in (4.15), is adopted for the current loop controller G_i(s), which can provide a high gain at 60 Hz without phase offset [81].

$$G_i(s) = k_p + \frac{2k_r\omega_c s}{s^2 + 2\omega_c s + \omega_0^2}. \tag{4.15}$$

Here, k_p is a proportional gain, k_r is a resonant gain, and ω_c is an equivalent bandwidth of the resonant controller. The QPR controller is designed to have the following parameters: $k_p = 1.5$, $k_r = 50$, $\omega_c = 10$ rad/s, and $\omega_o = 2\pi \times 60$ rad/s.

A proportional-integral (PI) controller, which is shown in (4.16), is adopted to balance the voltage across the two dc split capacitors, v_{c1} and v_{c2}. k_p is designed as small as possible to have less influence on the main control loop, and k_i is designed to have large time constant. In this design, $k_p = 0.6$ and $k_i = 60$.

$$G_{vb}(s) = k_p + \frac{k_i}{s}. \tag{4.16}$$

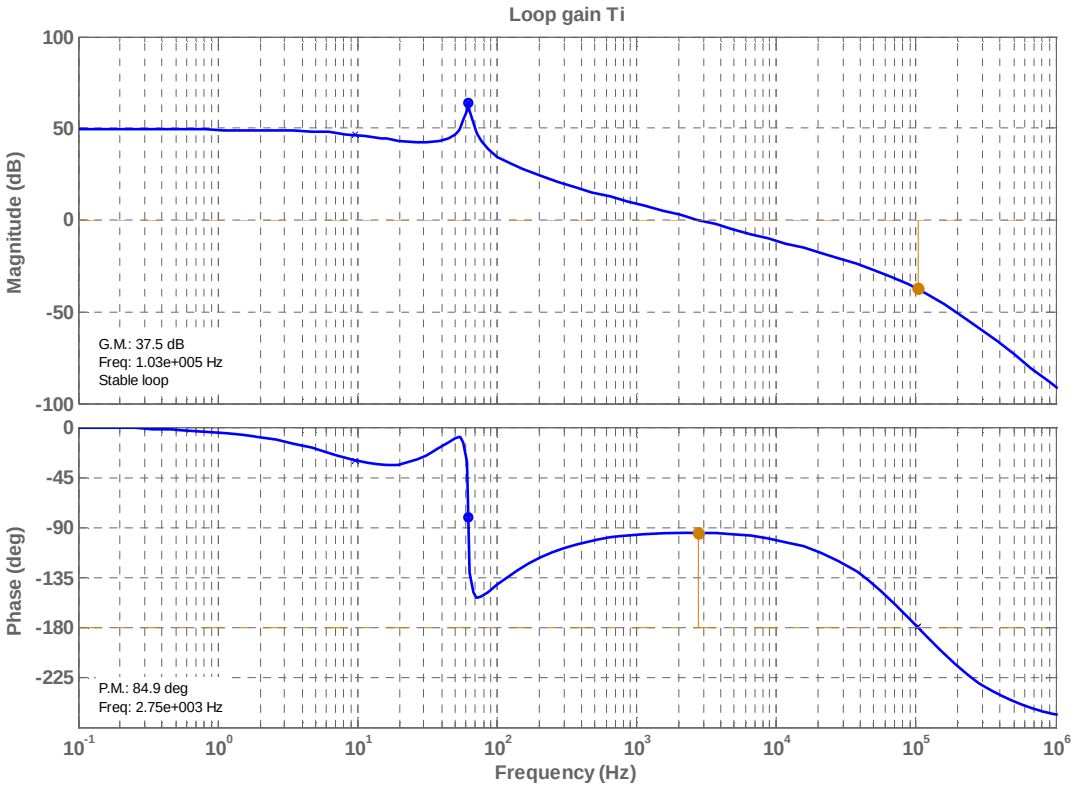

Figure 4.10 Bode plot of the compensated loop gain $T_i(s)$.

Using the above current loop controller and system parameters, the compensated loop gain $T_i(s) = G_i(s)F_mG_{id}(s)H_i$ is plotted in Figure 4.10. As shown in the bode plot, the crossover frequency and phase margin are 2.75 kHz and 84.9°, respectively.

4.3.3 Discretization of the QPR current controller

The current controller $G_i(s)$ obtained above has two parts: a proportional controller and a resonant controller shown in (4.17). Since the proportional controller is just a gain, this section focuses on the discretization of the resonant controller.

$$G_{i\_resonant}(s) = \frac{2k_r\omega_c s}{s^2 + 2\omega_c s + \omega_0^2} \tag{4.17}$$

where $k_r = 50$, $\omega_c = 10$ rad/s, and $\omega_o = 2\pi \times 60$ rad/s.

The trapezoidal integration based Z-transform shown in (4.18), also known as Tustin transform, is utilized because it preserves stability and minimum-phase for both gain and phase properties of the controller below one tenth of the sampling frequency.

$$s = \frac{2}{T_s} \cdot \frac{z-1}{z+1} \tag{4.18}$$

where $T_s = 20$ μs is sampling time.

Substituting the s variable in (4.17) with the expression indicated in (4.18), it can be found

$$G_{i\_resonant}(Z) = \frac{a_2 z^2 + a_1 z + a_0}{b_2 z^2 + b_1 z + b_0}. \tag{4.19}$$

where $a_2 = 0.00999786$, $a_1 = 0$, $a_0 = -0.00999786$, $b_2 = 1$, $b_1 = -1.99954325$, and $b_0 = 0.99960001$. Figure 4.11 represents a detailed description of the designed digital resonant converter.

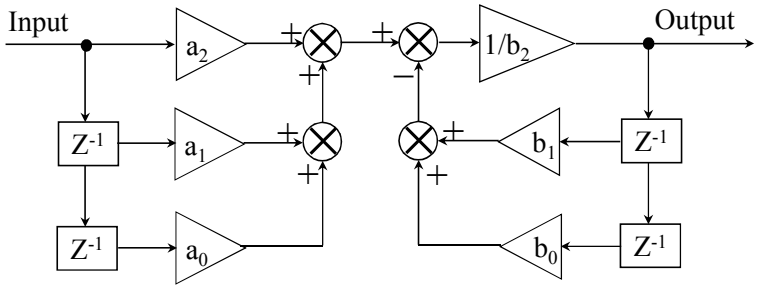

Figure 4.11 Block diagram representation of the digital resonant controller.

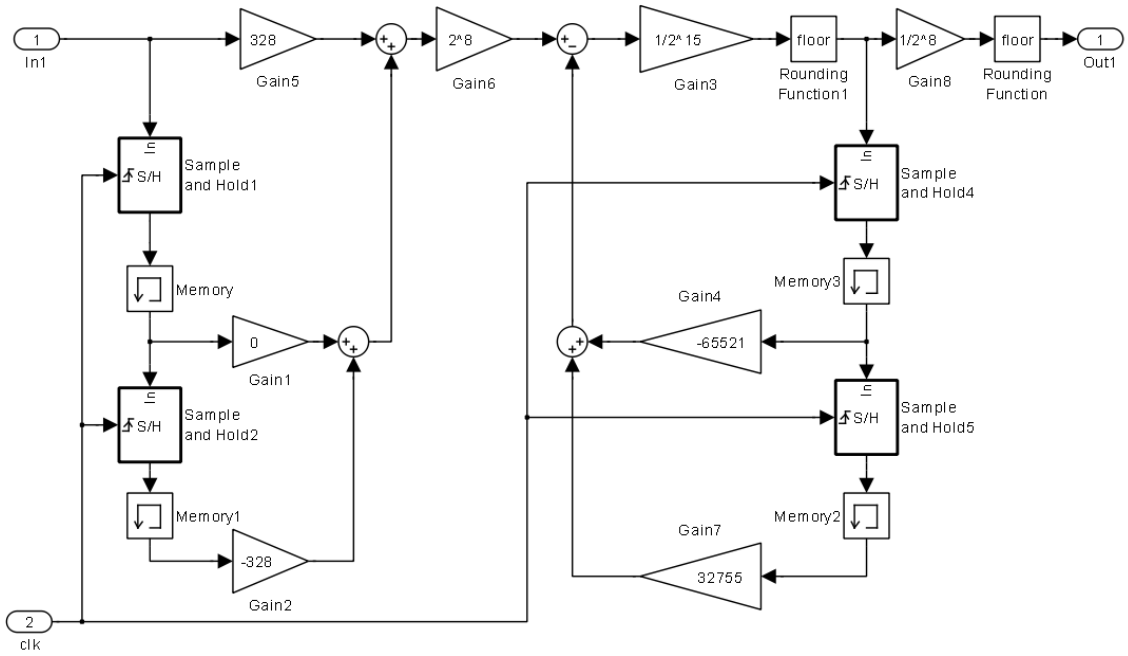

Figure 4.12 Digital implementation of resonant controller in FPGA.

In order to implement a controller on a FPGA, the controller coefficients must be truncated (or rounded) into certain word length binary representation, so as to be fit to the numbers of bits available to the FPGA for variables and constants. In general, the effect of coefficient result truncation (or rounding) leads to the shift of the system zeros and poles and therefore a distortion of the controller's frequency response.

The corresponding truncated coefficients are expressed as

$$G_{i\_resonant\_quantization}(Z) = \frac{c_2 z^2 + c_1 z + c_0}{d_2 z^2 + d_1 z + d_0}. \tag{4.20}$$

where $c_2 = 328$, $c_1 = 0$, $c_0 = -328$, $d_2 = 32768$, $d_1 = -65521$, and $d_0 = 32755$. The digital implementation of the resonant controller in FPGA and Simulink is indicated in Figure 4.12.

The Bode plots of the analog controller described in (4.17), the digital controller described in (4.19), and the digital controller with truncation described in (4.20), are shown in Figure 4.13. As can be seen, the analog and digital controllers are almost overlapped by each other. The two resonant poles of the truncated digital controller are shifted from 60 Hz to 62.18 Hz.

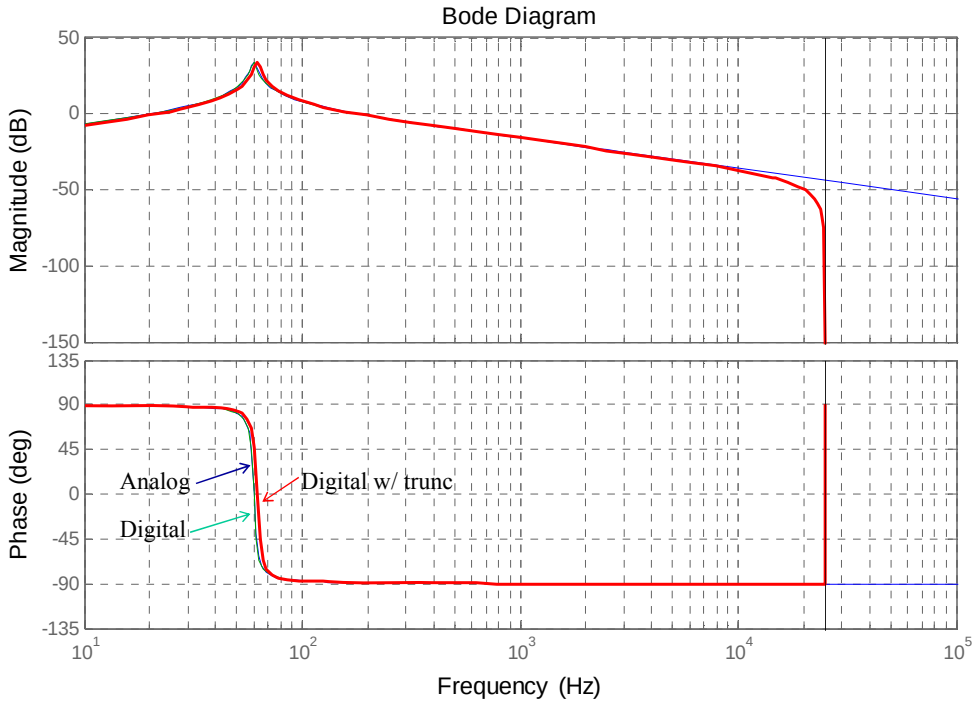

Figure 4.13 Bode plots of the analog controller, the digital controller, and the digital controller with truncation.

The frequency response magnitudes of the analog controller, the digital controller, and the digital controller with truncation, are shown in Figure 4.14. As can be seen, the frequency response magnitude of the analog controller has a peak value of 50 at 60 Hz.

However, the peak points for the digital and truncated digital controller are shifted. The frequency response magnitude is 37.35 for the digital controller and 35.57 for the truncated digital controller at 60 Hz.

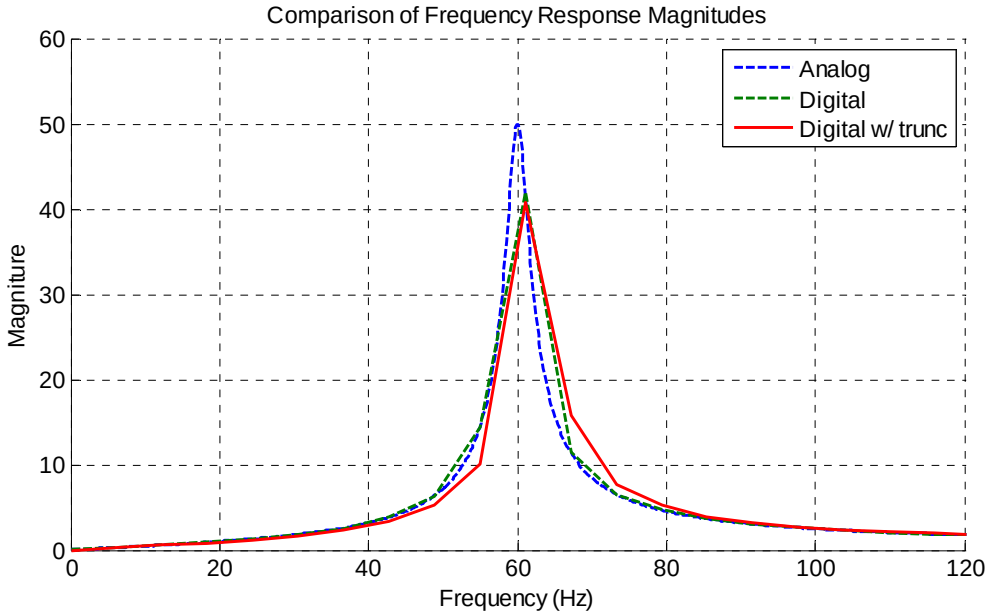

Figure 4.14 Comparison of frequency response magnitudes of the analog controller, the digital controller, and the digital controller with truncation.

4.4 Simulation Results

Two different simulation tools, PSIM and Simulink, are used to verify the operation of the dual-buck converter based single-phase bidirectional ac-dc converter.

4.4.1 PSIM Simulation

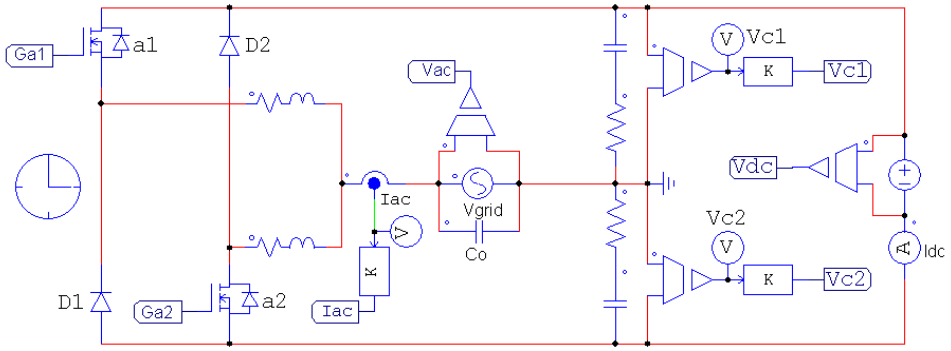

Figure 4.15 Power stage in PSIM.

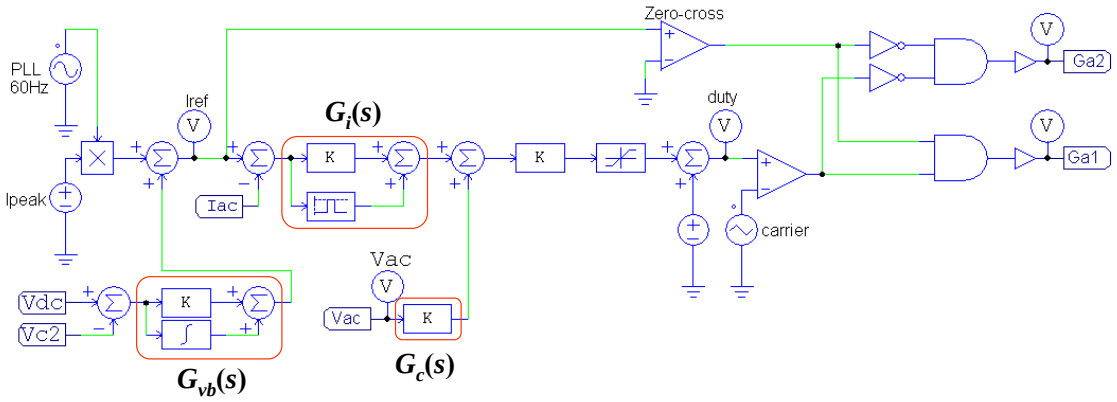

Figure 4.16 Control circuit in PSIM.

Figure 4.15 and Figure 4.16 show the power stage and control circuit in PSIM, respectively. In the PSIM simulation, the system is considered as continuous-time system since the digital controller and analog-to-digital converter (ADC) are not used.

Figure 4.17(a) and (b) shows the PSIM simulation results under both rectifier and inverter modes for the converter, respectively.

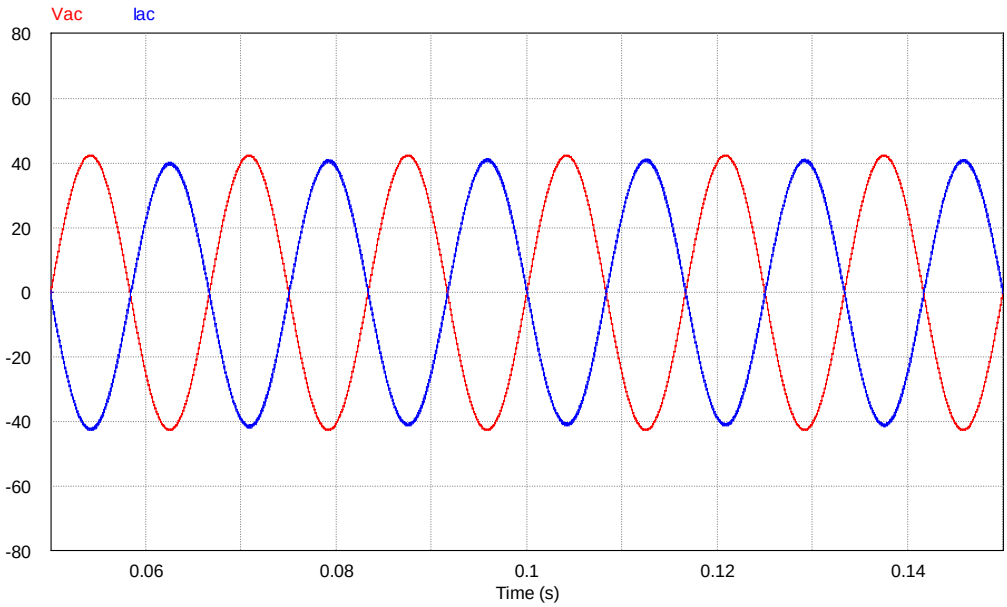

(a)

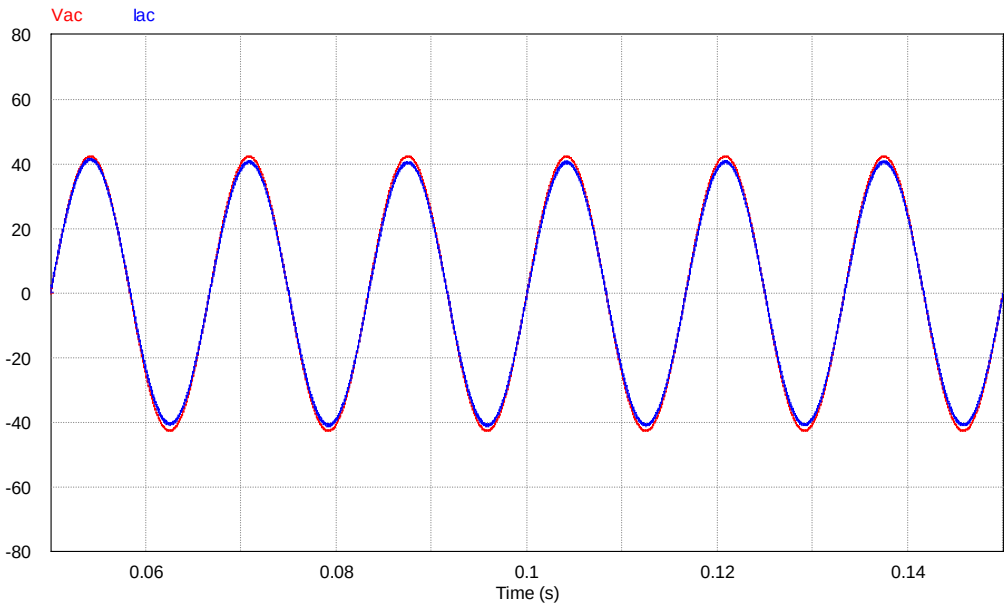

(b)

Figure 4.17 Simulation results under (a) rectifier mode and (b) inverter mode, both with v_{ac} = 30 V_{rms} and i_{ac} = 28 A_{rms}.

4.4.2 Simulink Simulation

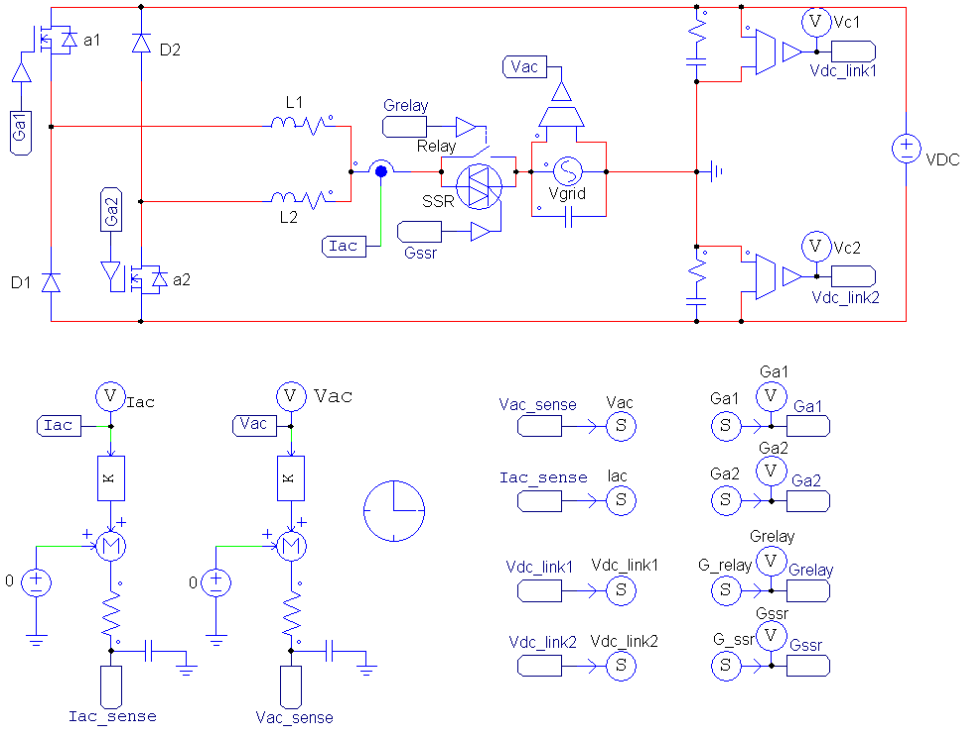

Figure 4.18 Power stage in PSIM.

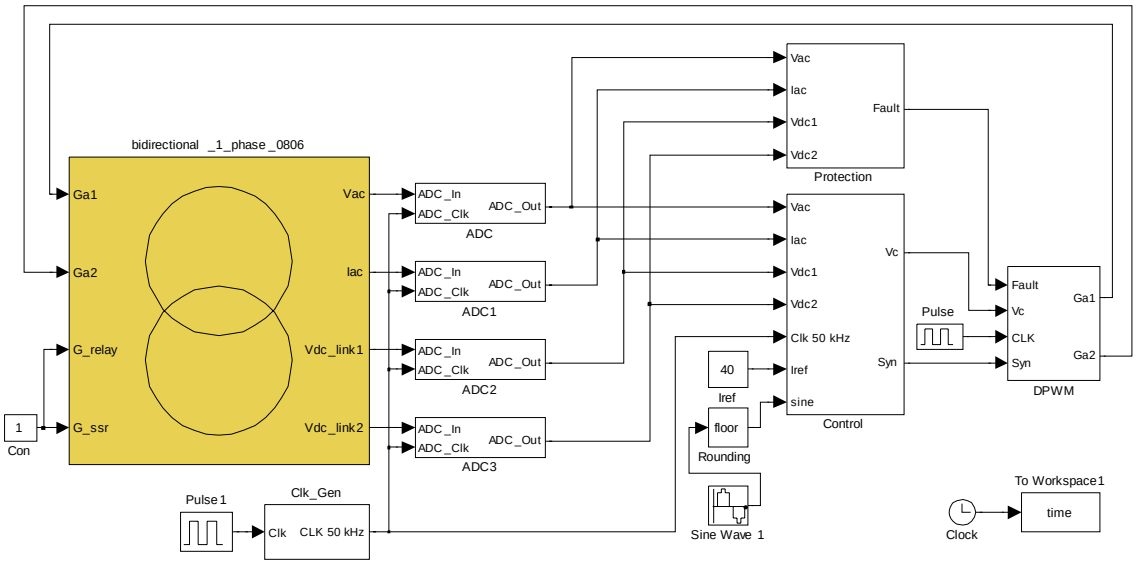

Figure 4.19 Control circuit in Simulink.

Although digital controller can be implemented in PSIM, Simulink is preferred to implement the controller for its capability of model-based design and multi-domain simulation.

Here are the steps to build the circuit in Simulink. First, the power stage circuit is built in PSIM, which is shown in Figure 4.18. Second, the power stage circuit built in PSIM is created as a model block in Simulink. Also, the digital control circuit is built in Simulink as shown in Figure 4.19. Finally, the power stage block and the digital control circuit are connected in Simulink. The sampling and computational delays with digital control are unavoidable and also considered in the simulation.

As can be seen from Figure 4.19, the circuit consists of a power stage block from PSIM, ADC, digital controller, and digital PWM module. All the modules are synchronized by a 50 kHz clock, which is set as the switching frequency. The control parameters in the Simulink simulation can be directly used in the FPGA code implementation.

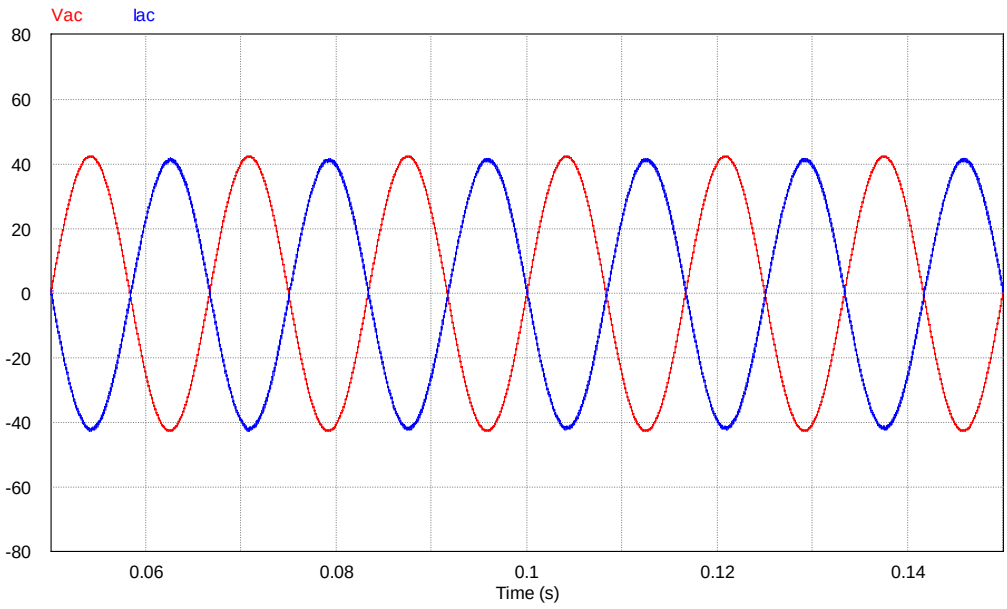

(a)

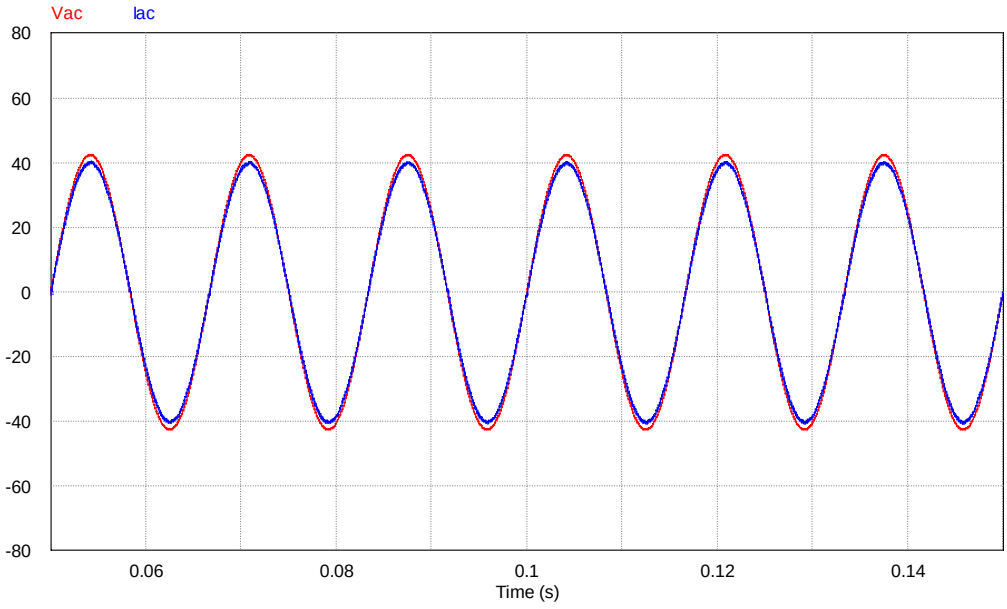

(b)

Figure 4.20 Simulation results under (a) rectifier mode and (b) inverter mode, both with v_{ac} = 30 V_{rms} and i_{ac} = 28 A_{rms}.

Figure 4.20(a) and (b) shows the Simulink simulation results under both rectifier and inverter modes for the converter, respectively.

4.5 Experimental Results

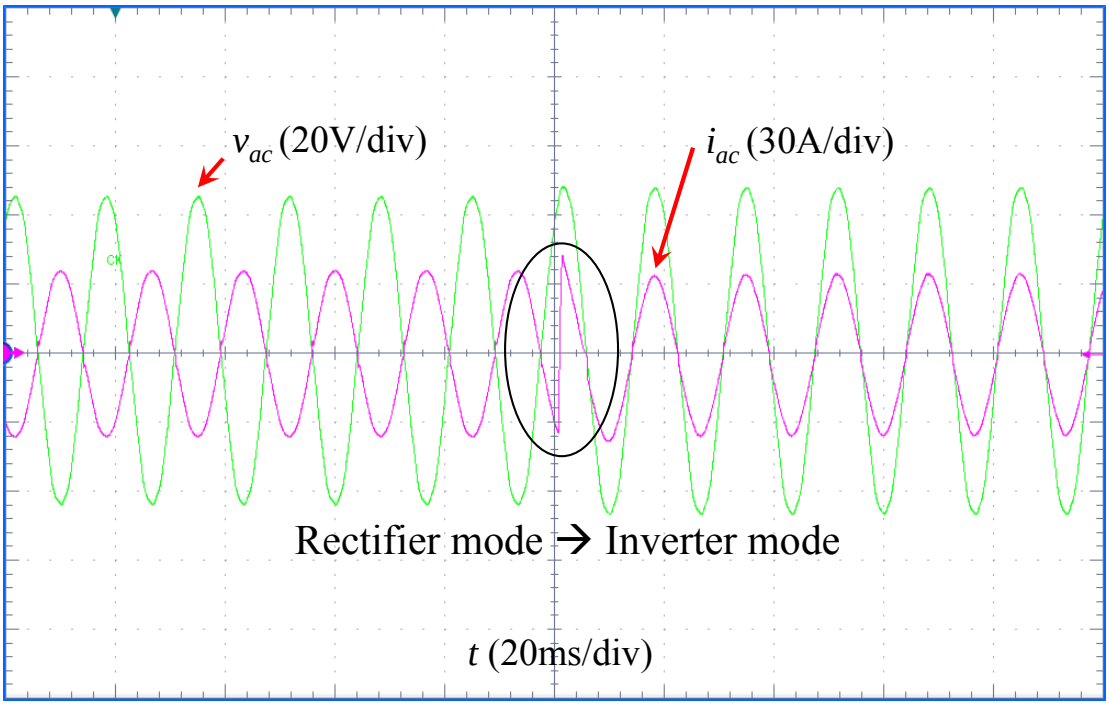

(a)

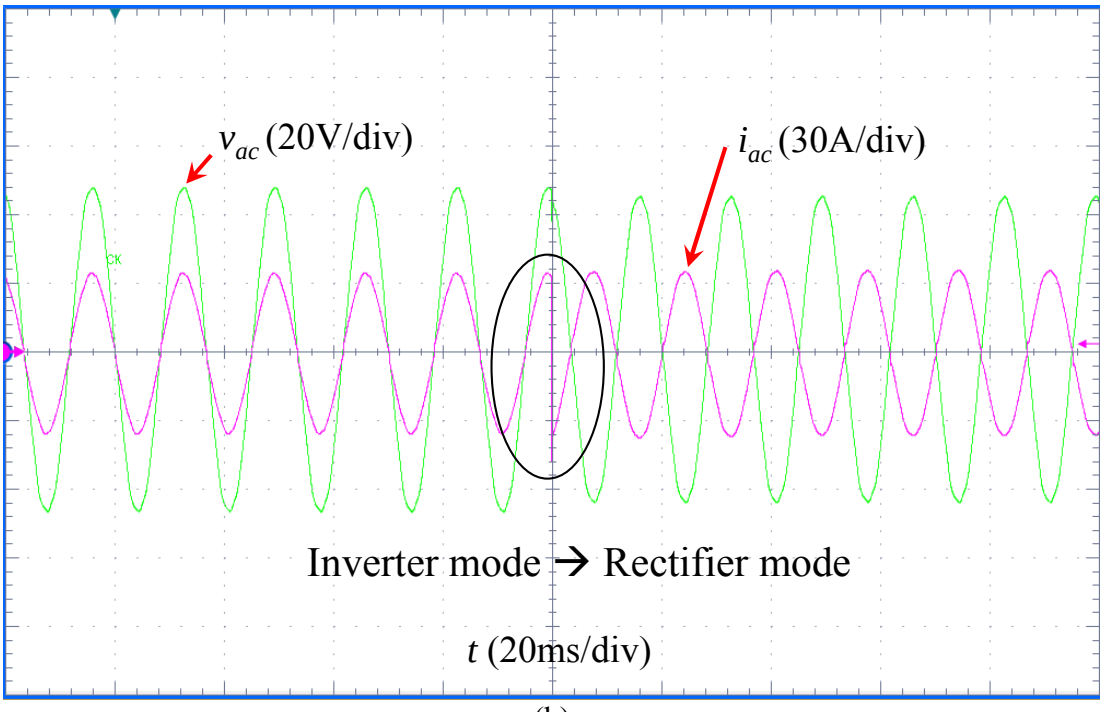

(b)

Figure 4.21 Experimental results of seamless energy transfer. (a) Changing from rectifier mode to inverter mode at the peak current point. (b) Changing from inverter mode to rectifier mode at the peak current point.

For the experiment, the bidirectional ac-dc converter is connected between the batteries and ac grid. Figure 4.21(a) shows transient waveforms from rectifier mode to inverter mode in 40 μs when the battery pack has a SOC value of around 70%. Figure 4.21(b) shows transient waveforms from inverter mode to rectifier mode in 40 μs when the battery pack has a SOC value of around 70%. These waveforms show seamless energy transfer.

4.6 Summary

In order to control the bidirectional power flow and at the same time stabilize the system in mode transition, a unified digital controller is proposed in this chapter. The basic concept of a unified controller is explained. The differences between individual controllers and unified controller are described.

The power stage small-signal model is derived for the dual-buck converter based single-phase bidirectional ac-dc converter. Based on the small-signal model, an admittance compensator along with a QPR controller is adopted to allow smooth startup and elimination of the steady-state error over the entire load range. The proposed QPR controller is designed and implemented with a digital controller. Then the coefficients of the digital controller are truncated into certain word length binary representation, so as to be fit to the numbers of bits available to the FPGA for variables and constants. The characteristics of the designed analog resonant controller, digital controller, and truncated digital controller are analyzed. The frequency responses of the three controllers are also obtained.

The entire system has been simulated in both PSIM and Simulink and verified with hardware experiments. Small transient currents are observed with the power transferred from rectifier mode to inverter mode at peak current point and also from inverter mode to rectifier mode at peak current point.

Chapter 5 Grid-Tie Battery Energy Storage System Design

5.1 Introduction

Recent developments in lithium-ion battery technology show many advantages compared to lead-acid, nickel-metal hydride and nickel-cadmium batteries, such as high open circuit voltage, low self-discharge rate, high power and energy density, and high charge-discharge efficiency [23]-[27].

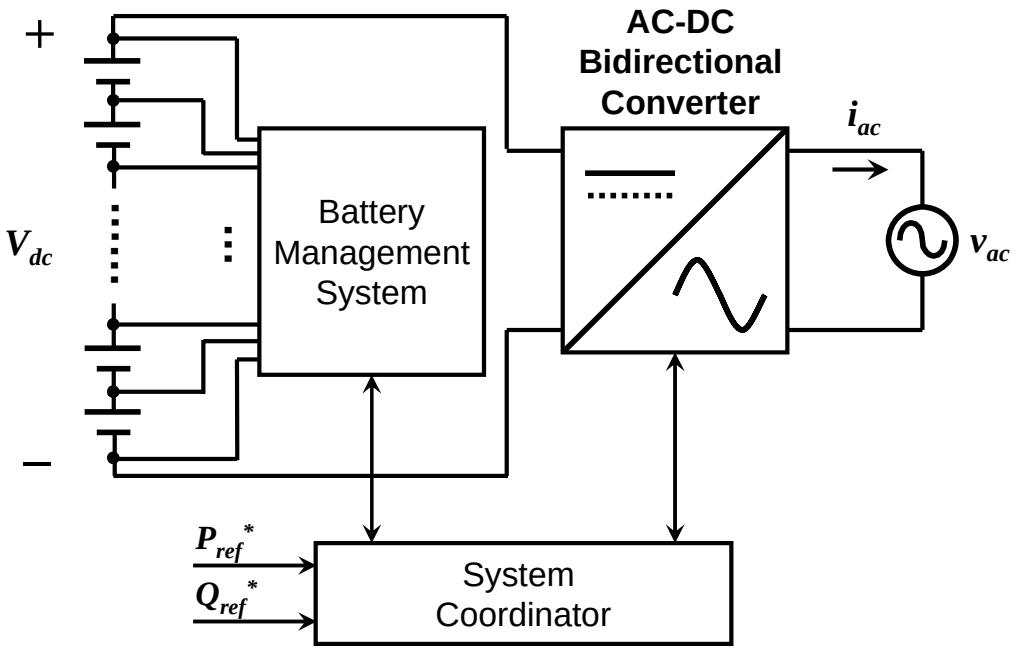

Figure 5.1 Circuit diagram of a lithium-ion battery energy storage system

As indicated in Figure 5.1, a battery energy storage system consists of three subsystems, a $LiFePO_4$ battery pack and associated BMS, a bidirectional ac-dc converter, and the central control unit which controls the operation mode and grid interface of the energy storage system. The BMS controller monitors the parameters of each battery cell,

such as cell voltage, temperature, charging and discharging current; estimates the SOC and SOH of each battery cell in the pack. The SOC information is then used to control the charge equalization circuits to mitigate the mismatch among the series connected battery cells. The SOC and SOH information is also used by the central control unit to determine the operating mode of the energy storage system. The bidirectional ac-dc converter works as the interface between the battery pack and the ac grid, which needs to meet the requirements of bidirectional power flow capability and to ensure high power factor and low THD as well as regulate the dc side power regulation.

In the previous chapters, novel bidirectional ac-dc converter topologies and related control schemes are proposed. The dual-buck converter based single-phase bidirectional ac-dc converter is proposed in chapter 2. To better utilize the dc bus voltage and eliminate the two dc bus capacitors, a novel bidirectional ac-dc converter is proposed by replacing the two-capacitor leg with a two-switch leg in chapter 3. In order to control the bidirectional power flow and at the same time stabilize the system in mode transition, a unified digital controller is proposed in chapter 4. This chapter will focus on the grid-tie battery energy storage system design and implementation.

5.2 Battery Management System Configuration

In a Lithium-ion battery system, BMS is the key component to ensure all cell voltages being strictly kept in boundaries for safety operation and cycle life. There are two key functions in the designed BMS: monitoring and charge equalization.

First, the BMS monitors the status of all the series connected lithium-ion battery cells in the system. The parameters being monitored includes cell voltage, cell temperature, charging and discharging current. The voltage measurements are performed by an analog front end integrated circuit, which is able to select and level shift the voltage across any of 12 stacked battery cells. All the signals are multiplexed to a differential analog to digital converter to convert into digital domain. The voltage, current and temperature information are then processed by the BMS controller to determine the SOC, SOH and capacity of each battery cell, and protect all the cells operate in the designed SOC range.

Second, the designed BMS applies active balancing to equalize the cells in the pack. In a Lithium-ion battery system, all cell voltages need to be strictly kept in boundaries to

ensure safety operation. However, due to production deviations, inhomogeneous aging and temperature difference within the battery pack, there are SOC or capacity imbalances between battery cells. Minimize the mismatches across all the cells are important to guarantee the power or energy performance of the pack, as they are limited by first cell which goes beyond the boundaries. In this system, an inductive based active cell balancing approach is used to regulate the amount of charge in and out of each individual cell to balance the mismatches across the cell to maintain the homogeneous status across the battery pack.

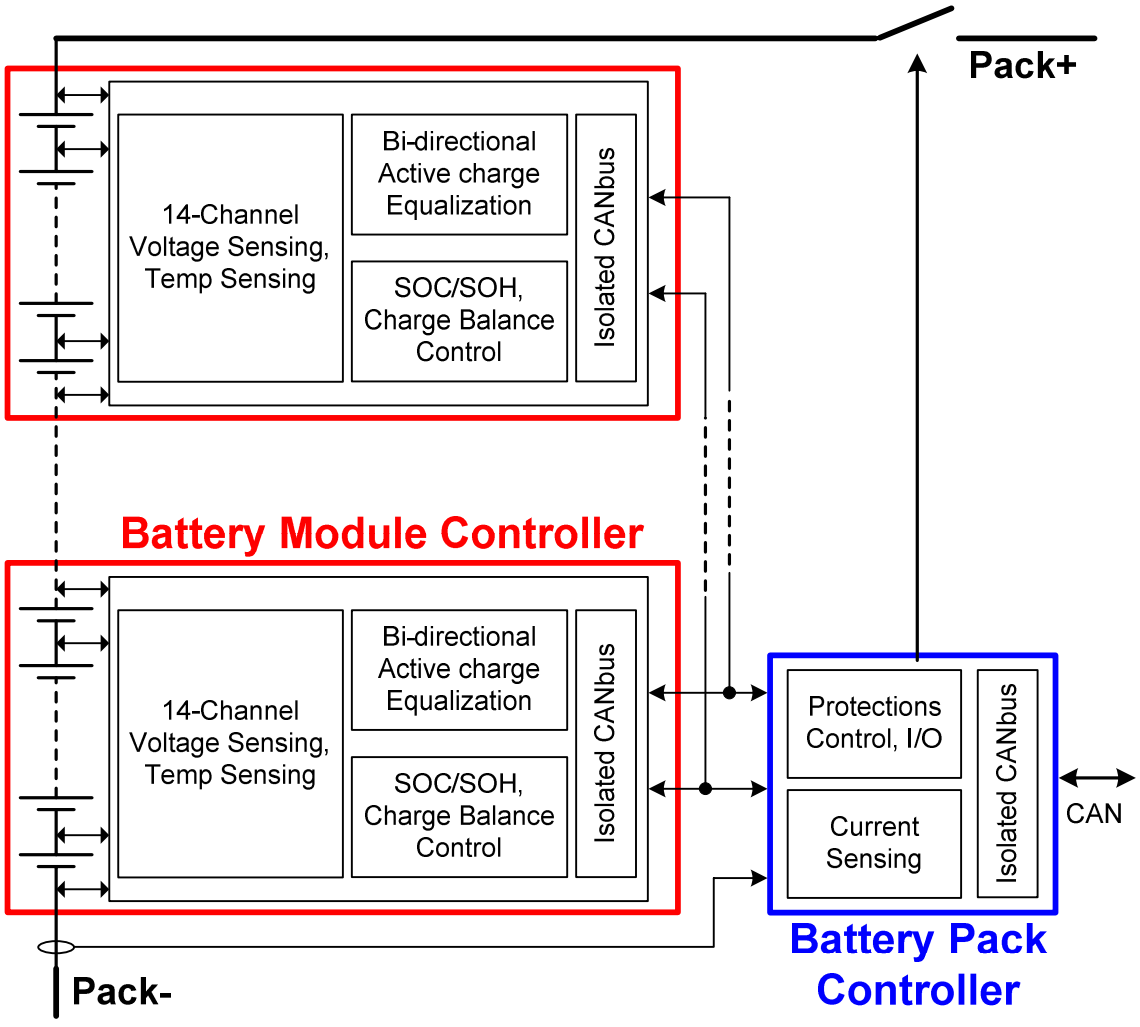

Figure 5.2 Proposed BMS configuration.

Figure 5.2 shows the configuration of the proposed BMS. It consists of module controllers, which manage up to twelve series connected battery cells, and central controller which manages the series connected battery modules, reports cell status and control the relays to protect the battery pack from over-charging or under-charging conditions. High voltage isolated CAN bus is used to communicate between the module controllers and central controller.

5.3 SOC Estimation

Table 5.1 Comparison of different SOC estimation schemes

Technique	Summarized Features	Pros	Cons
Discharge	Discharge with DC current and measure time to a certain threshold	Most accurate	Offline Time consuming
Coulomb counting	Counting charges that have been injected/pumped out of battery	Online Easy	Loss model Need accuracy
Open circuit voltage	VOC-SOC look-up table	Online Accurate	Time consuming
Artificial neural network	Adaptive artificial neural network system	Online	Training data needed
Impedance	Impedance of the battery (RC combination)	Online SOC and SOH	Cost Temp-sensitive
DC resistance	R_{dc}	Online Easy	Cost Temp-sensitive
Kalman filter	Get accurate information out of inaccurate data using Kalman filter	Online Dynamic	Large computing Model needed

SOC is a measure of the amount of electrochemical energy left in a cell or battery. It is expressed as a percentage of the battery capacity and indicates how much charges (energy) stored in an energy storage element. It has been a long-standing challenge for battery

industry to precisely estimate the SOC of lithium-ion batteries. The electrochemical reaction inside batteries is very complicated and hard to model electrically in a reasonably accurate way. So far, the state-of-the-art SOC accuracy for electric vehicle/plug-in hybrid EV (EV/PHEV) applications is in the range of 5%-10% [35]-[38].

Table 1.1 shows the comparison of different SOC estimation schemes. Among all the practical techniques, the Coulomb counting plus an accurate open-circuit voltage model is the algorithm being used here to estimate the SOC.

First, the initial SOC of the battery cell is established from look-up tables. The table consists of open circuit voltage and corresponding SOC information. An initial charge and discharge test cycle is necessary to generate such a look-up table. In the test cycle, the battery cell will perform a full 0.1C charging and discharging cycle. Two open circuit voltages, V_{charge} and $V_{discharge}$, versus SOC curves are plotted and the open circuit voltage (VOC) will be the average of the V_{charge} and $V_{discharge}$, as shown in Figure 5.3(a). This process will be repeated at different temperatures to generate a set of look-up tables to accommodate different temperature situations, as shown in Figure 5.3(b).

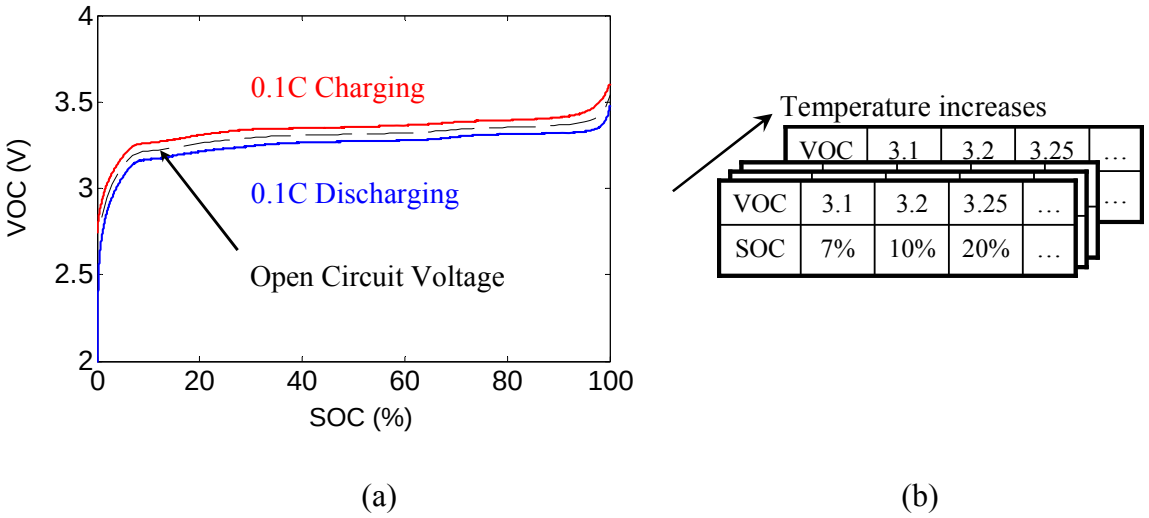

(a) (b)

Figure 5.3 (a) Open circuit voltage versus SOC curve. (b) SOC look-up tables for different temperatures.

Then, a Coulomb counter is initiated to count how many Coulombs of charge being pumped into or out of the battery cell. The Coulomb counter consists of an accurate battery current sense analog front end as well as a digital signal processing unit to perform the offset calibration as well as charge integration for coulomb counting purpose. Coulomb counting provides higher accuracy than most other SOC measurements since it measures the charge flow in and out of battery cell directly. However, it depends on the accuracy of the current measurement and does not take account of Columbic efficiency of the battery cell. Therefore, an accurate loss model is desired and necessary. The loss comes from different mechanisms, which includes physical resistance of the cathode, anode, metal materials, the lithium ion diffusion loss, as well as other chemical reaction thermal loss. An accurate model to include all these mechanisms is difficult to establish in reality. Hereby a combination of Coulomb counting with SOC adjustment by open circuit voltage look-up table method is applied. During battery charging or discharging, Coulomb counting is used to estimate the change of SOC for its accurate measurement of direct charge flow. The SOC of start and end of charging or discharging is being calibrated by using open circuit voltage look up table. This method combines the advantage of relative higher accuracy of both Coulomb counting and open circuit voltage, but mitigate the slow response time of open circuit voltage scheme and lacking relative reference point of Coulomb counting method.

5.4 Charge Equalization

Due to inevitable differences in chemical and electrical characteristics from manufacturing, aging, and ambient temperatures, there are SOC or capacity imbalances between battery cells. When these unbalanced batteries are left in use without any control, such as cell equalization, the energy storage capacity decreases severely. Thus, charge equalization for a series connected battery string is necessary to minimize the mismatches across all the cells and extend the battery lifecycle. Charge balancing methods can be classified into two categories: active and passive.

Active cell balancing helps balance the cells in a battery module to maintain the same voltage or SOC by monitoring and injecting appropriate balancing current into individual battery cell based on the balancing scheme. Compared with the traditional passive cell

balancing approach, the active cell balancing offers the advantage of high system efficiency and fast balancing time.

An inductive based active cell balancing scheme similar to the design in [27] is applied in this work to perform the cell equalization and mitigate the SOC mismatches among the cells. The unidirectional dc-dc converter is replaced by an isolated bidirectional dc-dc converter. The isolated bidirectional dc-dc converter regulates from the 12 cell battery stack voltage to each individual cell voltage. The average current mode control is employed such that the average inductor current is regulated to the command current which is set by the active cell balancing control algorithm. The voltage measurement circuit senses and converts all cell voltages into digital domain. Depend on the active cell balancing control algorithm, the battery cells could be balanced by targeting either towards the same SOC. The algorithm built into the embedded microcontroller determines which cells need to be injected with extra charges, the amount of injection current, the duration of the injection time and the sequence of the injection.

At the beginning of each balancing cycle, all battery cell voltages are measured and the digitized voltages are sent to the computation unit (customized logic or micro processor based unit). The computation unit then determines how much extra charge each battery cell needs and sends commands to the switch matrix to open the associated switches at certain time and sequence to perform the active cell balancing. Soft-start inductor current ramp and soft-shutdown inductor current ramp is added in the command current to avoid the overstress of the switching devices and potential saturation of the magnetic components.

5.5 System Control and Power Management

The battery pack consists of three series connected battery modules. Each battery module consists of twelve series connected battery units which have four parallel connected battery cells (= 2.3 Ah × 4) in one unit, as shown in Figure 5.4. The total energy capacity of the battery pack consisting of three series-connected battery modules is W = 1.09 kWh (= 2.3 Ah × 4 × 12 × 3 × 3.3 V). The dc voltage range is from 108 to 129.6 V (Assume working cell voltage is from 3.0 to 3.6 V).

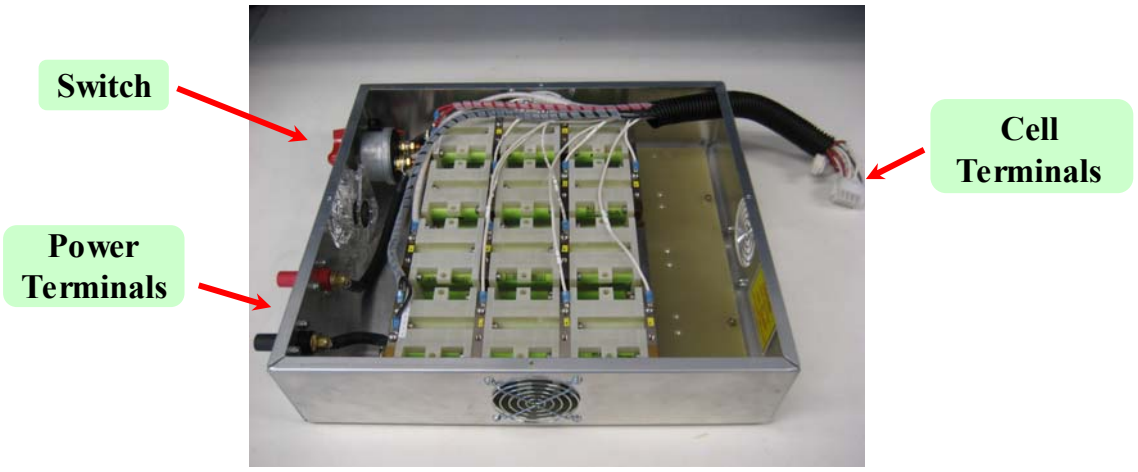

Figure 5.4 One battery module in the box.

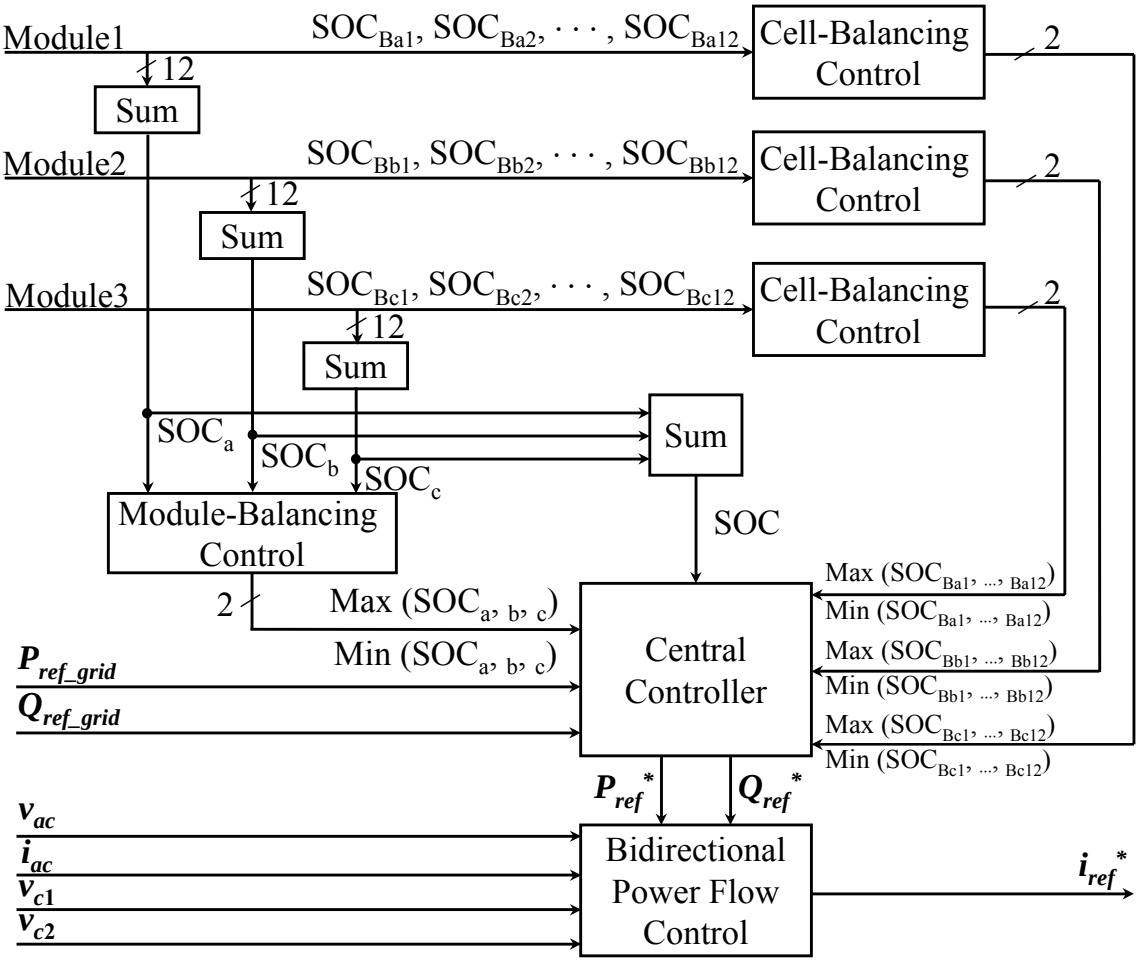

Figure 5.5 Control block diagram for the battery energy storage system

Figure 5.5 shows the control block diagram of the battery energy storage system. The whole control consists of three subcontrols: 1) central control; 2) bidirectional power flow control; 3) SOC balancing control.

The bidirectional power flow control is presented in Chapter 4. The SOC balancing control consists of cell-balancing control and module-balancing. The target of the cell-balancing control is to keep each of the 12-cell SOC values in a module (for example, SOC_{Ba1}, SOC_{Ba2}, ···, SOC_{Ba12}) equal to the mean SOC value of the corresponding module (SOC_{Ba}) shown in . Similarly, the target of module-balancing control is to keep each of the three module SOC values in a pack (SOC_a, SOC_b, ···, SOC_c) equal to the mean SOC value of the pack (SOC_{abc})

$$\begin{bmatrix} SOC_{Ba} \\ SOC_{Bb} \\ SOC_{Bc} \end{bmatrix} = \frac{1}{12}\begin{bmatrix} SOC_{Ba1} + SOC_{Ba2} + \cdots + SOC_{Ba12} \\ SOC_{Bb1} + SOC_{Bb2} + \cdots + SOC_{Bb12} \\ SOC_{Bc1} + SOC_{Bc2} + \cdots + SOC_{Bc12} \end{bmatrix} \tag{4.21}$$

$$SOC_{abc} = \frac{1}{3}(SOC_a + SOC_b + SOC_c) \tag{4.22}$$

$$\begin{bmatrix} SOC_a \\ SOC_b \\ SOC_c \end{bmatrix} = \begin{bmatrix} SOC_{Ba1} + SOC_{Ba2} + \cdots + SOC_{Ba12} \\ SOC_{Bb1} + SOC_{Bb2} + \cdots + SOC_{Bb12} \\ SOC_{Bc1} + SOC_{Bc2} + \cdots + SOC_{Bc12} \end{bmatrix} \tag{4.23}$$

$$SOC = SOC_a + SOC_b + SOC_c . \tag{4.24}$$

The central controller has three main inputs: P_{ref_grid} and Q_{ref_grid} commands from the grid and SOC estimation from the battery pack. When P_{ref_grid} is too large and beyond battery pack's capability, SOC will take charge of the control. Otherwise, P_{ref_grid} will be taken as the control reference.

The inputs Max ($SOC_{a, b, c,}$) and Min ($SOC_{a, b, c,}$) of the central controller are used to limit the power in and out of the battery pack. In case the total SOC meets the power transferring requirement but the three battery modules are not balanced very well, then

the maximum power transferred from battery pack to grid is limited by Min ($SOC_{a, b, c,}$) and the maximum power transferred from grid to battery pack is limited by Max ($SOC_{a, b, c,}$). The inputs Max ($SOC_{Ba1, \cdots, Ba12}$), Min ($SOC_{Ba1, \cdots, Ba12}$), Max ($SOC_{Bb1, \cdots, Bb12}$), Min ($SOC_{Bb1, \cdots, Bb12}$), Max ($SOC_{Bc1, \cdots, Bc12}$), and Min ($SOC_{Bc1, \cdots, Bc12}$) have the similar functions.

5.6 Experimental Results

This section shows the experimental results with the battery energy storage system at room temperature, which is around 20°C.

5.6.1 Battery Pack Charging and Discharging Waveforms

Figure 5.6 shows the experimental results when battery pack was repetitively charged to a SOC of 70% and discharged to a SOC of 30%. A wider window, for example, from 10% to 90%, may be used in an actual system. However, the lithium-ion batteries show longer lifecycle with a lower depth-of-discharge (DOD). The charging and discharging battery current is set at 9.2 A, which is equivalent to 1.0 C (= 9.2 A / 2.3 Ah / 4). The sampling rate of voltage and SOC is 2/s.

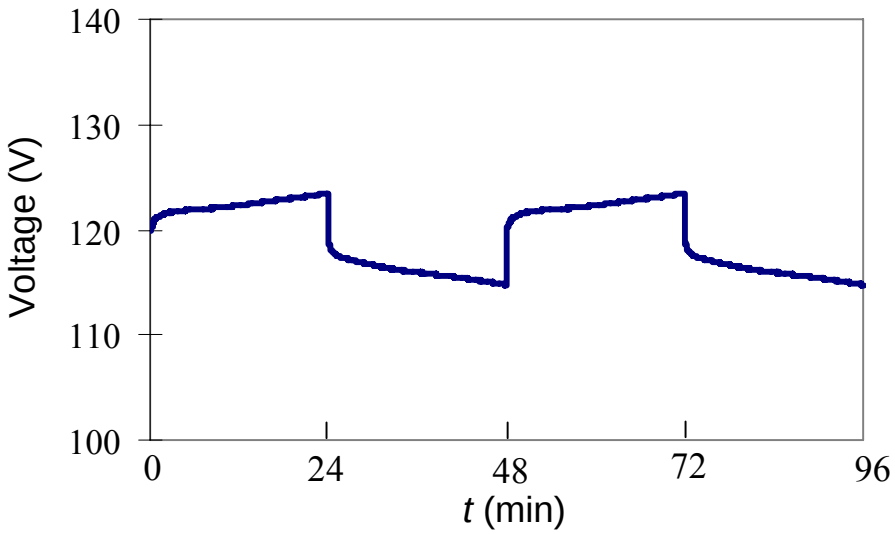

(a)

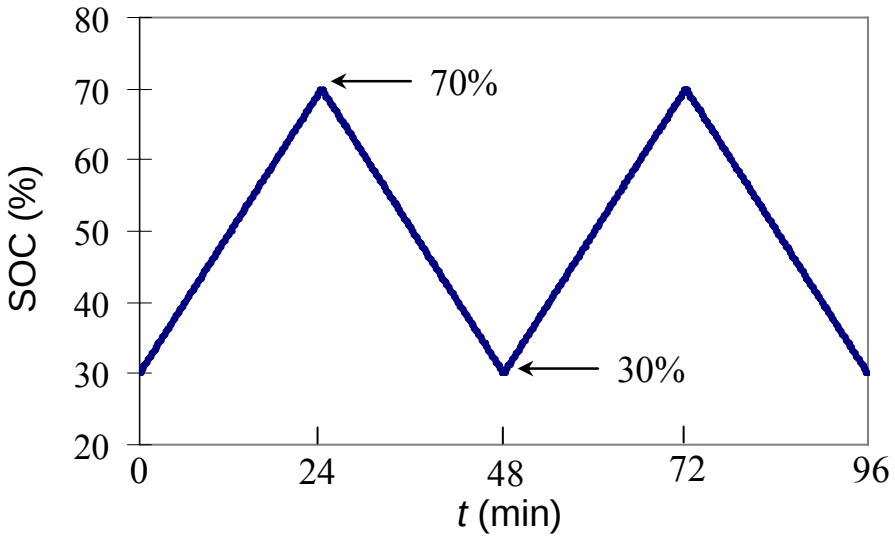

(b)

Figure 5.6 Experimental results of repetitively charging and discharging of the battery pack with a SOC between 30% and 70%. (a) Voltage versus time. (b) SOC versus time

5.6.2 Effectiveness of the SOC Balancing Control

The SOC balancing control is to keep each of the twelve unit SOC values in a module equal to the mean SOC value of the corresponding module. In the experiment, each unit consists of four parallel connected cells except one unit is configured to have three parallel connected cells. Thus there is a 25% capacity mismatch inside the module.

Figure 5.7 shows the test results with SOC balancing and without SOC balancing. For the test without SOC balancing, all the twelve units are charged up to 100% SOC in the initial point. For 1 C discharging, the total time for discharging the module from 100% SOC to 0 % is limited by the unit consisting of three parallel connected cells, which is around 45 minutes. For 1 C charging, the total time for charging the module from 0% SOC to 100 % is limited by the unit consisting of three parallel connected cells, which is also about 45 minutes. For the testing with SOC balancing, the corresponding discharging and charging time are both 55 minutes. It can be concluded that the system with SOC balancing has 22% more capacity than the system without SOC balancing.

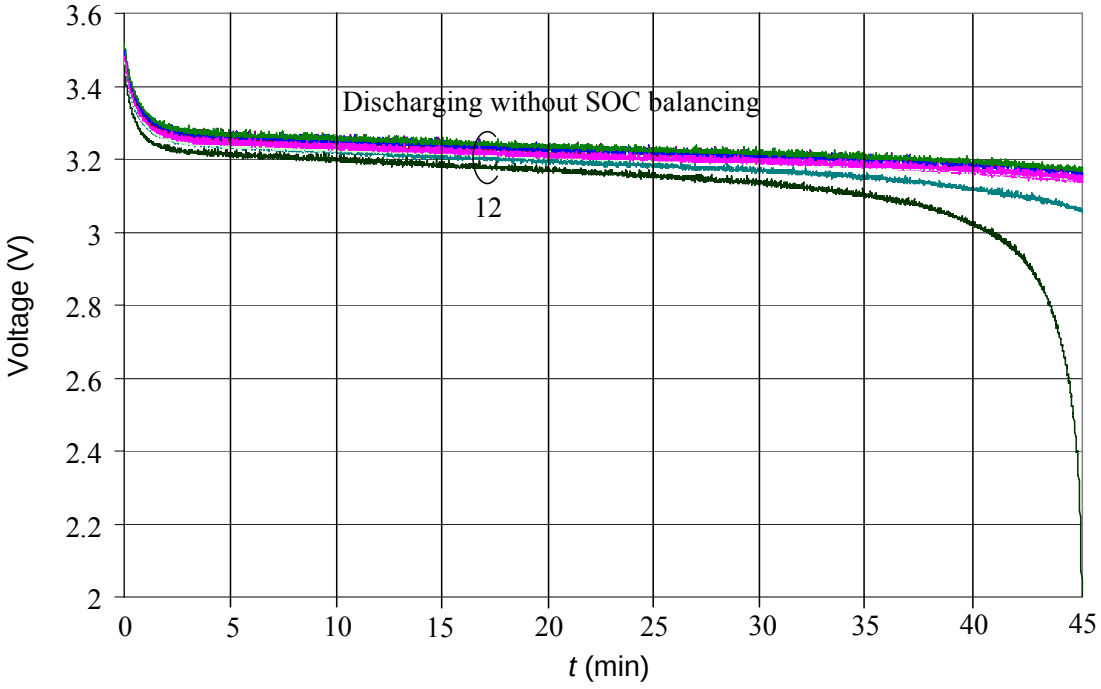
Discharging without SOC balancing
12
Voltage (V)
t (min)
3.6
3.4
3.2
3
2.8
2.6
2.4
2.2
2
0
5
10
15
20
25
30
35
40
45

(a)

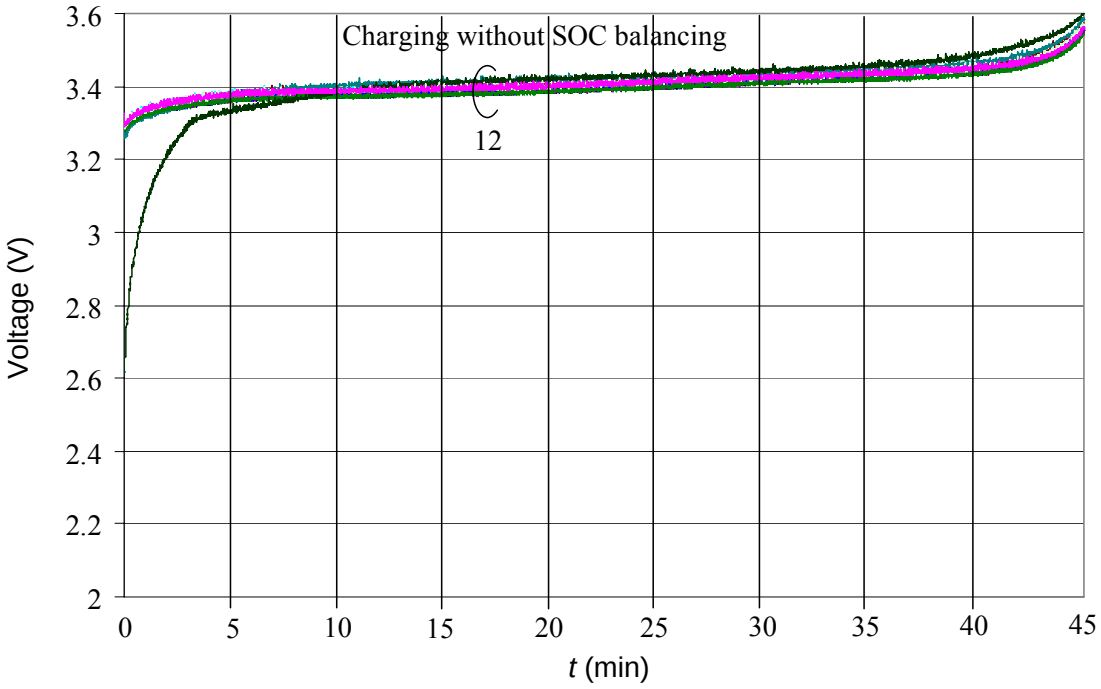
Charging without SOC balancing
12
Voltage (V)
t (min)
3.6
3.4
3.2
3
2.8
2.6
2.4
2.2
2
0
5
10
15
20
25
30
35
40
45

(b)

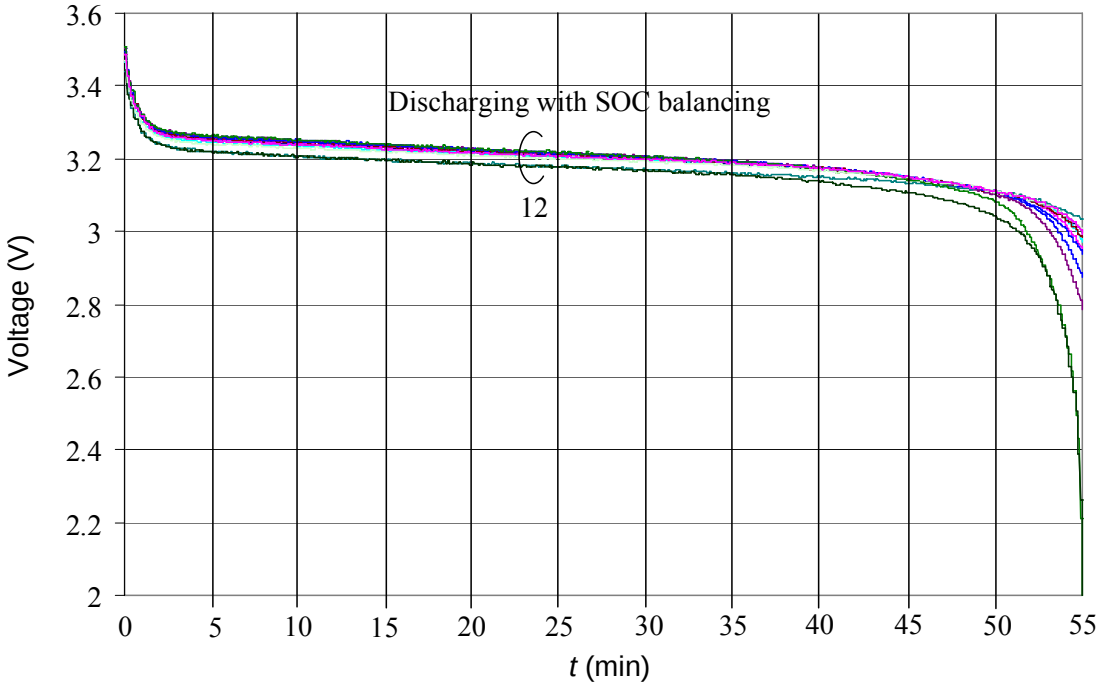

(c)

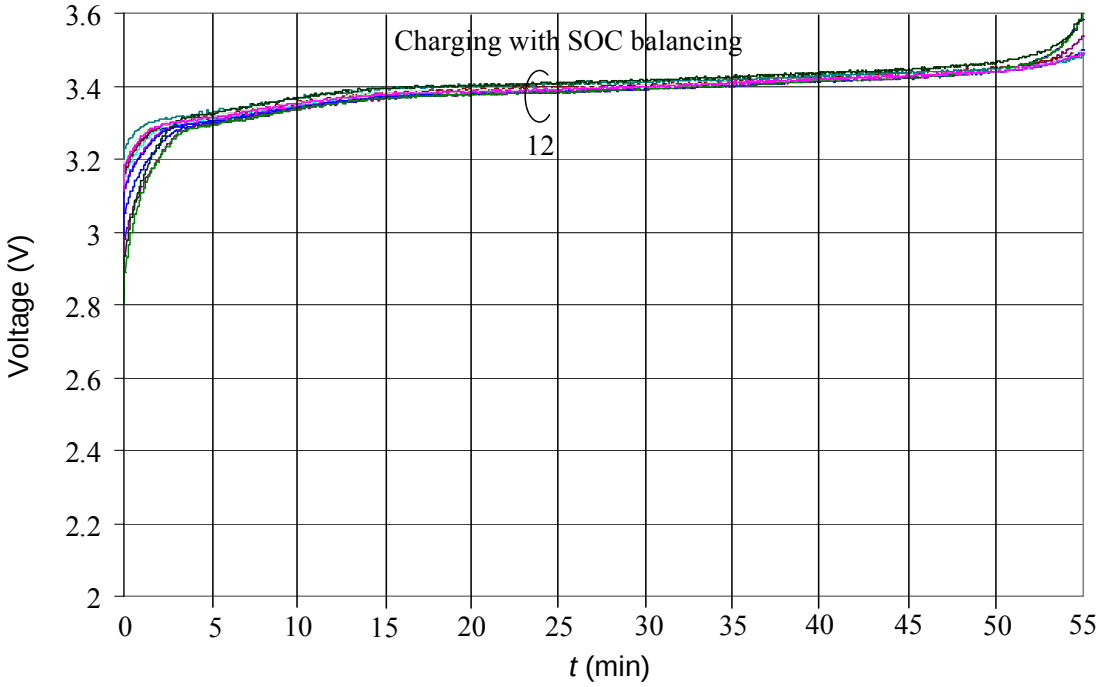

(d)

Figure 5.7 Experimental results of discharging and charging of one battery module. (a) Discharging without SOC balancing control. (b) Charging without SOC balancing control. (c) Discharging with SOC balancing control. (d) Charging with SOC balancing control.

In actual system, a SOC window between 30% and 70% may be used to extend battery cycle life time. For 1 C discharging without SOC balancing, the time for discharging the module from 70% SOC to 30 % is around 18 minutes. The time for charging the module from 30% SOC to 70 % is about 18 minutes. For the testing with SOC balancing, the corresponding discharging and charging time are both 24 minutes. It can be concluded that the system with SOC balancing has gained 33% more capacity than the system without SOC balancing when the SOC is between 30% and 70%. Without SOC balancing, lower capacity battery units in a battery module can be easily damaged with a higher DOD.

5.6.3 System Efficiency

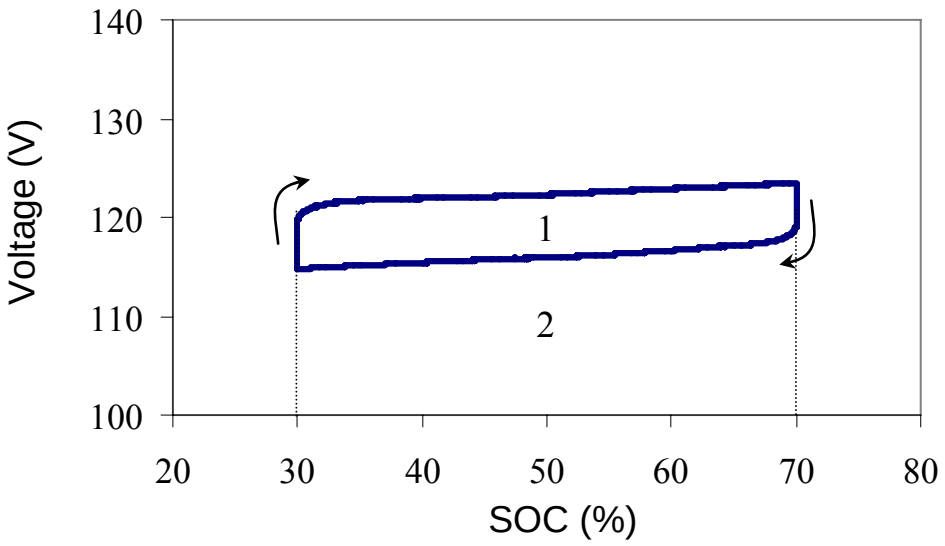

Figure 5.8 Experimental results of repetitively charging and discharging of the battery pack with SOC ranging between 30% and 70%.

For 1 C charging and discharging, the relationship between battery pack voltage and SOC is shown in Figure 5.8. The arrows show the charging and discharging directions. The area 1 inside the curve is the relative losses when the battery pack is charged from 30% SOC to 70% SOC and discharged back to 30%. The losses consist of battery loss

and BMS loss. The round-trip efficiency is 96.5% for the battery pack. The overall round-trip efficiency for the battery energy storage system consisting of battery pack with associated BMS and bidirectional ac-dc converter is 92.6%.

5.7 Summary

In this chapter, a high-efficiency grid-tie lithium-ion battery based energy storage system is presented. The system consists of three subsystems, a $LiFePO_4$ battery pack and associated BMS, a bidirectional ac-dc converter, and the central control unit which controls the operation mode and grid interface of the energy storage system.

The designed BMS monitors and reports all battery cells parameters in the pack, these include cell voltage, temperature, and charging and discharging current. Based on these parameters, the BMS controller estimates the SOC of each battery cell in the pack by using the Coulomb counting plus an accurate open-circuit voltage model. The SOC information is then used to control the isolated bidirectional dc-dc converter based active cell balancing circuits to mitigate the mismatch among the series connected cells. The SOC and SOH information is also used by the central control unit to determine the operating mode of the energy storage system. Using the proposed SOC balancing technique, the entire battery storage system has demonstrated more capacity than the system without SOC balancing. Under the charging condition from 0 to 100% SOC and discharging condition from 100% SOC to 0, the use of SOC balancing technique has 22% more capacity. Under the charging condition from 30% to 70% SOC and discharging condition from 70% to 30% SOC, the use of SOC balancing technique has 33% more capacity.

The overall round-trip efficiency for the battery energy storage system consisting of battery pack with associated BMS and bidirectional ac-dc converter is 92.6%.

Chapter 6 Conclusions and Future Work

6.1 Summary

This dissertation proposed a high-efficiency grid-tie lithium-ion battery based energy storage system. The system consists of three subsystems, a $LiFePO_4$ battery pack and associated BMS, a bidirectional ac-dc converter, and the central control unit which controls the operation modes and grid interface of the energy storage system. The BMS controller monitors the parameters of each battery cell and applies the charge equalization circuits to mitigate the mismatch among the series connected battery cells. The bidirectional ac-dc converter works as the interface between the battery pack and the ac grid, which needs to meet the requirements of bidirectional power flow capability and to ensure high power factor and low THD as well as regulate the dc side power regulation. The central control unit communicates with the battery management system and bidirectional ac-dc converter. It combines the SOC information and power command coming from the grid side to control the bidirectional power flow between ac grid and dc battery energy storage.

The following conclusions are drawn from the work.

1). Dual-buck converter based single-phase bidirectional ac-dc converter is proposed. The converter exhibits two distinct merits: first, there is no shoot-through issue because no active power switches are connected in series in each phase leg; second, the reverse recovery dissipation of the power switch is greatly reduced because there is no freewheeling current flowing through the body diode of power switches.

- A new SPWM scheme by using split SPWM as the main scheme and joint SPWM as the supplementary scheme for the zero-crossing region is proposed. On one hand, since split SPWM is utilized as the main scheme, conduction and switching losses are relatively low. On the other hand, because joint SPWM is employed for the zero-crossing region, the ac current becomes continues.

- The utilization of the magnetic components is improved by employing different coupled inductor structures. One is employing one coupled inductor in series with small inductors and the other one is utilizing two coupled inductors in series.

Overall, the implemented converter efficiency peaks at 97.8% at 50-kHz switching frequency for both rectifier and inverter modes.

2). To better utilize the dc bus voltage and eliminate the two dc bus capacitors, a novel bidirectional ac-dc converter is proposed by replacing the two-capacitor leg of the dual-buck converter based single-phase bidirectional ac-dc converter with a two-switch leg. The novel bidirectional ac-dc converter keeps the merits of the dual-buck converter based bidirectional ac-dc converter. Meanwhile the two large dc bus capacitors and related voltage-balancing control are eliminated.

- The utilization of the magnetic components is improved by integrating transformers and inductors on the same core. Two different structures of magnetic integration are presented. One is employing one coupled inductor in series with small inductors and the other one is utilizing two coupled inductors in series.
- Three novel three-phase bidirectional ac-dc converter topologies are proposed. They all preserve the merits of the novel single-phase bidirectional ac-dc converter with free of shoot through problems.

3). In order to control the bidirectional power flow and at the same time stabilize the system in mode transition, a unified digital controller is proposed.

- The power stage small-signal model is derived for the dual-buck converter based single-phase bidirectional ac-dc converter.
- Based on the small-signal model, an admittance compensator along with a QPR controller is adopted to allow smooth startup and elimination of the steady-state error over the entire load range.
- The proposed QPR controller is designed and implemented with a digital controller. Then the coefficients of the digital controller are truncated into certain word length binary representation, so as to be fit to the numbers of bits available to the FPGA for variables and constants.

The entire system has been simulated in both PSIM and Simulink and verified with hardware experiments. Small transient currents are observed with the power transferred from rectifier mode to inverter mode at peak current point and also from inverter mode to rectifier mode at peak current point.

4). A BMS is designed to monitor and balance each battery cell in the pack.

- The designed BMS monitors and reports all battery cells parameters such as cell voltage, temperature, and charging and discharging current. Based on these parameters, the BMS controller estimates the SOC of each battery cell in the battery pack by using the Coulomb counting plus an accurate open-circuit voltage model.
- The SOC information is used to control the isolated bidirectional dc-dc converter based active cell balancing circuits to mitigate the mismatch among the series connected cells. The SOC and SOH information is also used by the central control unit to determine the operating mode of the energy storage system.

Using the proposed SOC balancing technique, the entire battery storage system has demonstrated more capacity than the system without SOC balancing. Under the charging condition from 0 to 100% SOC and discharging condition from 100% SOC to 0, the use of SOC balancing technique has 22% more capacity. Under the charging condition from 30% to 70% SOC and discharging condition from 70% to 30% SOC, the use of SOC balancing technique has 33% more capacity. The round-trip efficiency is 96.5% for the battery pack. The overall round-trip efficiency for the battery energy storage system consisting of battery pack with associated BMS and bidirectional ac-dc converter is 92.6%.

6.2 Future Work

(1) A battery energy storage system that contains a single-phase bidirectional ac-dc converter tends to inject or draw an ac ripple current at twice the ac frequency. Although the battery current does not change the direction, such a ripple current may shorten battery life span. One approach is to modify the single-phase bidirectional ac-dc

converter topology to reduce the amplitude of the ac ripple current. Another approach is to add an additional bidirectional dc-dc converter stage to smooth the ac ripple current.

(2) A unified current controller is adopted to control the bidirectional power flow and at the same time stabilize the system in mode transition. A voltage control scheme needs to be developed for voltage mode charging or discharging when the SOC of the battery pack reaches 0% or 100%.

(3) When the grid is abnormal, the microgrid formed by the battery energy storage system needs to disconnect from the main grid while supporting critical loads. A smooth transitioning control scheme needs to be developed and further investigated to offer the battery energy storage system the capability to switch between grid-tie and islanding modes.

References

[1] E. Barklund, N. Pogaku, M. Prodanovic, C. Hernandez-Aramburo, and T. C. Green, "Energy Management in Autonomous Microgrid Using Stability-Constrained Droop Control of Inverters," *IEEE Trans. Power Electron.,* vol. 23, no. 5, pp. 2346–2352, Sep. 2008.

[2] Y. A.-R. I. Mohamed, and E. F. El-Saadany, "Adaptive Decentralized Droop Controller to Preserve Power Sharing Stability of Paralleled Inverters in Distributed Generation Microgrids," *IEEE Trans. Power Electron.,* vol. 23, no. 6, pp. 2806–2816, Nov. 2008.

[3] Y. W. Li, and C.-N. Kao, "An Accurate Power Control Strategy for Power-Electronics-Interfaced Distributed Generation Units Operating in a Low-Voltage Multibus Microgrid," *IEEE Trans. Power Electron.,* vol. 24, no. 12, pp. 2977–2988, Dec. 2009

[4] Z. Chen, J. M. Guerrero, and F. Blaabjerg "A Review of the Stage of the Art of Power Electronics for Wind Turbines," *IEEE Trans. Power Electron.,* vol. 24, no. 8, pp. 1859–1875, Aug. 2009.

[5] A. Timbus, M. Liserre, R. Teodorescu, P. Rodriguez, and F. Blaabjerg "Evaluation of Current Controllers for Distributed Power Generation Systems," *IEEE Trans. Power Electron.,* vol. 24, no. 3, pp. 654–664, Mar. 2009.

[6] F. Blaabjerg, R. Teodorescu, M. Liserre, and A. V. Timbus, "Overview of Control and Grid Synchronization for Distributed Power Generation Systems," *IEEE Trans. Ind. Electron.,* vol. 53, no. 5, pp. 1398–1409, Oct. 2006.

[7] N. Stretch, and N. Kazerani, "A Stand-Alone, Split-Phase Current-Sourced Inverter With Novel Energy Storage," *IEEE Trans. Power Electron.,* vol. 23, no. 6, pp. 2766–2774, Nov. 2008.

[8] H. Krishnaswami, and N. Mohan, "Three-Port Series-Resonant DC-DC Converter to Interface Renewable Energy Sources With Bidirectional Load and Energy Storage Ports," *IEEE Trans. Power Electron.,* vol. 24, no. 10, pp. 2289–2297, Oct. 2009.

[9] A. Payman, S. Piefederici and F. Meibody-Tabar, “Energy Management in a Fuel Cell/Supercapacitor Multisource/Multiload Electrical Hybrid System,” *IEEE Trans. Power Electron.,* vol. 24, no. 12, pp. 2681–2691, Dec. 2009.

[10] C. Zhao, S. D. Round and J. W. Kolar, “An Isolated Three-Port Bidirectional DC-DC Converter With Decoupled Power Flow Management,” *IEEE Trans. Power Electron.,* vol. 23, no. 5, pp. 2443–2453, Sep. 2008.

[11] L. Maharjan, T. Yamagishi, H. Akagi, and J. Asakura, “Fault-Tolerant Operation of a Battery-Energy-Storage System Based on a Multilevel Cascade PWM Converter With Star Configuration,” *IEEE Trans. Power Electron.,* vol. 25, no. 9, pp. 2386–2396, Sep. 2010.

[12] L. Maharjan, S. Inoue, and H. Akagi, “A Transformerless Energy Storage System Based on a Cascade Multilevel PWM Converter With Star Configuration,” *IEEE Trans. Ind. Electron.,* vol. 44, no. 5, pp. 1621–1630, Sep. 2008.

[13] R.-Y. Kim, J.-S. Lai, B. York, and A. Koran, “Analysis and Design of Maximum Power Point Tracking Scheme for Thermoelectric Battery Energy Storage System,” *IEEE Trans. Ind. Electron.,* vol. 56, no. 9, pp. 3709–3716, Sept. 2009.

[14] K. Jin, X. Ruan, M. Yang, and M. Xu, “Power Management for Fuel-Cell Power System Cold Start,” *IEEE Trans. Power Electron.,* vol. 24, no. 10, pp. 2391–2395, Oct. 2009.

[15] F. Z. Peng, M. Shen, and K. Holland, “Application of Z-Source Inverter for Traction Drive of Fuel Cell-Battery Hybrid Electric Vehicles,” *IEEE Trans. Power Electron.,* vol. 22, no. 3, pp. 1054–1061, May 2007.

[16] S. J. Chiang, K. T. Chang, and C. Y. Yen, “Residential Photovoltaic Energy Storage System,” *IEEE Trans. Ind. Electron.,* vol. 45, no. 3, pp. 385–394, Jun. 1998.

[17] Y.-K. Lo, T.-P. Lee, and K.-H. Wu, “Grid-Connected Photovoltaic System With Power Factor Correction,” *IEEE Trans. Ind. Electron.,* vol. 55, no. 5, pp. 2224–2227, May 2008.

[18] H.-S. Park, C.-E. Kim, C.-H. Kim, G.-W. Moon and J.-H. Lee, “A Modularized Charge Equalizer for an HEV Lithium-Ion Battery String,” *IEEE Trans. Ind. Electron.,* vol. 56, no. 5, pp. 1464–1476, May. 2009.

[19] Y.-S. Lee and M.-W. Cheng, “Intelligent control Battery Equalization for Series

Connected Lithium-ion Battery Strings," *IEEE Trans. Ind. Electron.,* vol. 52, no. 5, pp. 1297–1307, Oct. 2005.

[20] Y.-S. Lee and G.-T. Cheng, "Quasi-Resonant Zero-Current-Switching Bidirectional Converter for Battery Equalization Applications," *IEEE Trans. Power Electron.,* vol. 21, no. 5, pp. 1213–1224, Sep. 2006.

[21] L. Maharjan, S. Inoue, H. Akagi, and J. Asakura, "State-of-Charge (SOC)-Balancing Control of a Battery Energy Storage System Based on a Cascade PWM Converter," *IEEE Trans. Power Electron.,* vol. 24, no. 6, pp. 1628–1636, Jun. 2009.

[22] S. W. Moore and P. J. Schneider, "A Review of Cell Equalization Methods for Lithium ion and Lithium Polymer Battery Systems," in *Proc. SAE 2001 World Congr.*, Detroit, MI, Mar. 2001, Doc. 2001-01-0959.

[23] G. R. Stanley, and K. M. Bradshaw, "Precision DC-to-AC Power Conversion by Optimization of the Output Current Waveform-The Half Bridge Revisited," *IEEE Trans. Power Electron.,* vol. 14, no. 2, pp. 372–380, Mar. 1999.

[24] J. Liu, and Y. Yan, "A Novel Hysteresis Current Controlled Dual Buck Half Bridge Inverter," in *Proc. IEEE PESC*, Acapulco, Mexico, Jun. 2003, pp. 1615-1620.

[25] Z. Yao, L. Xiao, and Y. Yan, "Control Strategy for Series and Parallel Output Dual-Buck Half Bridge Inverters Based on DSP Control," *IEEE Trans. Power Electron.,* vol. 24, no. 2, pp. 434–444, Feb. 2009.

[26] Z. Yao, L. Xiao, and Y. Yan, "Dual-Buck Full-Bridge Inverter With Hysteresis Current Control," *IEEE Trans. Ind. Electron.,* vol. 56, no. 8, pp. 3153–3160, Aug. 2009.

[27] H. Qian, J. Zhang, J.-S. Lai, and W. Yu, "A High-Efficiency Grid-Tie Battery Energy Storage System," *IEEE Trans. Power Electron.,* vol. 26, no. 3, pp. 886–896, Mar. 2011.

[28] H. Qian, J.-S. Lai, J. Zhang, and W. Yu, "High-Efficiency Bidirectional AC-DC Converter for Energy Storage Systems," in *Proc. IEEE ECCE*, Atlanta, GA, Sep. 2010, pp. 3224-3229.

[29] H. Qian, J. Zhang, and J.-S. Lai, "A Grid-Tie Battery Energy Storage System," in *Proc. IEEE COMPEL'*2010, Boulder, CO, Jun. 2010, pp. 1-5.

[30] I.-S. Kim, "Nonlinear State of Charge Estimator for Hybrid Electric Vehicle

Battery," *IEEE Trans. Power Electron.,* vol. 23, no. 4, pp. 2027–2034, Jul. 2008.

[31] I.-S. Kim, "A Technique for Estimating the State of Health of Lithium Batteries Through a Dual-Sliding-Mode Observer," *IEEE Trans. Power Electron.,* vol. 25, no. 4, pp. 1013–1022, Apr. 2010.

[32] Y. -S. Lee, W. -Y. Wang, and T. -Y. Kuo, "Soft Computing for Battery State-of-Charge (BSOC) Estimation in Battery String Systems," *IEEE Trans. Ind. Electron.,* vol. 55, no. 1, pp. 229–239, Jan. 2008.

[33] M. Coleman, C. K. Lee, C. Zhu, and W. G. Hurley, "State-of-Charge Determination From EMF Voltage Estimation: Using Impedance, Terminal Voltage, and Current for Lead-Acid and Lithium-Ion Batteries," *IEEE Trans. Ind. Electron.,* vol. 54, no. 5, pp. 2550–2557, Oct. 2007.

[34] B. Lindemark, "Individual Cell Voltage Equalizers (ICE) for reliable battery performance," in *Proc. 13th Annu. Int. Telecommum. Energy Conf.*, Kyoto, Japan, Nov. 1991, pp. 196-201.

[35] V. L. Teofilo, L. V. Merritt, and R. P. Hollandsworth, "Advanced Lithium Ion Battery Charger," *IEEE Aerosp. Electron. Syst. Mag.,* vol. 12, no. 11, pp. 30–36, Nov. 1997.

[36] N. H. Kutkut, H. L. N. Wiegman, D. M. Divan, and D. W. Novotny, "Design Considerations for Charge Equalization of an Electric Vehicle Battery System," *IEEE Trans. Ind. Appl.*, vol. 35, no. 1, pp. 28–35, Jan./Feb. 1999.

[37] J. Cao, N. Schofield, and A. Emadi, "Battery Balancing Methods: A Comprehensive Review," in *Proc. IEEE Vehicle Power and Propuls. Conf.*, Harbin, China, Sep. 2008, pp. 1-6.

[38] N. H. Kutkut, "Non-Dissipative Current Diverter Using a Centralized Multi-Winding Transformer," in *Proc. 28th IEEE Power Electron. Spec. Conf.*, St. Louis, MO, Jun. 1997, pp. 648-654.

[39] N. H. Kutkut, "A Modular Non Dissipative Current Diverter for EV Battery Charge Equalization," in *Proc. 13th Annu. IEEE Appl. Power Electron. Conf. Expo.*, Anaheim, CA, Feb. 1998, pp. 686–690.

[40] J. Chatzakis, K. Kalaitzakis, N. C. Voulgaris, and S. N. Manias, "Designing a New Generalized Battery Management System," *IEEE Trans. Ind. Electron.*, vol. 50, no.

5, pp. 990–999, Oct. 2003.

[41] B. Singh, B. N. Singh, A. Chandra, K. Al-Haddad, A. Pandey, and D. P. Kothari, "A Review of Single-Phase Improved Power Quality AC-DC Converters," *IEEE Trans. Ind. Electron.*, vol. 50, no. 5, pp. 962–981, Oct. 2003.

[42] K. Thiyagarajah, V. T. Ranganathan, and B. S. Ramakrishna Iyengar, "A high switching frequency IGBT PWM rectifier/inverter system," *IEEE Trans. Power Electron.*, vol. 6, pp. 576–584, Oct. 1991.

[43] J. Chen and D. M. Divan, "Simple topologies for single phase AC line conditioning," *IEEE Trans. Ind. Applicat.*, vol. 30, pp. 406–412, Mar./Apr. 1994.

[44] V. R. Kanetkar and G. K. Dubey, "Current controlled boost-type single phase voltage source converters for bi-directional power flow," *IEEE Trans. Power Electron.*, vol. 12, pp. 269–277, Mar. 1997.

[45] V. R. Kanetkar and G. K. Dubey, "Series equivalence/operation of current-controlled boost-type single-phase voltage source converters for bi-directional power flow," *IEEE Trans. Power Electron.*, vol. 12, pp. 278–286, Mar. 1997.

[46] D. Shmilovitz, D. Czarkowski, Z. Zabar, and S. Y. Yoo, "A novel single stage unity power factor rectifier/inverter for UPS applications," in *Proc. IEEE INTELEC'98*, 1998, pp. 762–769.

[47] D. Shmilovitz, D. Czarkowski, Z. Zabar, and S. Zou, "A novel reversible boost rectifier with unity power factor," in *Proc. IEEE APEC'99*, 1999, pp. 363–368.

[48] D. K. Jackson and S. B. Leeb, "A power factor corrector with bi-directional power transfer capability," in *Proc. IEEE PESC'00*, vol. I, 2000, pp. 365–370.

[49] S. Y. R. Hui, H. Chung, and S. C. Yip, "A bidirectional ac-dc power converter with power factor correction," *IEEE Trans. Power Electron.*, vol. 15, pp. 942–948, Sept. 2000.

[50] S. K. Mazumder, A. H. Nayfet, and D. Boroyevich, "An investigation into the fast- and slow-scale instabilities of a single phase bidirectional boost converter," *IEEE Trans. Power Electron.*, vol. 18, no. 4, pp. 1063–1069, Jul. 2003

[51] S. C. Yip, D. Y. Qiu, H. S. Chung, and S. Y. R. Hui, "A novel voltage sensorless control technique for a bidirectional AC/DC converter," *IEEE Trans. Power Electron.*, vol. 18, no. 6, pp. 1346–1355, Nov. 2003.

[52] E. F. Vidal, and I. Barbi, “AC-DC Bidirectional Single-Phase Step-Down Converter with High Power Factor,” in *Proc. IEEE IECON’06*, Paris, France, Nov. 2006, pp. 2043–2048.

[53] Y.-J. Lee, A. Khaligh, and A. Emadi, “Advanced integrated bidirectional AC/DC and DC/DC converter for plug-in hybrid electric vehicles,” *IEEE Trans. Veh. Technol.*, vol. 58, no. 8, pp. 3970–3980, Oct. 2009.

[54] G. T. Kim and T. A. Lipo, “VSI-PWM rectifier/inverter system with a reduced switch count,” *IEEE Trans. Ind. Applicat.*, vol. 32, pp. 1331–1337, Nov./Dec. 1996.

[55] J.W. Choi and S. K. Sul, “Fast current controller in three-phase AC/DC boost converter using d-q axis crosscoupling,” *IEEE Trans. Power Electron.*, vol. 13, pp. 179–185, Jan. 1998.

[56] H. Mao, D. Boroyevich, and F. C. Lee, “Novel reduced-order small signal model of a three-phase PWM rectifier and its application in control design and system analysis,” *IEEE Trans. Power Electron.*, vol. 13, pp. 511–531, May 1998.

[57] P. Verdelho and G. D. Marques, “Four-wire current-regulated PWM voltage converter,” *IEEE Trans. Ind. Electron.*, vol. 45, pp. 761–770, Oct. 1998.

[58] C.-L. Chen, C.-M. Lee, R.-J. Tu, and G.-K. Horng, “A novel simplified space-vector-modulated control scheme for three-phase switch-mode rectifier,” *IEEE Trans. Ind. Electron.*, vol. 46, pp. 512–516, June 1999.

[59] D.-W. Chung and S.-K. Sul, “Minimum-loss strategy for three-phase PWM rectifier,” *IEEE Trans. Ind. Electron.*, vol. 46, pp. 517–526, June 1999.

[60] M.-T. Tsai and W. I. Tsai, “Analysis and design of three-phase AC-to-DC converters with high power factor and near-optimum feedforward,” *IEEE Trans. Ind. Electron.*, vol. 46, pp. 535–543, June 1999.

[61] H. Kömürcügil and O. Kükrer, “A novel current-control method for three-phase PWM AC/DC voltage-source converters,” *IEEE Trans. Ind. Electron.*, vol. 46, pp. 544–553, June 1999.

[62] H. S. Song and K. Nam, “Dual current control scheme for PWM converter under unbalanced input voltage conditions,” *IEEE Trans. Ind. Electron.*, vol. 46, pp. 953–959, Oct. 1999.

[63] S. Hansen, M. Malinowski, F. Blaabjerg, and M. P. Kazmierkowski, “Sensorless

control strategies for PWM rectifier," in *Proc. IEEE APEC'00*, 2000, pp. 832–838.

[64] R. Zhang, F. C. Lee, and D. Boroyevich, "Four-legged three-phase PFC rectifier with fault tolerant capability," in *Proc. IEEE PESC'00*, 2000, pp. 359–364.

[65] D.-C. Lee, G.-M. Lee, and K.-D. Lee, "DC-bus voltage control of three-phase AC/DC PWM converters using feedback linearization," *IEEE Trans. Ind. Applicat.*, vol. 36, pp. 826–833, May/June 2000.

[66] W. C. Lee, T. K. Lee, and D. S. Hyun, "Comparison of single-sensor current control in the DC link for three-phase voltage-source PWM converters," *IEEE Trans. Ind. Electron.*, vol. 48, pp. 491–505, June 2001.

[67] W. McMurray, "Resonant snubbers with auxiliary switches," *IEEE Trans. Ind. Appl.*, vol. 29, no. 2, pp. 355–362, Mar. 1993.

[68] R. W. De Doncker and J. P. Lyons, "Method for controlling a power converter using an auxiliary resonant commutation circuit," U.S. Patent 5 047 913, Sep. 10, 1991.

[69] J.-S. Lai, "Practical design methodology of auxiliary resonant snubber inverter," in *Proc. IEEE Power Electron. Spec. Conf.*, Baveno, Italy, Jun.1996, pp. 432–437.

[70] W. Dong, D. Peng, H. Yu, F. C. Lee, and J.-S. Lai, "A simplified control scheme for zero voltage transition (ZVT) inverter using coupled inductors," in *Proc. IEEE Power Electron. Spec. Conf.* Galway, Ireland, Jun. 2000, pp. 1221–1226.

[71] H. Yu, X. Huang, and J.-S Lai, "A novel load adaptive zero voltage switching utilizing diode reverse recovery current for soft-switching choppers and inverters," in *Proc. IEEE Power Electron. Spec. Conf.*, Vancouver, BC, Canada, Jun. 2001, pp. 146–151.

[72] J. P. Gegner and C. Q. Lee, "Zero-voltage-transition converters using inductor feedback techniques," in *Proc. IEEE Appl. Power Electron. Conf.*, Orlando, FL, Feb. 1994, pp. 862–868.

[73] X. Yuan and I. Barbi, "Analysis, designing, and experimentation of a transformer-assisted PWM zero-voltage switching pole inverter," *IEEE Trans. Power Electron.*, vol. 15, no. 1, pp. 72–82, Jan. 2000.

[74] K. M. Smith, Jr., and K. Smedley, "A comparison of voltage-mode soft switching methods for PWM converter," *IEEE Trans. Power Electron.*, vol. 12, no. 2, pp.

376–386, Mar. 1997.

[75] K. M. Smith, Jr., and K. Smedley, "Intelligent magnetic-amplifier controlled soft-switching method for amplifiers and inverters," *IEEE Trans. Power Electron.*, vol. 13, no. 1, pp. 84–92, Jan. 1998.

[76] J.-Y. Choi, D. Boroyevich, and F. C. Lee, "A novel ZVT three-phase inverter with coupled inductors," in *Proc. IEEE Power Electron. Spec. Conf.,* Charleston, SC, Jun. 1999, pp. 975–980.

[77] J.-S. Lai, R. W. Young, J. McKeever, and F. Z. Peng, "A delta configured auxiliary resonant snubber inverter," *IEEE Trans. Ind. Appl.*, vol. 32, no. 3, pp. 518–525, May/Jun. 1996.

[78] J.-S. Lai, J. Zhang, H. Yu, and H. E. Kouns, "Source and load adaptive design for a high-power soft-switching inverter," *IEEE Trans. Power Electron.*, vol. 21, no. 6, pp. 1667–1675, Nov. 2006.

[79] J.-S. Lai, W. S. Yu, and S.-Y. Park, "Variable timing control for wide current range zero-voltage soft-switching inverters," in *Proc. IEEE Appl. Power Electron. Conf.*, Washington, DC, Feb. 2009, pp. 407–412.

[80] W. Yu, J.-S. Lai, and S.-Y. Park, "An improved Zero-Voltage Switching Inverter Using Two Coupled Magnetics in One Resonant Pole," *IEEE Trans. Power Electron.*, vol. 25, no. 4, pp. 952–961, Apr. 2010.

[81] D. N. Zmwd and D. G. Holmes, "Stationary Frame Current Regulation of PWM Inverters with Zero Steady-State Error," *IEEE Trans. Power Electron.,* vol. 18, no. 3, pp. 814–822, May 2003.

[82] S.-Y. Park, C.-L. Chen, J.-S. Lai, and S.-R. Moon, "Admittance Compensation in Current Loop Control for a Grid-Tie LCL Fuel Cell Inverter," *IEEE Trans. Power Electron.,* vol. 23, no. 4, pp. 1716–1723, Jul. 2008.

[83] S.-Y. Park, C.-L. Chen, and J.-S. Lai, "A Wide-Range Active and Reactive Power Flow Controller for a Solid Oxide Fuel Cell Power Conditioning System," *IEEE Trans. Power Electron.,* vol. 23, no. 6, pp. 2703–2709, Nov. 2008.

[84] C.-L. Chen, Y. Wang, J.-S. Lai, Y.-S. Lee, and D. Martin, "Design of Parallel Inverters for Smooth Mode Transfer Microgrid Applications," *IEEE Trans. Power Electron.,* vol. 25, no. 1, pp. 6–15, Jan. 2010.

[85] J. L. Sawin and E. Martinot, "*Renewable 2010 Global Status Report*", Renewable Energy Policy Network for the 21st Century (REN21), pp. 15-16, 2010.

[86] U. Helman, "Preparing Power Markets for 2020," *CMTA Conference*, Jul. 2009

[87] E. Martinot and J. L. Sawin, "*Renewable Global Status Report: 2009 Update*", Renewable Energy Policy Network for the 21st Century (REN21), p. 12, 2009.

[88] C. Loutan, "Briefing on the California Independent System Operator Renewable Integration Study," *Board of Governors Meeting General Session*, Oct. 2007

[89] P. Ribeiro, B. Johnson, M. Crow, A. Arsoy, and Y. Liu, "Energy storage systems for Advanced Power Applications", *Proc. IEEE*, vol. 89, no. 12, pp. 1744–1756, Dec. 2000.

[90] Y. Jang and M. M. Jovanovic, "A Bridgeless PFC Boost Rectifier With Optimized Magnetic Utilization," *IEEE Trans. Power Electron.*, vol. 24, no. 1, pp. 85–93, Jan. 2009.